DESIGN AND CONTROL OF A BENCH-SCALE MOVING-BED THERMOCHEMICAL OXIDATION REACTOR FOR MAGNESIUM-MANGANESE OXIDE PARTICLES

By

Michael P. Hayes

A DISSERTATION

Submitted to
Michigan State University
in partial fulfillment of the requirements
for the degree of

Mechanical Engineering—Doctor of Philosophy

2024

ABSTRACT

The intermittency of renewable energy sources necessitates storage technologies that can help to provide consistent output on-demand. A promising area of research is thermochemical energy storage (TCES), which utilizes high-temperature chemical reactions to absorb and release heat. Due to these high operating temperatures, TCES technologies are well suited for industrial processes and other applications that require high grade heat. Metal oxides have been explored as excellent candidates for high temperature redox reactions, with various authors proposing stationary and moving energy storage systems. While promising, these technologies rely on storing chemically charged TCES materials at high temperatures, complicating handling and posing serious challenges to long-duration storage.

A pioneering approach known as SoFuel (solid state solar thermochemical fuel) proposed using counterflowing solid and gas streams in a particle-based moving-bed reactor to achieve heat recuperation and allow flows to enter and exit the reactor at ambient temperatures. Previous work has successfully demonstrated operation of a reduction (charging) reactor based on this concept; this dissertation describes the development of a companion oxidation (discharging) reactor. The countercurrent, tubular, moving bed oxidation setup permits solids to enter and exit at ambient temperatures, but the system also features a separate extraction port in the middle of the reactor for producing high-temperature process gas. A bench-scale experimental apparatus was fabricated for use with 5 mm particles comprised of a 1:1 molar ratio of MgO to MnO, a redox material that exhibits high oxidation temperatures (around 1000°C) and excellent cyclic stability.

The experimental oxidation system successfully demonstrated self-sustaining thermochemical oxidation at temperatures in excess of 1000°C, producing sufficient energy via exothermic chemical reaction to sustain heat extraction and offset system losses. Many trials achieved largely steady operation, demonstrating operational stability during hours-long experiments. With the aid of user-manipulated inputs, the reactor produced extraction temperatures in excess of 950°C and demonstrated efficiencies as high as 41.3%. Heat losses were observed to have a strong effect on the performance of the bench-scale reactor, leading to relatively low rates of energy extraction

on the order of 200-500 W. Furthermore, an extensive experimental campaign revealed thermal runaway in the upper reaches of the particle bed as a risk to safe, stable reactor operation. A rudimentary on/off recuperative gas flow control scheme was successfully implemented to mitigate runaway, although the method was unable to optimize other aspects of reactor behavior.

To better understand reactor dynamics and evaluate potential control schemes, a three phase, one-dimensional finite-volume computational model was developed. The model successfully emulated behavior from the on-reactor experiments and further illustrated the impacts of the three system inputs - solid flow rate, gas extraction flow rate, and gas recuperation flow rate - on overall behavior. A five-zone adaptive model predictive controller (MPC) was developed using a linearized control-volume model as its basis. The controller sought to regulate the size, temperature, and position of the chemically reacting region of the particle bed through several novel approaches. These approaches were tuned and refined iteratively using the 1D computational model, after which they were successfully deployed on the experimental setup. Multiple control strategies allowed for successful temperature regulation, reaction zone positioning, and high-temperature gas extraction from the bench-scale reactor. Future work concerns scaling up the oxidation system for larger rates of energy extraction, further analysis of optimal reactor startup procedures, and alternative controller formulations.

ACKNOWLEDGEMENTS

I am incredibly grateful for the many people who have made the completion of my doctoral degree possible. First and foremost, I would like to thank my wife, Meg, for her unwavering support over these past four years. I am also grateful to my parents, Ann and Bob, for instilling in me my concern for sustainability and the values and discipline necessary for pursuing a graduate degree. I additionally thank my brothers, Robert and Matthew, for their encouragement throughout my program.

Many people at Michigan State University have dedicated their time and energy toward assisting my studies, for which I am immensely thankful. Dr. James Klaunser first invited me to MSU, and he and my first advisor, Dr. Jörg Petrasch, helped to introduce me to thermochemical energy storage and the world of academic research. Dr. André Bénard, my second advisor, has been invaluable in helping me to complete my degree and prepare for the next stages in my academic journey. I am grateful to my dissertation committee, comprised of Dr. Benard, Dr. Klausner, Dr. Neil Wright, and Dr. Charles Petty, for their steadfast support and knowledgeable insights as well. Several faculty members, including Dr. Geoffrey Recktenwald, Dr. Rebecca Anthony, and Dr. Guoming Zhu, provided further support and mentoring as I completed my program - I would like to thank all of them as well. I would certainly not be here without the tireless efforts of Jessica Pung either, who was a constant source of knowledge and assistance as I completed my degree.

I would also like to thank the graduate students and postdoctoral researchers who created a supportive, collaborative working environment during my studies. To Dr. Philipp Schimmels, Aaron Feinauer, Aiman Aweeen, Dr. Keith King, Dr. Alessandro Bo, and Dr. Nima Rahmatian - thank you all for your friendship and intellectual curiosity. I would particularly like to acknowledge Dr. Kelvin Randhir for being a hugely supportive mentor during my first few years at MSU. I am grateful to him both as the architect of the oxidation reactor that I would eventually dedicate my studies to, but also as a teacher who freely shared his expertise and supported my studies.

Lastly, I would like to acknowledge the financial supporters that have made my studies possible. My dissertation material is based upon work supported by the U.S. Department of Energy's Office

of Energy Efficiency and Renewable Energy (EERE) under the Solar Energy Technology Office, award number DE-EE0008992. I gratefully acknowledge the financial support from the United States Advanced Research Projects Agency-Energy (ARPA-E) via award No. DE-AR0000991 for these efforts as well. I additionally thank MSU's University Distinguished Fellowship (UDF) program for its support of the research presented in this dissertation.

TABLE OF CONTENTS

LIST OF SYMBOLS

Greek Letters

α	Extent of conversion (-)
β	Percent mass change between the base reduction and oxidation states (-)
Γ	Extensive heat transfer coefficient (W/K)
γ	Heat transfer coefficient (W/m^2 K)
Δ	Change in a quantity (-)
ΔH_{rxn}	Enthalpy of reaction (kJ/mol O_2)
ε	Porosity (-)
η	Efficiency (-)
λ	Kinetics coefficient
μ	Dynamic viscosity (kg/m s)
ξ_{ox}	Oxygen mass fraction (-)
π_s	Specific extent of conversion (1/kg)
ρ	Density (m^3/kg)
σ	Chemical potential (J/mol)

Roman Letters

A	State matrix
A	Area (m^2)
A_0	Arrhenius constant (mol K/J/s)
Ar	Archimedes number (-)
a	Specific area (1/m)
B	Output matrix
C	Input matrix
C_{ox}	Oxygen concentration (kg/m^3)

c_p	Specific heat at constant pressure (J/kg K)
D	Diameter (m)
D_h	Hydraulic diameter (m)
d_p	Particle diameter (m)
E	Total energy (J)
E_a	Activation energy (J/mol)
H	Enthalpy (J)
h	Specific enthalpy (J/kg)
h_c	Controller control horizon (-)
h_p	Controller prediction horizon (-)
J	Cost (-)
k	Thermal conductivity (W/m K)
L	Length (m)
$\mathbf{M}_x$	Kalman gain
M	Molar mass (g/mol)
m	Mass (kg)
$\dot{m}$	Mass flow rate (kg/s)
$\dot{m}_{g,ext}$	Gas extraction mass flow rate (kg/s)
$\dot{m}_{g,recup}$	Gas recuperation mass flow rate (kg/s)
$\dot{m}_s$	Sold mass flow rate (kg/s)
Nu	Nusselt number (-)
$\dot{n}$	Molar flow rate (mol/s)
P	Pressure (Pa)
p	Solid chemical potential coefficient
Pe	Peclet number (-)

Pr	Prandtl number (-)
$\mathbf{Q}$	Input noise covariance matrix
$\dot{Q}$	Rate of heat transfer (W)
$\dot{Q}_{chem}$	Rate of energy release due to chemical reaction (W)
$\dot{Q}_{ext}$	Rate of energy extraction (W)
R	Ideal gas constant for air (J/kg K)
$\mathbf{R}$	Measurement noise covariance matrix
Re	Reynolds number (-)
r	Radius (m)
$\dot{r}_{ox}$	Rate of oxygen consumption (kg/s)
s	Scaling factor (-)
T	Temperature (K, or °C)
T_s	Controller sample period (s)
t	Time (s)
U	Overall heat transfer coefficient (W/m^2 K), internal energy (J)
u	Velocity (m/s)
$\mathbf{u}$	Input vector
V	Volume (m^3)
v	Oxygen chemical potential temperature coefficient
$\dot{V}$	Volumetric flow rate (SLPM)
$\dot{W}$	Rate of work transfer (W)
w	Weight (-)
$\mathbf{x}$	State vector
x	Axial length (m)
$\mathbf{y}$	Output vector

y	Mole fraction (-)

Subscripts

amb	Ambient
cond	Conduction
cv	Control volume
ext	Extraction
g	Gas
gs	Gas-solid
i	Inner
in	Inlet
initial	Initial
ins	Insulation
lm	Log-mean
minus	Relating to the boundary between the current cell and the one below it
N_2	Nitrogen
o	Outer
op	Operation
out	Outlet, outer reactor shell
ox	Oxidized/oxidation, oxygen
O_2	Oxygen
O_2 sep	Oxygen separation
p	Particle
plus	Relating to the boundary between the current cell and the one above it
pump	Pumping
recup	Recuperation

ref	Reference
red	Reduced/reduction
s	Solid
startup	Startup costs prior to reactor operation
stp	Standard temperature and pressure
w	Wall
water	Water
wg	Wall-gas
ws	Wall-solid
w,ins	Wall-insulation

CHAPTER 1

INTRODUCTION

A rapidly changing energy landscape has catapulted sustainability and reliability to the forefront of discussions concerning the future of power generation and storage. After decades of intensive fossil fuel use, elevated levels of carbon dioxide and other greenhouse gases in the atmosphere are altering global climactic conditions and contributing to more severe weather outcomes [3]. Besides transportation, industrial and residential applications are the largest fossil fuel-comsuming sectors in the U.S. [4]. Utilities that supply the power required for these sectors are accelerating their adoption of renewable, zero-carbon energy technologies, with rapid adoption expected to continue over the next 40 years [5]. Indeed, over the past decade there has been a strong proliferation in wind and solar energy research [6]. This adoption is in part a result of greater environmental consciousness, but is also driven strongly by the rapidly decreasing cost of these renewable energy sources.

At the same time, uncertainties in global markets and recent geopolitical events have exacerbated fossil fuel shortages and raised questions about the long-term availability of such energy sources [7]. Many countries are accelerating their plans to phase out carbon-intensive energy sources. Domestic energy production is becoming increasingly attractive as countries consider economic, environmental, and social pressures [8] [9]. The increasing affordability of renewable energy sources, then, means that these technologies are poised for even more rapid implementation. As referenced previously, the cost of production for solar PV and onshore wind have fallen precipitously in the last decade, decreasing by 82% and 39%, respectively, between 2010 and 2019 [10].

While utilities and consumers embrace these renewable sources, some challenges still remain that inhibit their wider use. The manufacture of many renewable technologies requires rare-earth metals, materials that are becoming increasingly desirable due to larger trends in electrification. Furthermore, rare-earth deposits tend to be geographically concentrated, with China currently controlling around one third of all reserves and dominating global production [11]. Besides

Some material in this chapter was originally published in [1] and [2].

manufacturing hurdles, one of the main drawbacks for energy sources such as wind and solar is inherent intermittency. The installed wind and solar capacity of many areas is, with consistent output, enough to completely provide for a region's energy needs. Problems arise when uncontrolled factors such as weather and time of day inhibit renewable sources from producing peak output continuously. An urgent need exists for energy storage technologies to smooth out the intermittent nature of renewable sources.

Various technologies have been developed to provide this desired grid consistency [12] [13]. Electrical batteries are perhaps the most familiar medium, with excellent energy density and reliability. A high cost of scaling and increasing material scarcity, however, make them difficult to adequately implement at grid scale [14]. Pumped hydropower provides another option for storage, utilizing the gravitational potential of high-elevation water reservoirs to store excess energy. While appropriate in some settings, such systems require immense amounts of water and favorable geology, making them unsuitable for most locations. Other storage technologies rely on thermal gradients rather than voltage or gravitational differences. Such systems are known simply as thermal energy storage, or TES. Molten salts and phase change materials are two such examples, but these are generally more expensive than batteries. In addition, many TES technologies rely on high temperatures (often exceeding 600°C), requiring specialized materials. Energy storage density is limited by the heat capacity of the storage medium or latent heat of phase change. In order to further increase storage density and widen applicability, recent research has considered the addition of high temperature chemical reactions to traditional thermal storage. Such technologies are known as thermochemical energy storage, or TCES.

1.1 Thermochemical Energy Storage

TCES is characterized by chemical reactions that convert materials into a high-energy state, often driven by elevated temperatures. This makes the technology a particularly good match for renewable sources like concentrated solar, which can be used to produce high temperatures [15] [16]. Metal oxides are particularly well suited for solar-driven TCES due to their ability to facilitate redox reactions. Wu [17], in a review on the subject, provides the following general characterization

for redox systems:

$$M_xO_y + \Delta H_{rxn} \rightarrow M_xO_{y-1} + \frac{1}{2}O_2 \tag{1.1}$$

$$M_xO_{y-1} + \frac{1}{2}O_2 \rightarrow M_xO_y + \Delta H_{rxn} \tag{1.2}$$

These equations showcase the fundamental operating principle of such systems: oxygen is dissociated from a metal oxide in an endothermic reduction step, while an exothermic oxidation process adds oxygen back to the metal and releases the stored energy. While metal oxides can be utilized for processes like solar thermochemical water splitting and other processes [18] [19] [20], renewed attention is being paid to redox materials as energy storage media in their own right. Numerous metal oxides have been considered for their usefulness in thermochemical redox processes [21] [22] [23]. Among these, cobalt oxides [24] and iron-manganese oxides [25] appear most frequently in reactor designs proposed in the literature.

1.1.1 Existing TCES Technologies

Traditionally, thermochemical energy technologies have focused on utilizing metal oxides as a transitory medium for storing sensible and chemical energy. Solar thermochemical redox reactors can generally be classified as one of two categories: stationary or moving. Stationary reactors consist of a fixed metal oxide medium that is either directly exposed to solar radiation or encounters gases preheated by incoming solar energy. Tescari et al. [26] consider the use of a honeycomb extrusion of cobalt oxide for stationary storage, with later experiments featuring charging and discharging in a range of around 640-970°C, a combined (sensible and chemical) energy density of 630 kJ/kg [27], and stability over the course of up to 22 charging and discharging cycles [28]. Wokon et al. [29] implement a packed bed of iron-manganese particles rather than a honeycomb structure, using hot gases to reduce particles at temperatures up to 1040°C before facilitating oxidation at temperatures over 920°C for 17 cycles. Wang et al. [30] propose another packed bed design, this time focusing solely on the reduction process. Iron-manganese particles are housed directly inside of a simulated solar cavity, where incident radiation and argon sweeping gas facilitate a peak solar-to-chemical efficiency of 9.3% at a reaction temperature of around 1100 K. The other common reactor category, defined by mobile metal oxide contents within the system, is similarly diverse.

Neises et al. [31] present a rotary kiln redox reactor for cobalt oxides, carrying out reduction at 900°C through simulated solar radiation and oxidation via the introduction of an external gas flow. The combined chemical and potential energy stored averaged close to 400 kJ/kg across 30 cycles. Oxidation occurred below 850°C. Other popular designs can be classified as moving bed reactors, where particles are typically reduced, carried downstream to an oxidation setup, and oxidized by a counterflow gas that additionally serves as an extracted working fluid. Bush et al. [32] consider the case of a moving bed reactor for use in an air Brayton cycle, predicting a cycle efficiency of 46% for the case of iron oxide particles. A similar study is performed by Schrader et al. [33], where a Brayton-coupled moving bed reactor is simulated. For this case, cobalt oxide particles are reduced at 1050 K and reach 44% oxidation efficiency at 30 bar. By utilizing mixed ionic-electronic conductors, Miller et al. [34] anticipate reaction enthalpies up to 390 kJ/kg for a curtain-like reduction reactor and connected counterflow oxidation reactor. Babiniec et al. [35] further elaborate on the work of Miller et al., predicting that extracted recuperation gas temperatures in the counterflow oxidation reactor can exceed the particles' inlet temperature, 1200°C compared to 1050-1150°C, respectively. Experimental studies by Preisner et al. [36] with iron-manganese particles in a counterflow moving bed produce around 2 kW and exhibit a combined sensible and chemical storage capacity of 569 kJ/kg. The maximum gas extraction temperature maintained at the onset of the experiment is 900°C, though this value decreases over time. Schrader et al. [37] further describe results utilizing aluminum-doped calcium manganite particles in a reduction setup to achieve an absorption efficiency of 64.7%, particle reduction temperature exceeding 1073 K, and storage rate of 5 kW thermal. Most recently, Tescari et al. [38] describe an iron-manganese oxide moving bed oxidation reactor coupled to a rotary kiln reduction setup. The authors document a release of 2.1 kW via the counterflow oxidation setup, producing gases heated up to 880°C. All three of these authors mention agglomeration among particles as a challenge of operation, particularly at high temperatures.

The reduction-oxidation designs discussed thus far assume that reduced products will be stored at high temperatures prior to oxidation. These high temperatures are identified as necessary for two

reasons: to provide the conditions necessary for the release of stored chemical energy and to provide sensible energy for extraction. Investigations have been performed into minimizing these losses [39] [40], but long duration storage remains challenging. For remote environments such as Alaska, which experiences periods of continuous sunlight eventually followed by periods of continuous night, long term storage is vital to ensure year-round energy availability [41]. Furthermore, hot particles must be stored on-site, necessitating oxidation reactors to be located proximate to the reduction setup. Without the ability to geographically decouple the production of reduced materials from their oxidation, thermochemical energy storage must remain largely centralized.

1.2 The SoFuel Project

A deficiency exists, then, in the capability of current TCES technologies to provide energy storage and subsequent usage that is spatially and temporally distanced from the charging process. This limits the applicability of these technologies, since grid-scale renewable energy sources tend to be distant from population and industrial centers. While electrical transmission may minimize some losses, extracted hot gases cannot be utilized directly for industrial or heating purposes, decreasing the applicability and use-cases of these technologies.

1.2.1 Project Overview

A novel approach has been developed to eliminate the current restrictions imposed on TCES. Dubbed SoFuel, the project is named for its paradigm-shifting way of considering TCES materials not as stationary storage media, but rather as **so**lid-state **fuel**. The term "fuel" is used here not to denote any kind of liquid hydrocarbons. Instead, considering the TCES material as fuel envisions a mobile, divisible energy storage technology that can be transported over large distances and utilized at the desired time.

Several key innovations are necessary to realize this design. First, the TCES material is pelletized in order to allow for ease of transportation and divisibility. Particles favor a moving-bed reactor design; current moving-bed designs, however, still store particles at elevated temperatures prior to energy extraction. The hallmark of the SoFuel project is its solution to this problem: rather than store sensible energy alongside chemical energy, the sensible energy of particles exiting the

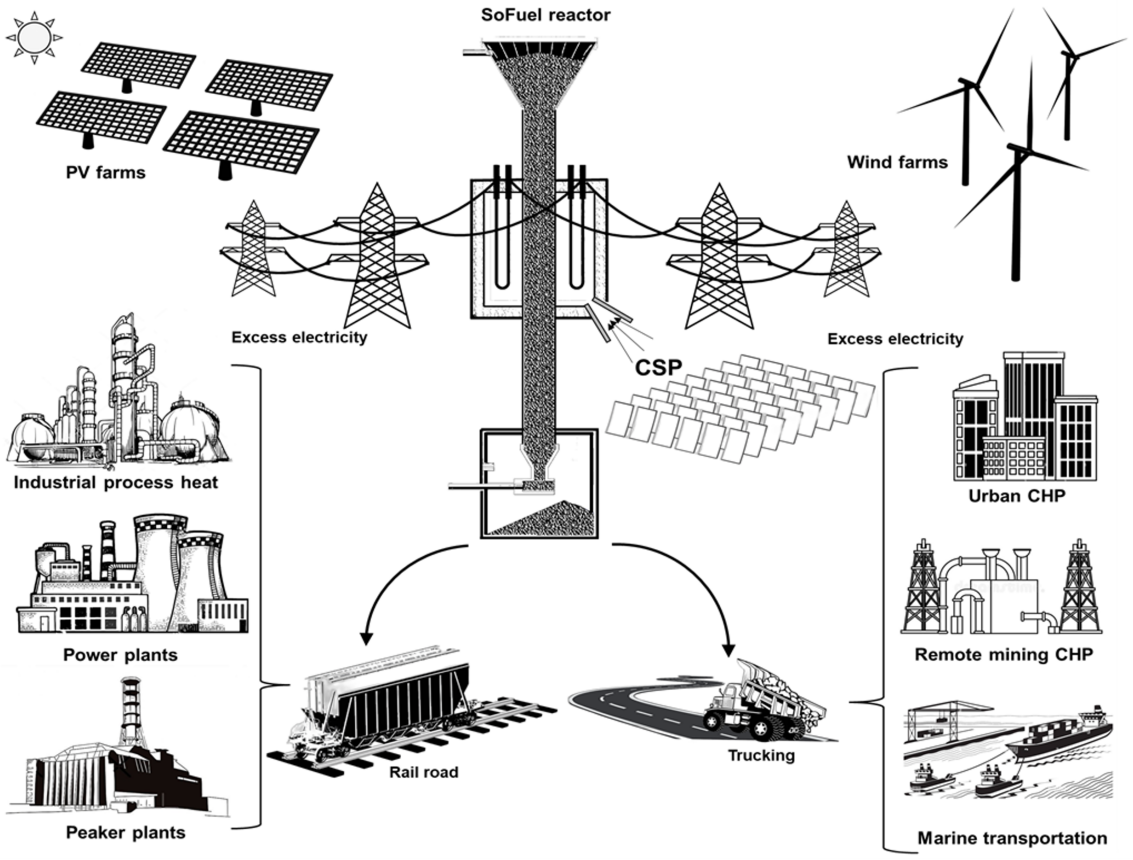

Figure 1.1 An overview of the SoFuel process. Renewable energy sources power the thermochemical reduction of a moving bed of Mg-Mn-O particles, which can then be stored or transported to various use cases. Originally printed in [1].

reactor is recuperated and used to preheat new incoming particles. As a result, the pelletized TCES material is collected outside the reactor at temperatures as low as ambient.

As depicted in Figure 1.1, the SoFuel concept fully decouples the production of charged TCES fuel from the end use. SoFuel particles enter the reduction reactor, undergo reaction at high temperatures (facilitated by either concentrated solar energy or an electric furnace driven by solar PV or wind), and exit the reactor at ambient temperature. From there the charged particles can be transported by any transportation available, including by truck, rail, or ship. These modes of transit enable SoFuel to then be delivered to its final usage destination, where the released chemical energy can drive industrial processes, support a peaker plant, or simply provide high-quality heat for remote applications. After undergoing oxidation and becoming depleted, the particles are simply transported back to the reduction reactor and charged once more.

1.2.2 Magnesium-Manganese Oxides

Redox material selection plays a key role in the viability of the SoFuel concept. A barrier to ambient-temperature particle storage is the necessity for the chemical energy stored during reduction to be large enough to reheat the particles to the elevated temperatures required for oxidation and subsequent heat extraction. Iron manganese oxide, for example, exhibits a chemical energy density of 188 kJ/kg [30], but the sensible energy required for heating from ambient to the minimum oxidation temperature is 235 kJ/kg. This inhibits iron manganese oxides from being a suitable candidate for the SoFuel concept.

A novel redox material with a suitable energy density for this application is magnesium manganese oxide, comprised of a 1:1 molar ratio of MgO and MnO (all further references to this material will simply use the term Mg-Mn-O). The 1:1 material has been previously deployed in a packed-bed reactor [42]. The following equation characterizes the reversible redox reaction of Mg-Mn-O:

$$\mathrm{MgMnO_{2+x}} + \frac{y-x}{2}\mathrm{O_2} \leftrightarrow \mathrm{MgMnO_{2+y}} + \Delta H_{rxn} \tag{1.3}$$

where ΔH_{rxn} is the enthalpy of reaction at a value of 380 ± 35 kJ per mole of O_2 absorbed [43] [44]. The same drop calorimetry experiments that determined this enthalpy of reaction also established a chemical energy density of 586.3 ± 55.0 kJ/kg for the material, as well as a total enthalpy change of 927.1 ± 8.5 kJ/kg on the temperature interval of 25 to 1000°C. This interval produces an average specific heat capacity of 950 ± 8.7 J/kg K. Based on Mg-Mn-O kinetics as modeled by Randhir et al. [45], an approximation for the minimum onset of oxidation is 600°C. Using the average specific heat, heating the material from ambient (25°C) to the onset of oxidation requires approximately 546 kJ/kg. This value is less than the chemical energy density of the material itself, making Mg-Mn-O an excellent choice for SoFuel.

The other key reason for selecting Mg-Mn-O as the SoFuel material is its excellent reactive stability, both cyclically and long-term. The SoFuel concept requires particles that are able to undergo repeated reduction and oxidation experiments without losing a significant amount of mass, as particles that fall apart over time lead to higher costs and more logistical challenges. Mg-Mn-O

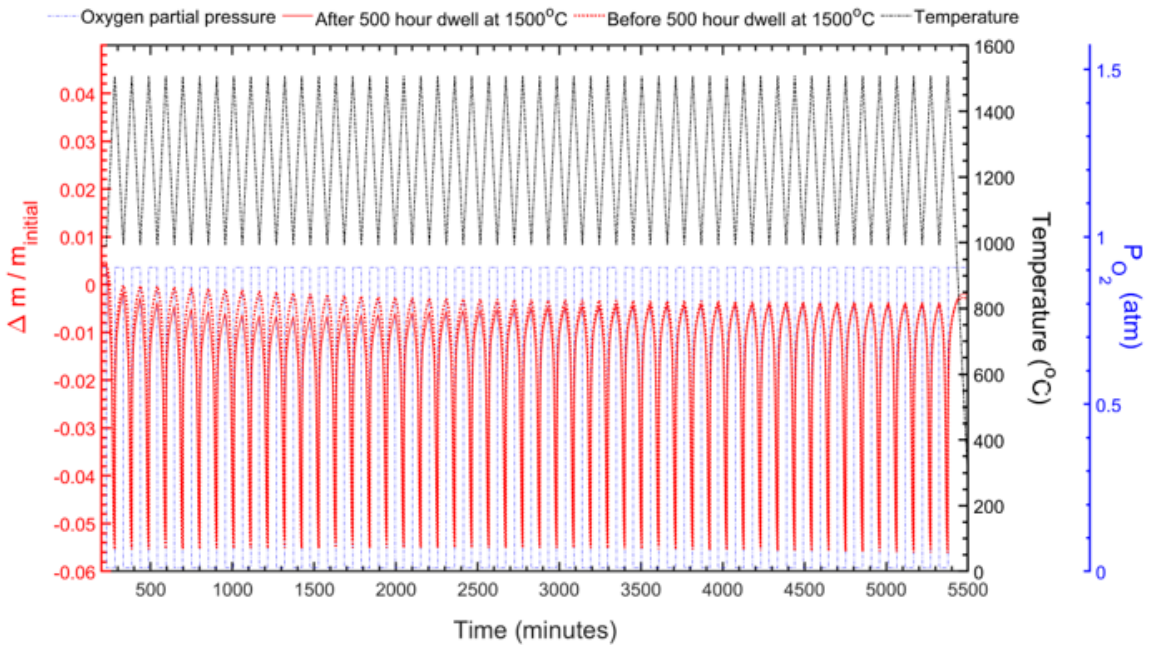

Figure 1.2 A 50 cycle temperature and oxygen partial pressure test profile for the Mg-Mn-O redox material. The material exhibits excellent cyclic stability, with little degradation in reactivity after the first 20 cycles. Originally printed in [1].

was tested in a Netzsch Jupiter F5 thermogravimetric analyzer (TGA), cycling between temperatures of 1000 and 1500 °C with oxygen partial pressures of 0.01 atm during heat up and 0.9 atm during cooling. The material was first cycled 50 times, then dwelled at 1500 °C for 500 hours. After this dwell, the material was once again subjected to 50 TGA cycles. The results of this cycling are shown in Figure 1.2. Although there are some minor discrepancies between the two profiles, after the initial ten to twenty cycles the Mg-Mn-O reaches a steady mass fluctuation in each cycle.

The remarkable cyclic stability of the SoFuel material is due in part to the conducive surface phenomena that occur on the face of individual SoFuel particles. Because the redox reaction depicted in Equation 1.3 requires either the uptake or expulsion of gaseous O_2, individual particle porosity is key to ensuring that high-temperature reactions penetrate as deeply into the particle as possible. A potential problem that can arise is the filling of pores over time - clogging events that restrict the diffusion of gases in and out of the particle. To assess whether the surface of the SoFuel particles become less porous over time, scanning electron microscope (SEM) images were produced before and after cycling using a JEOL 6610 L V. The produced scans are shown in Figure

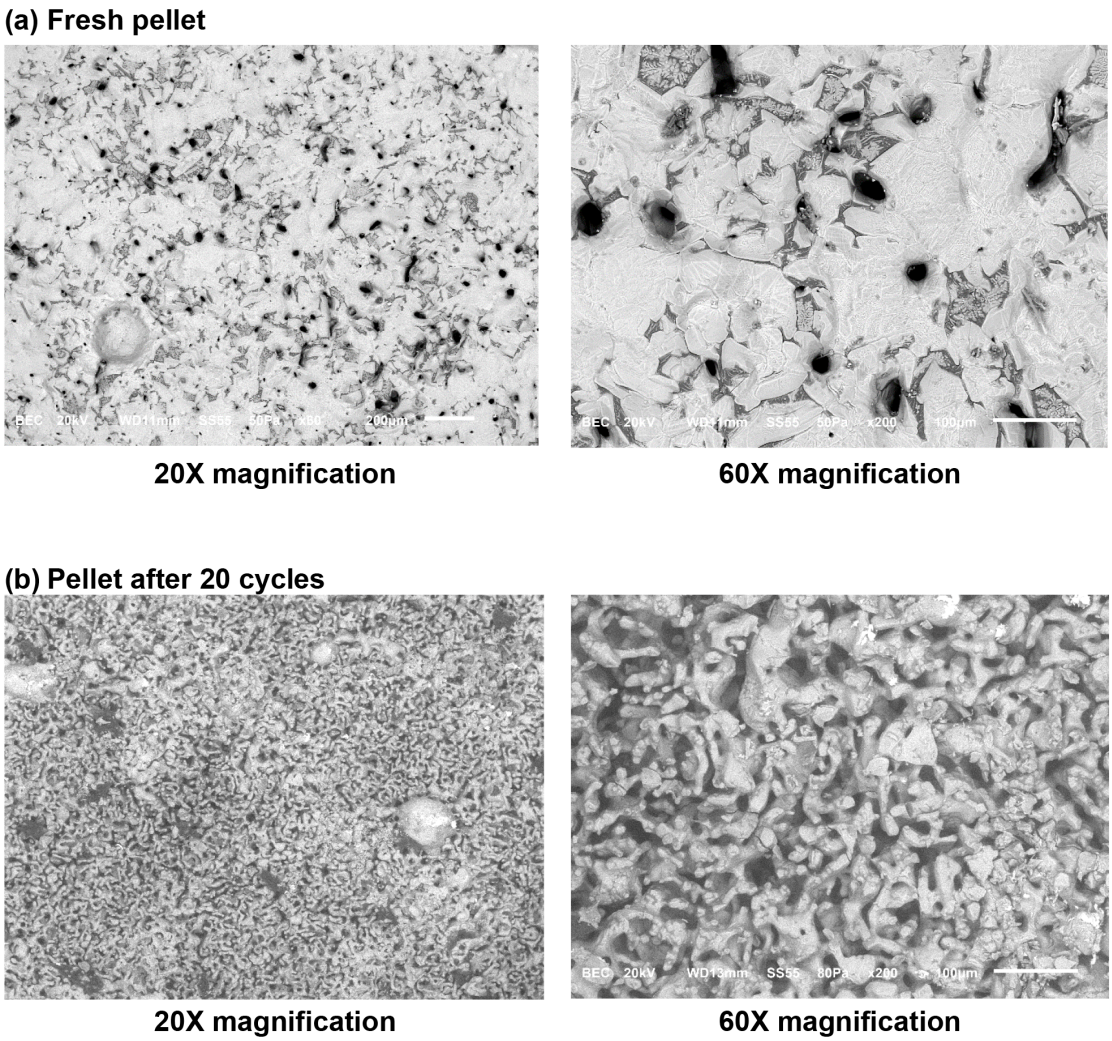

Figure 1.3 Pore proliferation on the surface of an Mg-Mn-O pellet. After 20 thermochemical cycles, the material still contains surface perforation to due pore regeneration mechanisms. The abundance of pores aids in gas exchange and facilitates the cyclic stability of the material. Originally printed in [1].

1.3. Rather than shrink, the pores on the surface of the SoFuel particle actually proliferate and regenerate, allowing the particle to maintain excellent reactivity even after many cycles.

The final aspect of stability exemplified by Mg-Mn-O is long-term reactivity and storage capacity. One of the primary functions of SoFuel is to allow for reduction and oxidation to occur not just in different places but also at different times. Months-long seasonal storage is a key use case for areas such as Alaska, which experience a high volume of solar energy at certain times of the year and a paucity in others. To assess Mg-Mn-O's long term stability, reduced particles were set aside in an unsealed container. Some of these particles were immediately assessed in the TGA for stored energy content, while others remained in the container for intervals of 125 days (> 3 months) and 190 days (> 6 months). These stored samples were tested in the TGA at the conclusion of each period. Changes to the stored energy between each sample were negligible, within the margin of measurement error across the three cases. This further supports the viability of Mg-Mn-O as an ideal material for use in the SoFuel project.

1.2.3 Reduction Reactor

As described in Section 1.2.1, one of the most important aspects of the SoFuel project is the entrance and exit of particles at ambient temperatures, achieved through a heat-recuperating gas counterflow. Specifically, this counterflow is designed to balance out the energy carried out of the main reaction zone by downward moving particles. In equation form, this relationship is expressed as:

$$\dot{m}_s c_{p,s} = \dot{m}_g c_{p,g} \tag{1.4}$$

where $\dot{m}_s$ and $\dot{m}_g$ are the particle and gas mass flow rates, respectively, and $c_{p,s}$ and $c_{p,g}$ are the solid and gas specific heat capacities, respectively. Based on this relationship, an appropriate gas counterflow can be initiated in response to a set solid flow rate.

With this functionality in mind, a reduction reactor was designed and fabricated. The reactor layout is depicted in Figure 1.4. The design features a ceramic reaction tube fitted within an electric furnace, although concentrated solar energy could be utilized as well. SoFuel particles are loaded into the top of the system, after which they make their way into the main reaction zone. The

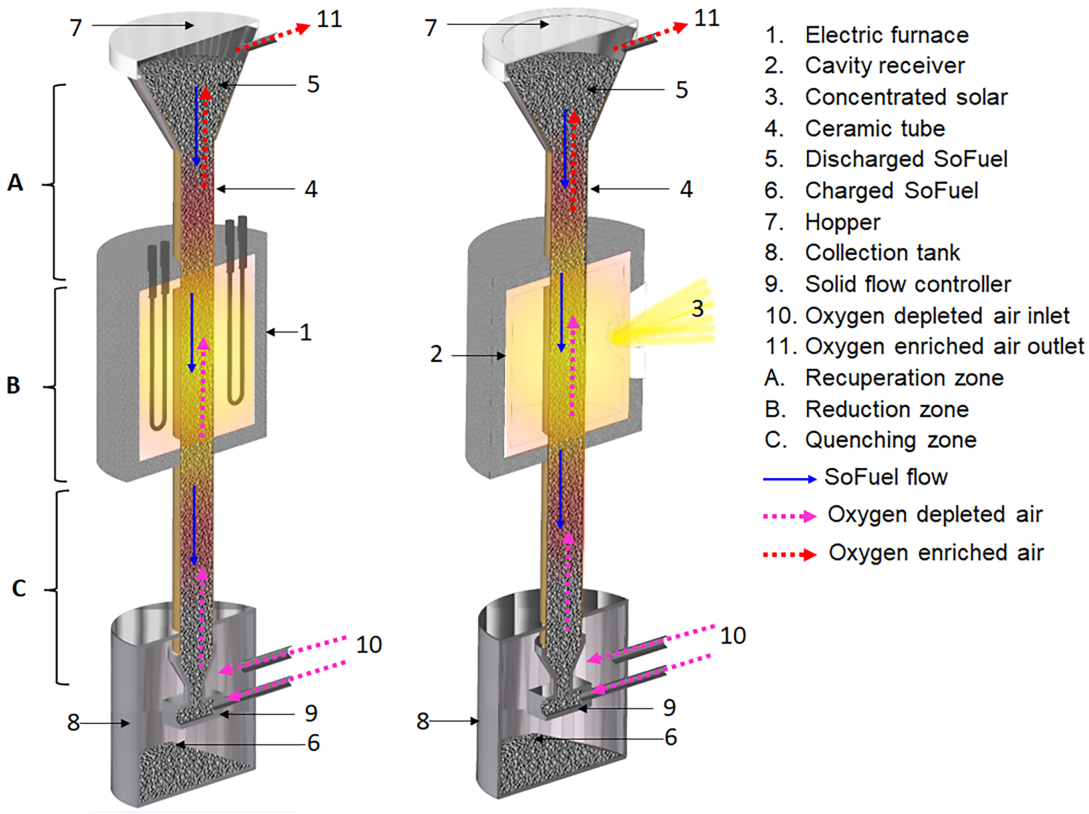

Figure 1.4 Two possible configurations of the SoFuel reduction reactor, driven by electricity on the left and solar energy on the right. Counterflowing solids and gases enable streams to enter and exit the reactor at close to ambient temperatures. Originally printed in [1].

particles become charged at temperatures high enough to facilitate reduction. Reduction is followed by further downward movement into a collection bin. Throughout the particles' path through the system, a counterflow of oxygen-depleted gas provides heat recuperation and an environment favorable to reaction. The upward-moving gas recovers heat from particles leaving the reaction zone, then promptly passes its own energy on to particles in the top section of the bed. This ensures that the gas, like the particles, also enters and exits the system at close to ambient temperatures. High surface area between the particle bed and the gas allows for elevated heat transfer between the two phases. This mechanism drastically decreases the axial losses of the system. Specifics regarding the design and operation of the reduction setup will not be discussed in detail here, though more information can be found in recent publications [1].

CHAPTER 2

OXIDATION REACTOR CONCEPT

The successful demonstration of the SoFuel reduction reactor necessitates the conceptualization and creation of a complimentary oxidation setup. Several concepts were considered over the course of the project. One such design, a fluidized bed reactor utilizing hollow wall-plates to facilitate heat exchange, is current in development. This design, which has a working fluid pass over the walls housing the fluidized particle bed, allows for isolation of the working fluid from any dust or fines produced during fluidized bed operation. One consequence of this design, however, is a departure from the simplicity that distinguishes the reduction reactor. The SoFuel reduction setup is geometrically simple and does not require any high-temperature or custom-machined parts beyond those that are widely available off-the-shelf. For applications that are unaffected by the occasional presence of fines or dust, such as industrial processes that simply seek to utilize heat, a direct heat transfer design, in which the working fluid directly interacts with the SoFuel particles, has many of the benefits of the SoFuel reduction setup. Direct contact between the particles and the working fluid yields more effective heat transfer, and the overall system can be designed to be simpler and more straightforward.

Several oxidation reactors were described previously in Section 1.1, including the moving-bed designs of Tescari et al. [38] and Preisner et al. [36]. While these reactors exhibit success in extracting energy from oxidizing particle beds, they rely on an upward-moving gas flow to carry energy out of the top of the particle bed. Such an approach is not well suited to the SoFuel concept; particles are fed into the reactor at ambient temperatures, so an extraction from the top of the bed would eliminate the utilization of low temperature materials. Such a design would also make it difficult to introduce new particles to the reactor for longer duration operation. This is not a problem for the previous authors' designs, as the presented reactors seek to extract both sensible and chemical energy from particles previously stored at high temperatures.

Some material in this chapter was originally published in [2].

2.1 Three-Port Design

A reactor design that maintains the ambient temperature of the SoFuel particles at the inlet and outlet, then, is imperative to the oxidation design. Rather than extract high temperature gases from the top of the bed, consider Figure 2.1. In this design, described as a "three port" reactor, particles enter and exit the system at ambient temperatures. Like the reduction design, a counterflow of gas cools down the particles exiting the main reaction zone while also providing preheating to the incoming SoFuel pellets. The third port, exiting the reactor from the main reaction zone, provides the major differentiation. A fraction of the gas introduced at the base of the reactor exits the system directly from the hottest area of the reactor. Due to the high rate of heat transfer between the gas and the oxidizing particles, the extracted gas exits the reactor at temperature comparable to those of the particles. Due to the high chemical energy density of Mg-Mn-O and its elevated temperature required for oxidation, the extracted gas is expected to reach temperatures exceeding 800°C.

Similar to the reduction reactor design, a gas counterflow is required to ensure that the apertures of the reactor (not including the extraction port) are maintained at ambient temperatures. Due to the addition of the outlet extraction gas flow, the recuperative flow in the oxidation reactor cannot simply be defined as the gas flow introduced at the base of the reactor. The relationship between the three flows, while straightforward, is helpful to define explicitly:

$$\dot{m}_{g,in} \approx \dot{m}_{g,recup} + \dot{m}_{g,ext} \tag{2.1}$$

where $\dot{m}_{g,in}$ is the inlet gas flow, $\dot{m}_{g,recup}$ is the recuperative gas flow, and $\dot{m}_{g,ext}$ is the extraction gas flow. The recuperative flow here is defined as the gas flow exiting the reactor at its top, where particles enter. The relationship between these three is defined as approximate due to the consumption of some oxygen during the oxidation reaction. This difference in oxygen, though large enough to be noticeable, is not so drastic as to inhibit the establishment of Equation 2.1 as an approximate relationship for general reactor consideration.

2.2 Operating Limits

The three-port design concept can be examined for an ideal case to evaluate the maximum operating parameters of the reactor. As established thus far, an idealized reactor design will

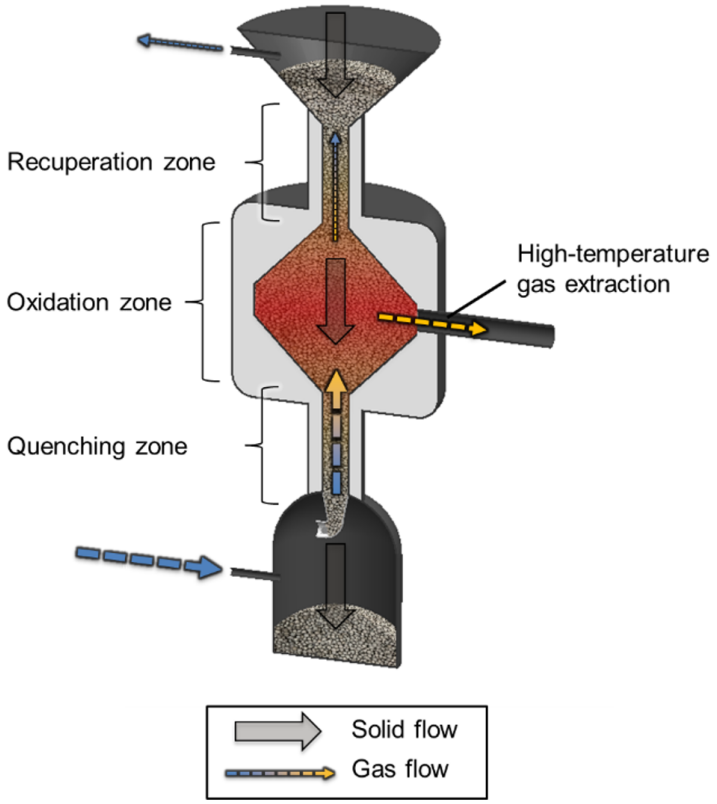

Figure 2.1 A conceptual design of a three-port oxidation reactor. Gases and solids flow counter to one another like in the reduction setup, but a fraction of the gas flow exits the middle of the reactor at high temperatures.

recuperate energy from high temperature particles exiting the reaction zone and remove produced energy from the particle bed via an extraction port inserted into the reaction zone. The only other requirement for the reactor is that the particle inlet and exit occur at approximately ambient temperature. Consider, then, the case shown in Figure 2.2. The dotted line denotes a control volume. Oxidized SoFuel particles are removed from a perfectly insulated reactor at a given solid mass flow rate, $\dot{m}_{s,out}$, and ambient temperature, T_{amb}. An oxygen-rich gas flow, $\dot{m}_{g,in}$, also enters the reactor at T_{amb}. The relationship between $\dot{m}_{s,out}$ and $\dot{m}_{g,in}$ is defined by Equation 1.4, which includes the solid and gas specific heats, $c_{p,s}$ and $c_{p,g}$, respectively. Gas exits the reactor at some extraction temperature T_{ext}.

During the course of operation, the SoFuel particles undergo some degree of oxidation. The extent of conversion, α, is a quantity used to characterize the reactive state of the Mg-Mn-O

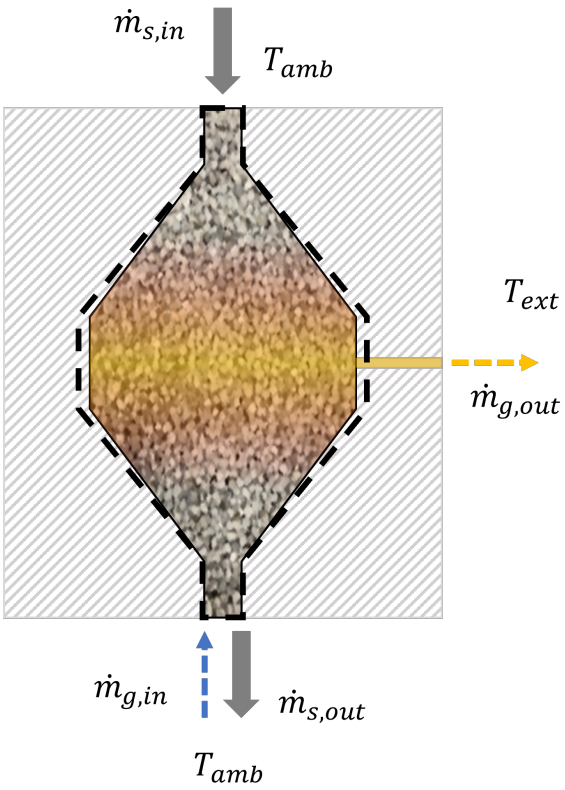

Figure 2.2 An idealization of the three-port oxidation reactor in which the extracted gas flow provides full recuperation to the lower reaches of the particle bed. The dashed line denotes the control volume boundary.

material. It is bounded by two points: a minimum extent of conversion of 0% corresponding to the state produced by dwelling at 1500°C with an oxygen partial pressure of 0.01 atm, and a maximum extent of 100% representing the state produced by 1000°C at an oxygen partial pressure of 0.9 atm. The quantity can be mathematically expressed as:

$$\alpha = \frac{m - m_{red}}{m_{ox} - m_{red}} \tag{2.2}$$

where m is the material mass, m_{red} is the reference reduced state, and m_{ox} is the reference oxidized state. Let β represent the percent mass change between these base reduction and oxidation states. For the Mg-Mn-O material, β = 0.0698. If $\Delta\alpha$ describes the magnitude of the change in extent of conversion, the solid flow rate entering the reactor can be defined as:

$$\dot{m}_{s,in} = \dot{m}_{s,out}(1 - \beta\Delta\alpha) \tag{2.3}$$

where $\dot{m}_{s,in}$ represents the inlet solid flow from the top of the reactor. Together with Equation 1.4,

the gas flow rate exiting the reactor, $\dot{m}_{g,out}$, is represented by:

$$\dot{m}_{g,out} = \dot{m}_{s,out}\left(\frac{c_{p,s}}{c_{p,g}} - \beta\Delta\alpha\right) \tag{2.4}$$

Having defined all mass flows in terms of $\dot{m}_{s,out}$, it is next useful to express the energy released during oxidation in terms of the solid exit flow as well. The energy released is related to the amount of oxygen consumed, previously defined as 380 kJ/mol of O_2. With this in mind, the rate of energy production within the reactor is determined to be:

$$\dot{Q}_{chem} = \frac{\Delta H_{rxn}(\dot{m}_{s,out} - \dot{m}_{s,in})}{M_{O_2}} \tag{2.5}$$

where $\dot{Q}_{chem}$ is the rate of heat released and M_{O_2} is the molar mass of oxygen gas. The difference in the solid flow rates is used here because any change to the solid mass flow rates must be due to oxygen absorbed during oxidation. Substituting into the previously developed equations, the rate of heat released is found to be:

$$\dot{Q}_{chem} = \dot{m}_{s,out}\frac{\Delta H_{rxn}\beta\Delta\alpha}{M_{O_2}} \tag{2.6}$$

This successfully establishes the reaction heating rate as it relates to the exiting solid flow rate.

Considering the control volume as drawn in Figure 2.2 and the perfectly insulated ideal reactor, an open system energy balance can be written as:

$$\frac{dE_{cv}}{dt} = \dot{Q}_{chem} + \dot{m}_{g,in}h_{g,in} - \dot{m}_{g,out}h_{g,out} + \dot{m}_{s,in}h_{s,in} - \dot{m}_{s,out}h_{s,out} \tag{2.7}$$

with $h_{g,in}$, $h_{g,out}$, $h_{s,in}$, and $h_{s,out}$ representing the gas inlet, gas outlet, solid inlet, and solid outlet specific enthalpies, respectively. Assuming steady operation of the reactor, the $\frac{dE_{cv}}{dt}$ term goes to zero. Since the flowing particles enter and exit the reactor at the same temperature, the solid enthalpies can be omitted from the energy balance. Any oxygen absorbed during the reaction similarly exits and enters the reactor at ambient temperatures, with enthalpies of formation described sufficiently by the released heat equation. With these simplifications, the enthalpy values can be considered solely related to the exit gas flow rate. In conjunction with the definition for the released heat, Equation 2.7 becomes:

$$0 = \dot{m}_{s,out}\frac{\Delta H_{rxn}\beta\Delta\alpha}{M_{O_2}} + \dot{m}_{g,out}(h_{g,in} - h_{g,out}) \tag{2.8}$$

Average Properties	Values
$c_{p,s}$	902 J/kg ° C
$c_{p,g}$	1100 J/kg ° C
T_{amb}	25 ° C
ΔH_{rxn}	380 kJ/kmol O_2

Table 2.1 Idealized reactor properties.

To further simplify the system, constant specific heats are assumed. This allows for the simplification of:

$$h_{g,in} - h_{g,out} = c_{p,g}(T_{amb} - T_{ext}) \tag{2.9}$$

Implementing this assumption in conjunction with Equation 2.4 yields a final form describing the gas extraction temperature for the reactor:

$$T_{ext} = \frac{\Delta H_{rxn}\beta\Delta\alpha}{M_{O_2}(c_{p,s} - \beta\Delta\alpha c_{p,g})} + T_{amb} \tag{2.10}$$

An important note in Equation 2.10 is the absence of any solid or gas flow rates. For an idealized reactor, the maximum operating temperature is principally dependent on the enthalpy of reaction of the redox material and the change in extent of conversion; the rest of the quantities involved are constants.

With this relationship defined, maximum operating temperatures can be determined for given changes in extent of conversion. Table 2.1 lists the properties relevant to determining idealized extraction temperatures. The result of Equation 2.10 mapped across a variety of changes in extent of conversion is depicted in Figure 2.3. The figure depicts an almost linear relationship between the two quantities, though a quadratic fit provides the best approximation. Of particular note is the maximum temperature achieved through complete oxidation of fully reduced SoFuel particles ($\Delta\alpha$ = 1) - greater than 1000°C, a temperature high enough to drive industrial processes and interact with gas power cycles.

2.2.1 The Effect of Oxidation Kinetics

While Figure 2.3 makes clear the possibility for high-temperature extraction, the actual chemical behavior of SoFuel particles is also affected by reaction kinetics. Chemical kinetics for Mg-Mn-O

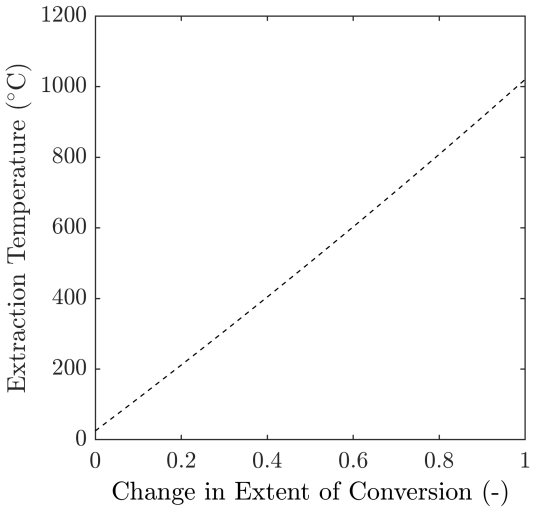

Figure 2.3 The relationship between change in extent of reduction and extraction temperature for an idealized reactor. Oxidation kinetics are negligible until close to 650°C, necessitating high conversion to drive idealized operation.

are well documented, and have been identified as being affected by factors such as temperature and oxygen partial pressure [45]. As a part of the broader SoFuel project, a semi-heuristic thermodynamic model was developed to determine changes to the extent of conversion (α) based on the thermophysical and chemical states of the Mg-Mn-O material and its surroundings. Mishra et al. [46], Huang et al. [47], and Korba et al. [48] all utilized the following general Arrhenius-style formulation for the rate of chemical conversion of the Mg-Mn-O material:

$$\left(\frac{d\alpha}{dt}\right)_{rxn} = A_0 e^{-\frac{E_a}{RT}} \left(\frac{P_{O_2}}{P_{ref}}\right)^n \frac{f(\alpha)}{T} \left(\sigma_{O_2,s} - \sigma_{O_2,g}\right) \tag{2.11}$$

where α is the extent of conversion, A_0 is the Arrhenius constant, E_a is the activation energy, P_{O_2} is the partial pressure of oxygen, P_{ref} = 1 atm, T is the temperature, and $\sigma_{O_2,s}$ and $\sigma_{O_2,g}$ are the apparent oxygen chemical potential in the solid and chemical potential in the gas phase, respectively. This formulation takes a highly simplified view of the actual chemical reaction at play, which features a series of stoichiometric and non-stoichiometric reactions due to the presence of multiple coexisting phases in the solid at different temperatures and oxygen partial pressures. Nevertheless, this simplified model is sufficient to capture the general chemical behavior of the Mg-Mn-O material. The difference between $\sigma_{O_2,s}$ and $\sigma_{O_2,g}$ denotes whether the material is at chemical equilibrium with its surroundings or will proceed with further reaction. For the case of

Index	v_i	p_i
0	-4704.268	-0.143
1	-169.821	1.140
2	-0.0788	0.195
3	5.133×10^{-5}	-0.0370
4	-2.514×10^{-8}	-0.0349
5	7.114×10^{-12}	0.00204
6	-8.56×10^{-16}	0.00259

Table 2.2 Polynomial coefficients for ${\sigma_{O_2}}^\circ$ and $\sigma_{O_2,s}$.

$\sigma_{O_2,s} > \sigma_{O_2,g}$, the Mg-Mn-O material experiences reduction, and Equation 2.11 implements the following parameters:

$$\text{if } \sigma_{O_2,s} > \sigma_{O_2,g}, \begin{cases} f(\alpha) = \alpha + 0.05 \\ A_0 = 10338.492 \text{ mol K/J/s} \\ E_a/R = 26469.564 \text{ K} \end{cases}$$

In contrast, when $\sigma_{O_2,s} < \sigma_{O_2,g}$ oxidation occurs and Equation 2.11 utilizes the following:

$$\text{if } \sigma_{O_2,s} < \sigma_{O_2,g}, \begin{cases} f(\alpha) = \begin{cases} 1 - \alpha + 0.04 & \text{if } T < 1273 \text{ K} \\ 1 - \alpha & \text{if } T <= 1273 \text{ K} \end{cases} \\ A_0 = 3.391/d_p \text{ mol K/J/s, where } d_p \text{ is in mm} \\ E_a/R = 13679.500 \text{ K} \end{cases}$$

Besides differing in the exact parameters employed, the oxidation model features scaling of A_0 as a function of the Mg-Mn-O particle size, d_p. Due to the nature of the reactor considered in this work, Equation 2.11 largely employs the conditions of the oxidation case when determining changes to chemical conversion.

The chemical potential in the gas phase, $\sigma_{O_2,g}$, is determined according to the following expression:

$$\sigma_{O_2,g} = {\sigma_{O_2}}^\circ + RT \ln\left(\frac{P_{O_2}}{P_{ref}}\right) \tag{2.12}$$

Properties	Values
α_0	0.167
λ_1	1.308 K
λ_2	2833.563 K
λ_3	-1.222
λ_4	-2764.565 K
λ_5	-0.318
λ_6	0.320
λ_7	-298296.113 J/mol
λ_8	83632.127 J/mol
λ_9	109.172 J/mol/K
P_{ref}	1 atm
n	0.220

Table 2.3 Additional parameters for the kinetics model.

where ${\sigma_{O_2}}^\circ$ is determined via a temperature dependent polynomial of the form:

$$ {\sigma_{O_2}}^\circ = \sum_{i=0}^{6} v_i T^i \tag{2.13} $$

where v_i is comprised of coefficients obtained from the thermochemical database Fact-Web [49]. Values for v_i are listed in Table 2.2 alongside p_i, polynomial coefficients used to determine $\sigma_{O_2,s}$ as described by:

$$ \sigma_{O_2,s} = \lambda_8 \sum_{i=0}^{6} X^i p_i + \lambda_7 - \lambda_9 T\alpha \tag{2.14} $$

with X defined as a coordinate encompassing extent of conversion and temperature effects as shown below:

$$ X = \frac{\ln(\alpha + \alpha_0) - \left(\frac{\lambda_2}{T} + \lambda_3\right)\left(\ln(\alpha + \alpha_0) - \frac{\lambda_1}{T}\right)\left(1 + \frac{\lambda_4}{T}\right) - \lambda_5}{\lambda_6} \tag{2.15} $$

Values for λ, α_0, P_{ref}, and n are listed in Table 2.3. The appropriate constants and coefficients for determining $\sigma_{O_2,s}$ were determined by fitting kinetics experiments performed on a Netzsch Jupiter F5 thermogravimetric analyzer. Taken collectively, the above equations provide a computational basis for describing the thermochemical reactions of the SoFuel particles.

By evaluating reaction behavior at various temperatures and an oxygen partial pressure of 0.209 atm, this kinetics model can anticipate SoFuel extent of conversion over time for a constant-temperature operation. Figure 2.4 showcases the results of an explicit first-order simulation with

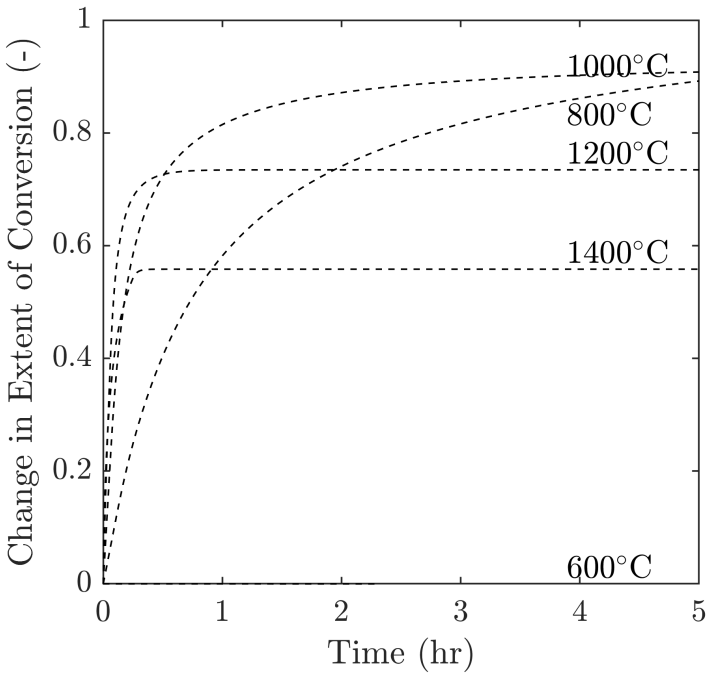

Figure 2.4 Results of constant temperature and oxygen partial pressure kinetics modeling for a 5 mm Mg-Mn-O particle. High temperatures of 1200°C and 1400°C exhibit rapid initial kinetics but limit overall conversion. 1000°C is observed to be an excellent tradeoff between total conversion and rate of chemical reaction.

a timestep of $t = 1$ s and particle size of 5 mm. The Mg-Mn-O material begins at a perfectly oxidized state ($\alpha = 0$). While the figure only displays results for a few reaction temperatures, a finer matrix of results can be determined simply by increasing the number of desired temperatures to investigate. Of note here is the negligible change in conversion achieved at a temperature of 600°C - elevated temperatures are necessary to ensure steady reaction.

With Figures 2.3 and 2.4 depicting the relationships between change in extent of conversion and steady reactor operating temperature and change in extent of conversion over time at different reaction temperatures, respectively, it is possible to determine an estimation for the feasible operating temperatures of an idealized reactor. The kinetics curves provide estimates for the change in extent of conversion after a given amount of time; by taking this change and utilizing Figure 2.3, a reactor operating temperature is determined. For actual operation, this reactor operating temperature should be equal to the oxidation temperature in use by the kinetics model. This procedure is repeated at every time step and temperature of the kinetics model. The reactor operating tempera-

ture can be divided by the kinetics model temperature at each point to provide a clear indication of feasibility; a value less than 1 indicates unsuitable kinetics for operation while a value greater than 1 suggests excess energy being produced. A value of exactly one corresponds to equilibrium and steady operation.

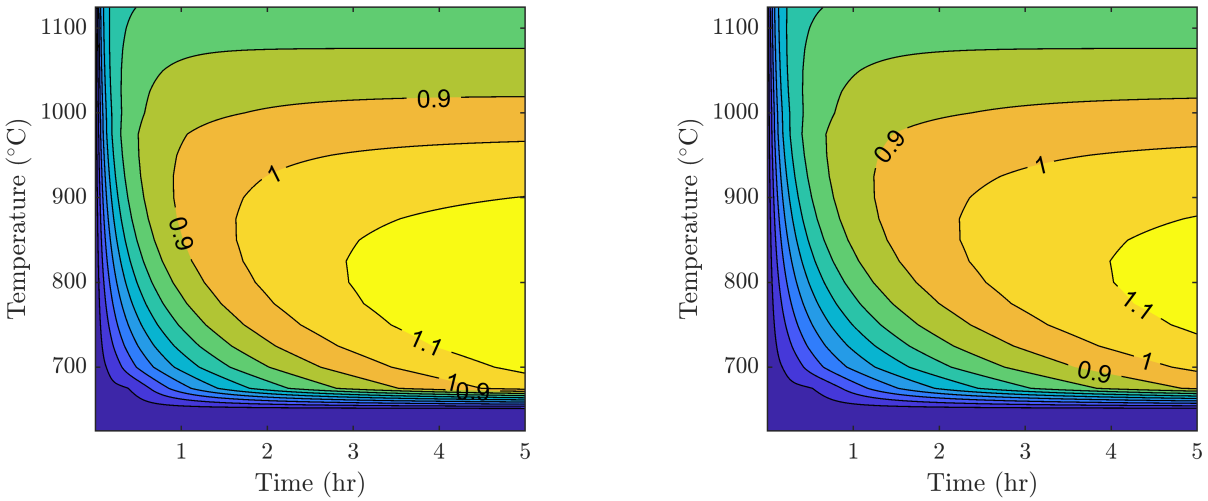

Figure 2.5 Ideal reactor operational feasibility for 3.66 mm (left) and 5 mm (right) particles. The curve marked as "1" in each subfigure denotes break even points at which the residence time of a particle is sufficient to release enough energy to supply gas extraction at the specified temperatures.

The results of this procedure are shown in Figure 2.5 for 3.66 mm and 5 mm particles. The lines depicted on the contour plots correspond to the previously described ratio. Due to the smaller size and greater reactivity of the 3.66 mm particle, it reaches the break-even point earlier than the 5 mm case. Both seem to be asymptotically approaching a maximum viability temperature of around 950°C. While the minimum operating temperature becomes lower as particle residence time in the reactor increases, the limitations of the Mg-Mn-O kinetics are clearly depicted by the absence of any reactivity below about 650°C. For a sufficiently large reactor design, SoFuel particles could achieve residence times in excess even of the 5 hour boundary imposed on these figures. At this timescale, though, the onset of steady operation and its general boundaries are clear.

2.3 The Necessity of Recuperative Flow

The previous section outlined the theoretical operational characteristics of a perfectly insulated reactor with the extraction gas flow sufficiently recuperating heat from downward-moving particles.

This idealization faces limitations when applied to real-world implementation and applications. First, the model described in Section 2.2 considers losses from the reactor to be negligible. While this may be the case for a sufficiently large reactor, for smaller designs or bench-scale demonstrations losses from the system can be expected within an order of magnitude of the energy released by the particles. This point can be illustrated by inserting a losses term into Equation 2.7. For losses of approximately 10% of the energy released by the particles, the required reaction time to achieve viability drastically increases, as depicted in Figure 2.6 for 5 mm particles. Similarly to previous figures, the marked contour lines denote whether the reactor can sustain itself, with a value of 1 signifying steady operation. Not only is the necessary reaction time higher than the lossless case, the break-even extraction temperatures have decreased as well. For reactors where these losses become too great, these losses can eventually eliminate any viability should temperatures decrease below approximately 700°C.

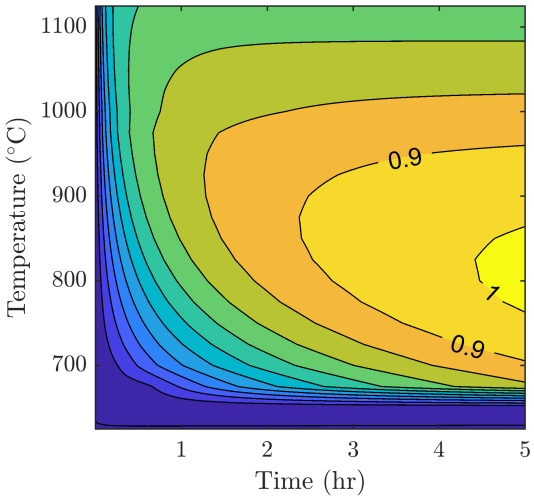

Figure 2.6 Operational feasibility for 5 mm particles with systems losses of 10%. Of particular note here are the large residence times and operating temperatures of the break even curve.

Particle residence time in the main reactor zone is another design factor where the ideal case deviates from potential real-world limitations. Residence time is affected by many factors: particle density, solid flow rates, and reactor size, to name a few. While systems can be designed to maximize residence times, kinetics modeling like that in Figure 2.4 shows that SoFuel particles

release most of their stored energy quickly at the beginning of oxidation, after which long periods of time are required to produce the remaining fraction of energy. This suggests that long residence times are not efficient for producing as much energy as quickly as possible. Rather, incomplete oxidation of many particles is preferable to complete oxidation of a few. This further conflicts with the ideal viability models, which suggest that particles must be oxidized to a high degree in order to sustain consistent operation.

With both losses and lower changes in extent of conversion, attempts at steady operation of a small-scale, non-ideal reactor will inevitably lead to lower extraction temperatures. This is not a trivial outcome, as high-temperature gas extraction (up to 1000°C) is a desired outcome of any SoFuel oxidation reactor in order to be useful for industrial processes or utilized by gas power cycles. The limitation of the ideal case is its reliance on the extraction gas flow to provide full recuperation of the sensible energy of the downward moving particles. The necessity to provide recuperation fixes the value of the entire extraction flow, which cannot be adjusted to accommodate any changes within the system or non-ideal behavior.

The simplest solution to this problem is to supply an additional flow of gas through the bed solely for heat recuperation purposes. Such a design is shown in Figure 2.7. While depicted in a similar fashion to Figure 2.2, this illustration includes heat losses during operation. It also changes the reactor geometry from a cavity-based design to a straight tube due to the simplicity of the latter. Gases enter and solids exit from the bottom of the reactor as previously discussed, but the gas flow now branches into two distinct channels, $\dot{m}_{g,recup}$ and $\dot{m}_{g,ext}$, or the recuperation and extraction flows, respectively. These combined flows obtain heat from the hot particles exiting the reaction zone. The extraction flow then exits the tube at high temperatures, while the recuperation flow continues up through the bed and exits the reactor from the top. In doing so it provides preheating to the incoming particles, augmenting the energy provided through reaction. In diverting energy away from the extraction to combat losses, the recuperation flow allows for the reactor to maintain its elevated temperatures. This design also allows for the shorter residence times alluded to previously, as particles do not need to react completely prior to exiting the reactor.

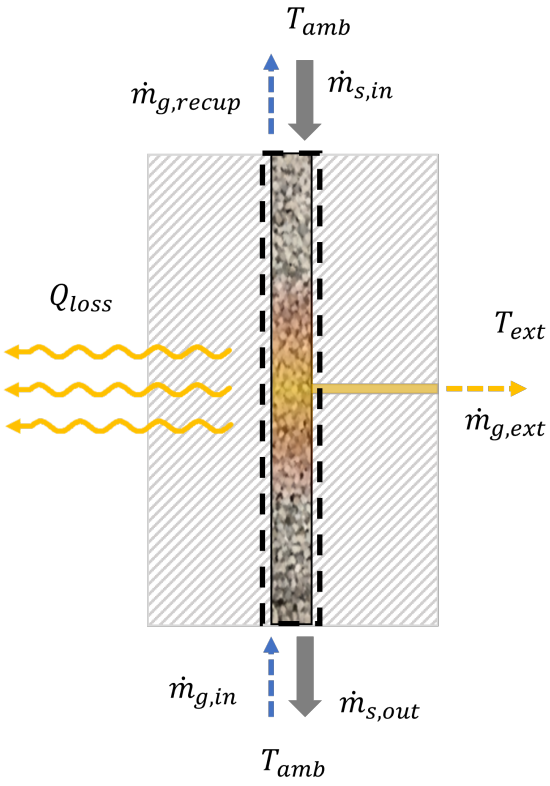

Figure 2.7 An oxidation reactor featuring additional recuperative gas flow. The addition of recuperative flow means that gas can be extracted at higher temperatures than the previously considered ideal case allows. Originally printed in [2].

The reactor design in Figure 2.7 will be the focus for the remainder of this work. This particular three-port design not only allows for greater operational control and customization than the idealized extraction-only case, but it is also more suitable for bench-scale experimentation and implementation.

CHAPTER 3

OXIDATION REACTOR SUBSYSTEMS AND FABRICATION

Based on the recommendations from Chapter 2, a three-port, combined recuperation and extraction flow oxidation reactor is the most feasible option for SoFuel oxidation with direct heat transfer. Such a design allows for the extraction of high-temperature gases while also allowing for control of the extraction temperature and indefinite steady operation. Figure 3.1 depicts the configuration fabricated and investigated in this work. Similar to the theoretical concepts described thus far, the reactor in Figure 3.1 implements a downward-moving bed of particles against a rising flow of air. It also features the extraction path necessary for producing high-temperature gas and a recuperation flow in the top of the bed to ensure continued high temperature operation at modest residence times. Figure 3.1 further illustrates the housing necessary for real-world implementation of the reactor - a steel pressure vessel packed with insulation to minimize losses. Further details on the reactor, its subsystems, and all sensors utilized are discussed in the rest of this chapter.

3.1 Particle Synthesis

Two sizes of SoFuel particles are considered for the oxidation reactor: 3.66 mm and 5 mm. The 3.66 mm particles were synthesized in-house for the earliest experiments in modest quantities (approximately 20 kg). The 5 mm particles, on the other hand, were produced by Powder Processing and Technology LLC. in larger amounts to facilitate longer operation. Regardless of the size, SoFuel pellets should be spherical and smooth for uninterrupted flow. In addition, the synthesis procedure for their mass production should be cost effective and scalable.

As detailed by Randhir et al. [1], the 3.66 mm particles were manufactured in-house via disc pelletization followed by spheronization, two widely used processes in industry. Particles were formed in batches, each beginning with a 500 g mixture of magnesium oxide (96% purity, CAS: 1309-48-4) and manganese (II) oxide (99% purity, CAS: 1344-43-0) powders from Fischer Scientific. These powders were combined in a 1:1 molar ratio of Mg:Mn in an EL1 Eirich Machines disc pelletizer. Following a ten-minute blending period, 60 mL of PVA binder (96% weight by

Some material in this chapter was originally published in [1], [50], and [2].

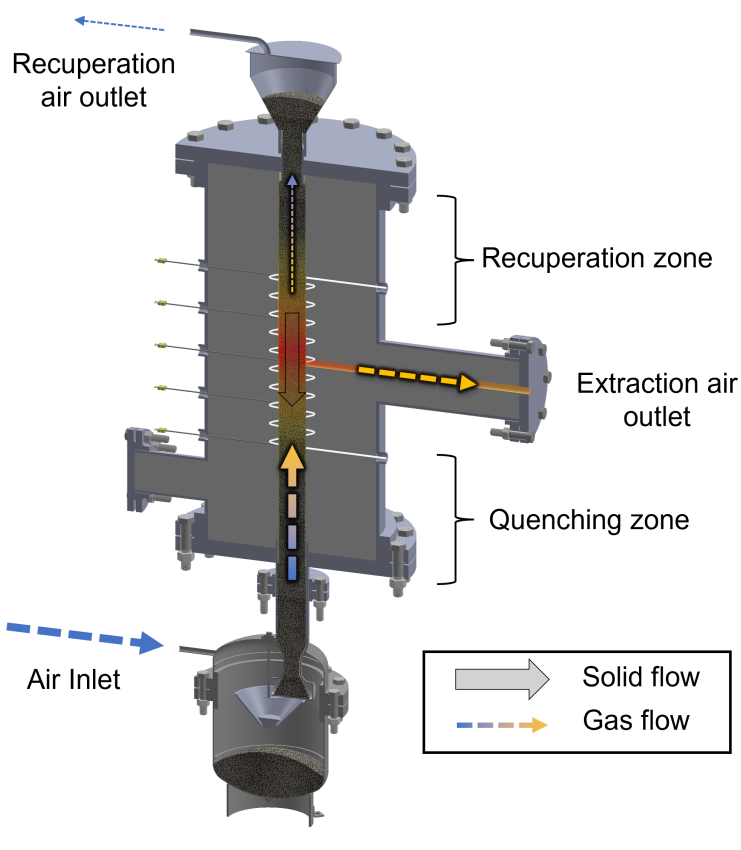

Figure 3.1 A rendering of the SoFuel oxidation reactor featuring the solid, gas recuperation, and gas extraction flows.

water) was added to the powder mixture to facilitate pelletization. Deionized water added at regular intervals provided additional moisture to the growing particles, producing 3 to 4 mm pellets. After 20-30 minutes of air drying, each batch of particles was spherodized in a cylindrical container featuring a smooth aluminum disc at its bottom. By tumbling particles over each other and the spinning disc, the rough or irregular edges of most particles were notably reduced. Batches were then cured at 150°C for 15 minutes, after which pellets were calcined at 1500°C for 24 hours in a muffle furnace. Following calcining, particles were sieved between 2.36 and 4.35 mm. Fines were further removed from the sieved particles through a controlled fluidization process.

The 5 mm particles were chosen over the 3.66 mm particles in later experiments because the larger size is favorable for particle flow at high temperatures. Sintering and fluidization are two challenges identified during operation of the reduction reactor for particles with small diameters; by implementing particles with an average diameter of 5 mm, the oxidation reactor was unlikely to

experience any operational disruptions due to agglomeration or particle clogging.

3.2 Solid Flow Control

A crucial factor in the operation of the oxidation reactor is solid flow control. While mechanical devices exist, pneumatic means of controlling solid flow are well-suited for this application due to their lack of abrasion, applicability to high temperature applications, and general ease of use [51]. The L-valve is among the most popular of these non-mechanical approaches; its name comes from the telltale "L" shaped junction through which the particles are passed. Knowlton and Hirsan [52] established the first theoretical basis for L-valve operation, defining general behavior and geometric effects. A number of other authors have expanded upon this work, offering additional experimental data and flow correlations [53] [54] [55] [56] [57]. Studies have been performed on a variety of materials and particle sizes, ranging through the Geldart particle classifications of A [58], B [59], and D [60].

L-valves are already a popular choice for fluidized bed systems, which share many operational behaviors with the oxidation reactor. Numerous studies have considered this use case [61] [62], including high-temperature applications [63] [64]. L-valves operating in fluidized bed systems exist across a variety of different industrial processes, from conveying spent coffee grounds [65] to facilitating chemical looping combustion [66]. Thermochemical energy storage is another field in which fluidized beds have some applicability [67]. Another popular design is the moving bed configuration, in which particles are conveyed downwards without the active circulation of a fluidized bed, as in this application. Previously proposed moving bed thermochemical reactors rely on either mechanical means [36] [68] or gravity [69] [37] to maintain particle progression. While these are viable options, they introduce challenges to system robustness. In the case of mechanical, augur-like control mechanisms, particle abrasion and fragility at high temperatures impose limits on operation; for gravity-fed designs, there may be no way to control the particle flow rate beyond the predetermined feed angle.

Although a traditional L-valve could remedy these issues, there is a limit on the minimum possible mass flow rates. Particles are conveyed by the drag force of the moving gas, a drag force

which must overcome the static friction of the particles. Once this is achieved the particles move at some threshold flow rate, halting again once the drag force fails to overcome kinetic friction forces. This phenomenon creates an array of particle flow rates that are unachievable using constant aeration.

3.2.1 Pulsating L-valve Design

L-valve pulsation was previously explored for use in the reduction reactor concept, but further investigation has been performed for the oxidation setup. By switching gas flow on and off, an L-valve can achieve particle flow rates below that of the minimum rate for continuous aeration, as illustrated in Figure 3.2. Such a pulsation concept was previously considered by Vogel et. al [70] for low-flow combustion applications but has not been rigorously investigated since. For the oxidation reactor, the solid flow control system consists of two major components: a custom-made L-valve and a particle "catchcan." Two L-valve geometries have been utilized to similar effect in the oxidation reactor; both are shown in Figure 3.3. The rightmost piece is an early fabrication, created by drilling and threading holes into a solid block of aluminum. It is designed for 3.66 mm particles. While functional, its smaller size enables sporadic particle bridging that can restrict flow in the throat of the valve. The second design, shown on the left of Figure 3.3, depicts the latest iteration for 5 mm particles. This L-valve is fabricated out of steel piping and features a larger diameter, mitigating clogging in the valve.

The "catchcan" utilized in the SoFuel oxidation reactor consists of a steel funnel suspended from a load cell. As particles are expelled from the L-valve, the catchcan collects and weighs them in real-time. A small, retracted pneumatic piston is situated inside the funnel along its primary axis. A cylindrical plug is threaded onto the tip of the piston, preventing particles from escaping the funnel. When the funnel has filled the piston fires, opening the bottom of the catchcan and allowing particles to drain into the bottom of the reactor. Once the load cell signifies that dumping is complete, the piston closes once more and the L-valve can commence expelling particles. The assembled catchcan, suspended from a Loadstar RRP1-010M-A load cell (capacity 10 kg), is shown in Figure 3.4.

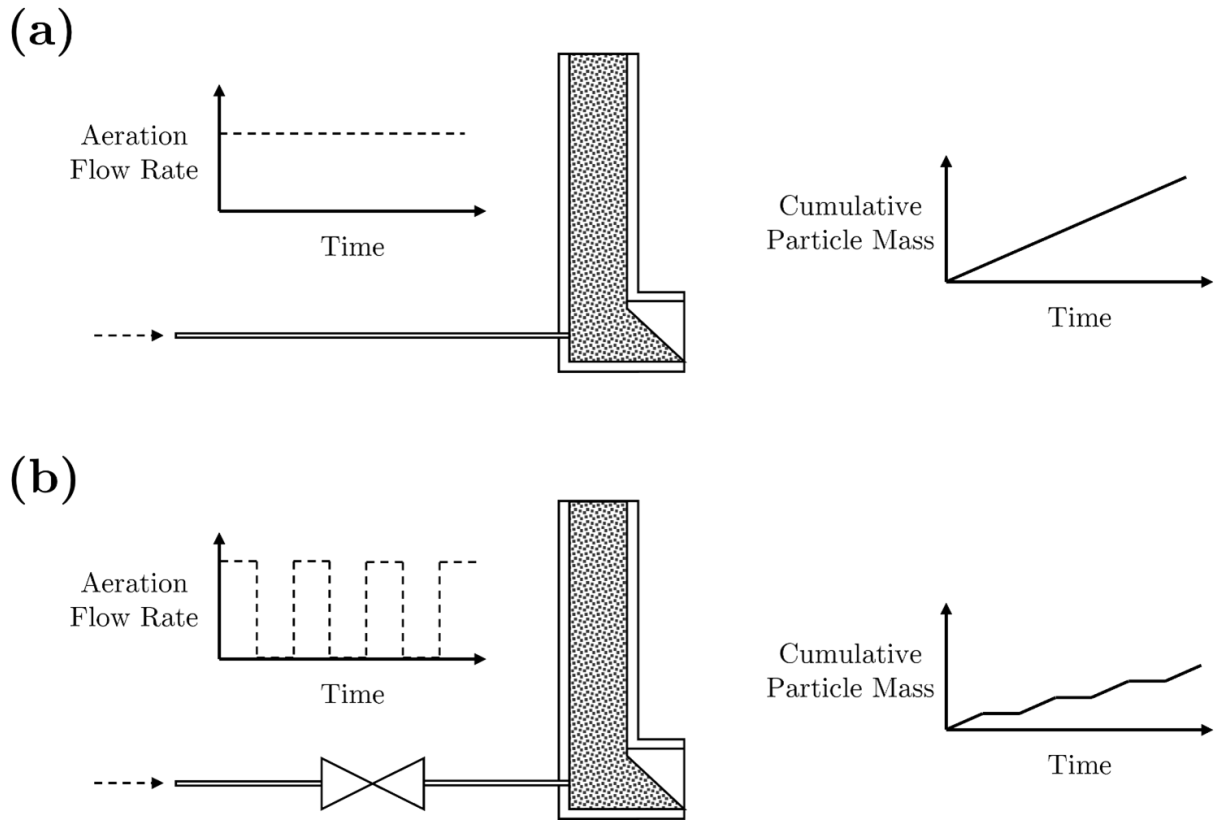

Figure 3.2 The operating principles of (A) A standard L-valve system, and (B) The pulsed concept. By pulsating the aerating gas flow, the second example can achieve lower flow rates than are possible through continuous aeration. Originally printed in [50].

Figure 3.3 The two L-valves utilized by the oxidation reactor, with the earliest design on the right and the latest iteration on the left. The right-angle junction of each valve allows the particle column to pause in between bursts of air.

Figure 3.4 The particle "catchcan," consisting of a plugged funnel suspended from a load cell. When full, the plug is removed via a pneumatic piston to allow particles to drain.

3.2.2 Pulsation Control

The effect of gas pulsation is illustrated through a parametric analysis. The 3.66 mm L-valve was suspended over the particle catchcan and connected to a vertical tube filled with 3.66 mm SoFuel particles. The L-valve was connected to a gas flow controller interfacing with LabVIEW. The controller's behavior was defined by a simple on/off square wave, with two controlling parameters: pulsation duty cycle and frequency. For this application, duty cycle is defined as the fraction of one on/off pulsation during which there is gas flowing through the L-valve. Real-time mass data was recorded for frequencies of 0.25, 0.5, 0.75, and 1 Hz and for a range of duty cycles between 0 and 100%.

The results of this investigation are shown in Figure 3.5. The interaction between duty cycle and mass flow rate is illustrated in Figure 3.5a. The dashed line in the figure indicates a 1:1 relationship between the duty cycle of gas pulsation and particle mass flow rate as a fraction of the maximum solid flow rate (that is, the rate at which particles are expelled without any pulsation). Even at a

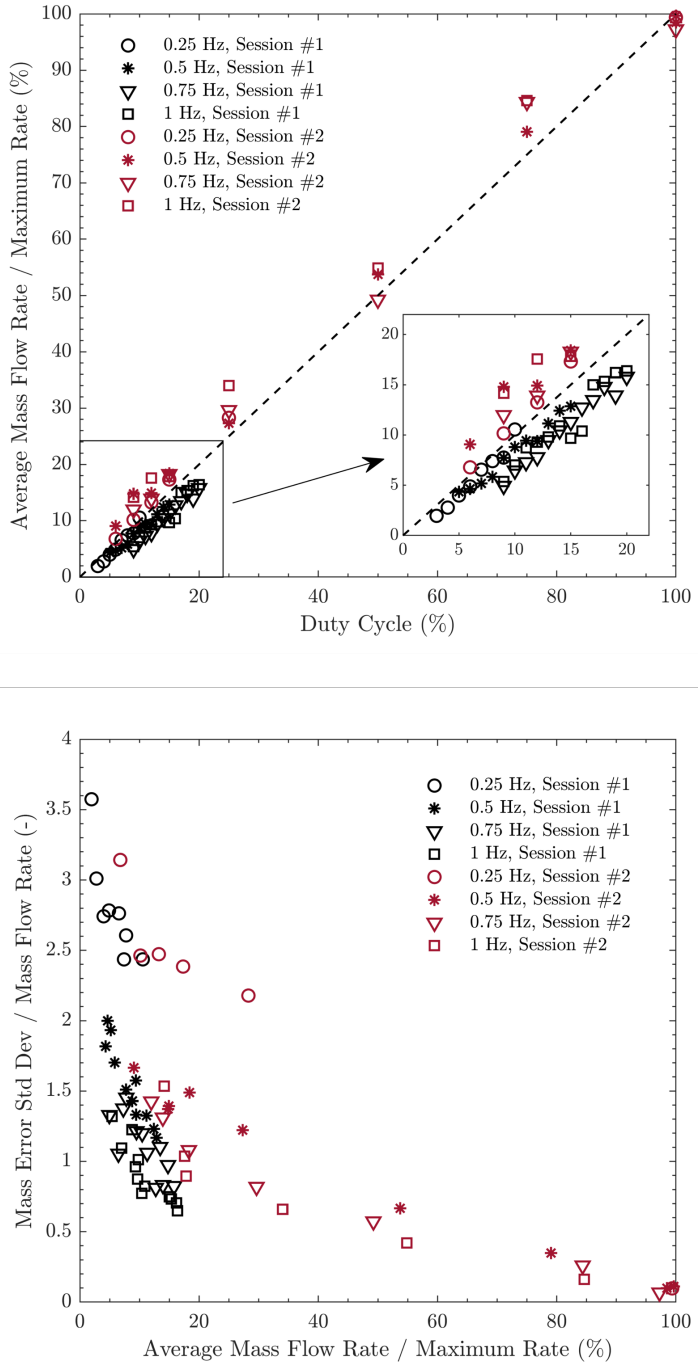

Figure 3.5 Operational behaviors of the L-valve pulsation scheme. In (A) on the top, the linear relationship between pulsation duty cycle and percentage of maximum solid flow rate. In (B) on the bottom, the impact of pulsation frequency on flow smoothness. Higher frequencies more closely imitate continuous flow. Originally printed in [50].

variety of frequencies the results cleave closely to the 1:1 line, affirming that lower particle flow rates correspond directly to lower gas pulsation duty cycles. In Figure 3.5b the criteria of interest is the "smoothness" of the particle flow - that is, how well the pulsating flow mimics a continuous solid flow. This smoothness is quantified as the standard deviation of the accumulated mass data from the anticipated accumulated mass profile for a constant solid flow rate. To compare between different duty cycles, this standard deviation is normalized by the observed solid flow rate for each case. As Figure 3.5b displays, higher pulsation frequencies produce a lower normalized deviation and thus a smoother flow. Limitations of the data acquisition hardware bounded the frequencies available for investigation to those seen here. Even so, the accumulated data strongly suggests that manipulating flow duty cycle at high frequencies is sufficient for attaining continuous-like solid flow control at low flow rates.

3.2.3 Bench-scale Implementation

The solid flow control scheme implemented in the SoFuel oxidation reactor takes into account the findings of the previous section. Rather than simply utilize an open-loop control based upon the solid flow rate at 100% duty cycle, a feedback control system was implemented to ensure accurate solid flow rates and to mitigate the effects of any bridging or particle irregularities. To this end, the system utilized a modified proportionality control to facilitate solid flow. The gas flow controller connected to the L-valve was driven by a pulse-width modulation (PWM) module that allowed the controller to release variable amounts of gas in each pulse. While this is not entirely analogous to the duty cycle experimentation described previously, the operational strategy and effects on flow were the same. The PWM signal supplied to the controller was managed by a closed-system feedback loop that anticipated the amount of gas required by the system while observing the current mass measurement. In this way, the system was highly flexible and able to adapt to most situations observed during operation. In the event of particle bridging within the L-valve, a failsafe mechanism within the controller programming blasted a short burst of high-velocity gas to restart particle flow.

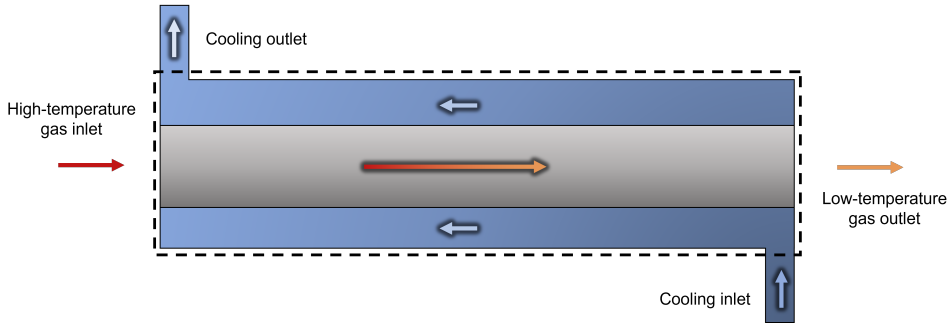

Figure 3.6 A schematic of the shell and tube heat exchanger designed for the oxidtion reactor.

3.3 Extraction Heat Exchanger

Another key mass flow in the oxidation reactor is the high-temperature gas extracted from the main reaction zone. While the objective of the experimental setup is to achieve gas temperatures of up to 1000°C, this extraction flow must be cooled before it can be safely exhausted to ambient. To this end, a rudimentary heat exchanger analysis was performed to estimate minimum acceptable specifications for a counterflow shell and tube design. These recommendations subsequently informed the final fabricated subsystem.

a counterflow shell and tube heat exchanger was .

3.3.1 Design Criteria

The heat exchanger was conceptualized as a typically shell and tube configuration, as shown in Figure 3.6. High temperature extraction gases up to 1000°C enter the exchanger from the left side, while cooling water is pumped through a jacket in the opposite direction. From Incropera et al. [71], the length of a shell and tube heat exchanger can be estimated as:

$$L = \frac{\dot{Q}}{U\pi D_i \Delta T_{lm}} \tag{3.1}$$

where $\dot{Q}$ is the rate of heat transfer between the streams, U is a heat transfer coefficient for the fluids, D_i is the innermost tube diameter, and ΔT_{lm} is the log-mean temperature difference. This temperature difference is expressed as:

$$\Delta T_{lm} = \frac{\left(T_{hot,in} - T_{cold,out}\right) - \left(T_{hot,out} - T_{cold,in}\right)}{\ln \frac{T_{hot,in} - T_{cold,out}}{T_{hot,out} - T_{cold,in}}} \tag{3.2}$$

where T_{hot} and T_{cold} denote the hot and cold streams, respectively, and the *out* and *in* subscripts signify outlet and inlet, respectively. The heat transfer coefficient from Equation 3.1 can be further

defined as:

$$U = \frac{1}{\frac{1}{\gamma_{water}} + \frac{1}{\gamma_g}} \tag{3.3}$$

where γ_{water} and γ_g are the convection coefficients for the cooling and extraction gas flows, respectively. γ is selected to represent heat transfer coefficients throughout this work in order to differentiate the quantities from specific enthalpies, which utilize the h notation. These convection coefficients are determined from the Nusselt number of each flow, defined as:

$$\mathrm{Nu} = \frac{\gamma D_h}{k} \tag{3.4}$$

with D_h representing the hydraulic diameter and k the fluid thermal conductivity. To estimate the Nusselt number for two concentric tubes, the Dittus-Boelter equation is implemented:

$$\mathrm{Nu} = 0.023\mathrm{Re}^{4/5}\mathrm{Pr}^{n} \begin{cases} n = 0.4 & \text{for cooling} \\ n = 0.3 & \text{for heating} \end{cases} \tag{3.5}$$

where Re represents the Reynolds number and Pr the Prandtl number. While more accurate Nusselt number correlations exist, specifically for the case of an annular region, the correlation presented in Equation 3.5 is implemented for this rough estimation of the minimum heat exchanger length. Average Prandtl numbers for the two flows are readily available, and Reynolds numbers for turbulent pipe flow can be calculated using the following formula:

$$\mathrm{Re} = \frac{4\dot{m}}{\pi D_h \mu} \tag{3.6}$$

with the mass flow rate as $\dot{m}$ and dynamic viscosity as μ. Average property values for use in the heat exchanger equations were obtained from Incropera et al. [71] and are displayed in Table 3.1. Table 3.1 also includes several operational assumptions that drive the heat exchanger calculations, in particular temperatures and mass flow rates. A gas flow rate of 100 SLPM (0.00213 kg/s) was assumed for the calculation, as well as a water flow rate of 0.0383 kg/s. The air is assumed to enter the exchanger at 1000°C and leaves at 100°C. By performing a First Law energy balance on the heat exchanger (and ignoring any losses) with the cooling water entering at 20 °C, the exit liquid temperature is approximately 34 °C. These values, in conjunction with the properties listed in the table, estimate a minimum heat exchanger length of 0.35 m.

Property	Value	Unit
$T_{g,in}$	1000	°C
$T_{g,out}$	100	°C
$T_{w,in}$	20	°C
$\dot{V}_g$	100	SLPM
$\dot{m}_{water}$	0.0383	kg/s
$D_{g,i}$	8.5	mm
$D_{g,o}$	9.5	mm
$D_{w,i}$	11.3	mm
μ_g	4.24×10^{-5}	kg/m s
μ_{water}	8.55×10^{-4}	kg/m s
Pr_g	0.726	-
Pr_{water}	5.83	-
k_g	6.67×10^{-2}	W/m K
k_{water}	0.613	W/m K

Table 3.1 Properties used to calculate the required heat exchanger size.

3.3.2 Fabrication

The heat exchanger implemented in the oxidation reactor is comprised of three nested sections of stainless steel tubing, with the primary exchange length consisting of $\frac{3}{8}$" and $\frac{1}{2}$" tubes. To keep the reactor compact and attach the extraction arm to its appropriate flow controller, the tubing was bent in several places. The total length of the heat exchanger outside of the reactor shell is 0.97 m. Figure 3.7 depicts the final design, as well as a cutaway showing the gas and cooling flows. In the section of the exchanger that is inserted into the reactor extraction arm (observable as mounted to the large flange), a third piece of tubing allows for cooling water to enter through the flange to cool the interior tubing. All nested tubes were cinched via Yorlok connectors to mitigate any leaks.

3.4 Reactor Body

The main housing of the oxidation reactor is its steel outer shell. This casing is necessary to ensure pressurization of the system. The reaction tube that houses the SoFuel particles is a 6.93 cm ID alumina tube aligned along the central axis of the steel chamber, as shown in Figure 3.8. This reaction tube extends 1.11 m. Due to the fragile nature of the connections this tube has to other parts of the system, the steel shell was necessary to mitigate leaks within the system and ensure

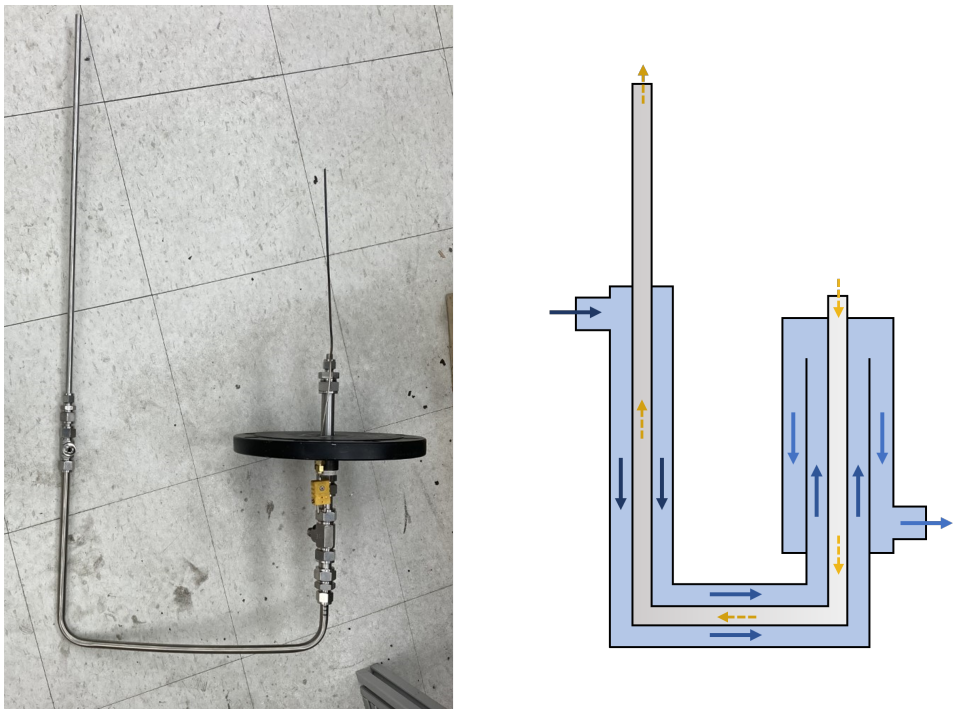

Figure 3.7 The finalized heat exchange deployed on the reactor. For (A) on the left, the assembled system. (B) on the right consists of a cutaway schematic of the fluid counterflows through the component.

that gas flows are consistent. The outermost casing also features two protruding arms. The first, located halfway up the shell, houses a small alumina extraction tube (0.5 m long with 1.91 cm ID) that penetrates the alumina reaction tube. It connects to the heat exchanger through a flange and provides a means for removing the extraction gas flow from the system. The other port, close to the base of the shell, is currently unused but could be implemented in the future for high-pressure injection. An image of the assembled outer shell is shown in Figure 3.9. Additional ports and feedthroughs are located throughout the shell; their locations will be discussed in greater detail in later sections.

Both ends of the steel shell include connections for particle flow. On the top, a custom-welded funnel threads to the upper flange. SoFuel particles are loaded into this funnel at the beginning of each experiment, and it features a threaded plug that allows for the top of the system to seal. The funnel is also connected to a stainless steel recuperation flow tube, which supplies gas to the flow controller responsible for regulating gases in the upper half of the particle bed. On the reactor's

Figure 3.8 The centering process for the alumina reactor tube within the steel shell.

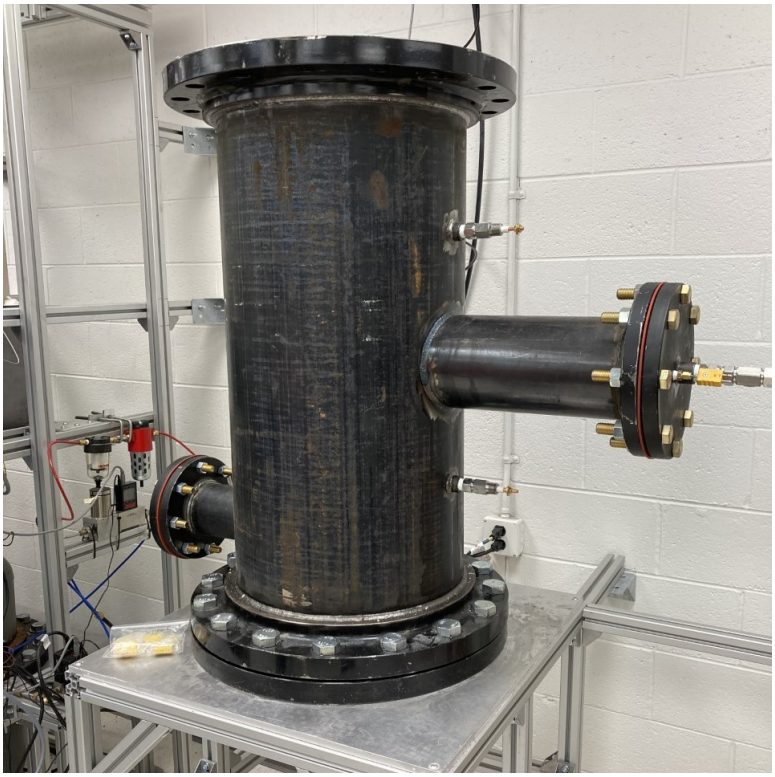

Figure 3.9 The outermost steel shell of the reactor. The tube lies at the center of the shell and is surrounded by fibrous insulation.

opposite end, a second steel chamber bolts to the main shell. This vessel serves as the particle collection tank, filling with oxidized SoFuel particles during operation. As a result, this tank houses the L-valve, load cell, and catchcan described previously. Feedthroughs are included for gas and sensor access. The inlet reactor gas flow, necessary for both recuperation and extraction, enters the system through the collection tank. The tank contains a plug at its bottom that allows for the draining of oxidized particles. Lastly, the tank is comprised of a top and bottom half, allowing for straightforward access to interior components.

All of these various sections combine to provide housing and conveyance to the moving bed of SoFuel particles. Loaded particles began in the top sealed funnel, progressed into the alumina reactor tube housed in the rigid, steel shell, oxidized, releasing their stored energy, and eventually were expelled by the L-valve and catchcan into the bottom of the collection tank.

3.5 Insulation

In the case of this bench-scale oxidation reactor, insulation is vitally important. As discussed in the previous chapter regarding operating limits of an ideal reactor, as the size of the reactor decreases system losses become more and more significant. For a bench-scale investigation, several inches of fibrous ceramic insulation are necessary to minimize losses and ensure that the net energy released by oxidation is sufficient to heat incoming gases. Figure 3.10 shows the outermost layer of this insulation. Concentric sheets of ceramic insulation line the inner wall of the reactor, with successive layers piled on top of each other. At radii close to the alumina reactor tube, individual, irregularly sized pieces of insulation were packed into the interior cavity. Sheets of insulation were also used to wrap the ceramic extraction tube housed in the extraction arm of the steel shell. In the event that maintenance must be performed on the inside of the reactor, much of the insulation must be removed from the central cavity.

Besides fibrous ceramic insulation, a second medium was used in the lower reaches of the steel shell. A castable ceramic insulation matrix was poured into the base of the shell prior to packing any fibrous insulation. This media's purpose is twofold: to provide insulation for the reactor and to hold the alumina reaction tube in place. After setting and hardening, the castable insulation

Figure 3.10 Layers of ceramic insulation surrounding the reactor tube. When the reactor is sealed, insulation fills the entire cavity shown in the image.

successfully anchored the reactor tube.

3.6 Heating Coil

A nichrome coil is utilized to preheat the reactor to temperatures necessary for oxidation (1̃000 °C). Components were obtained from Mor Electric Heating, and coils were comprised of Type 675 Nickel Chrome Alloy (nickel: 57-58%, chromium: 16%, silicon: 1.5%, iron: balance). "Coil" is an appropriate description in two ways: while the nichrome is wound around the alumina reactor tube, the element itself is preformed into a spring-like shape as well. The coil is connected to an external AC voltage source via insulated feedthroughs. Typical coil resistance was between 15 Ohm and 40 Ohm.

3.7 Sensors

A wide variety of sensors are necessary to adequately monitor the performance of the oxidation reactor. Figure 3.11 illustrates the many sensors and actuators at work in the system. Several, like the nichrome preheating coil and solid flow control system (L-valve, catchcan, and load cell),

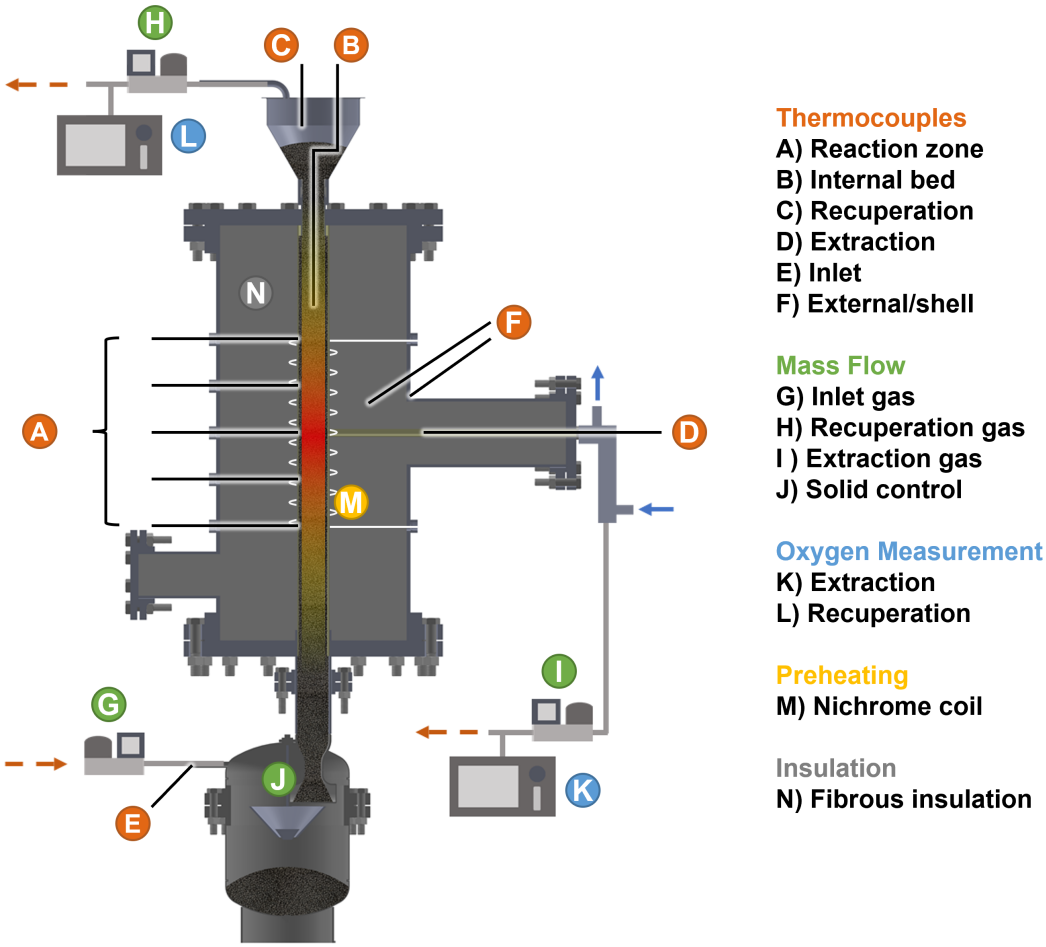

Figure 3.11 A map of the various sensors and actuators in the oxidation reactor. Major groups include thermocouples, mass flow devices, oxygen sensors, the nichrome preheating coil, and the fibrous insulation. Originally printed in [2].

have been previously described. The rest will be elaborated on in greater detail here. Signals were primarily monitored via a Graphtec GL840 data acquisition system with internal CJC, while solid flow was managed by two National Instruments NI-USB boards (6218 and 6211).

Thermocouples are essential to accurately determining the operating temperature of the reactor. The most common thermocouple type utilized in the system is K (accuracy ± 0.75%), while some J types (accuracy ± 0.75%) serve to monitor ambient conditions. Five thermocouples were equally spaced (11.43 cm apart) across the anticipated main reaction zone, with the third (center) thermocouple aligned with the extraction tube. This region is roughly the same as that encompassed by the nichrome preheating coil. In order to mitigate contact between the coil and the thermocouples,

alumina sleeves were placed over the length of each thermocouple. Thermocouples were swaged to the reactor shell in order to seal the system. Additional thermocouples extended into the bed and monitored the conditions at the top and bottom of the system. Due to extreme operating conditions and sensor degradation, the bed thermocouple is omitted from further analysis. Several type J thermocouples were fixed to the outside of the reactor to monitor shell temperature and "joint" temperature (the point at which the extraction arm attaches to the rest of the steel shell. In order to protect the data acquisition system from any adverse leakage current from the heating coil, 10 kΩ resistors were placed in series with the thermocouple leads to dissipate any AC voltage.

Initially only one pressure transducer was used to monitor conditions in the collection tank. This sensor verified minimal leaks in the system. In order to gather more pressure information in the system, in particular at the top of the reactor tube as well as the bottom, the system was outfitted with a pair of Dweyer Instruments transducers (Model 626-07-GH-P1-E1-S4-NIST). These transducers have a larger range than the previously used model, allowing them to capture a greater range of data. Pressure measurements were used primarily to provide additional data to a computational team collaborating on the SoFuel project.

While solid particle flow was managed by the system previously described, gas flows through the system were handled by a trio of Alicat flow controllers. The first controller (MCR-1000SLPM-D/10M), rated up to 1000 SLPM, introduced inlet air to the bottom of the system. The second controller (MCR-100SLPM-D-20X32/5M), handling up to 100 SLPM, was connected to the outlet of the extraction heat exchanger. A filter was positioned between the heat exchanger and the controller to keep the device free of any dust or contamination from the particle bed. The final controller (MCR-500SLPM-D-DB9/CM), functional up to 500 SLPM, was joined to the particle funnel at the top of the system via stainless steel tubing. Together, these three controllers regulated all gas flow throughout the oxidation reactor.

The final set of sensors that comprised the SoFuel oxidation reactor were the oxygen sensors. Both are manufactured by Advanced Micro Instruments,with the recuperation flow employing a 201LC oxygen analyzer and the extraction utilizing the 70R1 model. These devices can provide

measurements of oxygen content up to and beyond 20.9% (atmospheric concentrations). For an oxidation reactor that consumes incoming oxygen, this range is acceptable.

CHAPTER 4

BENCH-SCALE REACTOR CONCEPT EVALUATION

Thirteen experiments were performed on the fabricated oxidation reactor to assess performance. A summary of these trials and their operating parameters are shown in Table 4.1. The experiments are further subdivided into several different categories that reflect their purpose. The earliest tests demonstrate self-sustaining oxidation and successful high-temperature extraction (Group A). Two experiments assessing chemical conversion and suitability of the reactor as a companion for the reduction setup are also included (Group B). The largest category of tests were performed with constant inputs to evaluate reactor dynamics (Group C). The final experiments attempted rudimentary operational control through the use of simple on/off switching of the recuperation flow (Group D).

Group	**Experiment**	d_p (mm)	$\dot{m}_s$ (g/s)	$\dot{V}_{recup}$ (SLPM)	$\dot{V}_{ext}$ (SLPM)
A	1	3.66	1.5	variable	-
	2	3.66	1.5	variable	variable
	3	3.66	1.5	variable	variable
B	4	5	1.5	variable	variable
	5	5	1.5	variable	variable
C	6	5	0.75	27	21
	7	5	1.25	45	16
	8	5	1.25	29	16
	9	5	2	45	25
	10	5	2	45	25
	11	5	2	45	25
D	12	5	1.5	50	19
	13	5	2	60	19

Table 4.1 Oxidation reactor evaluation experiments. Trials are divided into four groups: A, Maintaining reaction and extraction, B, Process feasibility, C, Assessing reactor dynamics, and D, On/off control.

Some material in this chapter was originally published in [2].

4.1 Calculations

Several calculations are required to quantify the performance of the reactor. First, the values provided by the recuperation and extraction flow controllers must be converted into molar flow rates:

$$\dot{V}_{STP,actual} = \frac{\dot{V}_{STP,air}\mu_{air}}{(1 - y_{O_2})\mu_{N_2} + y_{O_2}\mu_{O_2}} \tag{4.1}$$

$$\dot{n}_{N_2} = \dot{V}_{STP,actual} * \frac{1 \text{ mol}}{22.4 \text{ SL}} * \frac{1 \text{ s}}{60 \text{ min}} * (1 - y_{O_2}) \tag{4.2}$$

$$\dot{n}_{O_2} = \dot{V}_{STP,actual} * \frac{1 \text{ mol}}{22.4 \text{ SL}} * \frac{1 \text{ s}}{60 \text{ min}} * y_{O_2} \tag{4.3}$$

with $\dot{V}_{STP,actual}$ as the flow rate specified on the controller, in standard liters per minute (SLPM), y_{O_2} representing the molar oxygen percentage in the flow, and μ as the dynamic viscosity of the specified air, nitrogen, and oxygen. Other quantities in Equations 4.2 and 4.3 serve as unit conversions. These calculations are necessary as the flow controllers are programmed in units of SLPM with air as the set fluid. The same calculations are performed for both the recuperation and extraction flows, yielding $\dot{n}_{N_2,recup}$ and $\dot{n}_{N_2,ext}$ as well as $\dot{n}_{O_2,recup}$ and $\dot{n}_{O_2,ext}$. Other gases are considered to exist in negligible quantities. With these values, the total nitrogen entering the bottom of the reactor is determined to be:

$$\dot{n}_{N_2,in} = \dot{n}_{N_2,recup} + \dot{n}_{N_2,ext} \tag{4.4}$$

and the inlet oxygen, for a constant atmospheric composition of 20.9%, is:

$$\dot{n}_{O_2,in} = \frac{0.209\dot{n}_{N_2,in}}{1 - 0.209} \tag{4.5}$$

The change in the molar flow rate of oxygen, then, is simply:

$$\Delta\dot{n}_{O_2} = \dot{n}_{O_2,in} - (\dot{n}_{O_2,recup} + \dot{n}_{O_2,ext}) \tag{4.6}$$

Considering an enthalpy of reaction for the SoFuel particles of ΔH_{rxn} = 380 kJ/mol O_2, the rate of energy released during oxidation can simply be determined by multiplying ΔH_{rxn} by $\Delta\dot{n}_{O_2}$:

$$\dot{Q}_{chem} = \Delta\dot{n}_{O_2}\Delta H_{rxn} \tag{4.7}$$

Coefficient	N_2	O_2
A	-1.5535×10^{-18}	-1.4598×10^{-18}
B	9.8408×10^{-15}	7.1669×10^{-15}
C	-24.4917×10^{-12}	-11.3302×10^{-12}
D	29.1015×10^{-9}	2.4682×10^{-9}
E	-15.1586×10^{-6}	9.5266×10^{-6}
F	3.6729×10^{-3}	-4.7443×10^{-3}
G	28.7168	29.7902

Table 4.2 Temperature-dependent enthalpy coefficients for N_2 and O_2.

For rate of energy extraction from the reactor, the key quantity is the total enthalpy change of the entering and exiting gases. To determine the specific enthalpy at the inlet and extraction, polynomial correlations for specific heat at constant pressure [72] were integrated for both oxygen and nitrogen gas. These integrations yield the following expressions:

$$\Delta h_{O_2} = A_{O_2}(T_{ext}^7 - T_{in}^7) + B_{O_2}(T_{ext}^6 - T_{in}^6) + C_{O_2}(T_{ext}^5 - T_{in}^5) + D_{O_2}(T_{ext}^4 - T_{in}^4) + E_{O_2}(T_{ext}^3 - T_{in}^3) + F_{O_2}(T_{ext}^2 - T_{in}^2) + G_{O_2}(T_{ext} - T_{in}) \quad (4.8)$$

$$\Delta h_{N_2} = A_{N_2}(T_{ext}^7 - T_{in}^7) + B_{N_2}(T_{ext}^6 - T_{in}^6) + C_{N_2}(T_{ext}^5 - T_{in}^5) + D_{N_2}(T_{ext}^4 - T_{in}^4) + E_{N_2}(T_{ext}^3 - T_{in}^3) + F_{N_2}(T_{ext}^2 - T_{in}^2) + G_{N_2}(T_{ext} - T_{in}) \quad (4.9)$$

The coefficients for the specific enthalpy equations are listed in Table 4.2. The total rate of energy extraction from the reactor is specified as:

$$\dot{Q}_{ext} = \dot{n}_{N_2,ext} M_{N_2} \Delta h_{N_2} + \dot{n}_{O_2,ext} M_{O_2} \Delta h_{O_2} \quad (4.10)$$

$\dot{Q}_{ext}$ and $\dot{Q}_{chem}$ are the two key quantities necessary for evaluating overall reactor performance.

4.2 Group A: Maintaining Reaction and Extraction

The aim of the earliest oxidation experiments was twofold. First, the viability of SoFuel particles to drive a self-sustaining oxidation reaction needed to be definitely established. Once this was determined, the following experiments focused on demonstrating extraction flow while maintaining chemical reaction.

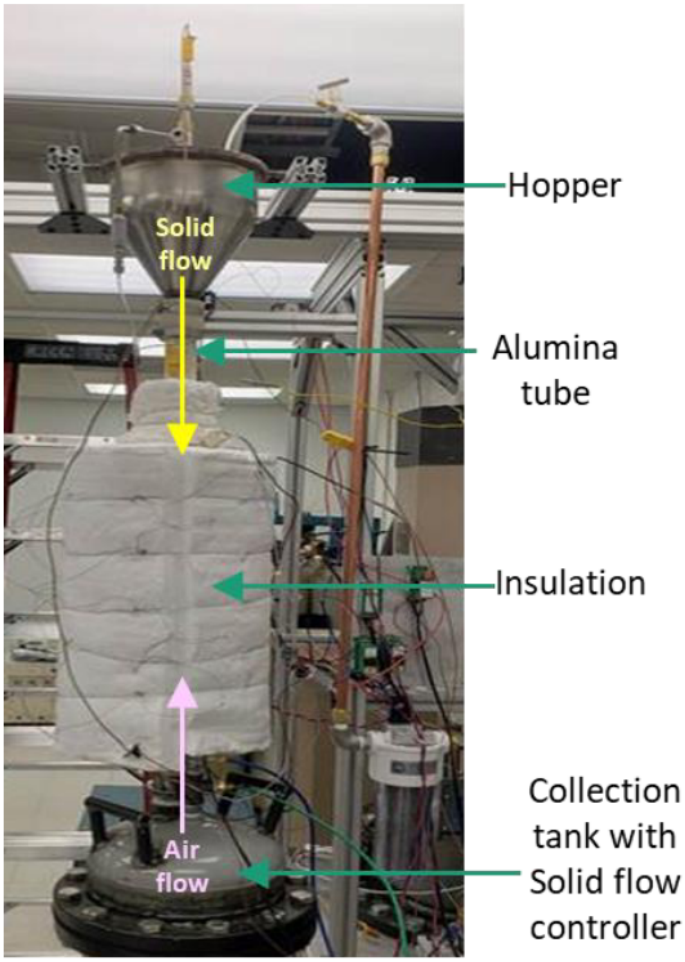

Figure 4.1 The earliest oxidation reactor, consisting of an alumina tube wrapped in insulation. The prototype features no mid-reactor gas extraction.

4.2.1 Experiment 1

Prior to utilizing the reactor described thus far, a basic pilot reactor was assembled to test the ability of the particles to sustain a high-temperature reaction. Shown in Figure 4.1, the apparatus features the same inlet hopper and outlet collection tank as the final reactor design. A 1.2 m long, 44.5 mm ID alumina tube connected to both of these. 0.45 m of the tube was wrapped in a nichrome coil, which was subsequently covered in a fibrous insulation blanket. A type-K thermocouple was inserted inside the bed of particles to monitor system temperature. The apparatus featured no extraction tube, as the objective of the experiment was simply to assess whether the reacting particles could sustain a reaction without any outside interference.

Reduced (1.75 g/s, 1400°C) 3.66 mm SoFuel particles were loaded into the reactor at room

temperatures. The tube was preheated to 1000°C and dwelled for 20 minutes, after which both downward particle and upward gas flows commenced. The particle flow rate was set to 1.5 g/s, and the gas controller featured an oscillating scheme with an average value around 49 SLPM. The practice of osciallating the gas counterflow had been utilized with the reduction reactor to mitigate fluidization in the bed. The experiment concluded once there were no more particles entering the reactor. Results are shown in Figure 4.2. Due to the oscillatory nature of the recuperation flow, $\dot{V}_{recup}$ is an average value over 200 seconds. An area deemed to be near steady operation is depicted by the shaded region. After the initial 20 minutes of dwell time (which are included in the runtime of this particular experiment), the bed temperature rises drastically before leveling out at an average steady value of 1182 ± 11°C. The system is able to maintain oxidation over a long duration, with the rate of released chemical energy exceeding the rate of heat loss at 1000°C. This suggests that excess energy being used to elevate the temperature of the bed could be utilized via an extraction flow.

4.2.2 Experiment 2

A subsequent experiment was carried out on the oxidation reactor described in Section 3. The complete experimental setup is displayed once more in Figure 4.3. Enough oxygen sensors had not yet been installed to facilitate chemical energy calculations, but an experiment was designed to assess extraction viability. The reactor tube was filled with 3.66 mm diameter reduced SoFuel particles and heated to 1000°C under a small flow of nitrogen gas. Particle flow was initiated during preheating at regular intervals to ensure bed mobility. After dwelling at 1000°C for 20 minutes, flow rates of 1.5 g/s, 60 SLPM, and 31 SLPM commenced for $\dot{m}_s$, $\dot{V}_{recup}$, and $\dot{V}_{ext}$, respectively. At t = 0 min the gas composition was changed from nitrogen to air as well. The experiment progressed for nearly an hour with varying gas flow rates before concluding.

Results from the experiment are illustrated in Figure 4.4. Due to technical issues during operation, mass flow measurements for this experiment are incomplete and not shown. The sharp increase in the extraction temperature around t = 7.5 min is similarly due to an initial connectivity issue. The results indicate a narrow, well-controlled reaction zone even with high temperature gas

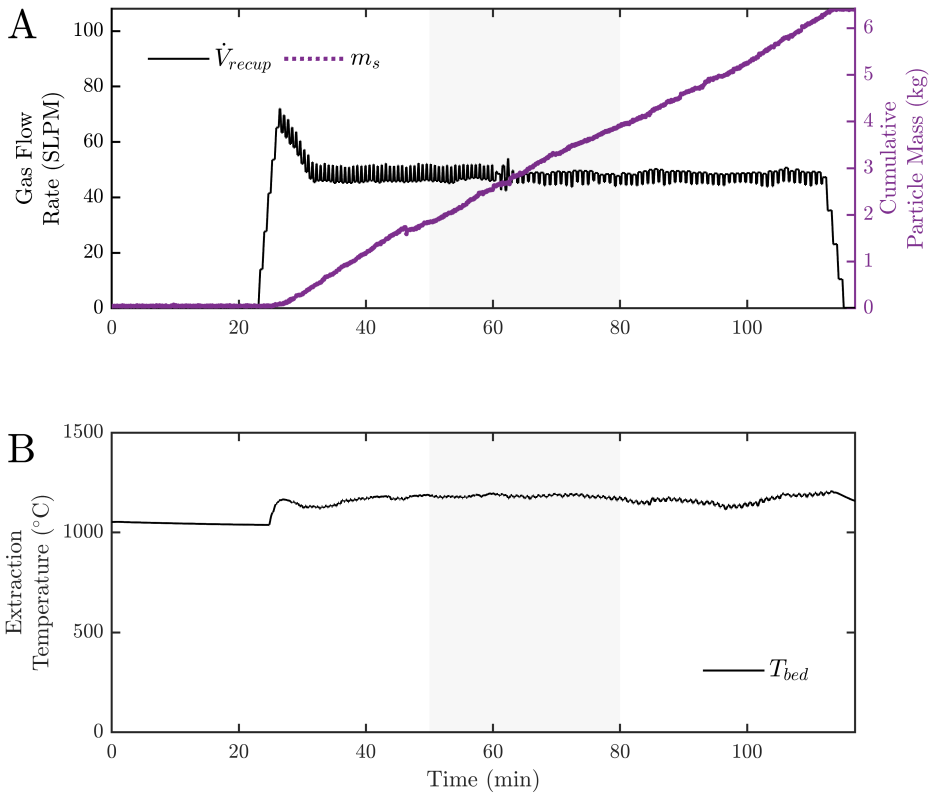

Figure 4.2 Experiment 1, the first self-sustaining oxidation reaction using Mg-Mn-O. Subplots include (A) Solid and gas flows, and (B) Internal bed temperature.

extraction from the system. Due to user input to gas flows, the reaction zone is managed to remain stationed near the center of the observation area. The shaded region in Figure 4.4 b indicates an area of steady operation. Within this region the average value for T_{ext} is 952 ± 9, indicating sustained high temperature extraction. T_{ext} does appear to decrease over the course of the experiment, though, suggesting that continuing changes to the bed temperature distribution affect the extraction flow.

4.2.3 Experiment 3

The third oxidation experiment was the first to feature oxygen concentration measurements in both the extraction and recuperation flows, providing the information necessary to estimate the chemical energy released by the particles. Reduced 3.66 mm particles were loaded into the reactor. The typical preheating process was followed to 1000 °C under a small flow of nitrogen gas. Measurements from the experiment are depicted in Figure 4.5. The results are split into three

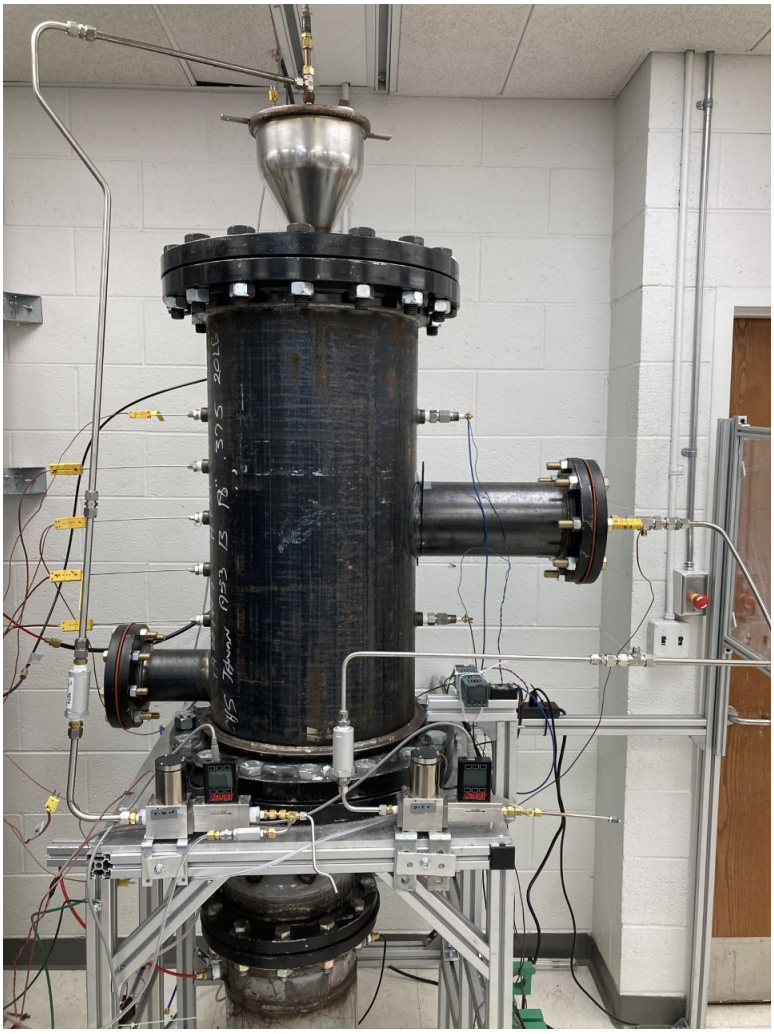

Figure 4.3 The assembled oxidation reactor setup. The various subcomponents, sensors, and actuators of the previous chapter are visible. Originally printed in [2].

subfigures; this configuration is utilized for all following experimental data. Figure 4.5a depicts the temperature of the bed as recorded by the five reaction zone thermocouples. These thermocouples are stationed between H/L = 0 and 1 in intervals of 0.25. All intermediate shading is the result of linear interpolation. Figure 4.5b displays the gas and solid flow characteristics of the reactor. Figure 4.5c includes $\dot{Q}_{ext}$, $\dot{Q}_{chem}$, and T_{ext}, illustrating the performance of the reactor. The shaded region indicates an area considered to be operating near steady-state.

As shown in Figure 4.5a, the hot zone initially moves downward as the particle bed begins to move at $\dot{m}_s$ = 1.5 g/s. After a slight delay in connecting the oxygen sensors, Figure 4.5c showcases the elevated chemical energy production initiated by the introduction of air to the particle bed.

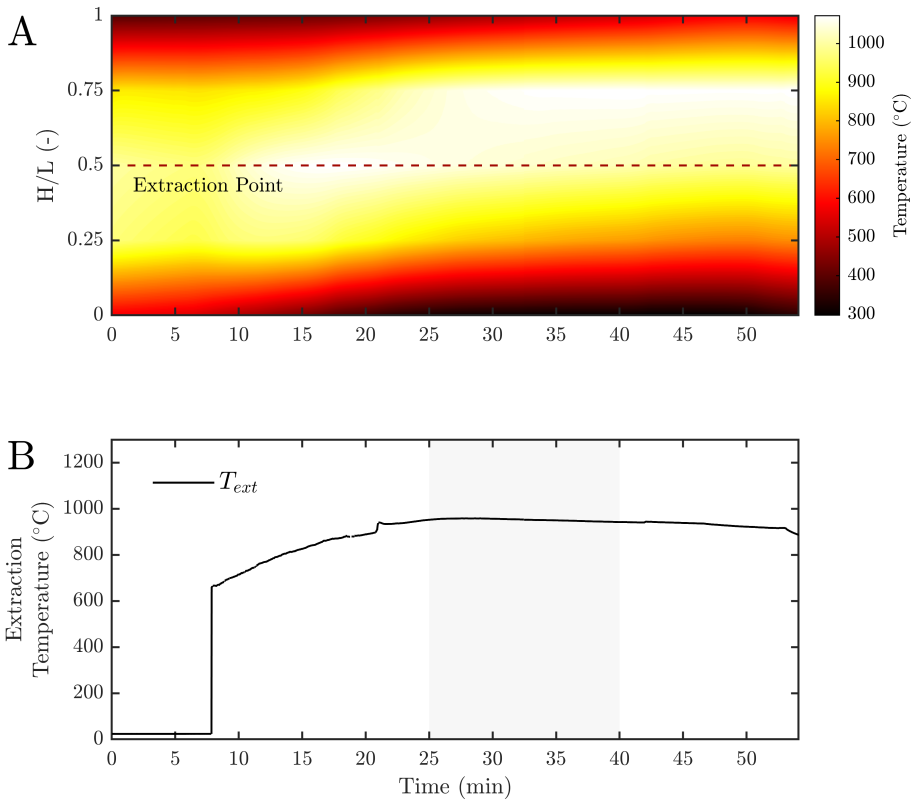

Figure 4.4 Experiment 2, an early user-controller oxidation experiment. Subplots include (A) Bed temperature contour, and (B) Extraction temperature.

The bed achieves nearly steady operation by t = 20 min, but changing gas flow rates continue to raise the extraction temperature. With an extraction flow rate of 23 SLPM around t = 60 min, the bed operates steadily for nearly twenty minutes. The temperatures in the reaction zone noticeably decrease during this time, and T_{ext} begins to decrease as well. Furthermore, the reaction zone gradually shifts upwards, especially after increasing $\dot{m}_{g,ext}$ around t= 60 min. The experiment concludes and the bed is cooled back to room temperature.

4.3 Group B: Process Feasibility

By attaining a runtime of nearly 90 minutes, Experiment 3 demonstrated consistent chemical reaction and potential long-duration stability. Two additional experiments were devised to further assess the chemical conversion of the reactor, its capacity for steady operation, and its feasibility as a companion for the previously devised reduction setup. Each of these experiments was preceded

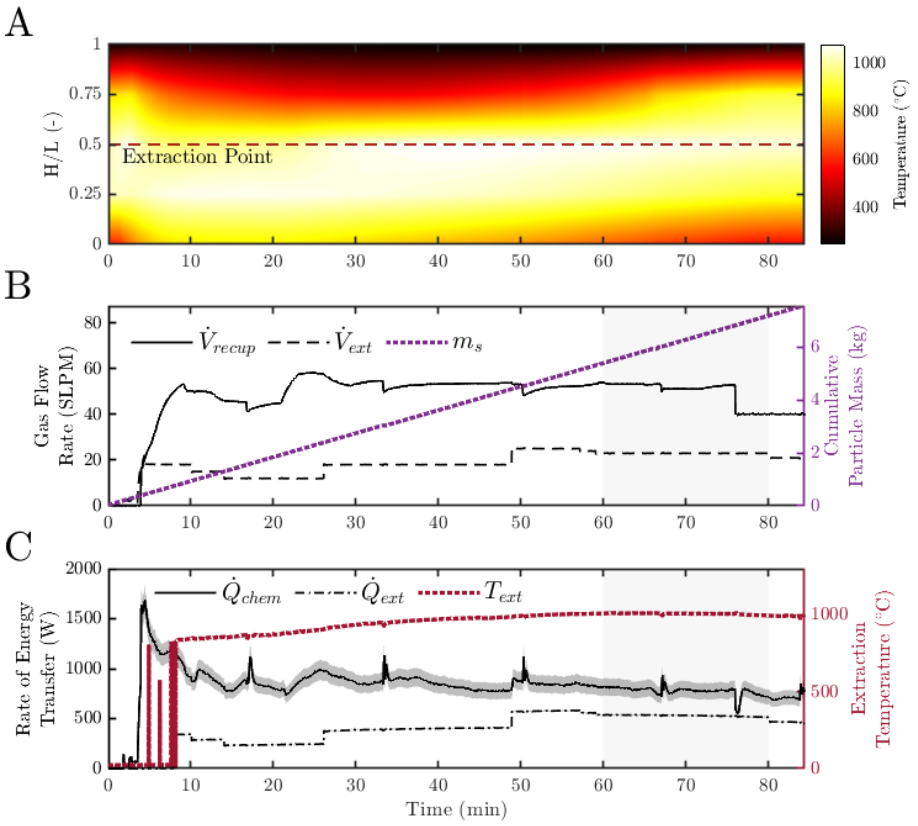

Figure 4.5 Experiment 3, the first experiment to implement oxygen measurement to estimate chemical energy release. Subplots include (A) Bed temperature contour, (B) Solid and gas flows, and (C) Energy transfer rates and extraction temperature.

by a reduction process performed on the companion reduction reactor at a particle flow rate of 1.25 g/s. Three random particles from each reduction were tested in a Netzsch STA Jupiter F5 thermogravimetric analyzer (TGA) to determine extent of reduction. Approximately 13 kg and 15 kg of reduced particles were produced for the the experiments, respectively. For these and all remaining experiments, the average particle size was increased from 3.66 mm to 5 mm. This chnage in size was primarily implemented to facilitate easier operation of the reduction reactor, where elevated temperatures can cause fluidization and halt downward bed flow for small particles.

4.3.1 Experiment 4

Experiment 4 began with a bed of reduced particles, initially at rest and kept from reacting by a small flow (4 SLPM) of N_2 gas. This experiment models the startup behavior for a larger-scale

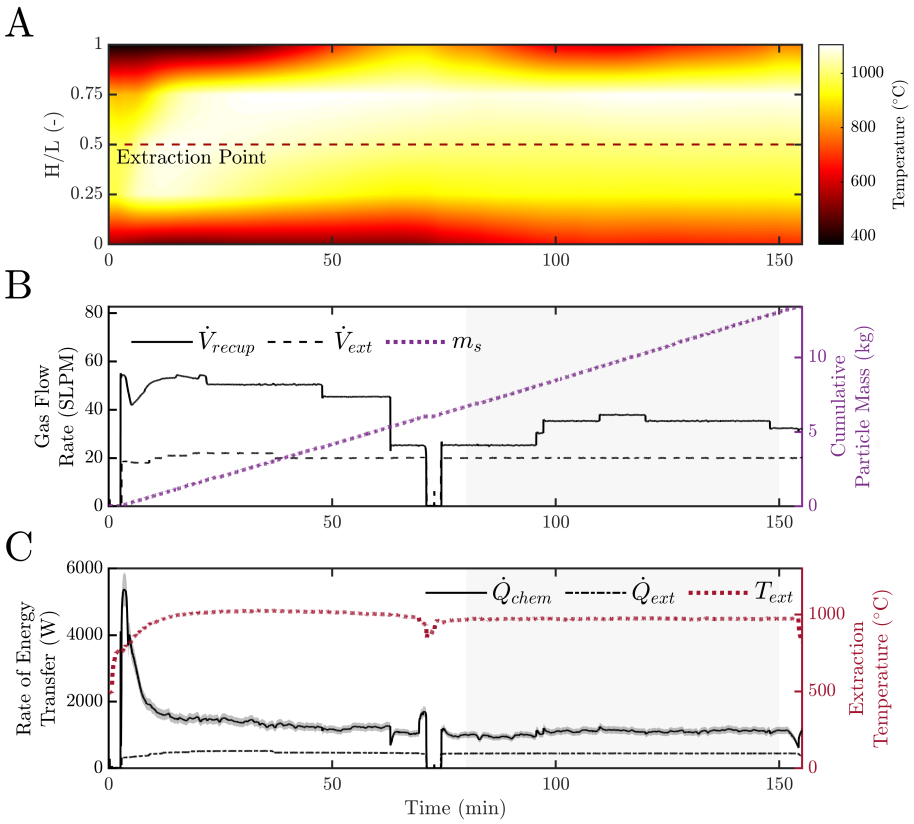

Figure 4.6 Experiment 4, the first user-controlled feasibility experiment. Subplots include (A) Bed temperature contour, (B) Solid and gas flows, and (C) Energy transfer rates and extraction temperature. Minor modifications have been made to a figure originally printed in [2].

reactor that has been freshly filled with reduced particles. The bed was preheated to 1000°C to prepare the system for operation. At t = 0 min, 1) the preheating nichrome coil was disconnected, 2) the particle bed began moving downward at 1.5 g/s, and 3) the N_2 counterflow was set to 50 SLPM. Once movement was confirmed at the top of the bed, the input gas was switched from nitrogen to air. The hopper was filled with reduced particles and sealed. Recuperation and extraction flows were varied to encourage steady operation, eventually attaining values of around 25 SLPM and 20 SLPM, respectively. All flows halted at t = 80 min to depressurize the system and add more particles to the hopper. After resuming operation, flows were halted again at t = 150 min and the bed cooled to ambient temperatures. Three samples of oxidized particles were extracted and analyzed in the TGA.

Measurements from Experiment 4 are depicted in Figure 4.6. The beginning of the experiment

is characterized by a shrinking reaction zone, as depicted by initially decreasing temperatures in Figure 4.6a. The rate of heat losses at first outpaces the exothermic oxidation reaction. As the particles in the heated zone all react at once, the bed releases a large amount of energy. This spike is observable in Figure 4.6c, as $\dot{Q}_{chem}$ exceeds 5000 W. Various gas flow rates are implemented, primarily for the recuperation flow, to maintain a steady reaction zone. The discontinuity near the midpoint of the experiment is due to the depressurization of the vessel and addition of new particles. Steady-state behavior is observed across all plots between 80 and 150 minutes, with only the recuperation flow varying. This region is designated as the shaded sections of Figure 4.6b and 4.6c. Both the extraction temperature and rate of energy extraction remain consistent for over one hour, demonstrating the steady-state operational capabilities of the reactor. The reaction zone generally maintains a consistent size and distribution.

4.3.2 Experiment 5

The second study evaluated a different operational case. Here, the conditions emulated those of a semi-continuous reactor beginning another period of operation after some period of downtime. Reduced particles were once again loaded into the reactor, but dwelled overnight at 1000°C in air. As experimental operation began, then, the reaction zone contained fully oxidized particles while the rest of the tube and hopper remained reduced. The bed began moving downward at 1.5 g/s with an air counterflow of 60 SLPM. The nichrome coil continued to supply heat to the reactor as reduced particles moved toward the reaction zone. This input heat decayed over time as the reduced particles began to react, eventually reaching a value of zero. The hopper was filled with particles and sealed close to 60 minutes after the onset of data collection. Recuperation and extraction flows were set to 35 SLPM and 20 SLPM, respectively. Flows halted after 140 minutes for depressurization and the addition of more particles to the system. Upon resuming the experiment, gas flows were heavily adjusted to attain a steady bed temperature profile. Recuperation and extraction flow rates eventually settled around 20 SLPM and 25 SLPM, respectively. The experiment ended around 230 minutes, after which the reactor was cooled to ambient temperatures. Three samples (each less than 10 g) of oxidized particles were extracted from the bottom of the reactor and analyzed in the

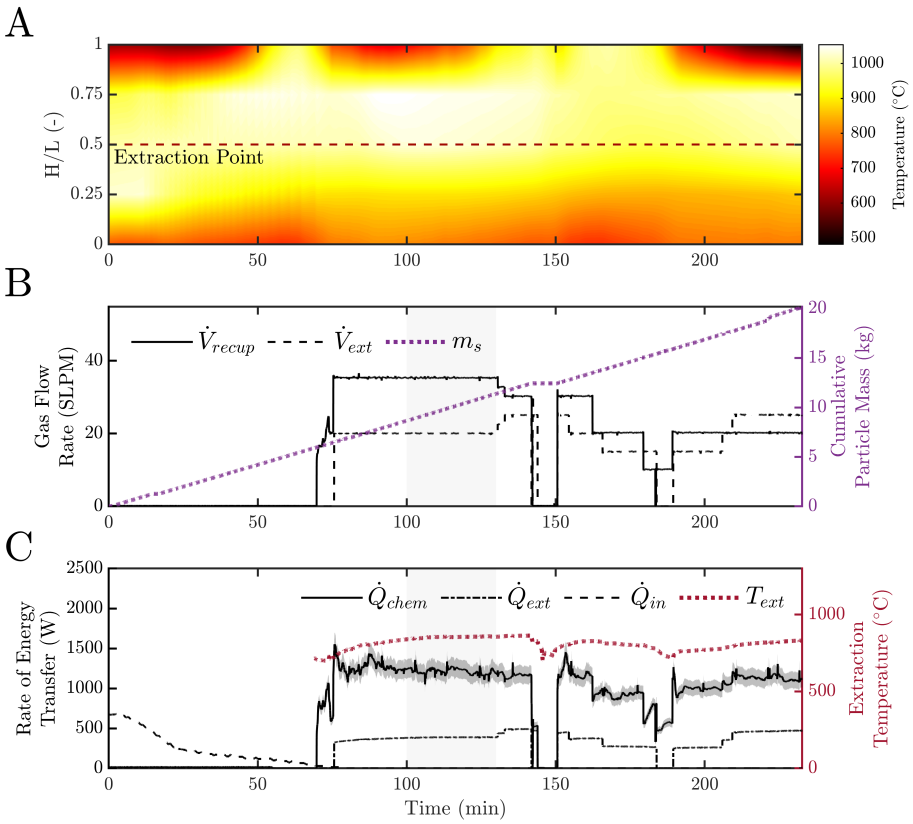

Figure 4.7 Experiment 5, the second user-controlled feasibility experiment and the first investigation with a bed of oxidized particles. Subplots include (A) Bed temperature contour, (B) Solid and gas flows, and (C) Energy transfer rates and extraction temperature. Minor modifications have been made to a figure originally printed in [2].

TGA.

Figure 4.7 presents measurements from Experiment 5. In contrast with Experiment 4, at t = 0 min the tube is filled with oxidized particles rather than reduced ones. The nichrome preheating coil remains powered during the beginning of the experiment to maintain a reaction zone temperature of 1000°C. Figure 4.7c includes an additional plotted line for input energy to the reactor provided by the nichrome coil. It illustrates the decrease in the energy needed by the coil as reduced particles move into the reaction zone. Indeed, Figure 4.7a depicts an upward-moving reaction zone, as the oxidation reaction seemingly climbs up the tube to reach unreacted particles. When the system is properly sealed and other measurements initiated, the reaction zone is steady for a time. The addition of new particles around t = 150 min coincides with another spatial rise in the reaction

zone. This behavior is remedied by drastically reducing the recuperation flow rate, as shown in Figure 4.7b. The eventual stabilization of the system occurs with a higher extraction flow rate and lower recuperation flow rate than initially employed. While vertical creep of the reaction zone is not a desired outcome, this experiment showcases the ability to employ differing gas inputs and achieve a desired operating state.

4.3.3 Operational and Measurement Feasibility Analyses

TGA data from both experiments provide insight into the conversion efficiency of the oxidation reactor. Results for samples before and after Experiment 4 and Experiment 5 are shown in Figures 4.8a and 4.8b, respectively. The left vertical axis depicts the change in mass of each sample normalized by the initial mass, while the right axis records the temperature of the analysis process. There is some variation among samples for each experiment, but this can be attributed to random inhomogeneities among particles. Both figures show a marked difference between inlet (reduced) and outlet (oxidized) particles. Previous investigations of the companion reduction reactor produced the following expression for characterizing extent of conversion [1]:

$$\alpha_{TGA} = 1 - \frac{\Delta m}{(\Delta m + m_{initial})\,\beta} \tag{4.11}$$

Based on this equation, the average inlet extent of conversion for Experiment 4 is 0.009 ± 0.0560 and the average outlet extent is 0.872 ± 0.0261, denoting a difference of 0.863 ± 0.0821. The same quantities for Experiment 5 are -0.085 ± 0.125 (signifying a reduced state beyond the reference state), 0.875 ± 0.0283, and 0.960 ± 0.0545. Both experiments exhibit high rates of conversion from the reduced to the oxidized state, suggesting that this reactor configuration is well-suited to adequately extract energy from reduced particles.

The extent of conversion measurements from Experiments 4 and 5 can be further employed to verify the accuracy of using oxygen concentrations to estimate the $\dot{Q}_{chem}$. Assuming a constant solid mass flow rate, the energy released by the oxidation reaction can be expressed in a manner similar to Equation 2.6:

$$\dot{Q}_{chem,TGA} = \frac{(\alpha_{out} - \alpha_{in})\,\beta \dot{m}_s \Delta H_{rxn}}{M_{O_2}} \tag{4.12}$$

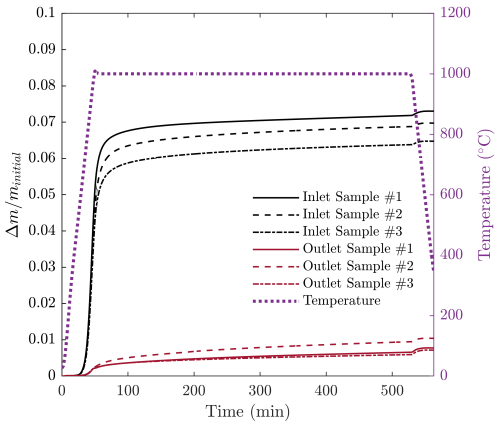

(a) Experiment 4 TGA results.

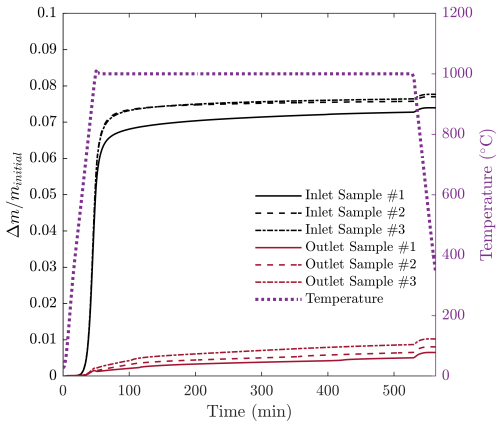

(b) Experiment 5 TGA results.

Figure 4.8 TGA results for the two feasibility experiments. Inlet and outlet here correspond to particles collected from the reactor inlet and outlet, respectively. The difference in percent change in mass between the inlet and outlet samples signifies high amounts of chemical conversion. Originally printed in [2].

The values of $\dot{Q}_{chem,TGA}$ for Experiments 4 and 5 are 1073 ± 102 W and 1193 ± 67 W, respectively. The average measurements of $\dot{Q}_{chem}$ based on runtime oxygen measurements are 1083 ± 126 W and 1215 ± 121 W, respectively, for the two experiments. The difference between the two methods for calculating the average rate of chemical energy release is less than 2% for each experiment, suggesting that both approaches are appropriate for determining average values for $\dot{Q}_{chem}$. Due to the ease with which oxygen data can be obtained during operation, this method is favored for all subsequent experiments.

4.4 Group C: Assessing Reactor Dynamics

The experiments in Groups A and B successfully showcase chemical conversion and long-duration operation of the oxidation reactor. Because these experiments were meant to demonstrate these objectives, inputs to the system were manually adjusted to steer the system toward desired operational states. The experiments in Group C are characterized by leaving system inputs constant in order to observe reactor behavior.

4.4.1 Experiment 6

Experiment 6 featured inputs of $\dot{m}_s$ = 0.75 g/s, $\dot{V}_{recup}$ = 27 SLPM, and $\dot{V}_{ext}$ = 21 SLPM. The reactor initially contained fully oxidized particles, with reduced particles gradually moving into

the reaction zone in a similar way to Experiment 5. The desired reaction zone was preheated to a temperature of 1000°C prior to the experiment, and the bed dwelled at elevated temperatures for several hours to achieve thermal homogeneity. At t = 0 min, solid and gas flows were initiated. The temperature-controlled nichrome heating coil remained active throughout the experiment, adding energy to the system both before and during the reaction of oxidizing particles. System pressure was maintained around 0.75 bar. The results of this experiment are shown in Figure 4.9. As Figure 4.9a illustrates, temperatures in the particle bed remain largely unchanged throughout the first hour of the experiment, as reduced particles slowly work their way down the reactor tube toward the high temperature zone. As these particles reach the high temperature zone around t = 60 min, the reaction zone drastically moves upward. The hottest part of the reactor quickly shifts to the upper reaches of the alumina tube, with the nichrome coil continuing to provide input power to maintain the temperature of the area around the extraction point. With relatively constant recuperation and extraction flow rates, the experiment proceeded for over 2.5 hours before concluding.

The results illustrate in greater detail some of the phenomena identified in previous experiments. The runaway reaction zone, observed in Experiment 5, appears once again here as the particles react above the extraction zone. The hottest part of the reactor lies well above the extraction point, releasing chemical energy that will largely escape as losses. While $\dot{Q}_{chem}$ remains relatively consistent over the course of the experiment (with a value of 749 ± 73 W), the fact that the power supplied to the nichrome heating coil does not decay to zero demonstrates that these flow rates are not suitable for self-sustaining operation. The extraction temperature remains low as well, with a value of only 858 ± 6°C, notably lower than previous experiments that implemented user controls.

4.4.2 Experiment 7

Figure 4.10 displays data from Experiment 7. Input parameters for the experiment were $\dot{m}_s$ = 1.25 g/s, $\dot{V}_{recup}$ = 45 SLPM, and $\dot{V}_{ext}$ = 16 SLPM. In contrast to Experiment 6, the particle bed contained reduced particles preheated under a small nitrogen flow to avoid premature oxidation, in a manner similar to Experiment 4. At t = 0 min the nitrogen input to the system was switched to oxygen, initiating oxidation within the bed. The solid flow rate was erroneously set to 2.5 g/s

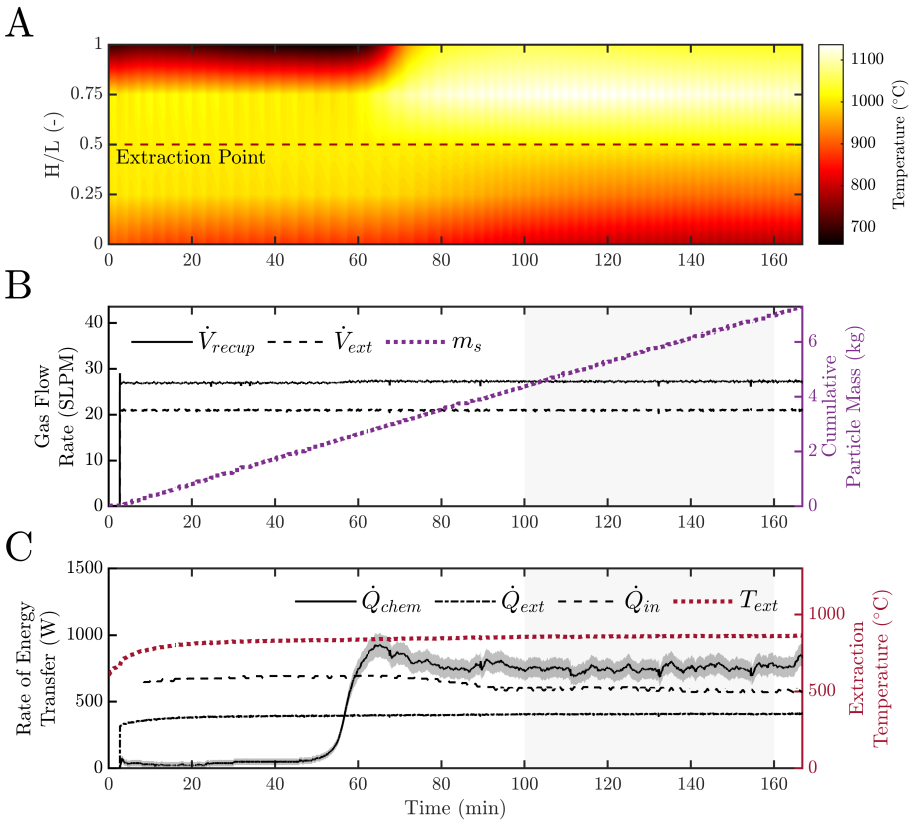

Figure 4.9 Experiment 6, assessing reactor behavior at low flow rates. Note the usage of the nichrome heating coil throughout reactor operation. Subplots include (A) Bed temperature contour, (B) Solid and gas flows, and (C) Energy transfer rates and extraction temperature.

early in the experiment, but this mistake was rectified near t = 14 min. As depicted in Figure 4.10a, the reaction zone once again shifted, passing beyond the observation zone by t = 40 min. The bed continued to operate in a largely steady fashion until the conclusion of the experiment around t = 100 min.

The erroneous solid flow rate during the onset of the experiment provides some useful insights. While Figure 4.10c still showcases the typical high initial release of chemical energy, the temperature profile of the bed in Figure 4.10a stays relatively consistent prior to t = 14 min. The rapid ascent of the reaction zone after this period suggests that the relationship between the solid flow rate and recuperation flow rate plays an important role in dictating the position of the reaction zone. Reactor performance once again suffers due to the reaction zone shift. Although the average extraction temperature during steady-state operation is 881 ± 7°C, the temperature decays over the course

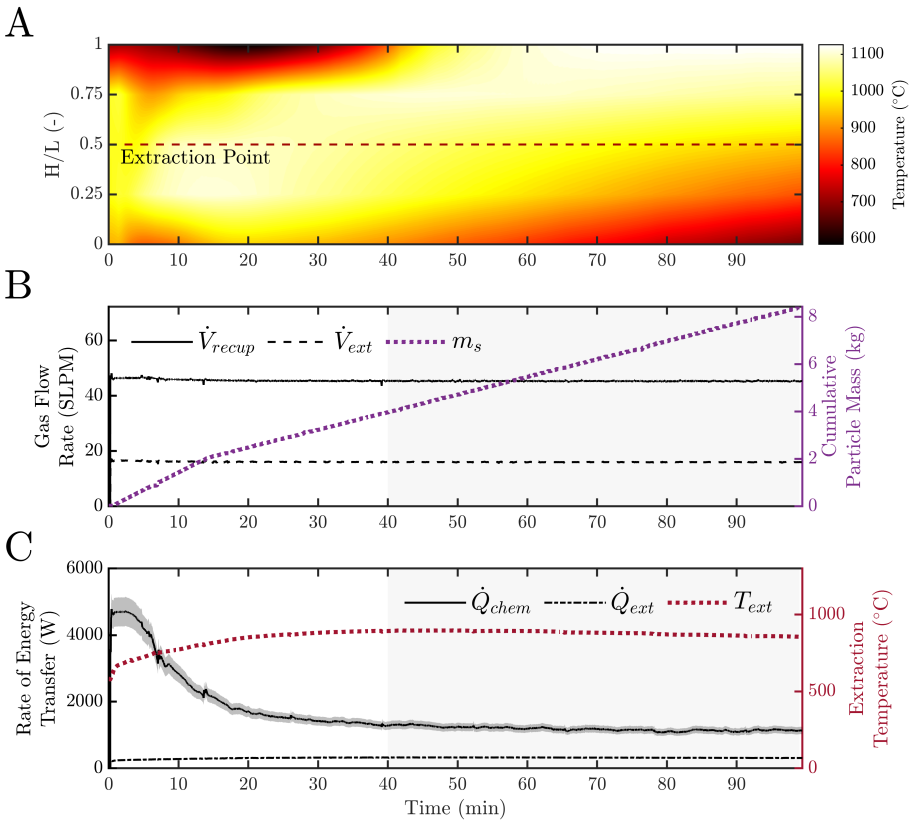

Figure 4.10 Experiment 7, showcasing thermal runaway caused by excessive recuperative gas flow. Subplots include (A) Bed temperature contour, (B) Solid and gas flows, and (C) Energy transfer rates and extraction temperature.

of the experiment. While the performance is clearly not optimal, the reactor still exhibits good long-duration stability.

4.4.3 Experiment 8

Experiment 8 sought to achieve a more favorable outcome than Experiment 7 for the same solid flow rate, $\dot{m}_s$ = 1.25 g/s. For this trial, $\dot{V}_{recup}$ was reduced to 29 SLPM and $\dot{V}_{ext}$ remained that same at 16 SLPM. The experiment began in the same fashion as Experiment 7, with a bed of reduced particles preheated to 1000°C. At t = 0, 1) particles began to flow, 2) nitrogen was switched to air, and 3) power was no longer supplied to the nichrome heating coil. Experimental data is shown in Figure 4.11. The measurements exhibit the same initial rise in $\dot{Q}_{chem}$ as all other trials featuring an initially reduced bed. The system operates steadily until near t = 120 min, when the setup is

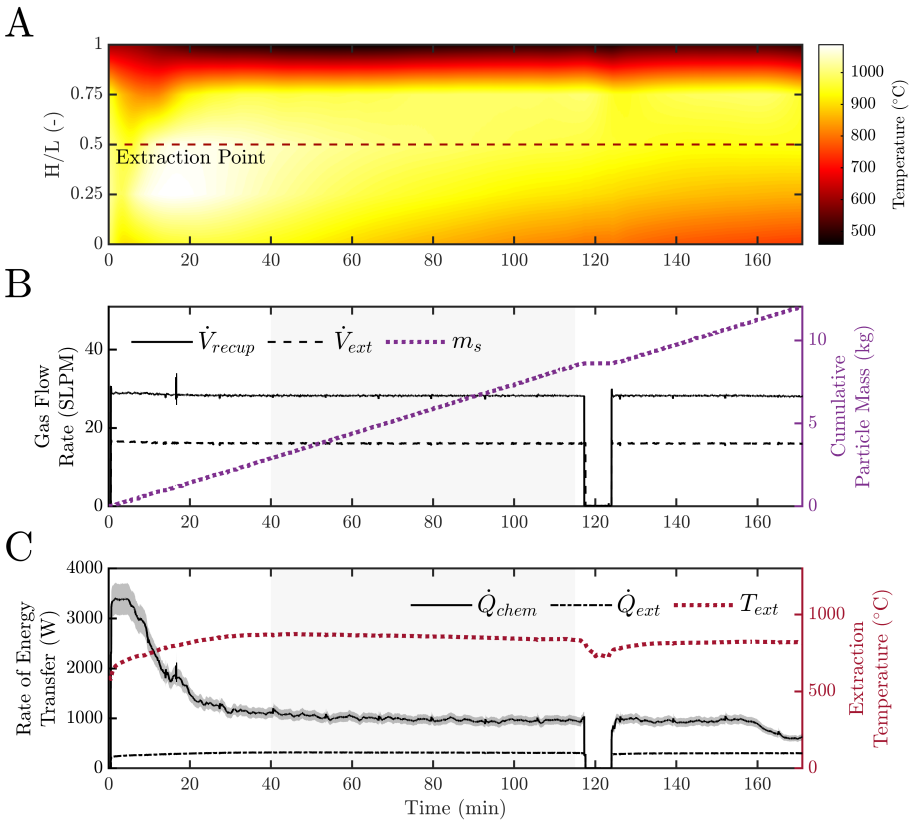

Figure 4.11 Experiment 8, investigating the same $\dot{m}_s$ as Experiment 7 but with a lower $\dot{V}_recup$ to mitigate thermal runaway. Subplots include (A) Bed temperature contour, (B) Solid and gas flows, and (C) Energy transfer rates and extraction temperature.

depressurized to allow for the addition of more particles. The discontinuities in Figure 4.11 are the result of this loading procedure. In order to facilitate longer operation, the last particles loaded into the system are some partially oxidized particles. These are reflected at the end of the experiment, as Figure 4.11c shows $\dot{Q}_{chem}$ decrease around t = 160 min. The experiment is concluded shortly thereafter.

The average T_{ext} for Experiment 8 is 857 ± 6°C. While this is notably lower than the average extraction temperature for Experiment 7, the reaction zone exhibits no upward movement in this trial. The bed temperature distribution, as illustrated in Figure 4.11a, remains bounded in its upper reaches. Cooling is visible in the lower half of the observation zone. After t = 60 min there is consistent narrowing of the reaction zone, until around t = 140 min. The average steady $\dot{Q}_{chem}$ for this experiment is 991 ± 94 W, lower than $\dot{Q}_{chem}$ = 1182 ± 114 W for Experiment 7. This

discrepancy is likely due to a combination of differences in the initial reduction state of the loaded particles and higher rates of chemical reaction produced by the runaway reaction zone. Since the $\dot{Q}_{ext}$ for the two experiments are similar (320 ± 4 W and 314 ± 3 W for Experiments 7 and 8, respectively), Experiment 8 is removing a greater share of the released chemical energy from the reactor. This may contribute to the narrowing reaction zone and lower extraction temperature, which both decay over time.

The most important outcome of Experiment 8 is the confirmation of the impact of the recuperative gas flow on the position of the main reaction zone. While Experiment 7 featured an oxidation zone consistently climbing the reactor tube, the temperature profile of Figure 4.11a shows no such behavior. Although $\dot{V}_{recup}$ is low enough to avoid thermal runaway, it still remains high enough to ensure adequate high recuperation in the lower reaches of the particle bed, as evidenced by the cooling of the bottom two thermocouples.

4.4.4 Experiment 9

Further runtime data produced during Experiment 9 is presented in Figure 4.12. For this trial, $\dot{m}_s$ = 2 g/s, $\dot{V}_{recup}$ = 45 SLPM, and $\dot{V}_{ext}$ = 25 SLPM, with an initial bed of reduced particles. The gas flow rates utilized in this experiment were scaled versions of those used in Experiment 8. Figure 4.12 illustrates typical operation, which follows the same procedure as Experiment 8. This includes the discontinuity around t = 70 min, when additional particles were added to the depressurized system. Steady operation is achieved for one hour between t = 80 and 140 with an average T_{ext} of 890 ± 7°C. Unlike Experiment 8, reduced particles are used until the conclusion of the experiment around t = 145 min. Operation is once again maintained for a long duration of time. According to Figure 4.12, the reaction zone remains centered near the extraction point.

4.4.5 Repeatability Experiments (Experiments 10 and 11)

The Group C experiments described thus far illustrate a variety of operational parameters. Consistent repeatability, however, was complicated by several factors. The most prominent of these was changes to the experimental setup due to routine maintenance. The nichrome coil used to preheat the reactor typically lasted 3-4 experiments before high operational temperatures degraded

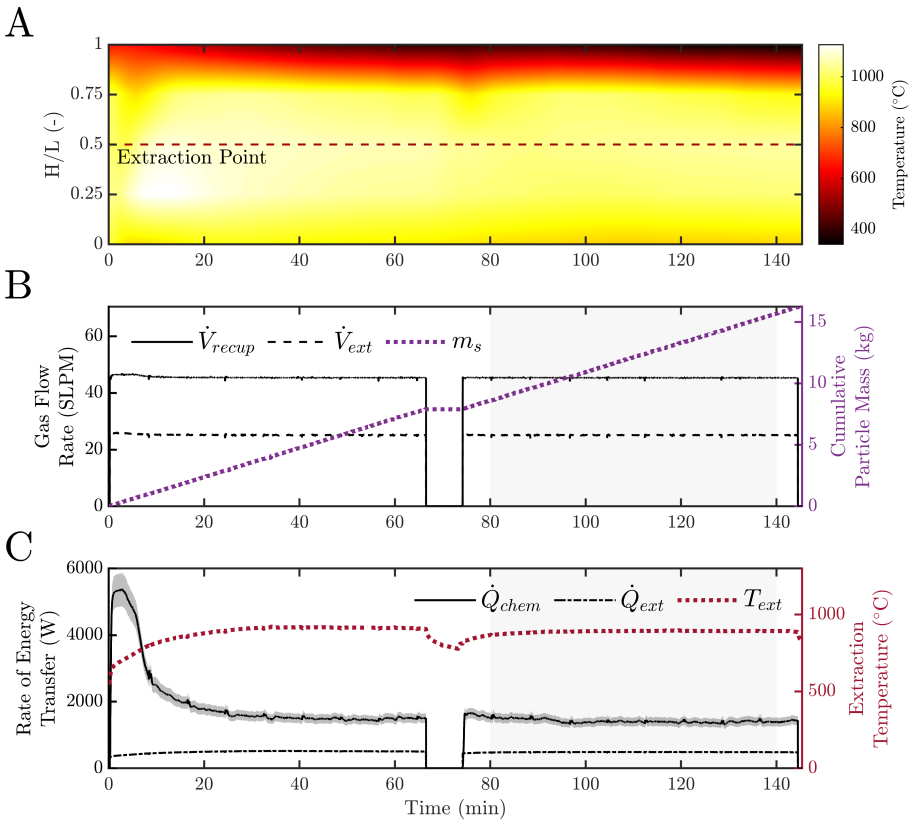

Figure 4.12 Experiment 9, depicting stable reactor operation at a higher solid flow rate. Subplots include (A) Bed temperature contour, (B) Solid and gas flows, and (C) Energy transfer rates and extraction temperature.

it to the point of failure. Additionally, the tube occasionally experienced fractures due to stresses within the system. Both of these components could only be repaired by opening the steel shell, removing the system insulation, and performing necessary maintenance. It was impossible to place the coil or pack the insulation in the exact same configuration every time the reactor was reassembled, leading to random variations in losses and the initial position of the reaction zone across experiments. Repeatability was further impacted by limitations to experimental runtime. The upper particle funnel can only contain a limited number of particles, necessitating depressurization and reloading during long-duration tests. These tests are useful for showcasing continuing operation, but were difficult to faithfully replicate.

Experiments 10 and 11 were two shorter-duration trials performed one after the other without any system maintenance. Similar to other experiments, particles were reduced and loaded into the

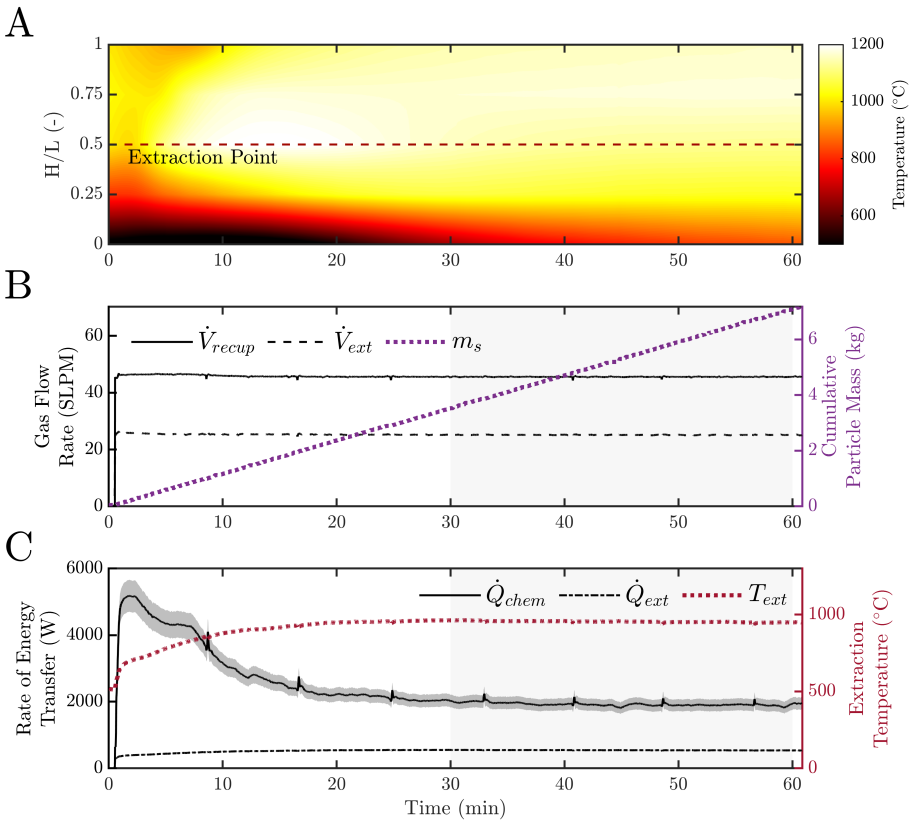

Figure 4.13 Experiment 10, the first repeatability experiment with $\dot{m}_s$ = 2 g/s. Subplots include (A) Bed temperature contour, (B) Solid and gas flows, and (C) Energy transfer rates and extraction temperature. Minor modifications have been made to a figure originally printed in [2].

main reactor tube. The system was preheated to 1000°C under a small nitrogen counterflow and left to dwell for at least 3 hours. Particle flowability was confirmed prior to the onset of the experiment, and the system was sealed and pressurized to approximately 0.75 bar. At t = 0 min, 1) $\dot{m}_s$ = 2 g/s, 2) the inlet gas was switched from nitrogen to air, 3) the preheating coil was turned off, and 4) $\dot{V}_{recup}$ = 45 SLPM and $\dot{V}_{ext}$ = 25 SLPM. The reactor operated steadily throughout each experiment until the particle hopper was empty. After this, the bed cooled down to ambient temperatures.

Results for Experiments 10 and 11 are shown in Figures 4.13 and 4.14, respectively. The most easily observed visual difference between the two experiments is the dark, lower-temperature band present in Figure 4.13. While such a discrepancy may seem dramatic, the thermocouples used to generate these temperature contours are spaced only 11.43 cm apart from one another. Temperature gradients on the edges of the reaction zone are incredibly steep; minute differences

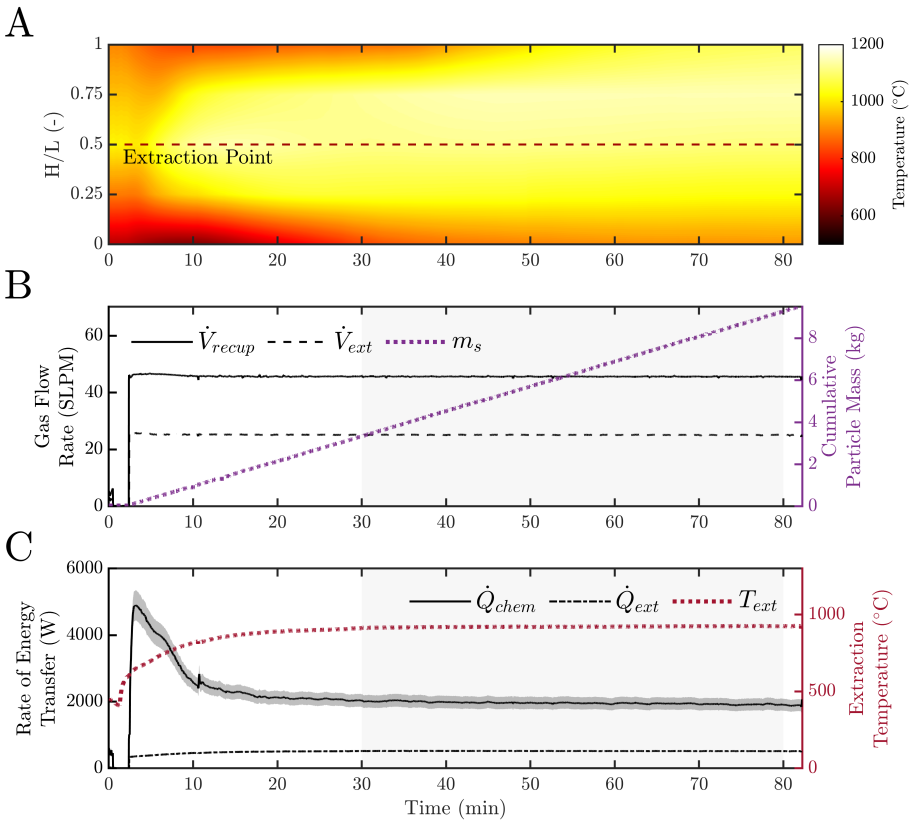

Figure 4.14 Experiment 11, the second repeatability experiment showcasing steady reactor behavior. Subplots include (A) Bed temperature contour, (B) Solid and gas flows, and (C) Energy transfer rates and extraction temperature. Minor modifications have been made to a figure originally printed in [2].

in the experimental process appear to have outsize affects in these regions. A better indicator of repeatability is the comparison between performance metrics for the two processes, which are shown in Figures 4.13c and 4.14c. To aid in comparing $\dot{Q}_{chem}$, $\dot{Q}_{ext}$, and T_{ext}, separately plots for these quantities are shown in Figure 4.15. The percent differences for $\dot{Q}_{chem}$, $\dot{Q}_{ext}$, and T_{ext} during steady operation are 1.94%, 4.57%, and 3.46%, respectively. Among these three metrics $\dot{Q}_{chem}$ is the most immune from small fluctuations in temperature. All of these quantities differ by less than 5%, suggesting good repeatability between the experimental runs.

4.5 Group D: On/Off Control

The final group of evaluation experiments performed on the oxidation reactor provided insights into possible control strategies for the system. As illustrated in Experiments 5, 6, and 7, with

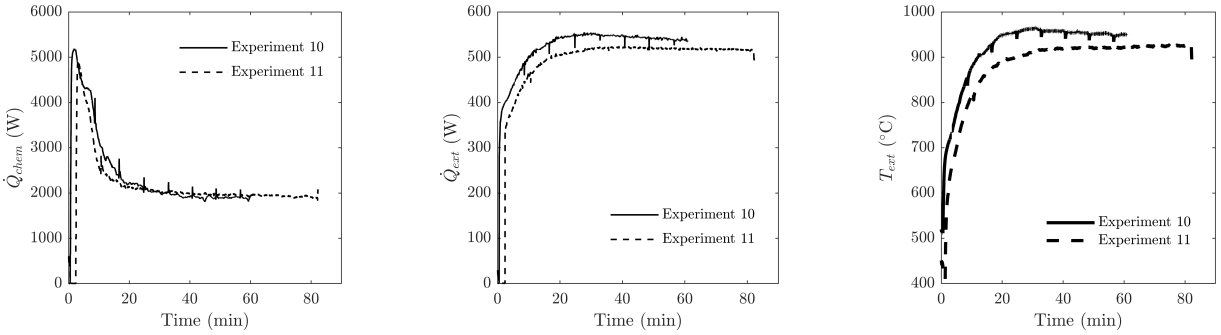

(a) $\dot{Q}_{chem}$ (b) $\dot{Q}_{ext}$ (c) T_{ext}

Figure 4.15 Performance metric comparisons between Experiments 10 and 11. High levels of agreement between these quantities suggests excellent repeatability of the oxidation reactor.

improper inputs it was possible for the reaction zone to move up the tube in an uncontrolled fashion. This phenomenon has been observed to adversely impact reactor performance but also raises safety concerns. Experiment 8 confirmed that the location of the reaction zone is strongly influenced by the magnitude of the recuperation flow. This is in line with conceptual observations as well, as upward moving gases in the reactor carry energy and oxygen to unreacted particles. The simplest scheme for controlling the reaction zone is an on/off switch for the recuperation flow, determined by regulating a chosen thermocouple measurement. For the experiments in Group D, the thermocouple stationed at H/L = 0.75 (second from the top and one above the extraction point) was chosen as the measured input. A logic switch considered whether this measurement exceeded a chosen threshold; if so, the recuperation flow was set to 0 SLPM.

4.5.1 Experiment 12

For Experiment 12, the maximum allowable temperature for the sensing thermocouple was limited to 1000°C. Similar to other experiments, this test began with the reactor tube full of reduced particles heated to 1000°C under a small flow of nitrogen gas. After dwelling for some time at 1000°C, the system gas was switched to air and flow rates of $\dot{m}_s$ = 1.5 g/s, $\dot{V}_{recup}$ = 30 SLPM, and $\dot{V}_{ext}$ = 20 SLPM were set. The 30 SLPM chosen at the beginning of the experiment, however, could not sufficiently raise temperatures high enough to trigger the alarm during the first hour of operation. $\dot{V}_{recup}$ was increased to 50 SLPM to encourage the bed reaction zone to shift upwards and trip the alarm. At around t = 90 min, Figure 4.16b depicts the temperature condition being

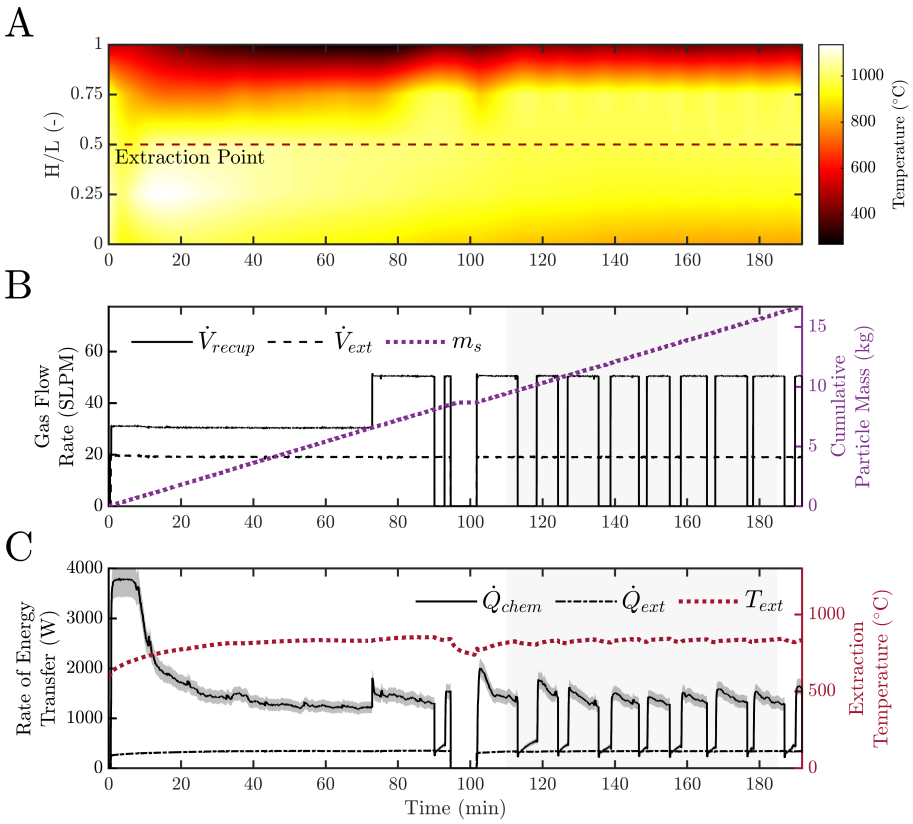

Figure 4.16 Experiment 12, considering the effectiveness of an on/off switch to regulate thermal runaway. The procedure is successfully in establishing a consistent reaction zone. Subplots include (A) Bed temperature contour, (B) Solid and gas flows, and (C) Energy transfer rates and extraction temperature.

met in the top of the bed and the recuperation flow being switched off. More particles were added to the system shortly after this, resulting in the discontinuity in the data. After the addition of more particles, the recuperation flow behaved in an oscillating on/off manner, continuing until the conclusion of the experiment near t = 200 min.

As shown in Figure 4.16a, the switching method successfully mitigated the upward movement of the reaction zone. With the increase to $\dot{V}_{recup}$ around t = 70 min, the reaction zone noticeably rises. While the duty cycle for the first few switches is inconsistent, the reactor eventually settles into a regular rhythm with a steady temperature profile and consistent average T_{ext} of 890 ± 7°C. Drastic swings in $\dot{Q}_{chem}$, as depicted in Figure 4.16c, are likely poor indicators of instantaneous rates of energy transfer at the moment of switching. Average values are more useful for capturing

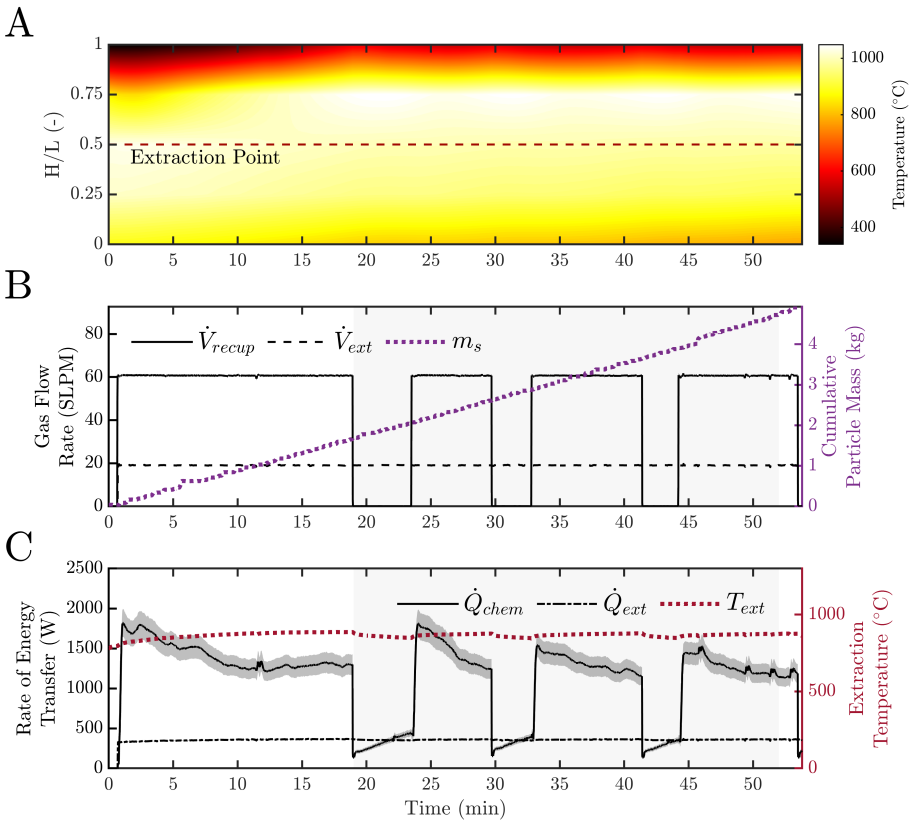

Figure 4.17 Experiment 13, once again regulating the placement of the reaction zone using on/off recuperative gas flow. Subplots include (A) Bed temperature contour, (B) Solid and gas flows, and (C) Energy transfer rates and extraction temperature.

the overall behavior of the system.

4.5.2 Experiment 13

The second experiment in Group D was a continuation of Experiment 9. After the conclusion of the constant-parameter investigation, Experiment 13 commenced with $\dot{m}_s$ = 1.5 g/s, $\dot{V}_{recup}$ = 60 SLPM, and $\dot{V}_{ext}$ = 20 SLPM. The same switching scheme as Experiment 12 was utilized, this time with a temperature cutoff of 1050°C. Results from this test are depicted in Figure 4.17. The switching scheme successfully controls the reaction zone, which once again displays no upward movement in Figure 4.17a after the first on/off switch just before t = 20 min. All other parameters show steady operation for the duration of the experiment.

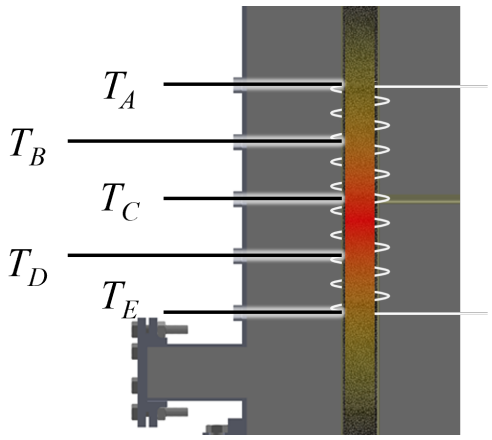

Figure 4.18 Labels for the five thermocouples in contact with the reactor tube, where T_A is the topmost thermocouple and T_E is the bottommost.

4.6 Performance Summary and Efficiency Evaluations

Performance characteristics for all experiments (except for Experiments 1, 2, and 3) are presented in Table 4.3 alongside the inputs for each experiment. Metrics of note include quantities such as $\dot{Q}_{chem}$, $\dot{Q}_{ext}$, and T_{ext}, as well as T_C, the reaction zone thermocouple stationed opposite the extraction tube as depicted in Figure 4.18. All experiments exhibit extraction temperatures in excess of 850°C, with average T_C values greater than or within the margin of error of 1000°C in all cases. Prior to assessing overall trends in the data, some experiments must be omitted from further analysis. $\dot{Q}_{chem}$ for Experiment 3 is notably lower than expected for a trial with $\dot{m}_s$ = 1.5 g/s. Whether this corresponds to an oxygen sensor error or is a side effect of using 3.66 mm particles is inconclusive, but its performance metrics can be reasonably excluded from ensuing analyses. The rest of the experiments in Group A are omitted as well. Experiment 6 features inlet nichrome heating for the duration of the experiment, so its metrics do not capture true operating performance either. The experiments in Group D feature switching, which lead to large uncertainties due to error propagation calculations.

The remaining experiments feature steady operation without significant gas oscillation or nichrome energy input. To provide further comparison, normalized values for $\dot{Q}_{chem}$, $\dot{Q}_{ext}$, and T_{ext} are illustrated in Table 4.4. Heat transfer rates are normalized by the experimental solid flow rates, and the extraction temperature is normalized by the tube temperature at the extraction point.

Considering measurement uncertainties and deviation among experiments, the overall uncertainties of the averages of $\dot{Q}_{chem}/\dot{m}_s$, $\dot{Q}_{ext}/\dot{m}_s$, and T_{ext}/T_C are 17%, 7%, and 5% of each average overall value, respectively. While these normalized values exhibit some consistency, differing operational procedures and reactor behavior still lead to variation among the experiments.

Group	**Exp.**	$\dot{m}_s$ (g/s)	$\dot{V}_{recup}$ (SLPM)	$\dot{V}_{ext}$ (SLPM)	$\dot{Q}_{chem}$ (W)	$\dot{Q}_{ext}$ (W)	T_{ext} (°C)	T_C (°C)
A	1	1.5	variable	-	-	-	-	1182 ± 11
	2	1.5	variable	variable	-	-	952 ± 9	1037 ± 14
	3	1.5	variable	variable	777 ± 93	530 ± 9	1007 ± 9	1068 ± 11
B	4	1.5	variable	variable	1084 ± 126	447 ± 5	973 ± 8	1020 ± 8
	5	1.5	variable	variable	1215 ± 121	388 ± 5	853 ± 8	1032 ± 9
C	6	0.75	27	21	749 ± 76	407 ± 5	859 ± 7	1011 ± 8
	7	1.25	45	16	1182 ± 129	320 ± 7	881 ± 15	1004 ± 32
	8	1.25	29	16	991 ± 106	314 ± 5	857 ± 13	1006 ± 22
	9	2	45	25	1416 ± 145	487 ± 6	890 ± 9	1049 ± 11
	10	2	45	25	1924 ± 188	544 ± 8	954 ± 8	1136 ± 12
	11	2	45	25	1961 ± 188	519 ± 6	921 ± 8	1119 ± 9
D	12	1.5	50	19	1118 ± 487	341 ± 6	829 ± 11	995 ± 8
	13	2	60	19	1001 ± 519	358 ± 6	866 ± 11	995 ± 8

Table 4.3 Experiment evaluation metrics measured during steady-state behavior.

Exp.	$\dot{Q}_{chem}/\dot{m}_s$ (J/kg)	$\dot{Q}_{ext}/\dot{m}_s$ (J/kg)	T_{ext}/T_C (-)
4	723 ± 84	298 ± 4	0.95 ± 0.01
5	810 ± 81	258 ± 3	0.83 ± 0.01
7	946 ± 104	256 ± 5	0.88 ± 0.02
8	793 ± 85	251 ± 4	0.85 ± 0.01
9	708 ± 73	243 ± 3	0.85 ± 0.01
10	962 ± 94	272 ± 4	0.84 ± 0.01
11	981 ± 94	260 ± 3	0.82 ± 0.01
Avg.	846 ± 145	263 ± 18	0.86 ± 0.05

Table 4.4 Normalized metrics during steady-state behavior for selected experiments.

4.6.1 Descriptions of System Efficiency

Efficiency calculations are useful for characterizing the performance of the oxidation reactor, both on its own and as one component of a round-trip reduction-oxidation process. The integrated equations presented here are based on those first presented in the work on the reduction reactor [28]. The first of these quantities is the chemical-to-thermal energy extraction efficiency, which is given by:

$$\eta_{\text{chem to thermal}} = \frac{\int_0^{t_{op,ox}} \dot{Q}_{ext} dt}{\int_0^{t_{op,ox}} \dot{Q}_{chem,ox} dt + Q_{startup,ox}} \tag{4.13}$$

where $\dot{Q}_{ext}$ and $\dot{Q}_{chem,ox}$ are the previously defined rates of extraction and chemical energy release, respectively, $t_{op,ox}$ is the continuous operational time of the oxidation setup, and $Q_{startup}$ is the energy required to preheat the reactor. Based on preheating measurements, $Q_{startup}$ for the experimental oxidation reactor is estimated to be on the order of 1.48×10^7 J. If the pump work required to flow gases through the particle bed is included, the total oxidation reactor efficiency becomes:

$$\eta_{\text{ox reactor}} = \frac{\int_0^{t_{op,ox}} \dot{Q}_{ext} dt}{\int_0^{t_{op,ox}} \left(\dot{Q}_{chem,ox} + \dot{W}_{pump,ox}\right) dt + Q_{startup,ox}} \tag{4.14}$$

with the rate of pumping work $\dot{W}_{pump}$ generally defined as[73]:

$$\dot{W}_{pump} = \frac{\Delta P_{avg} \dot{V}_{avg}}{\eta_{pump}} \tag{4.15}$$

where ΔP_{avg} is the average inlet pumping pressure difference (approximately 0.75 bar for this experimental setup), $\dot{V}_{avg}$ is the average volumetric gas flow rate, and η_{pump} is the compressor

efficiency. η_{pump} is assumed to be a typical value of 0.5. Considering the oxidation reactor in conjunction with the previously developed reduction concept [1], a round-trip energy efficiency for the entire energy storage system can be established:

$$\eta_{\text{round trip}} = \frac{\int_0^{t_{op,ox}} \dot{Q}_{ext} dt}{\int_0^{t_{op,red}} \left(\dot{Q}_{in,red} + \dot{W}_{O_2 sep} + \dot{W}_{pump,red}\right) dt + \int_0^{t_{op,ox}} \left(\dot{W}_{pump,red}\right) dt + Q_{startup,ox} + Q_{startup,red}} \tag{4.16}$$

The leftmost integral in the denominator considers the reduction system energy inputs, including the rate of heat input to the reactor ($\dot{Q}_{in,red}$), rate of work required for oxygen separation ($\dot{W}_{O_2,sep}$), and the rate of pumping work necessary for operation ($\dot{W}_{pump,red}$). $Q_{startup,red}$ is estimated at a value of 2.08×10^7 J from reduction preheating measurements. Estimates for the other reduction reactor characteristics are obtained from Experiment 3.b performed by Randhir et al. [1]. These include values of 2357 ± 95 W, 935 ± 96 W, 265 ± 18 W, and 61 ± 3 W for $\dot{Q}_{in,red}$, $\dot{Q}_{chem,red}$, $\dot{W}_{O_2,sep}$, and $\dot{W}_{pump,red}$, respectively. The reduction operational time, $t_{op,red}$, is defined on the basis of $t_{op,ox}$ such that the total amount of chemical energy stored during reduction and released during oxidation are equal:

$$\int_0^{t_{op,ox}} \dot{Q}_{chem,ox} dt = \int_0^{t_{op,red}} \dot{Q}_{chem,red} dt \tag{4.17}$$

For large-scale, well-optimized reactors, system heat losses are expected to be negligible compared to the rate of energy release and extraction. For these ideal cases, $\dot{Q}_{ext}$ and $\dot{Q}_{chem,ox}$ are approximately equal. This same assumption is also extended to $\dot{Q}_{in,red}$ and $\dot{Q}_{chem,red}$. Under such conditions, system efficiencies reach their maximum values and can be expressed as:

$$\eta_{\text{chem to thermal, max}} = \frac{\int_0^{t_{op,ox}} \dot{Q}_{chem,ox} dt}{\int_0^{t_{op,ox}} \dot{Q}_{chem,ox} dt + Q_{startup,ox}} \tag{4.18}$$

$$\eta_{\text{ox reactor, max}} = \frac{\int_0^{t_{op,ox}} \dot{Q}_{chem,ox} dt}{\int_0^{t_{op,ox}} \left(\dot{Q}_{chem,ox} + \dot{W}_{pump,ox}\right) dt + Q_{startup,ox}} \tag{4.19}$$

$$\eta_{\text{round trip, max}} = \frac{\int_0^{t_{op,ox}} \dot{Q}_{chem,ox} dt}{\int_0^{t_{op,red}} \left(\dot{Q}_{in,red} + \dot{W}_{O_2 sep} + \dot{W}_{pump,red}\right) dt + \int_0^{t_{op,ox}} \left(\dot{W}_{pump,red}\right) dt + Q_{startup,ox} + Q_{startup,red}} \tag{4.20}$$

Exp.	$\eta_{\text{chem to thermal}}$ (%)	$\eta_{\text{ox reactor}}$ (%)	$\eta_{\text{round trip}}$ (%)	$\eta_{\text{ox reactor, max}}$ (%)	$\eta_{\text{round trip, max}}$ (%)
4	41.3 ± 4.8	36.2 ± 3.7	13.7 ± 6.1	87.7 ± 1.6	67.2 ± 15.9
5	31.9 ± 3.2	28.2 ± 2.5	10.6 ± 5.2	88.3 ± 1.4	67.5 ± 15.2
7	27.1 ± 3.0	23.6 ± 2.3	9.0 ± 4.9	87.0 ± 1.8	66.8 ± 15.7
8	31.7 ± 3.4	28.0 ± 2.7	10.6 ± 4.9	88.4 ± 1.7	67.6 ± 14.8
9	34.4 ± 3.6	30.2 ± 2.8	11.4 ± 5.9	87.8 ± 1.8	67.2 ± 16.3
10	28.3 ± 2.8	25.8 ± 2.3	9.5 ± 6.2	91.3 ± 1.2	69.2 ± 18.4
11	26.5 ± 2.6	24.2 ± 2.1	8.9 ± 6.0	91.3 ± 0.8	69.3 ± 18.3
12	30.5 ± 13.3	26.8 ± 10.4	10.2 ± 15.3	87.9 ± 6.2	67.3 ± 48.5
13	35.7 ± 18.5	30.5 ± 13.6	11.7 ± 18.2	85.3 ± 8.7	65.7 ± 54.2

Table 4.5 Normalized efficiency values for selected experiments.

An initial assessment of four experiments is performed using Equations 4.13-4.20, considering actual and maximum efficiencies of the feasibility Experiments 4 and 5 and the repeatability Experiments 10 and 11. Oxidation measurements are taken to be the average steady-state values for each experiment listed in Table 4.3; the various efficiencies are plotted as functions of time in Figure 4.19. Efficiency values are low for short time spans, as the energy required to initiate reactor operations is of a comparable magnitude to the cumulative inputs and outputs. Beyond approximately 100 hours of operation, efficiencies across all experiments converge to steady values. Contrary to early operation, at large times the initial energy investment required is significantly smaller than the cumulative inputs and outputs of the system. At such durations, steady-state efficiencies can be determined without considering $Q_{startup,ox}$ and $Q_{startup,red}$. Steady state values for the rest of the considered experiments are listed in Table 4.5. Because $\eta_{\text{chem to thermal,max}}$ tends toward 100% for a lossless, ideal reactor system, it is omitted from Table 4.5.

Of the experiments listed in Table 4.5, Experiment 4 stands out as the highest-performing trial. By assessing the corresponding Figure 4.6, several factors are observed that seem related to the experiment's success. First, the main reaction zone of Figure 4.6a stays relatively narrow. In many other experiments that feature constant solid and gas flows, the reaction zone widens or expands, leading to greater losses. This narrow reaction zone is seemingly facilitated by the variable gas inputs of Experiment 4. Inputs were specifically manipulated in an effort to control system

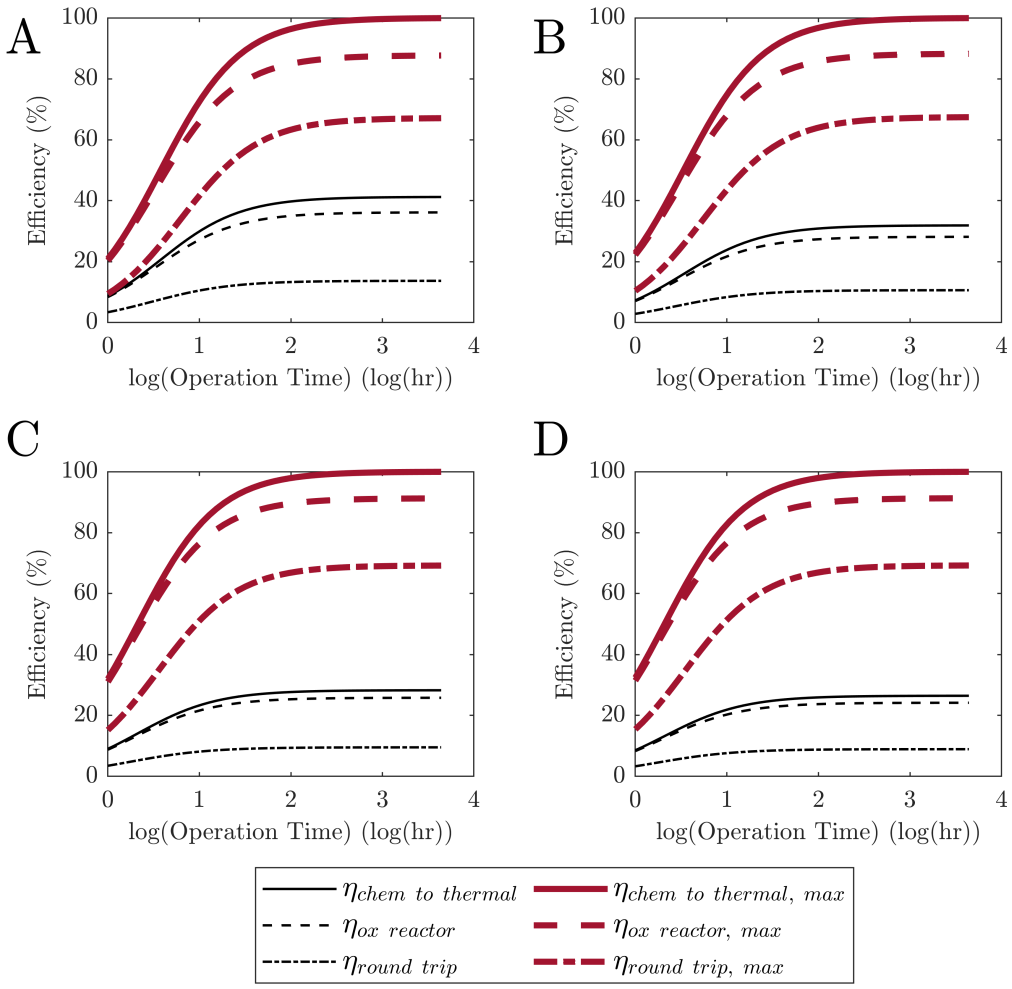

Figure 4.19 The evolution of various reactor efficiencies over time. All quantities approach asymptotic steady values at large times. Subplots depict (A) Experiment 4, (B) Experiment 5, (C) Experiment 10, and (D) Experiment 11. Originally printed in [2].

performance and maintain a consistent reaction zone. The normalized extraction temperature is also notably higher in this case, 0.07 greater than the next highest value. While this may be due to differences in bed packing and losses, the results seem to suggest that the operating procedure for Experiment 4 affects T_{ext}/T_C.

Through user control, Experiment 4 also avoids the runaway reaction zone present in trials such as Experiment 7. While the experiments in Group D are successfully able to use a rudimentary on/off control to mitigate such an occurrence, they underperform Experiment 4 both in terms of efficiency and temperature of extraction. Indeed, the average steady-state T_C measurements for the

experiments in Group D are both below the 1000°C benchmark. While Experiment 3 also features user input, Figure 4.7a depicts a much less homogeneous reaction zone than Experiment 4. All of these results suggest that with a sufficient degree of control reactor efficiency and extraction temperature can be managed to desired levels.

CHAPTER 5

1D MODELING AND SYSTEM DYNAMICS

While experimental campaigns are the most accurate method for gaining insights into system behavior, such investigations require a great deal of time, materials, and labor. This chapter details the construction of a computational model that offers a straightforward, adaptable framework for assessing reactor dynamics and control approaches. One dimensional (1D) models are a popular choice for quick, computationally cheap simulation of thermal energy storage systems. Models for sensible energy storage, typically featuring packed rather than moving particle beds, have been well-described by several investigators. Mertens et al. [74] provide a two-phase model (solid and gas) to illustrate behavior in a rock-bed thermocline system. Hoffman et al. [75] explored a similar system, introducing both a two-phase model that also accounts for the reactor wall and an even simpler one-phase model that assumes thermal equilibrium between the solid and gas phases at all times. Neither of these approaches consider a moving solid phase or chemical reaction, two key characteristics of the SoFuel oxidation reactor. Vahedi et al. [76] examined a packed-bed cobalt oxide thermochemical system, similarly following a 1D, two-phase methodology but omitting consideration of any wall effects. Zhou et al. [77] investigated cobalt oxides, while Shao et al. [78] used a comparable approach to evaluate calcium hydroxide as a storage mediums.

One-dimensional moving-bed thermochemical reactor approaches have favored similar methods to their stationary bed counterparts. Saade et al. [79] examined a solar-thermal reactor using a method analogous to that of Hoffman et al.'s two-phase approach for a packed bed. This model, though one-dimensional, offers good agreement with experimental results in the form of a 5% error in terms of steady state operating temperatures. The merits of a 1D moving bed approach are further explored by Preisner et al. [80], who validate their model using packed bed experimental data and implement the model to predict operational characteristics of a moving bed $(Mn,Fe)_3O_4$ reactor. Lastly, a 1D model has been developed for the SoFuel reduction reactor, the counterpart to the system described in this dissertation. Huang et al. [47] investigated the efficacy of a two-phase model that also considers wall effects through comparison to experimental data. Their simulations

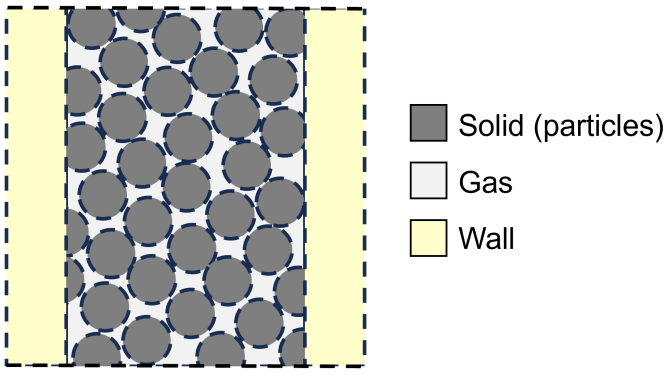

Figure 5.1 One axial cell in the oxidation reactor model containing the solid, gas, and wall phases.

matched up well in the cases of both pressure-dependent Ergun flow and the assumption of constant flow, suggesting the broad applicability of the 1D modeling approach.

While further modeling approaches related to this dissertation have continued to explore the reduction and oxidation systems in more dimensions [81], these authors have not extended the 1D treatment of the reduction reactor to its oxidation counterpart. The extraction gas flow introduces added complexity to the counterflow oxidation reactor, making the finite difference solution method implemented in the 1D reduction investigation more difficult to apply. As a result, this chapter details a control-volume approach to modeling the SoFuel oxidation reactor constructed and operated earlier in this work. The model provides a straightforward, first-principles framework for quickly assessing reactor dynamics without the need to run on-reactor experiments.

5.1 Overall Approach

An illustration of the general modeling approach employed in this work is depicted in Figure 5.1. The entire square represents one of many axial cells stacked on top of each other that comprise the complete reactor tube. Each cell consists of three phases of interest: the solid phase, made up of magnesium-manganese oxide particles, the gas phase, comprised of an oxygen-nitrogen mixture, and the wall phase, consisting of the alumina tube surrounding both the solid and gas phases. This finite volume approach relies on conservation equations to illustrate transient behavior in each cell.

These include solving for the energy of the solid, gas, and wall phases, as well as transport equations describing the migration of solid chemical conversion and oxygen concentration throughout the reactor. The formulation and discretization of these equations are elaborated on in Section 5.2.

Prior to performing these derivations, assumptions and simplifications for the model must be established. First, as previously stated, the computational model assumes that axial effects dominate and the reactor can be approximated as a one-dimensional system. Another key simplification is the implementation of steady mass flow for both the solid and gas phases. Zhou et al. [77], Mertens et al. [74], and Huang et al. [47] all evaluated assumptions of constant flow, be it mass or velocity, with results suggesting reasonable agreement with experimental results. The present model still considers the effect of oxygen consumption due to chemical reaction, but this phenomenon is incorporated into the steady flow assumption. Furthermore, properties are assumed to be uniform among each phase within a cell, and the solid phase is considered to be comprised of a homogeneous distribution of uniform-diameter (5 mm) particles. The gas phase is approximated as having the thermophysical properties of air treated as an ideal gas. Most thermophysical properties for the solid, gas, and wall phases are evaluated as functions of temperature, while the effect of pressure is neglected due to the relatively low operating pressures of the system. Further information on these temperature-dependent property calculations is provided in Section 5.5. The counterflow between the solid and gas phases merits the inclusion of diffusive heat effects, as properly balanced flow rates essentially cancel out thermal advection. In contrast, the unidirectional flows for solid and gas species dominate the transport of these properties, leading to the omission of diffusion terms for these quantities. Kinetic and potential energy are neglected as well in this analysis.

The finite volume model is discretized in a manner analogous to the Crank-Nicolson approach [82] for finite difference models; that is, combining forward and backward methods. For the energy balances that undergo a combination of advective and diffusive effects, the QUICK scheme [83] is used to evaluate properties at the boundaries of each cell. An example of the ordinating nomenclature is shown in Figure 5.2. For a cell i of interest, the cell above it (spatially higher up the reactor tube) is cell $i + 1$, while the cell below it (spatially lower) is designated $i - 1$. The interface

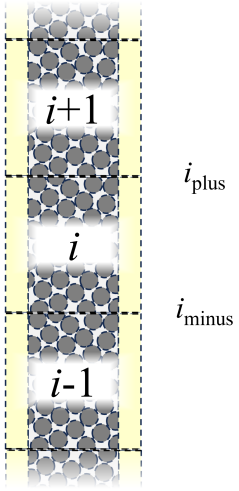

Figure 5.2 The discretization scheme for the computational model. The cell of interest, i, features boundaries of i_{plus} and i_{minus} with its neighbors $i+1$ and $i-1$, respectively.

between i and $i+1$ is specified as the i_{plus} interface, while i_{minus} corresponds to the bottom boundary. This labeling convention is applied to all of the individual conservation equations of Section 5.2. Outside of the energy equations, a simple upwind scheme is employed for species transport due to the dominance of movement in the flow direction. This approach does not implement the i_{plus} and i_{minus} interfaces, but rather approximates properties moving into a cell as analogous to the properties of the cell the flow is exiting.

5.2 Conservation Equations

As previously described, the foundations of the control volume model are five conservation equations describing the energy balances of the solid, gas, and wall phases, as well as species transport equations for extent of conversion in the solid and oxygen concentration in the gas. These five quantities and their corresponding balances are discussed in detail in the following subsections. Prior to exploring these properties, the steady flow assumption is presented for the solid and gas phases through the lens of mass conservation.

5.2.1 Conservation of Mass

The mass of the solid and gas phases in an individual cell are assumed to be unchanging with respect to time. As a result, the control volume mass conservation equations for each can be written

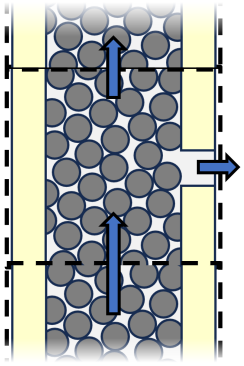

Figure 5.3 Gas flow behavior in the extraction zone. After taking into consideration the consumption of oxygen via reaction, the inlet gas flow is split into recuperative and extraction components.

as shown:

$$0 = \dot{m}_{s,in} - \dot{m}_{s,out} \tag{5.1}$$

$$0 = \dot{m}_{g,in} - \dot{m}_{g,out} - \dot{r}_{ox} \tag{5.2}$$

where $\dot{m}_s$ and $\dot{m}_{g,in}$ are the solid and gas mass flow rates, respectively, and $\dot{r}_{ox}$ is the rate of oxygen consumption due to chemical reaction. Equation 5.1 yields the straightforward result that the rate of solid flow is constant for all cells. In contrast, the gas flow rate experiences a maximum at the inlet of the reactor, where oxygen concentration is the highest, and gradually decreases over the length of the system. The rate of oxygen consumption is described in further detail in Section 5.2.6.

The two-component nature of the gas flow, with $\dot{m}_{g,recup}$ and $\dot{m}_{g,ext}$, adds some additional complications to calculating gas flow rates at cell boundaries. Figure 5.3 depicts gas flow behaviors in the extraction cell; that is, the cell from which the extraction gas flow exits the reactor. The removal of $\dot{m}_{g,ext}$, shown with the horizontal arrow, results in a greatly reduced gas flow entering the next cell. At the same time, the energy and oxygen carried by the extraction flow are removed from the cell, simulating the operating conditions of the experimental reactor. The control volume nature of the computational model is well suited to handle this phenomenon, and only minor modeling adjustments must be made.

5.2.2 Energy Equation for Solid-Phase

A First Law energy balance of the solid phase yields the following equation:

$$\frac{\partial H_s}{\partial t} = \sum \dot{m}_s h_s - \dot{Q}_{cond,s} + \dot{Q}_{rxn} + \dot{Q}_{gs} + \dot{Q}_{ws} \tag{5.3}$$

where H_s is the extensive solid enthalpy, $\dot{m}_s$ is the mass flow rate of the solid, h_s is the intensive solid enthalpy, $\dot{Q}_{cond,s}$ represents the conduction throughout the solid phase, $\dot{Q}_{rxn}$ is the rate of energy released through chemical reaction, and $\dot{Q}_{gs}$ and $\dot{Q}_{ws}$ are the heat transfer rates between the gas and solid and wall and solid, respectively. Enthalpy is used here instead of internal energy due to the flowing nature of the solid particles. By extracting the mass of the solid cell from the left hand side of the equation and expanding the summation on the right hand side, the following equation is produced:

$$V_s \rho_s \frac{\partial h_s}{\partial t} = \dot{m}_s h_{s,plus} - \dot{m}_s h_{s,minus} + \dot{Q}_{cond,s} + \dot{Q}_{rxn} + \dot{Q}_{gs} + \dot{Q}_{ws} \tag{5.4}$$

Here the solid mass is represented as the product of the cell volume occupied by the solid, V_s, and the density of the solid, ρ_s. The specific enthalpy values entering and exiting the cell are specified as $h_{s,plus}$ and $h_{s,minus}$, respectively, according to the nomenclature of Section 5.1. Values for these quantities are determined according to the QUICK computational scheme:

$$h_{s,plus} = \frac{6}{8} h_{s,i+1} + \frac{3}{8} h_{s,i} - \frac{1}{8} h_{s,i+2} \tag{5.5}$$

$$h_{s,minus} = \frac{6}{8} h_{s,i} + \frac{3}{8} h_{s,i-1} - \frac{1}{8} h_{s,i+1} \tag{5.6}$$

Furthermore, the rate of chemical energy released by the solid is represented by:

$$\dot{Q}_{rxn} = \frac{V_s \left(\rho_{ox} - \rho_{red}\right) \Delta H_{rxn}}{M_{O_2}} \left(\frac{\partial \alpha_s}{\partial t}\right)_{rxn} \tag{5.7}$$

This expression features several new quantities, including the difference in solid density between the fully oxidized and fully reduced state, $(\rho_{ox} - \rho_{red})$, and the rate of chemical conversion due to reaction, $\left(\frac{\partial \alpha_s}{\partial t}\right)_{rxn}$. This rate of chemical conversion due to reaction was first introduced in Chapter 2 as Equation 2.11, and details concerning its calculation can be found there. Conduction

in the solid phase is evaluated as the combination of conduction out of a cell into its neighbors, as described below:

$$\dot{Q}_{cond,s} = A_s k_{s,plus} \left.\frac{\partial T_s}{\partial x}\right|_{plus} - A_s k_{s,minus} \left.\frac{\partial T_s}{\partial x}\right|_{minus} \tag{5.8}$$

with A_s as the cross sectional area of the solid phase, where due consideration is given to the porosity of the particle bed. To convert the $\frac{\partial T_s}{\partial x}$ terms to an enthalpy basis, the following transformation can be performed:

$$\dot{Q}_{cond,s} = A_s k_{s,plus} \left(\frac{\partial T_s}{\partial h_s}\frac{\partial h_s}{\partial x}\right)_{plus} - A_s k_{s,minus} \left(\frac{\partial T_s}{\partial h_s}\frac{\partial h_s}{\partial x}\right)_{minus} \tag{5.9}$$

h_s can be determined as a function of T_s and the temperature dependent specific heat, $c_{p,s}$, according to the standard definition of a change in specific enthalpy. As a result, the $\frac{\partial T_s}{\partial h_s}$ term allows for straightforward conversion of the conduction equation to an enthalpy basis. When discretized according to the control volume approach, the following expression is produced:

$$\dot{Q}_{cond,s} = A_s k_{s,plus} \left.\frac{\partial T}{\partial h_s}\right|_{plus} \frac{h_{s,i+1} - h_{s,i}}{\Delta x} + A_s k_{s,minus} \left.\frac{\partial T}{\partial h_s}\right|_{minus} \frac{h_{s,i-1} - h_{s,i}}{\Delta x} \tag{5.10}$$

Lastly, the rates of heat transfer for between the solid and gas and solid and wall phases can be expressed as the following, respectively:

$$\dot{Q}_{gs} = \Gamma_{gs} \left(T_g - T_s\right) \tag{5.11}$$

$$\dot{Q}_{ws} = \Gamma_{ws} \left(T_w - T_s\right) \tag{5.12}$$

Correlations for determining the heat transfer coefficients Γ_{gs} and Γ_{ws} are elaborated on in Section 5.3. Plugging all of the individual components into the original equation and discretizing the advective and diffusive components according to the Crank-Nicolson methodology, the final form

of Equation 5.4 is:

$$2V_s\rho_s\frac{h_{s,i}^{n+1}-h_{s,i}^{n}}{\Delta t}=\dot{m}_s\left(\frac{7}{8}h_{s,i+1}^{n+1}-\frac{3}{8}h_{s,i}^{n+1}-\frac{3}{8}h_{s,i-1}^{n+1}-\frac{1}{8}h_{s,i+2}^{n+1}\right)$$
$$+\dot{m}_s\left(\frac{7}{8}h_{s,i+1}^{n}-\frac{3}{8}h_{s,i}^{n}-\frac{3}{8}h_{s,i-1}^{n}-\frac{1}{8}h_{s,i+2}^{n}\right)$$
$$+A_sk_{s,plus}\left.\frac{\partial T}{\partial h_s}\right|_{plus}\left(\frac{h_{s,i+1}^{n+1}-h_{s,i}^{n+1}}{\Delta x}+\frac{h_{s,i+1}^{n}-h_{s,i}^{n}}{\Delta x}\right)$$
$$+A_sk_{s,minus}\left.\frac{\partial T}{\partial h_s}\right|_{minus}\left(\frac{h_{s,i-1}^{n+1}-h_{s,i}^{n+1}}{\Delta x}+\frac{h_{s,i-1}^{n}-h_{s,i}^{n}}{\Delta x}\right)$$
$$+\frac{2V_s\left(\rho_{ox}-\rho_{red}\right)\Delta H_{rxn}}{M_{O_2}}\left(\frac{\partial\alpha_s}{\partial t}\right)_{rxn,i}+2\Gamma_{gs}(T_{g,i}-T_{s,i})+2\Gamma_{ws}(T_{w,i}-T_{s,i}) \quad (5.13)$$

where the n and $n+1$ superscripts denote quantities evaluated at the current and next timesteps, respectively. By rearranging all of the $n+1$ quantities to the left hand side of the equation and the n quantities to the right, the equation can be easily converted into a solvable matrix form.

5.2.3 Energy Equation for Gas Phase

The energy of the gas phase can be described using a First Law balance similar to that used for the solid phase:

$$\frac{\partial H_g}{\partial t}=\sum\dot{m}_gh_g+\dot{Q}_{cond,g}-\dot{Q}_{gs}+\dot{Q}_{wg} \quad (5.14)$$

where this time the subscript g signifies the gas phase. Enthalpy is once again favored over internal energy due to the mobile nature of the phase. The sign for $\dot{Q}_{gs}$ is reversed in order to utilize the formulation presented in Equation 5.11. Using the same approach as the solid phase, Equation 5.14 is be expanded into:

$$V_g\rho_g\frac{\partial h_g}{\partial t}=\dot{m}_{g,in}h_{g,minus}-\dot{m}_{g,out}h_{g,plus}+\dot{Q}_{cond,g}-\dot{Q}_{gs}+\dot{Q}_{ws} \quad (5.15)$$

Of note is the absence of a chemical reaction term in the gas energy balance, a component only present when considering the solid phase. Furthermore, the *plus* and *minus* labels denote the same physical position but now correspond to the cell outlet and inlet, respectively. The individual components of the energy balance are solved in an identical manner to that of the solid phase. The

intermediate equations are listed below:

$$h_{g,minus} = \frac{6}{8}h_{g,i-1} + \frac{3}{8}h_{g,i} - \frac{1}{8}h_{g,i-2} \tag{5.16}$$

$$h_{g,plus} = \frac{6}{8}h_{g,i} + \frac{3}{8}h_{g,i+1} - \frac{1}{8}h_{g,i-1} \tag{5.17}$$

$$\dot{Q}_{cond,g} = A_g k_{g,plus} \left.\frac{\partial T}{\partial h_g}\right|_{plus} \frac{h_{g,i+1} - h_{g,i}}{\Delta x} + A_g k_{g,minus} \left.\frac{\partial T}{\partial h_g}\right|_{minus} \frac{h_{g,i-1} - h_{g,i}}{\Delta x} \tag{5.18}$$

Similar to the formulation of $\dot{Q}_{gs}$, the rate of heat transfer between the gas phase and the wall, $\dot{Q}_{wg}$, is represented by:

$$\dot{Q}_{wg} = \Gamma_{wg}\left(T_w - T_g\right) \tag{5.19}$$

with Γ_{wg} as another heat transfer coefficient to be described later in the chapter. The final discretized formulation becomes:

$$\begin{aligned} 2V_g\rho_g\frac{h_{g,i}^{n+1} - h_{g,i}^{n}}{\Delta t} &= \dot{m}_{g,i-1}\left(\frac{6}{8}h_{g,i-1}^{n+1} + \frac{3}{8}h_{g,i}^{n+1} - \frac{1}{8}h_{g,i-2}^{n+1} + \frac{6}{8}h_{g,i-1}^{n} + \frac{3}{8}h_{g,i}^{n} - \frac{1}{8}h_{g,i-2}^{n}\right) \\ &+ \dot{m}_{g,i}\left(\frac{6}{8}h_{g,i}^{n+1} + \frac{3}{8}h_{g,i+1}^{n+1} - \frac{1}{8}h_{g,i-1}^{n+1} + \frac{6}{8}h_{g,i}^{n} + \frac{3}{8}h_{g,i+1}^{n} - \frac{1}{8}h_{g,i-1}^{n}\right) \\ &+ A_g k_{g,plus}\left.\frac{\partial T}{\partial h_g}\right|_{plus}\left(\frac{h_{g,i+1}^{n+1} - h_{g,i}^{n+1}}{\Delta x} + \frac{h_{g,i+1}^{n} - h_{g,i}^{n}}{\Delta x}\right) \\ &+ A_g k_{g,minus}\left.\frac{\partial T}{\partial h_g}\right|_{minus}\left(\frac{h_{g,i-1}^{n+1} - h_{g,i}^{n+1}}{\Delta x} + \frac{h_{g,i-1}^{n} - h_{g,i}^{n}}{\Delta x}\right) \\ &- 2\Gamma_{gs}(T_{g,i} - T_{s,i}) + \Gamma_{wg}(T_{w,i} - T_{g,i}) \end{aligned} \tag{5.20}$$

Terms may once again be rearranged to obtain an easily deployed matrix formulation of the gas energy balance.

5.2.4 Energy Equation for Reactor Walls

The alumina wall phase differs from the solid and gas phases in that it is a stationary medium. As such, internal energy U_w is sufficient for describing the energy balance within the wall:

$$\frac{\partial U_w}{\partial t} = \dot{Q}_{cond,w} - \dot{Q}_{ws} - \dot{Q}_{wg} + \dot{Q}_{w,ins} \tag{5.21}$$

Similar to the previous derivations, the w subscript denotes the reactor wall. Among the familiar quantities is $\dot{Q}_{w,ins}$, which describes the rate of energy transfer to the fibrous insulation outside of

the reactor tube. Due to the lack of advective components, Equation 5.21 can easily be converted from an energy to a temperature basis:

$$V_w \rho_w c_{p,w} \frac{\partial T_w}{\partial t} = \dot{Q}_{cond,w} - \dot{Q}_{gs} - \dot{Q}_{wg} + \dot{Q}_{w,ins} \tag{5.22}$$

with V_w, ρ_w, and $c_{p,w}$ as the volume, density, and specific heat of the wall, respectively. The conduction term can be quickly discretized without the enthalpy conversion factor necessary in the previous analyses:

$$\dot{Q}_{cond,w} = A_w \left(\frac{k_{w,i} + k_{w,i+1}}{2} \right) \frac{T_{w,i+1} - T_{w,i}}{\Delta x} + A_w \left(\frac{k_{w,i} + k_{w,i-1}}{2} \right) \frac{T_{w,i-1} - T_{w,i}}{\Delta x} \tag{5.23}$$

Without the interface calculations of the QUICK scheme, an average thermal conductivity is calculated between cells to ensure consistent rates of conduction between each cell. Returning to the loss term, $\dot{Q}_{w,ins}$, the rate at which heat conducts out of the wall and into the surrounding insulation can be approximated as:

$$\dot{Q}_{w,ins} = -2\pi r_o k_{ins} \frac{\partial T}{\partial r} \tag{5.24}$$

where r_o is the outer radius of the wall and k_{ins} is the thermal conductivity of the insulation at the wall temperature. By discretizing the radial derivative, the equation can be put in the form of:

$$\dot{Q}_{w,ins} = 2\pi r_o k_{ins} \frac{T_{w,i} - T_{ins,i,r_o}}{\Delta r} \tag{5.25}$$

with Δr as the radial spacing of insulation cells and T_{ins,i,r_o} as the temperature of the insulation in contact with the tube wall. Further information regarding the insulation temperature and loss calculations are elaborated on in Section 5.4. Bringing the various components together and discretizing with respect to time produces a final implementable equation:

$$\begin{aligned} 2V_w \rho_w c_{p,w} \frac{T_{w,i}^{n+1} - T_{w,i}^{n}}{\Delta t} = {} & A_w \left(\frac{k_{w,i} + k_{w,i+1}}{2} \right) \left(\frac{T_{w,i+1}^{n+1} - T_{w,i}^{n+1}}{\Delta x} + \frac{T_{w,i+1}^{n} - T_{w,i}^{n}}{\Delta x} \right) \\ & + A_w \left(\frac{k_{w,i} + k_{w,i-1}}{2} \right) \left(\frac{T_{w,i-1}^{n+1} - T_{w,i}^{n+1}}{\Delta x} + \frac{T_{w,i-1}^{n} - T_{w,i}^{n}}{\Delta x} \right) \\ & - 2\Gamma_{ws}(T_{w,i} - T_{s,i}) - 2\Gamma_{wg}(T_{w,i} - T_{g,i}) + \frac{2\pi r_o k_{ins}}{\Delta r}(T_{w,i} - T_{ins,i,r_o}) \end{aligned} \tag{5.26}$$

5.2.5 Transport Equation for Extent of Conversion

Changes in the extent of conversion of the solid phase, α_s, were first introduced in Equation 2.2. The s subscript is added to further specify that the extent of conversion is tied to the solid particle phase. A value of $\alpha_s = 0$ corresponds to a fully reduced particle, while $\alpha_s = 1$ signifies fully oxidized material. Extent of conversion, like the other conserved quantities, can also be described via a control volume analysis:

$$\frac{\partial \alpha_s}{\partial t} = \sum \dot{m}_s \pi_s + \left(\frac{\partial \alpha_s}{\partial t}\right)_{rxn} \tag{5.27}$$

with the term $\left(\frac{\partial \alpha_s}{\partial t}\right)_{rxn}$ representing the same rate of conversion due to chemical reaction as in the solid energy equation. The specific extent of conversion for a given cell, π_s, is defined as:

$$\pi_s = \frac{\alpha_s}{\rho_s V_s} \tag{5.28}$$

Plugging the definition for the specific extent of conversion into Equation 5.27, the expression becomes:

$$\frac{\partial \alpha_s}{\partial t} = \frac{\dot{m}_s \alpha_{s,in}}{\rho_s V_s} - \frac{\dot{m}_s \alpha_{s,out}}{\rho_s V_s} + \left(\frac{\partial \alpha_s}{\partial t}\right)_{rxn} \tag{5.29}$$

After employing the Crank-Nicolson discretization strategy in conjunction with a simple upwind approach for advective terms, the final equation for determining change in extent of conversion is:

$$\frac{\alpha_{s,i}^{n+1} - \alpha_{s,i}^{n}}{\Delta t} = \frac{\dot{m}_s}{2\rho_s V_s}\left[\left(\alpha_{s,i+1}^{n+1} + \alpha_{s,i+1}^{n}\right) - \left(\alpha_{s,i}^{n+1} + \alpha_{s,i}^{n}\right)\right] + \left(\frac{\partial \alpha_s}{\partial t}\right)_{rxn,i} \tag{5.30}$$

5.2.6 Transport Equation for Oxygen Concentration

The equation describing the concentration of oxygen in the gas phase follows a similar structure to the expression for extent of conversion:

$$\frac{\partial \left(V_g C_{ox}\right)}{\partial t} = \sum \frac{\dot{m}_g C_{ox}}{\rho_g} - \dot{r}_{ox} \tag{5.31}$$

with C_{ox} as the concentration of oxygen in a given gas cell, further defined as $C_{ox} = \rho_g \xi_{ox}$, and ξ_{ox} is the mass fraction of oxygen. $\dot{r}_{ox}$ represents the rate of oxygen consumption due to chemical reaction. This quantity can be approximated by considering the rate of conversion due to chemical

reaction:

$$\dot{r}_{ox} = V_s \left(\rho_{red} - \rho_{ox}\right) \left(\frac{\partial \alpha_s}{\partial t}\right)_{rxn} \tag{5.32}$$

where $(\rho_{red} - \rho_{ox})$ is the same change in density of the solid phase previously considered in the solid energy equation. This rate equation assesses the conversion of oxygen mass from the gaseous to the solid phase. Specifying inlets and outlets and plugging in the rate of chemical consumption, the initial equation becomes:

$$V_g \frac{\partial C_{ox}}{\partial t} = \frac{\dot{m}_{g,in} C_{ox,in}}{\rho_{g,in}} - \frac{\dot{m}_{g,out} C_{ox,out}}{\rho_{g,out}} - V_s \left(\rho_{red} - \rho_{ox}\right) \left(\frac{\partial \alpha_s}{\partial t}\right)_{rxn} \tag{5.33}$$

Applying the upwind Crank-Nicolson discretization yields the final form to be solved in matrix form:

$$\frac{C_{ox,i}^{n+1} - C_{ox,i}^{n}}{\Delta t} = \frac{\dot{m}_{g,i-1}}{2\rho_{g,i-1} V_g} \left(C_{ox,i-1}^{n+1} + C_{ox,i-1}^{n}\right) - \frac{\dot{m}_{g,i}}{2\rho_{g,i} V_g} \left(C_{ox,i}^{n+1} + C_{ox,i}^{n}\right) - \frac{V_s \left(\rho_{red} - \rho_{ox}\right)}{\rho_{g,i} V_g} \left(\frac{\partial \alpha_s}{\partial t}\right)_{rxn,i} \tag{5.34}$$

5.3 Heat Transfer Correlations

Several heat transfer correlations are employed to determine appropriate values for Γ_{gs}, Γ_{ws}, and Γ_{wg}. These consist of the following general form:

$$\Gamma = \left(V_s + V_g\right) a\gamma \tag{5.35}$$

where $\left(V_s + V_g\right)$ is the total volume occupied by the particle bed within a cell, a is the specific area, and γ is the heat transfer coefficient. For the case of heat transfer between the gas and the solid, γ_{gs}, the correlation of Yang et al. [84] is deployed:

$$\gamma_{gs} = \left(2 + 1.2\mathrm{Re}^{1/2}\mathrm{Pr}^{1/3}\right) \frac{k_g}{d_p} \tag{5.36}$$

where Re is the Reynolds number of the solid-gas counterflow, Pr is the Prandtl number of the gas phase, k_g is the thermal conductivity of the gas, and d_p is the particle diameter. This formulation is paired with a specific area, a_{gs}, of:

$$a_{gs} = \frac{6(1 - \varepsilon)}{d_p} \tag{5.37}$$

where ε is the porosity of the particle bed. According to Sullivan et al. [85], the heat transfer coefficient between a moving bed of solid particles and a surrounding wall can be approximated as:

$$\gamma_{ws} = \frac{k_g}{d_p \left(0.085 + 0.5\sqrt{\frac{\pi}{\mathrm{Pe}_L}}\right)} \tag{5.38}$$

with Pe_L as the Peclet number. This coefficient is paired with the wall-based specific area utilized by Mertens et al. [74]:

$$a_{ws} = \frac{4}{D_i} \tag{5.39}$$

where D_i is the reactor tube inner diameter. The gas-wall coefficient uses the same specific area in conjunction with the Dittus-Bolter correlation [86]:

$$\gamma_{wg} = \left(0.023\mathrm{Re}^{4/5}\mathrm{Pr}^{2/5}\right)\frac{k_g}{d_i} \tag{5.40}$$

The calculations of Γ_{wg} and Γ_{ws} both approach zero as the speeds of the gas and solid phases approach zero. Minimum heat transfer coefficients, based on simple conduction, are therefore implemented to ensure accuracy at low flow rates:

$$\Gamma_{ws,min} = \frac{(1-\varepsilon)\pi D_i \Delta x}{D_i + 0.5(D_o - D_i)}\left(\frac{k_w(D_o - D_i) + k_s D_i}{D_o}\right) \tag{5.41}$$

$$\Gamma_{wg,min} = \frac{\varepsilon\pi D_i \Delta x}{D_i + 0.5(D_o - D_i)}\left(\frac{k_w(D_o - D_i) + k_g D_i}{D_o}\right) \tag{5.42}$$

where D_o is the outer diameter of the alumina tube. These conduction limits help to make the model more accurate at lower flow rates.

5.4 Estimation of Thermal Losses

Due to the large radius of the insulation surrounding the relatively narrow reactor tube, a separate one-dimensional radial conductivity model is implemented for each axial reactor cell. An illustration of this computational scheme is depicted in Figure 5.4. Cells radiate outward from the tube wall to the steel reactor shell. Each cell is characterized by a general energy balance:

$$\frac{\partial U_{ins}}{\partial t} = \dot{Q}_{cond,ins,minus} - \dot{Q}_{cond,ins,plus} \tag{5.43}$$

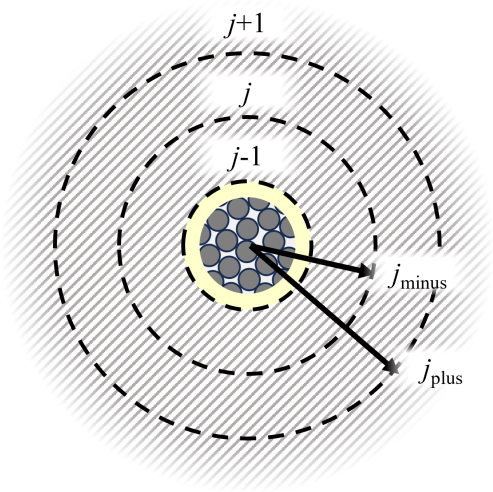

Figure 5.4 The radial loss model through the reactor insulation. Loss calculations are performed for each axial cell but omit axial conduction in the insulation.

where $\dot{Q}_{cond,plus}$ and $\dot{Q}_{cond,minus}$ are analogous to the "plus" and "minus" terms of the axial reactor model. Taking into account the differing volume of each radial cell, these are written as:

$$\dot{Q}_{cond,ins,plus} = 2\pi r_{plus}\Delta x\left(\frac{k_{ins,j}+k_{ins,j+1}}{2}\right)\frac{\partial T_{ins}}{\partial r} \tag{5.44}$$

$$\dot{Q}_{cond,ins,minus} = 2\pi r_{minus}\Delta x\left(\frac{k_{ins,j}+k_{ins,j-1}}{2}\right)\frac{\partial T_{ins}}{\partial r} \tag{5.45}$$

Combining these expressions with Equation 5.43 and discretizing yields the following form:

$$\begin{aligned}\rho_{ins}c_{p,ins}\pi\left(r_{plus}^2-r_{minus}^2\right)\Delta x\frac{T_{ins,j}^{n+1}-T_{ins,j}^{n}}{\Delta t} = \\ 2\pi r_{plus}\Delta x\left(\frac{k_{ins,j}+k_{ins,j+1}}{2}\right)\left(\frac{T_{ins,j+1}^{n+1}-T_{ins,j}^{n+1}}{\Delta r}+\frac{T_{ins,j+1}^{n}-T_{ins,j}^{n}}{\Delta r}\right) \\ +2\pi r_{minus}\Delta x\left(\frac{k_{ins,j}+k_{ins,j-1}}{2}\right)\left(\frac{T_{ins,j-1}^{n+1}-T_{ins,j}^{n+1}}{\Delta r}+\frac{T_{ins,j-1}^{n}-T_{ins,j}^{n}}{\Delta r}\right)\end{aligned} \tag{5.46}$$

The above equation can be easily manipulated into a matrix-solvable form.

5.5 Thermophysical Properties

Properties for the solid, gas, wall, and insulation phases can be divided into two groups: those with temperature dependence and those treated as being relatively constant. The first group is depicted in Table 5.1. Among these, properties sourced from Moran et al. [87] and Incopera et

al. [71] are polynomials fitted to tabulated data. Furthermore, temperature-based polynomials are provided for the solid and gas enthalpies. These correlations are predominantly used in the reverse direction, to determine temperatures from the specific enthalpy equations, but the temperature-based form is provided here for the sake of consistency. Constant property values are listed in Table 5.2.

5.6 Boundary Conditions and Computational Setup

Boundary conditions for the computational model are consistent across all cases. T_{amb} is taken to be 25°C. For the 1D reactor model, conditions are applied at each end of the reactor tube, with a subscript of "$x = 0$" denoting the bottom of the reactor and "$x = L$" applying to the top. For the solid energy equation, these conditions are $\left.\frac{\partial h_s}{\partial x}\right|_{x=0} = 0$ and $h_{s,x=L} = h_s\,(T_{amb})$. The enthalpy of the solid as it exits the tube receives a Neumann boundary condition, while the particles are specified to enter the top of the reactor at a specific enthalpy corresponding to ambient temperatures. The gas phase features the opposite conditions, with $h_{g,x=0} = h_g\,(T_{amb})$ and $\left.\frac{\partial h_g}{\partial x}\right|_{x=L} = 0$. The tube wall is specified to have Neumann conditions at both ends, characterized by $\left.\frac{\partial T_w}{\partial x}\right|_{x=0} = 0$ and $\left.\frac{\partial T_w}{\partial x}\right|_{x=L} = 0$. Solid extent of conversion is characterized in a similar way to solid energy, with $\left.\frac{\partial \alpha_s}{\partial x}\right|_{x=0} = 0$ and $\alpha_{s,x=L} = 0.05$. Lastly, the oxygen concentration calculation observes $C_{ox,x=0} = 0.23197\rho_g$ and $\left.\frac{\partial C_{ox}}{\partial x}\right|_{x=L} = 0$, with 0.23197 being the average mass fraction of oxygen in air.

The radial heat loss through the insulation also requires boundary conditions for implementation. On the outer face of the insulation the temperature is assumed to be roughly equal to ambient, $T_{ins,x=D_{out}} = T_{amb}$, for each axial coordinate. While on the experimental reactor a steel shell ensconces the insulation, the high thermal conductivity of the shell leads to its omission from the loss calculations. On the innermost insulation face (corresponding to the alumina tube's outer diameter, D_o), Equation 5.25 is used to estimate the rate of heat transfer from the tube into the insulation. Due to the one dimensional nature of the insulation energy balances, axial boundary conditions are not necessary.

The solid and gas enthalpy equations, as well as the wall and insulation temperature expressions, are nondimensionalized in order to minimize the computational strain of large values. The specific

Property	Correlation	Unit	Source
$h_s\,(T_s)$	$1.043\times10^{-1}T_s^2+7.080\times10^{1}T_s-1.965\times10^{5}$	J/kg	
$h_g\,(T_g)$	$8.673\times10^{-2}T_s^2+9.562\times10^{1}T_s+3.962\times10^{3}$	J/kg	[87]
k_s	$2.576\times10^{-17}T_s^6-1.04\times10^{-13}T_s^5$ $+1.730\times10^{-10}T_s^4-1.527\times10^{-7}T_s^3$ $+8.023\times10^{-5}T_s^2-3.157\times10^{2}T_s+12.966$	W/m K	[88]
k_g	$1.018\times10^{-20}T_g^6-1.710\times10^{-17}T_g^5$ $-2.263\times10^{-14}T_g^4+8.535\times10^{-11}T_g^3$ $-1.036\times10^{-7}T_g^2+1.143\times10^{-4}T_g-1.086\times10^{-3}$	W/m K	[71]
k_w	$31634\,(T_w)^{-1.192}$	W/m K	[71]
k_{ins}	$1.291\times10^{-12}T_{ins}^4-2.424\times10^{-9}T_{ins}^3$ $+2.295\times10^{-6}T_{ins}^2-1.017T_{ins}+0.187$	W/m K	[48]
$c_{p,s}$	$-2.503\times10^{-16}T_s^6+1.4394\times10^{-12}T_s^5$ $-3.228\times10^{-9}T_s^4+3.6473\times10^{-6}T_s^3$ $-2.3635\times10^{-3}T_s^2+1.0435T_s+676.24$	J/kg K	[48]
$c_{p,g}$	$-1.339\times10^{-16}T_g^6+8.171\times10^{-13}T_g^5$ $-1.662\times10^{-9}T_g^4+1.206\times10^{-6}T_g^3$ $+5.536\times10^{-5}T_g^2-0.172T_g+1.032*10^{3}$	J/kg K	[71]
$c_{p,w}$	$-1.27\times10^{6}T_w^{-1.346}+1340$	J/kg K	[71]
ρ_g	$\frac{175000}{287T_g}$	kg/m^3	
μ_g	$\frac{1.458\times10^{-6}T_g.^{1}.5}{T_g+110.4}$	kg/m/s	[48]
Pr_g	$2.807\times10^{-19}T_g^6-1.128\times10^{-15}T_g^5$ $+1.783\times10^{-12}T_g^4-1.860\times10^{-9}T_g^3$ $+1.677\times10^{-6}T_g^2-8.857\times10^{-4}T_g+0.859$		[71]

Table 5.1 Temperature-dependent thermophysical properties of the oxidation reactor.

Property	Value	Unit	Source
$c_{p,ins}$	1070	J/kg K	
ρ_s	4525	kg/m^3	
ρ_w	3970	kg/m^3	[71]
ρ_{ins}	128	kg/m^3	
ε	0.36	-	

Table 5.2 Constant thermophysical properties for the oxidation reactor.

enthalpy reference is taken to be $h_{ref} = 1.7226 \times 10^6$ J/kg, while the temperature reference is $T_{ref} = 1573$ K. The four equations are converted into nondimensional forms of:

$$h_s^* = \frac{h_s}{h_{ref}}, \quad h_g^* = \frac{h_g}{h_{ref}}, \quad T_w^* = \frac{T_w}{T_{ref}}, \quad T_{ins}^* = \frac{T_{ins}}{T_{ref}}$$

Boundary conditions are modified as well to satisfy the new dimensionless formulations.

The 1.11 m reactor tube is divided into 50 axial cells for evaluation. Such a number is consistent with the methods of Saade et al. [79] and Zhou et al. [77], who use 65 and 60 cells, respectively, to model reactors on the order of 0.5 m. Generally speaking, the last two cells on each end are used to enforce the boundary conditions for a given phase, in order to comply with the QUICK and upwind computational schemes. The accompanying loss estimation consists of 50 sets of 10 cells radiating outward from the reactor tube. While the Crank-Nicolson-like approach yields greater stability than a purely explicit method, the chosen simulation timestep is 0.001 s for these simulations.

5.7 Model Validation

To verify the applicability of the computational model for reactor controller evaluation, the model's performance was compared to several experimental cases. These cases are listed in Table 5.3, labeled according to their numbering from Chapter 4. Also included in Table 5.3 are the initial temperatures of the five reaction zone thermocouples for each experiment. These measurements were used to generate initial conditions for the validation simulations. Such conditions arise from

Exp.	$\dot{m}_s$ (g/s)	$\dot{V}_{recup}$ (SLPM)	$\dot{V}_{ext}$ (SLPM)	T_E (°C)	T_D (°C)	T_C (°C)	T_B (°C)	T_A (°C)
7	1.25	45	16	930.5	1004.3	1008.3	1011.7	709
8	1.25	29	16	987	1027.6	1010.4	949	603.1
11	2	45	25	469.7	817	1006.5	1025.4	1002.5
12	2	45	25	689	890.4	1017.6	963.1	901.7

Table 5.3 Initial temperature conditions and operational inputs for the simulation validation.

imposing the five thermocouple temperatures on their respective cells for the solid, gas, and wall phases, linearly interpolating the temperatures between them, and completing a five-hour simulation without any flow through the system. This process generated the thermal gradients in the top and bottom of the reactor tube, as well as in the radial insulation, that are necessary to replicate the preheating of the reactor during experimental use. Besides temperature initial conditions, the extent of conversion of all initial particles was approximated as $\alpha_s = 0.05$, while the oxygen concentration in the reactor began at $C_{ox} = 0$ for all cells. Boundary conditions for these simulations were consistent with those previously established for the computational model.

Comparisons between the temperature contour plots of the experimental and simulated data sets are illustrated in Figure 5.5. The experimental contour plots are once again generated via the five thermocouples protruding into the oxidation reactor, while the simulation contours utilize five model cells corresponding to the locations of the thermocouples. Both contours implement linear interpolation in between the dimensionless measurement locations of 0, 0.25, 0.5, 0.75, and 1. Across all of the experiments, the simulated results track the position and temperatures of the reaction zone relatively well. The behavior of Experiment 7, with its dramatically shifting reaction zone, is well captured by the model. The other simulated cases tend to underpredict the temperature of the upper reaches of the particle bed, although the modeled results for Experiment 8 in particular hold a consistent profile for nearly one and a half hours of simulated time prior to decreasing in temperature. A more focused look at individual temperature measurements is provided by Figure 5.6. In their three-dimensional modeling of the oxidation reactor, Korba et al.[48] evaluated the three centermost thermocouples (the top-middle T_B, middle T_C, and bottom-middle T_D) when

performing model comparison, so the practice is continued here. Experiment 8, as the contour plots suggested, captures the behavior of the reactor and adheres to the experimental trends reasonably well. The simulations for Experiments 8 and 12 both underpredict values for T_B at long simulation times, but otherwise demonstrate reasonable agreement with the experimental results. Experiment 11 performs well, with disagreement on the value of T_D being the only notable discrepancy.

Variations in the temperature profiles demonstrated by the experimental setup and the 1D model can be attributed to a variety of factors. First, the axial thermal gradients in the bench-scale reactor can be very large around the reaction zone, showcasing temperature changes of hundreds of degrees over the span of a few centimeters. Errors introduced to the system model through thermophysical property estimation, constant flow assumptions, estimated system losses, and other factors can be amplified into differences of hundreds of degrees for some measurements. Furthermore, the laboratory system features nonuniformities including non-spherical particles, inconsistent insulation packing, and varying extents of conversion among individual particles that introduce variability to experimental operation. For this reason, while the comparisons of T_B, T_C, and T_D are useful, the general trends in transient behavior of the system are more informative of the applicability of the computational model.

Figure 5.7 compares the experimentally measured oxygen signals to those predicted by the computational model. The simulation underpredicts oxygen consumption in the reactor across all cases, especially with regard to the oxygen concentration at the extraction point. Huang et al. [47] reported some difficulty in accurately predicting oxygen concentrations in a 1D reduction model as well, although that formulation considered reduction rather than oxidation. The simulated results follow comparable trends over time to their experimental counterparts, with the discrepancy appearing as an offset. Two factors in the model are likely the dominant contributors to the oxygen concentration error: the steady-flow assumption and the dependence of the gas density on temperature. By approximating the gas flow through the reactor as largely steady, the model does not take into account the more complex behaviors of the continuity and momentum equations. This decision is made intentionally to reduce computational runtime and allow for rapid testing

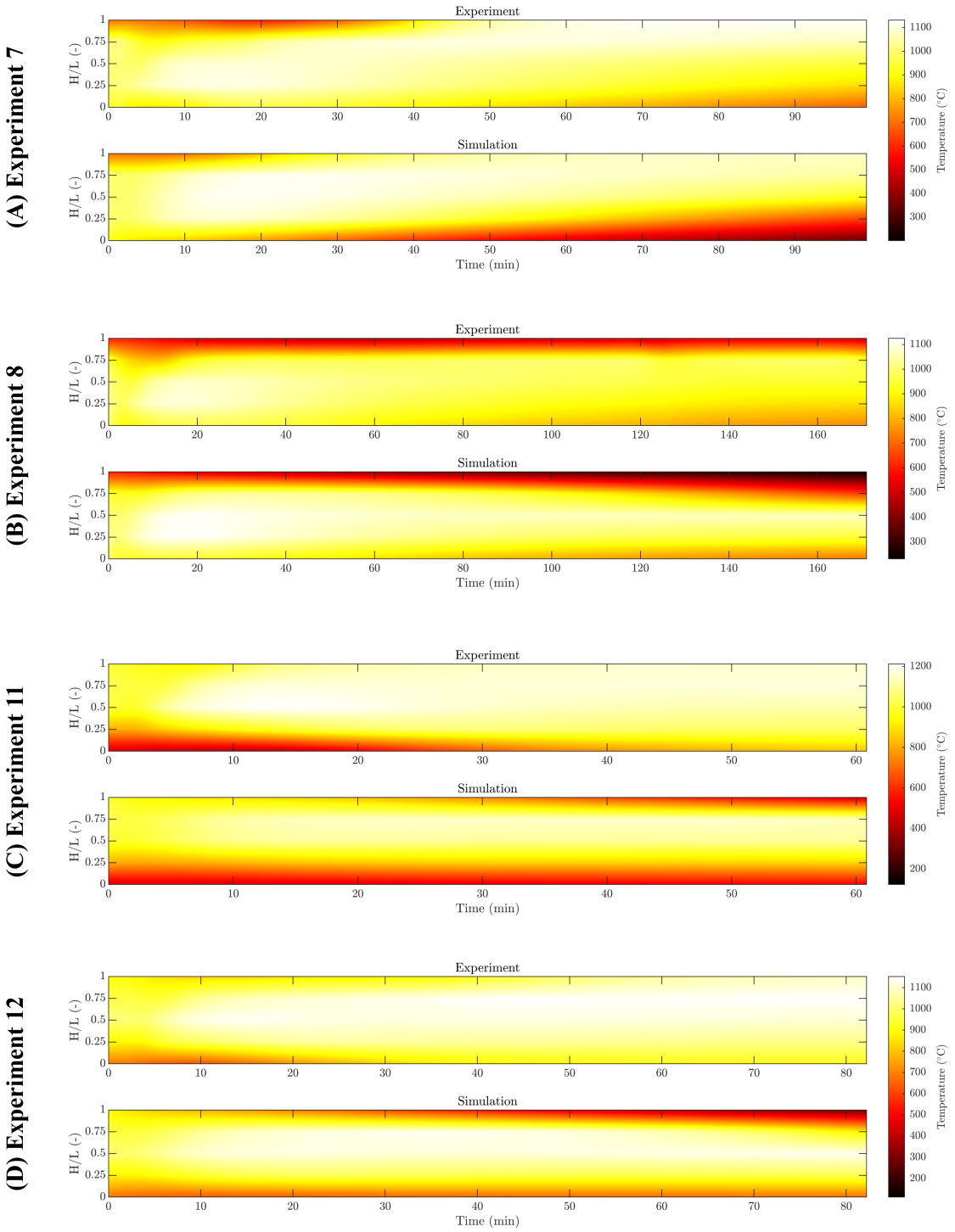

Figure 5.5 Experimental and simulated temperature contour plots for (A) Experiment 7, (B) Experiment 8, (C) Experiment 11, and (D) Experiment 12. The contour plots illustrate generally good agreement between the experimental measurements and the computational model. Both feature five measurements with linear interpolation between each point.

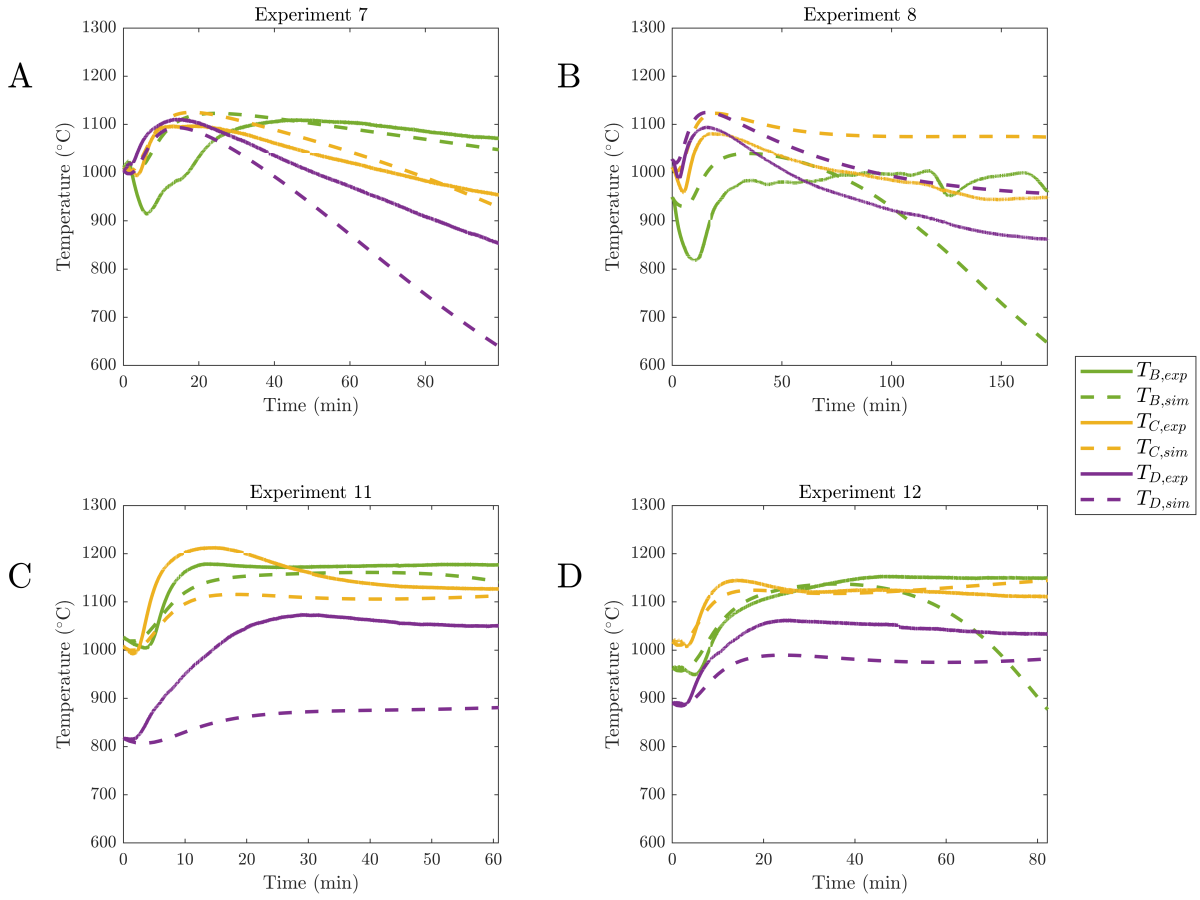

Figure 5.6 Comparisons of the experimental and simulated three middle temperature measurements (T_B, T_C, and T_D) for (A) Experiment 7, (B) Experiment 8, (C) Experiment 11, and (D) Experiment 12.

and iteration. Further errors may arise from utilizing the ideal gas law for determining the density of the gas phase. Changes to the density are incorporated into the oxygen concentration, C_{ox}, but updating the gas density at each time step inevitably results in higher or lower mass fractions of oxygen over time. The discrepancies in the oxygen signals, however, do not correspond to errors in the chemical conversion of the solid particles. Extents of conversion above 80% are recorded in each of the simulations, in line with experimentally illustrated values. Furthermore, the level of agreement among the temperature contours suggests that the model adequately replicates the energy released due to oxidation, even if the oxygen concentrations are higher than experimentally observed.

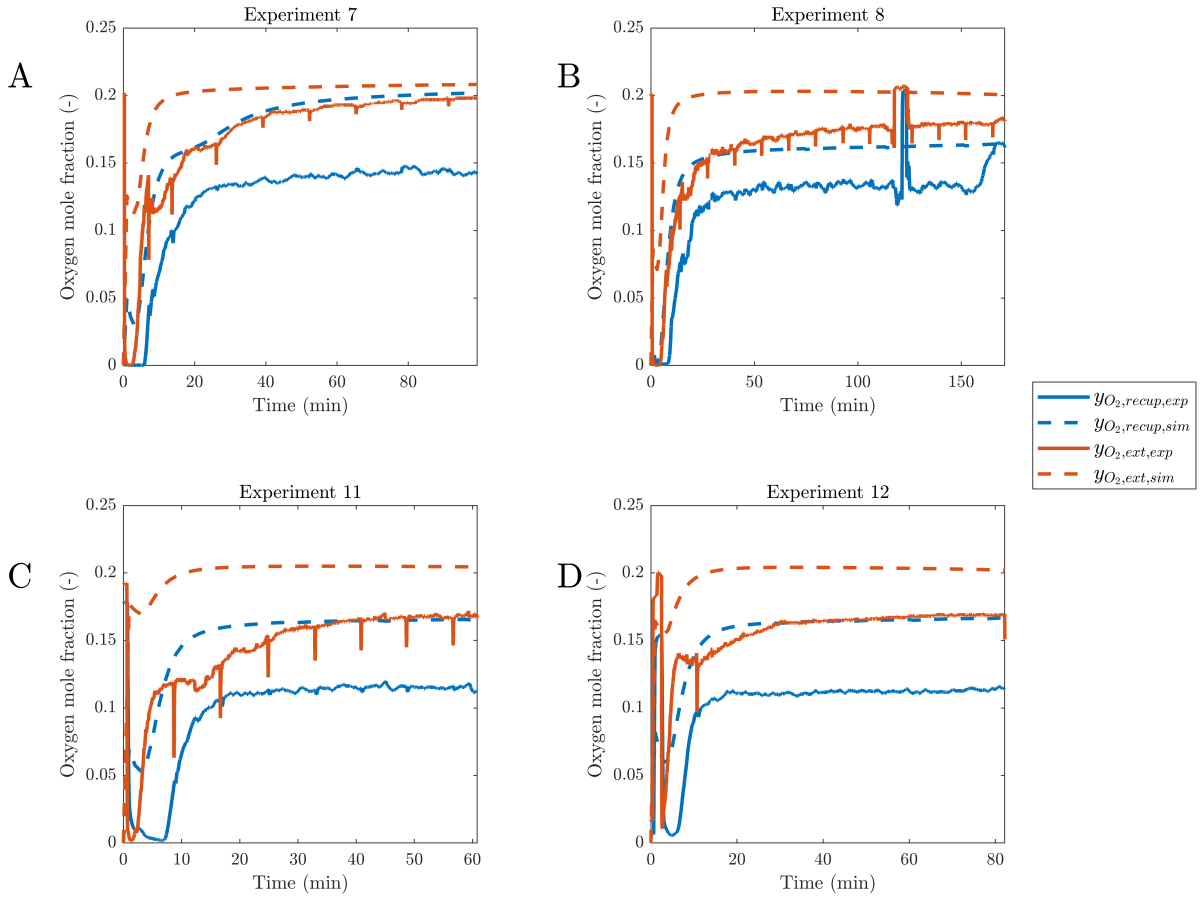

Figure 5.7 Comparisons of the experimental and simulated recuperative and extraction oxygen concentrations ($y_{O_2,recup}$ and $y_{O_2,ext}$) for (A) Experiment 7, (B) Experiment 8, (C) Experiment 11, and (D) Experiment 12.

Overall, the control-volume model provides a reasonable prediction of reactor operation as a result of differing solid and gas flow rates. Replicating temperature profiles within the reactor is the primary objective of such a model, and the 1D code predicts chemical reaction and sensible energy transfer sufficiently well for emulating lab-scale operation. While oxygen concentrations are not as faithfully replicated, the system model still predicts appropriate trends in oxygen consumption within the reactor. These results are sufficient for utilizing the model to evaluate general input-response behavior and to iteratively develop control strategies for the oxidation reactor.

Case	$\dot{m}_s$ (g/s)	$\dot{m}_{g,recup}$ (g/s)	$\dot{m}_{g,ext}$ (g/s)
Baseline	1.25	0.617	0.340
1	1.25	0.308	0.340
2	1.25	0.462	0.340
3	1.25	0.771	0.340
4	1.25	0.925	0.340
5	1.25	0.617	0.170
6	1.25	0.617	0.255
7	1.25	0.617	0.425
8	1.25	0.617	0.510
9	0.625	0.617	0.340
10	0.938	0.617	0.340
11	1.563	0.617	0.340
12	1.875	0.617	0.340

Table 5.4 Inputs for the system response simulations. Cases 1-4, 5-8, and 9-12 evaluate $\dot{m}_{g,recup}$, $\dot{m}_{g,ext}$, and $\dot{m}_s$, respectively.

5.8 System Input Response

Validating that the computational model captures the general behavior of the experimental oxidation reactor allowed for its use in assessing the system response to varying inputs. Such investigations were similar to the dynamics experiments carried out on the experimental setup, but the computational model allowed for rapid evaluation and straightforward parametric comparison. Furthermore, the computational model can provide a depiction of the entire reactor, not simply the central length of the system, providing a larger view of system behavior. The input response simulations considered here bear a resemblance to the step-input analysis of traditional control approaches, but the counterflow nature of the reactor means that long-duration operational stability can only be achieved by carefully manipulating multiple system inputs in tandem. Even so, these single-input evaluations are useful in precisely quantifying the phenomena at work in the system to better understand strategies to reliably and safely operate the reactor. All of the following analyses used the initial conditions of Experiment 8 as a starting point, as this case showed particularly good stability in both experimental and simulation demonstration. Table 5.4 summarizes the various inputs provided to the model for each case.

The first reactor input considered was the gas recuperation flow rate, $\dot{m}_{g,recup}$. The baseline

case featured a gas flow rate of 29 SLPM, corresponding to a mass flow rate of roughly 0.617 g/s. This input was manipulated to 50%, 75%, 125%, and 150% of its original value, with three-hour simulations depicting the long-duration impact such changes had on system behavior. Computational results of the wall temperature, T_w, are depicted in Figure 5.8. As suggested by the experimental dynamics campaign as well, the recuperative gas flow has a strong impact on the position of the main oxidation zone. Increasing and decreasing the flow rate by just 25% makes a noticeable difference on the temperature profile, with even more drastic results produced by differences of 50%. Another feature of note is the relatively consistent size of the reaction zone across all cases. While the axial placement of the hottest part of the reactor varies in each case, the width of the reacting particles is not drastically affected by different recuperation flow rates. This suggests that the increased oxygen supplied by a larger flow does not have a large impact on the rate of chemical reaction. As a result, the simulations suggest that the recuperative gas flow primarily serves as a means to adjust the axial position of the reaction zone.

A similar analysis was performed with the extraction gas flow, $\dot{m}_{g,ext}$. In this case the baseline flow rate was 0.340 g/s. Figure 5.9 showcases the impact on T_w caused by varying the flow to the same 50%, 75%, 125%, and 150% thresholds as $\dot{m}_{g,recup}$. Varying the extraction flow rate does not appear to cause as strong of a change in the location of the high-temperature zone - in fact, increasing $\dot{m}_{g,ext}$ to some extent succeeds in positioning the main reaction zone in the middle of the reactor tube. Thermal gradients in the top and bottom of the bed, however, are not balanced for most flow rates and tend to favor the lower reaches of the bed. The most visually striking feature of an increased extraction flow is the narrowing of the reaction zone. The computational results depicted in Figure 5.9 clearly illustrate the high removal of energy from the system in the 125% and 150% cases, as these simulations depict energy extraction outpacing chemical energy production.

Figure 5.10 depicts the behavior associated with manipulating the solid flow rate $\dot{m}_s$, the final system input. While $\dot{m}_{g,recup}$ and $\dot{m}_{g,ext}$ each appear to have a single dominating effect on reactor operation - shifting the position and changing the size of the reaction zone, respectively - Figure 5.10 suggests that the solid flow rate impacts both reaction zone position and chemical energy

release. Such results are in line with experimental observations, but the phenomena are still worth considering in this parametric evaluation. At a solid flow rate of 50% of 1.25 g/s, the nominal value, the reactor not only displays a movement of the reaction zone to the reaches of the system but also a general cooling of this high temperature area. In contrast, at the highest simulated flow rate of 150% the nominal value the reactor exhibits a hotter reaction zone than the baseline case, coupled with a downward shift. These results establish the twofold impact of the solid flow on chemical energy production and sensible energy transfer.

The general behavior depicted in the previous figures is presented in a different form in Figure 5.11, which assesses the final simulation results (at $t = 180$ min) using two different metrics. Figure 5.11a provides a measure for quantifying reaction zone size in the form of counting the number of cells at the conclusion of each simulation with a wall temperature in excess of 800°C. As depicted in the Figure, when $\dot{m}_{g,recup}$ and $\dot{m}_s$ are varied individually there is limited impact on the general size of the oxidation reaction zone, with only a modest increase in zone size as flow rates increase. The extraction gas flow, by contrast, strongly affects the span of the reaction zone, displaying a ten cell difference between the 50% and 150% cases. Figure 5.11b presents the maximum temperature present at the end of each simulation. $\dot{m}_{g,recup}$ once again shows only a modest effect on the quantity, while $\dot{m}_{g,ext}$ depicts a modest decrease in maximum temperatures as flow rates increase. Changes in reaction zone temperature are dominated by $\dot{m}_s$, which illustrates how closely linked chemical energy production is to the operating temperature of the reactor.

The dynamics of the computational model observed across the input variation study are in good agreement with those observed throughout the experimental campaigns. Generally, speaking, the system inputs fulfill the following roles: $\dot{m}_{g,recup}$ provides sufficient gas counterflow to favorably position the reaction zone, $\dot{m}_{g,ext}$ specifies the rate of energy extraction and size of the reaction zone relative to the supplied chemical energy, and $\dot{m}_s$ delivers chemical energy to the system and dictates the necessary gas flow rates required for recuperation. Due to its comparability with the experimental setup, the 1D model will be further employed in the following section as a surrogate upon which to test reactor control approaches.

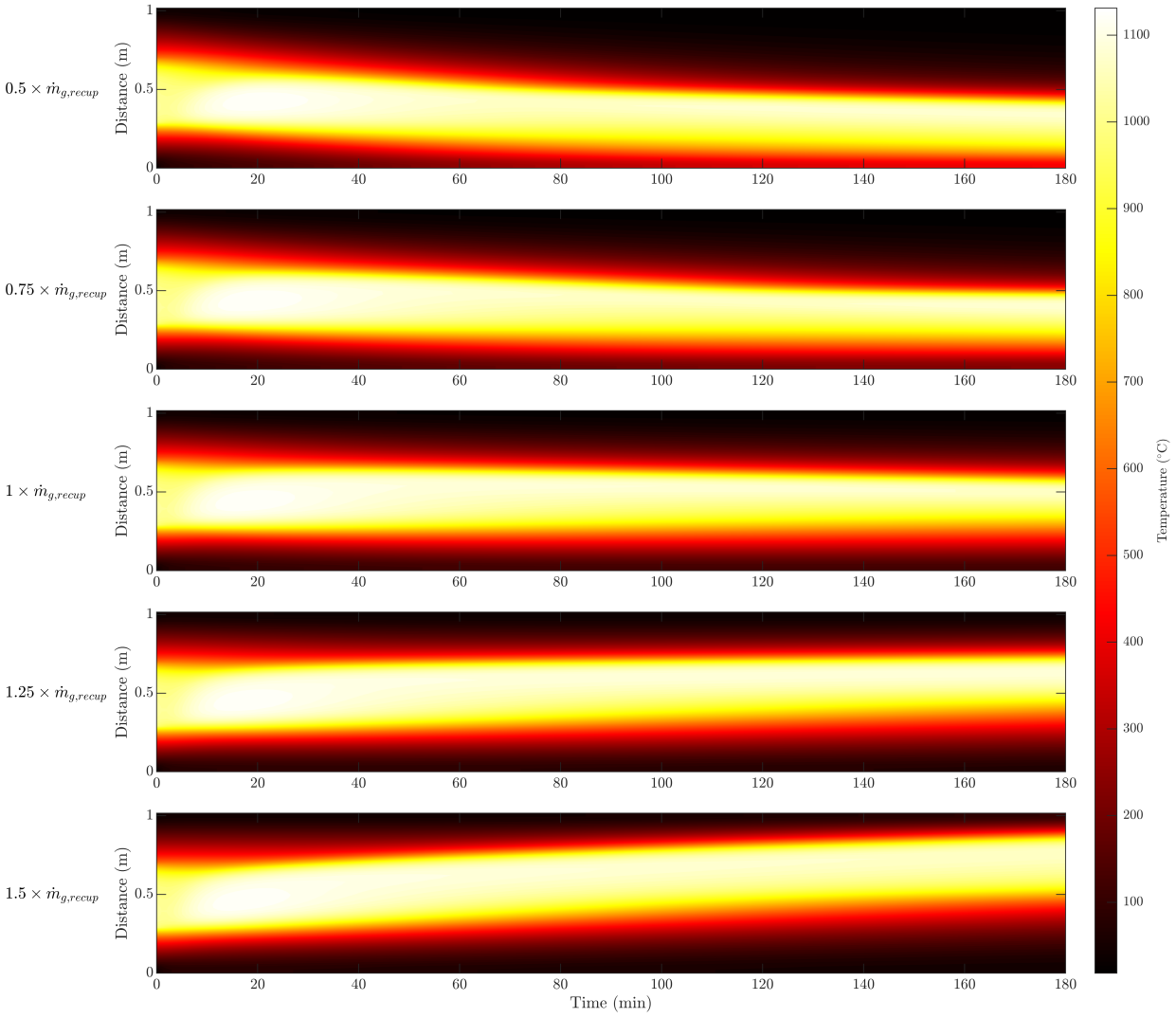

Figure 5.8 The effect of recuperation gas flow on reactor behavior. For constant $\dot{m}_s$ and $\dot{m}_{g,recup}$, the recuperative gas flow dictates the position of the reaction zone.

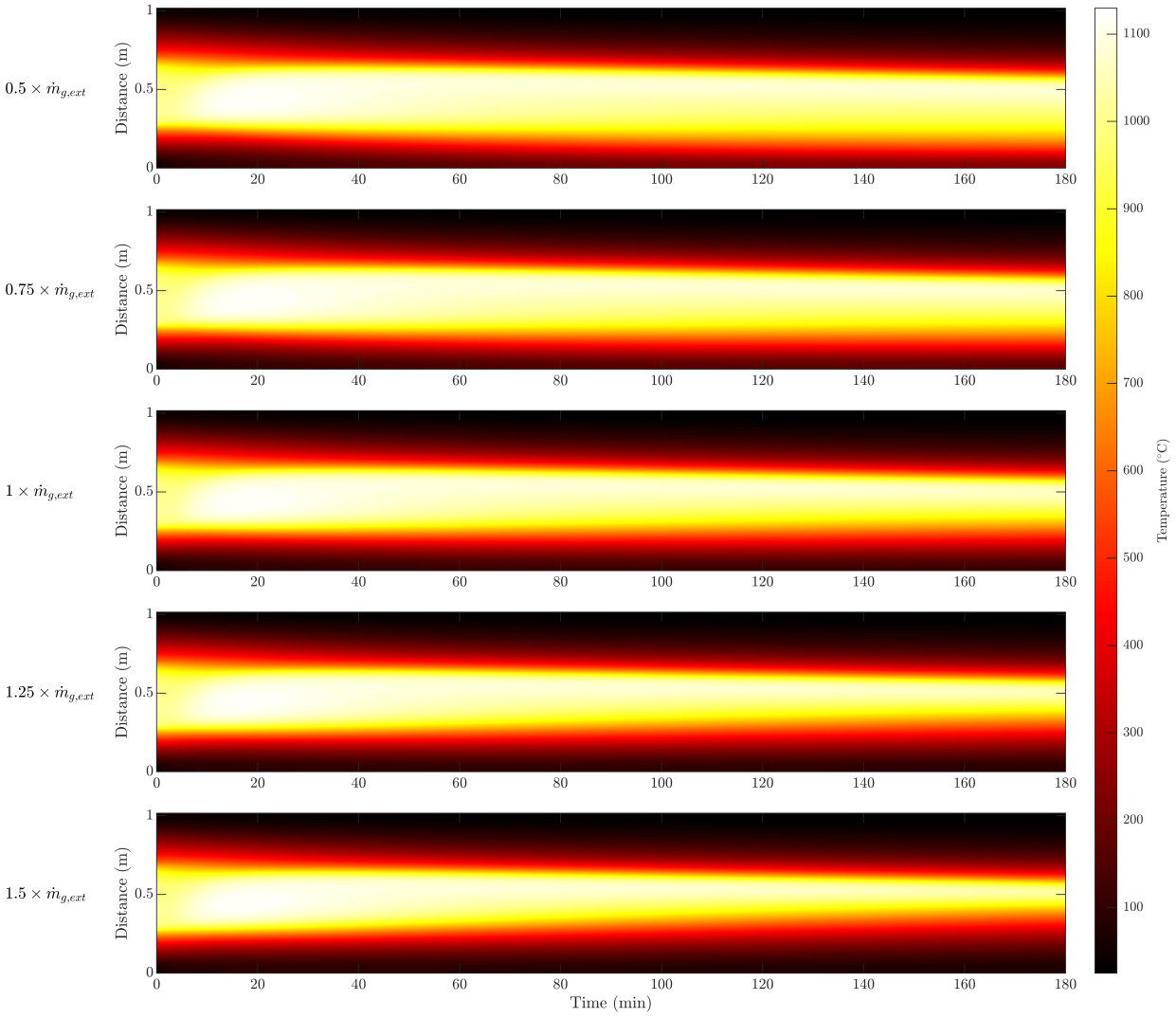

Figure 5.9 The effect of extraction gas flow on reactor behavior. For constant $\dot{m}_s$ and $\dot{m}_{g,recup}$, the extraction gas flow impacts the width and temperature of the reaction zone.

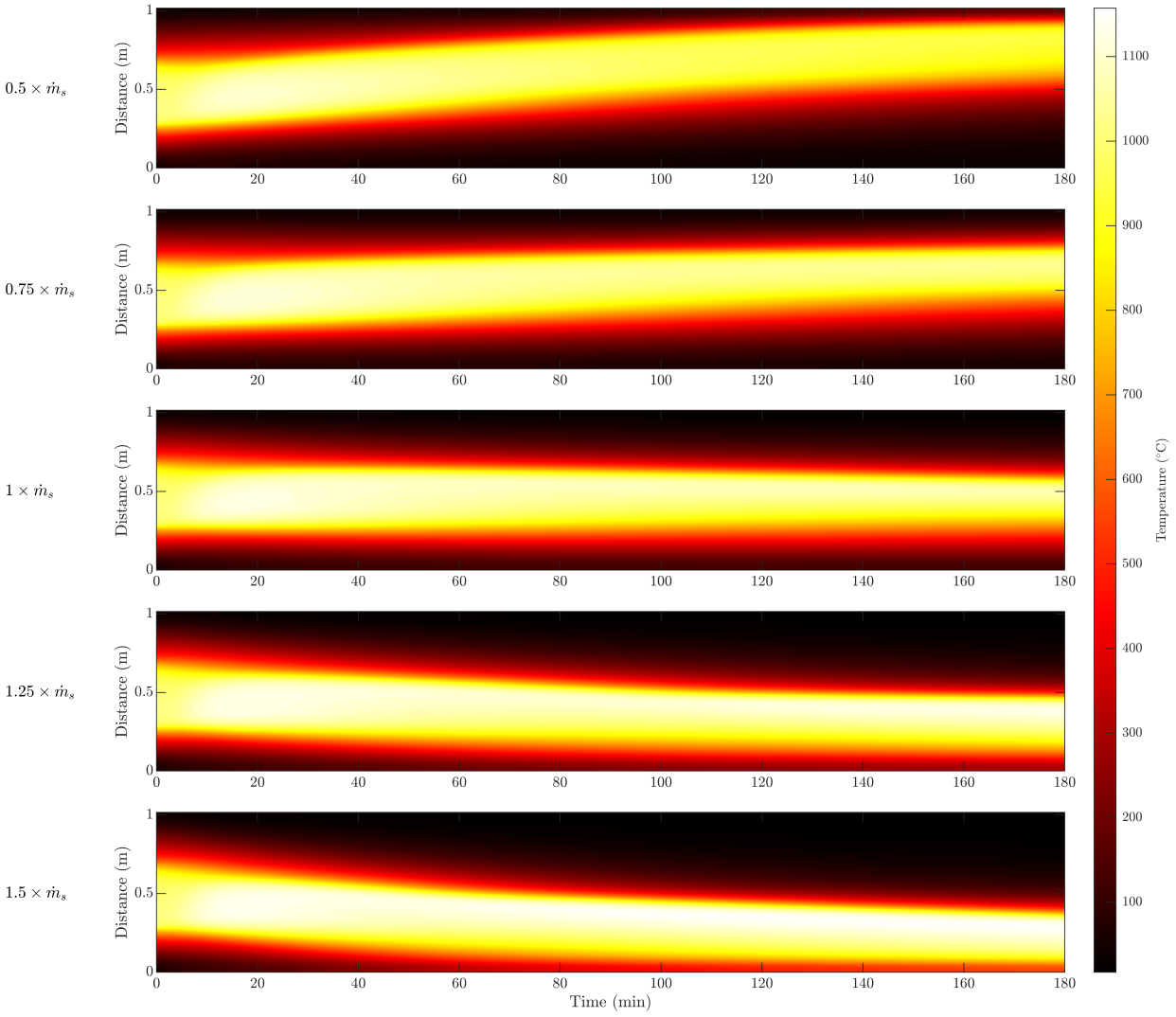

Figure 5.10 The effect of solid flow on reactor behavior. For constant $\dot{m}_{g,recup}$ and $\dot{m}_{g,ext}$, the solid flow rate contributes both to reaction zone positioning and reaction zone temperature.

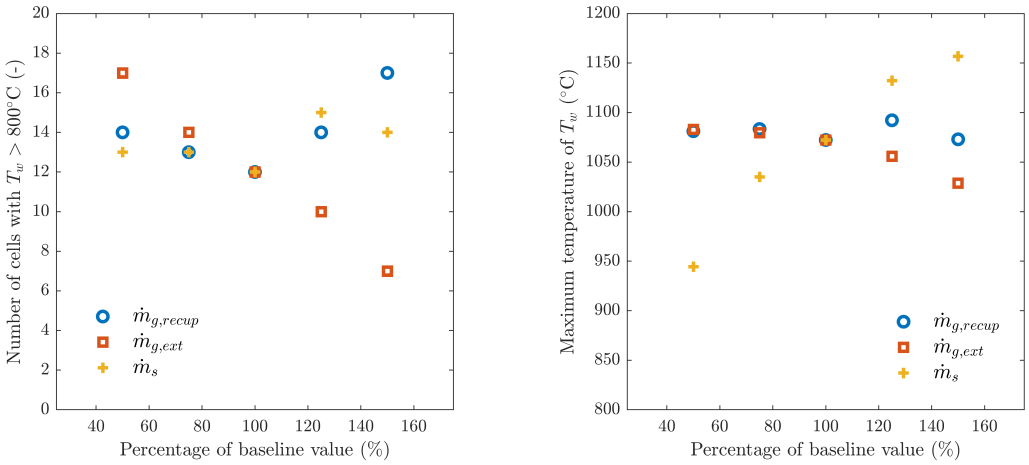

Figure 5.11 The impact of system inputs on (A) Reaction zone size, and (B) The maximum measured wall temperature, at $t = 180$ min. $\dot{m}_{g,ext}$ is observed to have the strongest effect on the size of the reaction zone, while $\dot{m}_s$ most strongly impacts the maximum temperature of T_w.

CHAPTER 6

MODEL PREDICTIVE CONTROL IMPLEMENTATION

Although the bench-scale oxidation reactor was successfully demonstrated across a variety of test cases in Chapter 4, the lack of a unifying operational strategy yielded a wide array of operational outcomes. Within chemical engineering, process control is a well-established discipline [89] [90] that seeks to regulate a reactive process to achieve a desired outcome. Model predictive control (MPC) is a particularly attractive control approach for chemical processes due to its ability to handle multi-input multi-output (MIMO) systems, as well as the ease with which targets and constraints may be implemented. Furthermore, adaptive MPC allows for on-the-fly changes to the controller in response to changing system properties, opening the door to relatively straightfoward regulation of nonlinear processes. Further details regarding the fundamentals of MPC will be provided in Section 6.1.

MPC is well documented across a variety of chemical applications, including two-phase reactors [91], nuclear applications [92], and steam methane reforming [93]. Petrasch et al. [94] were among the first to apply such a framework to solar thermochemical processes, positing a linear feedback controller for regulating a reduction reaction. Their work considered the reactor as a single lumped entity with average properties throughout, an approximation popularly referred to as a continuously stirred tank reactor (CSTR). A similar CSTR controller was presented by Saade et al. [95], evaluated on the computational model previously developed by the author [79]. Both Petrasch et al. and Saade et al. consider the effects of intermittent solar energy, a concept explored further by Habib [96], Rowe et al. [97], and Karout et al. [98] for thermochemical systems. A previous collaborator on the SoFuel project, Al Sahlani et al., developed an MPC approach for the reduction reactor [99], as well as forward feedback [100] and PID control [101] systems.

Although the previously described works establish a precedent for using MPC to regulate thermochemical energy processes, the applications differ from the SoFuel oxidation reactor in some key ways. Aside from the investigations of Al Sahlani et al., previous works have not featured a counterflow reactor design. Steady state responses to step inputs may be straightforwardly

determined for cocurrent flow, but the unstable nature of a counterflow system to such an input makes such analysis difficult. Furthermore, all of the previously mentioned authors are focused on endothermic thermochemical processes, in contrast to the exothermic nature of the SoFuel oxidation reactor. Investigations into controlling thermochemical oxidation processes are not well documented in the literature.

Outside of thermochemical energy storage applications, there are numerous investigations into counterflow and exothermic reactor control methodologies. Smets et al. [102] presented a bang-bang approach for a plug-flow, counterflow reactor based in optimal control theory, and Vojtesek et al. [103] and Sudhakar et al. [104] provide further insights into counterflow concepts. Such applications still fall short of describing the SoFuel oxidation reactor in that they omit a separate system outlet for extracting high temperature gas from the system. Chemical looping combustion, a well-documented [105] exothermic process similar to thermochemical energy storage, has enjoyed some controls investigations as well [106], but the fluidized nature of such combustors differs from the moving bed format of the SoFuel reactor.

This chapter describes the design, tuning, and deployment of an adaptive MPC for regulation of the thermochemical SoFuel oxidation reactor. The controller relies on similar species and energy balances to those detailed in Chapter 5, but with additional constraints and simplifications to allow for real-time deployment. Experimental evaluations of the MPC on the oxidation reactor showcase flexible operation that enables a high degree of user customization.

6.1 Theory of Model Predictive Control

Model predictive control is a well-established methodology that has found broad applicability in industry and academia since its inception [107] [108]. As the name implies, MPC is reliant on a numerical system model to predict future system responses to varying inputs. A diagram illustrating the major operating principles of MPC is shown in Figure 6.1. The most common approach for MPC is to operate in discrete rather than continuous time - that is, data is processed and decisions are made over the course of regularly spaced timesteps. Such steps are labeled in Figure 6.1, with k denoting the current discrete time, $k + 1$ signifying the next step, and T_s

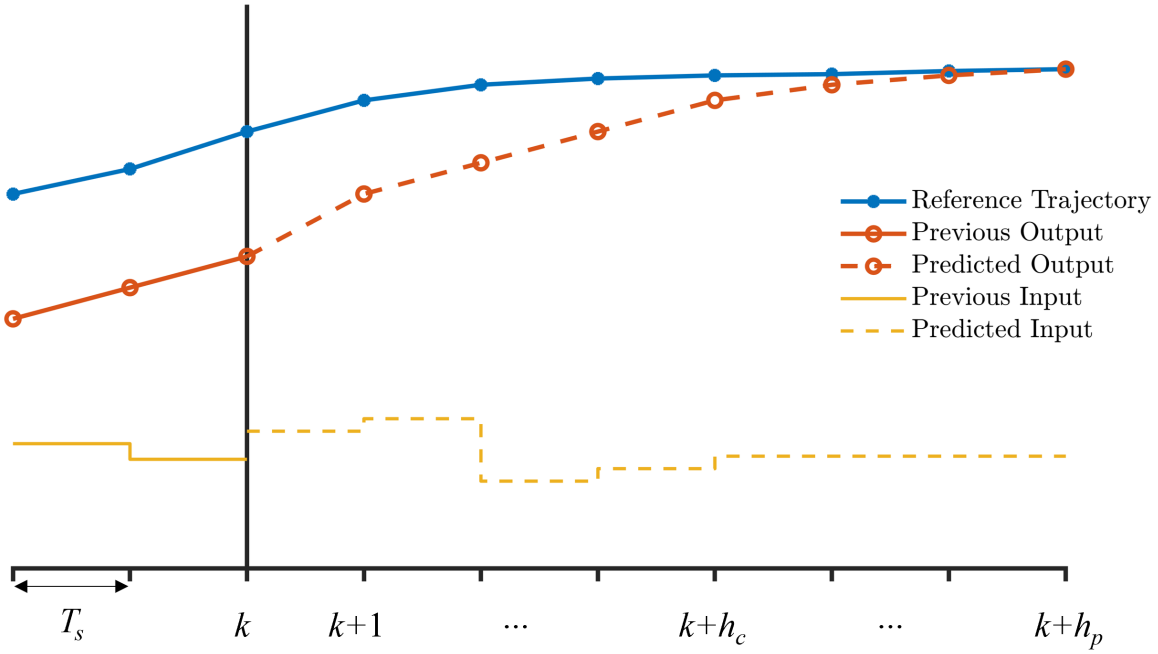

Figure 6.1 A general illustration of model predictive control theory, with k as the current timestep. The system seeks to attain it reference trajectory over the course of the prediction horizon, h_p.

representing the sampling period that passes between each step. Furthermore, MPC features two "horizons" that dictate controller operation. The first, h_p, is the prediction horizon. The prediction horizon determines how many timesteps into the future the MPC should consider while evaluating potential actions, with shorter prediction horizons typically corresponding to more rapid system response. Besides prediction there is also the control horizon, h_c, which specifies the number of timesteps that the MPC may utilize for changing system inputs. The control horizon must always be within the prediction horizon.

Returning to Figure 6.1, the reference trajectory provides the baseline behavior that the MPC desires to emulate. For the SoFuel oxidation reactor, for example, the key setpoint for tracking is the extraction temperature. The output is the actual measurement showing how well the system is adhering to the provided reference signal. The output may be further divided into two components: the previous output, which features actual measurements obtained from the physical system, and the predicted output. The predicted output is formulated by the MPC in response to simulated inputs to determine how best the system can achieve reference tracking. The inputs themselves are

similarly broken into two components: the previous input deployed on the actual system, and the predicted inputs that the MPC recommends for best reaching the reference trajectory. All of these predicted values are dictated by the system model at the heart of the MPC; using a mathematical representation of the system of interest, the controller can evaluate which inputs will lead to the optimal outputs for reaching the desired reference.

While MPC may calculate many recommended system inputs to be implemented in order to reach the reference trajectory, only the first input (corresponding to the discrete interval between k and $k + 1$) is implemented on the actual system. Once time $k + 1$ is reached, $k + 1$ becomes the new k and the process is begun anew utilizing the most up-to-date measurements of the inputs and outputs. For standard MPC, a single system model is utilized at all timesteps to determine the action necessary to achieve optimal operation. An alternative method is to generate a new system model at each time step; such an approach is known as adaptive MPC. The adaptive approach has a long history of utilization in industry [109], and it creates a unique opportunity for controlling nonlinear systems. MPC is straightforward to implement when dealing with linear systems, but nonlinear dynamics, such as chemical reactions, can complicate controller calculations. By creating a new system model at each timestep, adaptive MPC can utilize linearized models to approximate nonlinear behavior over short intervals. The nonlinear reaction dynamics of the oxidation reactor make it a suitable candidate for adaptive MPC control.

6.2 Controller Formulation

Constructing an adaptive model predictive control system requires the assembly of a wide array of components, including a linearized system model, state estimator, cost function, and the establishment of system constraints. The following subsections elaborate on these features, presenting rationale for their formulation and illustrating the way in which together they create a functioning MPC.

6.2.1 Problem Setup

Similar to the computational model of Chapter 5, the system model employed by the controller is based on a control-volume framework. The central reaction area of the oxidation reactor is

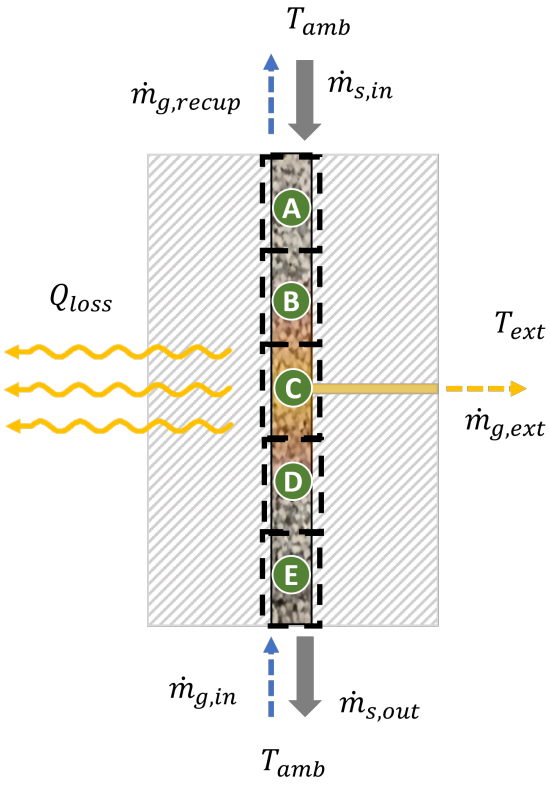

Figure 6.2 The five-zone control volume model implemented by the controller. Each zone corresponds to one of the five thermocouples inserted into the side of the experimental setup.

broken into five distinct zones that correspond to the five thermocouples protruding into the reactor to measure the axial tube temperature. Depicted in Figure 6.2, the five 6.93 cm diameter and 11.43 cm long cells do not encompass the entire reactor tube, but rather the 57.15 cm long region centered on the extraction point.

Within each control volume there are three key system properties of interest: temperature (T), extent of conversion of the solid (α_s), and oxygen mass fraction (ξ_{ox}). Taking into account all five zones, these quantities are collectively referred to as the state variables and are described as the 15×1 column vector **x**:

$$\mathbf{x} = \begin{bmatrix} T_E & \dots & T_A & \alpha_{s,E} & \dots & \alpha_{s,A} & \xi_{ox,E} & \dots & \xi_{ox,A} \end{bmatrix}^{\mathrm{T}} \tag{6.1}$$

where the added subscripts denote the appropriate cell for each quantity. Besides the system states, three familiar inputs are identified as well: solid flow rate $\dot{m}_s$, recuperation gas flow rate $\dot{m}_{g,recup}$,

and extraction gas flow rate $\dot{m}_{g,ext}$. The system inputs are collected in the 3×1 column vector **u**:

$$\mathbf{u} = \begin{bmatrix} \dot{m}_s & \dot{m}_{g,recup} & \dot{m}_{g,ext} \end{bmatrix}^{\mathrm{T}} \tag{6.2}$$

The final column vector to be defined is **y**, the system outputs. These include real-time measurements supplied to the controller, as well as linear combinations of measurements. The complete list of outputs considered for the oxidation reactor system are:

$$\mathbf{y} = \begin{bmatrix} T_E & T_D & T_C & T_B & T_A & \xi_{ox,E} & \xi_{ox,C} & \xi_{ox,A} & \Delta T \end{bmatrix}^{\mathrm{T}} \tag{6.3}$$

where ΔT is a customizable function measuring the difference between two temperature measurements. The five other temperature measurements are provided by the bed thermocouples, while the oxygen mass fractions are determined based on the input, extraction, and recuperation oxygen values, respectively.

6.2.2 Conservation Equations and Boundary Conditions

Further modeling simplifications are made beyond those employed in the computational model of Chapter 5 to describe the transient behavior of the system states. While the constant solid flow assumption is maintained, the gas flow behavior is further simplified to neglect the effect of oxygen consumption on overall flow rate. Another key assumption of the control model is that the solid and gas phases are in thermal equilibrium and can be described using a single average temperature for a specified cell; furthermore, the tube wall is neglected in this analysis. Insulation heat losses rely on a single average thermal conductivity value to estimate losses rather than a 1D radial model. Additionally, properties that were previously considered temperature-dependent are reduced here to constant average values, shown in Table 6.1. This includes the density of the gas phase, which is approximated as a constant value throughout the reactor to simplify the model and allow oxygen mass fraction (ξ_{ox}) to be used instead of oxygen concentration (C_{ox}). Thermal diffusion in the solid and gas are also neglected due to their comparatively small size when compared to energy transfer due to mass flow. These simplifications are made in order to create a computationally efficient system model that can be rapidly evaluated by the MPC during operation to determine appropriate behavior.

Property	Value	Unit
$c_{p,s}$	900	J/kg K
$c_{p,g}$	1200	W/m K
m_s	1.24	kg
m_g	8.84×10^{-5}	kg

Table 6.1 Constant property values utilized by the controller.

An upwind scheme is again deployed to describe advective effects on extent of conversion and oxygen mass fraction. The counterflow character of the reactor again makes this technique inapplicable for determining the temperature distribution in the system. The QUICK method is also unsuitable for deployment here. This is due in part to the large temperature differences across cells, but such an approach would also make the controller's task of balancing and regulating the reactor impossible. A QUICK framework would never predict satisfactory heat recuperation between the solid and gas phases, leaving the controller to conclude that balancing the two flows to achieve a steady state would be impossible. To combat this, boundary temperature values are considered to be simple averages between cell temperatures.

With the described simplifications and strategies in mind, the energy balance of a control zone, or cell of interest, can be described by a simple control volume assessment:

$$\frac{\partial H}{\partial t} = \sum \dot{m}_s h_s + \sum \dot{m}_g h_g - \dot{Q}_{loss} + \dot{Q}_{rxn} \tag{6.4}$$

where H is the total enthalpy of the zone and the rest of the quantities are previously introduced from Chapter 5. By implementing constant specific heats for the solid and gas phases, a constant insulation thermal conductivity, and average temperatures at each cell boundary, Equation 6.4 becomes:

$$\begin{aligned}\left(m_s c_{p,s} + m_g c_{p,g}\right)\frac{\partial T}{\partial t} &= \dot{m}_s c_{p,s}\left(\frac{T_{i+1}+T_i}{2} - \frac{T_{i-1}+T_i}{2}\right) \\ &+ \dot{m}_g c_{p,g}\left(\frac{T_{i-1}+T_i}{2} - \frac{T_{i+1}+T_i}{2}\right) - 2\pi\Delta x k_{ins}\frac{T_i - T_{amb}}{\ln\left(r_{out} - r_o\right)} + \dot{Q}_{rxn}\end{aligned} \tag{6.5}$$

Making further simplifications with regard to T_i and substituting in the previously determined

expression for $\dot{Q}_{rxn}$, the equation reaches its final form of:

$$\left(m_s c_{p,s} + m_g c_{p,g}\right) \frac{\partial T}{\partial t} = \dot{m}_s c_{p,s} \left(\frac{T_{i+1} - T_{i-1}}{2}\right) + \dot{m}_g c_{p,g} \left(\frac{T_{i-1} - T_{i+1}}{2}\right) - 2\pi \Delta x k_{ins} \frac{T_i - T_{amb}}{\ln\left(r_{out} - r_o\right)} + \frac{V_s \left(\rho_{ox} - \rho_{red}\right) \Delta H_{rxn}}{M_{O_2}} \left(\frac{\partial \alpha_s}{\partial t}\right)_{rxn,i} \tag{6.6}$$

The expression for extent of conversion for the control model remains largely the same as that of the higher fidelity computational model:

$$\frac{\partial \alpha_s}{\partial t} = \frac{\dot{m}_s}{m_s} \left(\alpha_{s,i+1} - \alpha_{s,i}\right) + \left(\frac{\partial \alpha_s}{\partial t}\right)_{rxn,i} \tag{6.7}$$

Lastly, the oxygen mass fraction closely imitates the formulation of the computational model as well, with the major difference being the utilization of mass fraction rather than concentration:

$$\frac{\partial \xi_{ox}}{\partial t} = \frac{\dot{m}_g}{m_g} \left(\xi_{ox,i-1} - \xi_{ox,i}\right) + \frac{V_s \left(\rho_{ox} - \rho_{red}\right)}{m_g} \left(\frac{\partial \alpha_s}{\partial t}\right)_{rxn,i} \tag{6.8}$$

Dirichlet boundary conditions define behavior on the edges of the system. The lower boundary of the bottom zone, corresponding to the gas inlet to the system, features $T_{x=0}$ = 300 K and $\xi_{ox,x=0}$ = 0.23197, while the upper boundary featuring the solid inlet is characterized by $T_{x=0}$ = 300 K and $\alpha_{s,x=H} = 0$. Furthermore, the equations are readily nondimensionalized in order to improve future matrix operations. Utilizing the same T_{ref} = 1573 K to linearize temperature expressions and new reference value $\xi_{ox,ref}$ = 0.23197 to normalize oxygen mass fraction, the following dimensionless expressions are established:

$$T^* = \frac{T}{T_{ref}}, \quad \xi_{ox}^* = \frac{\xi_{ox}}{\xi_{ox,ref}}$$

6.2.3 Linearization Approach

The nonlinear model of the previous section provides information as to the transient behavior of the system state variables. Through a linearization procedure, the nonlinear model can be converted into a linear approximation suitable for small deviations from the current state and appropriate for an adaptive MPC. Seborg et al. [89] elaborates on a standard Taylor series approach to converting nonlinear systems. For a variable z with a model of the form $\dot{z} = f(z)$, a first-order Taylor

approximation yields the following:

$$f(z) \approx f(z_s) + \left.\frac{\partial f}{\partial z}\right|_{z_s} (z - z_s) \tag{6.9}$$

where the "s" subscript denotes the current operating point. Under the assumption that such an operating point is relatively steady, the expression can be simplified to:

$$f(z) \approx \left.\frac{\partial f}{\partial z}\right|_{z_s} z' \tag{6.10}$$

With z' representing the change in z from the operating point z_s. This approach can be extended to the oxidation reactor model by following Seborg's approach for multistate systems and generally establishing:

$$\dot{\mathbf{x}} = \mathbf{f}(\mathbf{x}, \mathbf{u}) \tag{6.11}$$

Where $\mathbf{x}$ is the 15×1 state vector, $\mathbf{u}$ is the 9×1 input vector, and $\mathbf{f}$ is comprised of the conservation equations of Section 6.2.2. Using the framework of Equations 6.9 and 6.10, linear coefficient matrices of the following forms can be produced:

$$A_{ij} = \left.\frac{\partial f_i}{\partial x_j}\right|_{x_s,u_s}, \quad B_{ij} = \left.\frac{\partial f_i}{\partial u_j}\right|_{x_s,u_s} \tag{6.12}$$

where the "s" subscript again denotes that the linearization is evaluated at the current operating point. A detailed procedure for the linearization of each state's conservation equation, as well as the framework used to linearize $\left(\frac{\partial \alpha_s}{\partial t}\right)_{rxn}$, can be found in the Appendix. The resulting matrix equation for the entire system is:

$$\dot{\mathbf{x}} = \mathbf{A}\mathbf{x}' + \mathbf{B}\mathbf{u}' \tag{6.13}$$

Due to the fact that the derivatives of $\mathbf{x}$ and $\mathbf{x}'$ are the same (as a result of simply being offset values of one another), Equation 6.13 can be written in a final form describing the rate of change of $\mathbf{x}'$:

$$\dot{\mathbf{x}}' = \mathbf{A}\mathbf{x}' + \mathbf{B}\mathbf{u}' \tag{6.14}$$

A similar procedure can be followed to determine $\mathbf{y}'$, the variation of the system output. Because $\mathbf{y}$ can be expressed as a function of the model states, then:

$$\mathbf{y} = \mathbf{g}(\mathbf{x}) \tag{6.15}$$

And the linearization procedure is identical to that of Equations 6.12 and 6.14:

$$C_{ij} = \left.\frac{\partial g_i}{\partial x_j}\right|_{x_s} \tag{6.16}$$

$$\mathbf{y}' = \mathbf{C}\mathbf{x}' \tag{6.17}$$

The "′" superscript is dropped now, as the system is understood to be in the form of deviation from the operating point. The model now fits the standard continuous-time linear system form of:

$$\dot{\mathbf{x}} = \mathbf{A}\mathbf{x} + \mathbf{B}\mathbf{u}, \quad \mathbf{y} = \mathbf{C}\mathbf{x} \tag{6.18}$$

The final operation that must be completed before the linear model can be utilized by the MPC is conversion from continuous time to discrete time. The MPC approach works in specific, periodic timesteps, and thus relies on a discrete-time basis to operate. MATLAB®'s native "c2d" function is employed to convert the system of Equation 6.18 into discrete form. A period of 10 seconds is chosen for the discretization. This interval is selected to avoid wearing out the gas flow controllers utilized in the bench-scale reactor system. The final form of the linearized system features the "d" subscript to specify its discrete form, and the k index specifies the current step:

$$\mathbf{x}(k+1) = \mathbf{A_d}\mathbf{x}(k) + \mathbf{B_d}\mathbf{u}(k), \quad \mathbf{y}(k) = \mathbf{C_d}\mathbf{x}(k) \tag{6.19}$$

6.2.4 State Estimation

The absence of complete state knowledge necessitates the use of a state estimation procedure. The Kalman filter is one of the most popular techniques for approximating system states based on measured output. For a linear, discrete system, a Kalman filter considers the addition of Gaussian noise $\mathbf{w}$ on the input and measurement noise $\mathbf{v}$ on the system output:

$$\mathbf{x}(k+1) = \mathbf{A_d}\mathbf{x}(k) + \mathbf{B_d}\mathbf{u}(k) + \mathbf{G}\mathbf{w}(k), \quad \mathbf{y}(k) = \mathbf{C_d}\mathbf{x}(k) + \mathbf{v}(k) \tag{6.20}$$

For the oxidation reactor system, input noise is considered as a means to quantify uncertainty within the system. $\mathbf{w}$ is here considered to be a 6×1 column vector corresponding to thermal "noise" within the system among the five thermocouples, as well as uncertainty as to the exact extent of conversion

of particles entering the system. **G** applies **w** to the appropriate rows of **x**. Estimation of **x** is achieved via a Kalman gain, $\mathbf{M_x}$, which in turn is generated by the MATLAB® function "kalman." Besides the disturbance model presented in Equation 6.20, "kalman" also relies on **R** and **Q**, the covariance matrices of the measurement and input noises. respectively. Through trial-and-error tuning, the matrices employed in the oxidation MPC controller are:

$$\mathbf{R} = \begin{bmatrix} 0.0001 & 0 & 0 & 0 & 0 & 0 & 0 & 0 & 0 \\ 0 & 0.0001 & 0 & 0 & 0 & 0 & 0 & 0 & 0 \\ 0 & 0 & 0.0001 & 0 & 0 & 0 & 0 & 0 & 0 \\ 0 & 0 & 0 & 0.0001 & 0 & 0 & 0 & 0 & 0 \\ 0 & 0 & 0 & 0 & 0.0001 & 0 & 0 & 0 & 0 \\ 0 & 0 & 0 & 0 & 0 & 0.01 & 0 & 0 & 0 \\ 0 & 0 & 0 & 0 & 0 & 0 & 0.01 & 0 & 0 \\ 0 & 0 & 0 & 0 & 0 & 0 & 0 & 0.01 & 0 \\ 0 & 0 & 0 & 0 & 0 & 0 & 0 & 0 & 0.01 \end{bmatrix}$$

$$\mathbf{Q} = \begin{bmatrix} 0.1 & 0 & 0 & 0 & 0 & 0 \\ 0 & 0.1 & 0 & 0 & 0 & 0 \\ 0 & 0 & 0.1 & 0 & 0 & 0 \\ 0 & 0 & 0 & 0.1 & 0 & 0 \\ 0 & 0 & 0 & 0 & 0.1 & 0 \\ 0 & 0 & 0 & 0 & 0 & 0.1 \end{bmatrix}$$

Using these covariance matrices, $\mathbf{M_x}$ can be computed at each step of the MPC to update its estimation of unknown states.

6.2.5 Cost Function and Objective Identification

Section 6.2 provided the underlying linear system model used by the MPC to predict reactor behavior and dynamics. Another necessary component of the MPC is a cost function for determining optimal performance. Cost functions quantify the performance of a system as a function of its inputs and outputs; for optimal control strategies like MPC, the controller's objective is to minimize the

cost function. MATLAB®'s Model Predictive Control Toolbox [110] contains the "mpc" class, which implements a four-part objective function for determining optimal system inputs:

$$J(z_k) = J_y(z_k) + J_u(z_k) + J_{\Delta u}(z_k) + J_\varepsilon(z_k) \tag{6.21}$$

where z_k is the control decision, J represents cost, and the y, u, Δu, and ε subscripts denote output tracking, input tracking, change of input, and constraint violation, respectively. ε is not considered in this work, leaving the other three components to dictate controller behavior. Each is expressed as a linear quadratic (LQ) expression. The first, $J_y(z_k)$[111], is specified as:

$$J_y(z_k) = \sum_{j=1}^{n_y} \sum_{i=1}^{h_p} \left[\frac{w_j^y}{s_j^y} \left(r_j(k+i|k) - y_j(k+i|k) \right) \right]^2 \tag{6.22}$$

where n_y is the number of outputs, h_p is the previously defined prediction horizon, w_j^y and s_j^y are the weight and scaling factor for a given output, respectively, and r_j and y_j are the reference and output values, respectively. The purpose of the output tracking cost is to steer the MPC toward minimizing the difference between r_j and y_j; that is, for system outputs to reach a desired setpoint. Due to the nondimensionalized nature of the control model, no scaling factors are required for output tracking of the oxidation reactor. The primary quantity of investigation is w_j^y, as differing the weights assigned to each output influences controller priority and affects overall behavior. The input tracking, $J_u(z_k)$[111], is similarly structured as:

$$J_u(z_k) = \sum_{j=1}^{n_u} \sum_{i=0}^{h_c-1} \left[\frac{w_j^u}{s_j^u} \left(u_j(k+i|k) - u_{target,j}(k+i|k) \right) \right]^2 \tag{6.23}$$

with n_u as the number of inputs and h_c the control horizon. All other quantities are equivalent to their output tracking counterparts, as the controller once again weighs the priority of regulating inputs to specified levels. The final cost subfunction is associated with the change of input, $J_{\Delta u}(z_k)$:

$$J_{\Delta u}(z_k) = \sum_{j=1}^{n_u} \sum_{i=0}^{h_c-1} \left[\frac{w_j^{\Delta u}}{s_j^u} \left(u_j(k+i|k) - u_j(k+i-1|k) \right) \right]^2 \tag{6.24}$$

$J_{\Delta u}(z_k)$ differs from the previous subfunctions due to the fact that it does not track any user-supplied setpoint. Rather, the function compares the ith input value to its predecessor; as a result,

high weighting would steer the reactor toward small changes in system inputs. In light of this phenomenon, $J_{\Delta u}(z_k)$ is also known as the input move suppression cost.

On-reactor oxidation experiments have previously identified several key objectives for operation. First, a temperature setpoint is desired in order to specify the temperature of gas exiting the reactor through the extraction port. This user-defined value is labeled $T_{C,ref}$ and serves as the target for reference tracking. A specified rate of energy extraction is required for supplying appropriate energy to end-use applications as well. This extraction energy reference value, $\dot{Q}_{ext,ref}$, can be coupled with $T_{C,ref}$ to determine a setpoint for $\dot{m}_{g,ext}$:

$$\dot{m}_{g,ext,ref} = \frac{\dot{Q}_{ext,ref}}{c_{p,g}\left(T_{C,ref} - T_{amb}\right)} \tag{6.25}$$

$\dot{m}_{g,ext,ref}$ and $T_{C,ref}$ are consistently deployed across all considered control schemes in this work. The most important remaining functionality of the controller is the maintenance of reaction zone stability. The controller must be cognizant of the location of the exothermic reaction zone in order to ensure safe operation of the reactor. Sections 6.3-6.5 consider several approaches to creating this operational stability, taking into account various input, output, and move suppression weighting schemes.

6.2.6 System Constraints

MPC's are well-suited to multiple-input multiple output systems like the oxidation reactor, but they are also attractive controllers due to their ability to handle constraints to system operation. Controller constraints primarily relate to the system inputs, dictated by limitations of the gas flow controllers supplying air to the reactor. Like the controller objectives, system constraints may vary from one control approach to another and are described in greater detail in the following sections.

6.3 Control Approach 1: Minimizing $\Delta T = T_C - T_D$

The first MPC scheme for regulating the size and position of the reaction zone, labeled in this work as Approach 1, follows a simple premise: directing the controller to seek equivalence between reactor Zones C and D. A diagram depicting the conceptualized temperature distribution of this approach is shown in Figure 6.3. Positioning the hottest part of the particle bed below the extraction

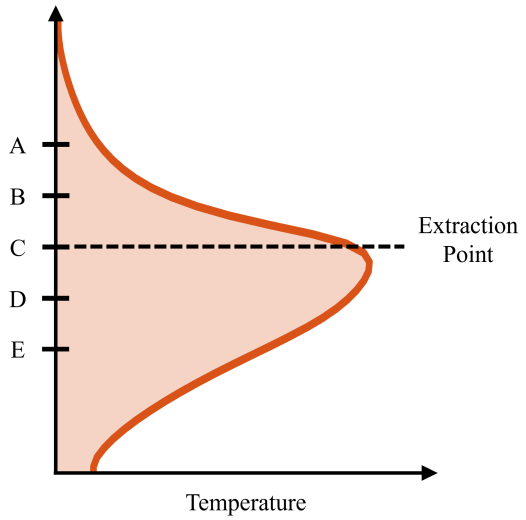

Figure 6.3 Reaction zone positioning for a $\Delta T = T_C - T_D$ tracking control scheme. This approach seeks to place the hottest zones of the particle bed below the extraction point to bolster heat transfer to the extraction gas.

point, as is expected utilizing this control approach, has several advantages. First, thermal runaway in the upper reaches of the bed is mitigated, and the gas flows specified by the controller are expected to be sufficient for recuperation in the lower reaches of the bed as well. Having the hottest part of the reactor outside of the extraction point provides a thermal reservoir within the particle bed as well, allowing the MPC to quickly deliver energy to the extraction zone as needed to better regulate the extraction temperature. From a heat transfer perspective, a lower-positioned reaction zone is preferable for ensuring high temperature extraction gas as well. Excellent particle-gas heat transfer is predicted by the system model throughout the reactor, but elevated temperatures below the extraction point provide the extracted gas with a greater temperature difference to drive convective heat transfer.

Tracking the temperature difference between Zones C and D can be achieved by setting the ΔT term of the output vector $\mathbf{y}$ to the following expression:

$$\Delta T = T_C - T_D \tag{6.26}$$

Because temperature equivalence between the two zones is desired, a tracking value of zero is specified. Besides the inclusion of a setpoint for ΔT, Approach 1 also considers two setpoint

calculations for $\dot{m}_s$ and $\dot{m}_{g,recup}$ in order to encourage steady reactor behavior. First, the tracking value for $\dot{m}_s$ is set to a value capable of supplying sufficient energy for stable operation assuming full conversion ($\Delta\alpha_s = 1$):

$$\dot{m}_{s,ref} = \frac{\left(\dot{Q}_{ext,ref} - \dot{Q}_{loss}\right) M_{O_2}}{\beta \Delta H_{RXN}} \tag{6.27}$$

where $\dot{Q}_{loss}$ is defined using the expression from Equation 6.5 and considering all zones:

$$\dot{Q}_{loss} = 2\pi \Delta x k_{ins} \frac{\sum_{i=1}^{5} T - T_{amb}}{\ln\left(r_{out} - r_o\right)} \tag{6.28}$$

By determining a solid flow setpoint using Equations 6.27 and 6.28, the MPC seeks a feed rate that can provide sufficient chemical energy to satisfy extraction and system losses. The reference value for $\dot{m}_{g,recup}$, in contrast, focuses on providing a baseline gas flow rate for adequate heat recuperation:

$$\dot{m}_{g,recup,ref} = \frac{c_{p,s}}{c_{p,g}} \dot{m}_s - \dot{m}_{g,ext,ref} \tag{6.29}$$

where the setpoint $\dot{m}_{g,recup,ref}$ is based on the current solid flow rate and the gas extraction setpoint. In conjunction with the previously established setpoints for T_C and $\dot{m}_{g,ext}$ from Section 6.2.5, these expressions establish additional input and output reference tracking that define Approach 1.

6.3.1 Parametric Tuning Study for Approach 1

The tuning process for the MPC of this work was a long-term, iterative process evaluating a wide array of control approaches on computational models of differing levels of complexity. These investigations tested out various ideas through trial-and-error as well as parametric approaches over the span of several months. In order to present the findings of this complex process in a coherent, accessible format, parametric studies on the computational model of Chapter 5 were performed to illustrate the overarching controller trends for various strategies and weights.

Tuning parameters for the characterization of Approach 1 are listed in Table 6.2. The table contains the previously described setpoints for various inputs and outputs, as well as constraints for the three system inputs. Upper bounds for $\dot{m}_s$ and $\dot{m}_{g,recup}$ are on the order of those implemented successfully on the experimental reactor, while $\dot{m}_{g,ext}$ is capped at a value twice the calculated setpoint. A modest minimum value of 0.75 g/s was applied to the solid flow rate in order to ensure a

Quantity	Target	Lower Limit	Upper Limit	Weights
T_C	$T_{C,ref}$	-	-	1, 5, 20
$\dot{m}_{g,ext}$	$\frac{\dot{Q}_{ext,ref}}{c_{p,g}\left(T_{C,ref}-T_{amb}\right)}$	0	$2 \times \dot{m}_{g,ext,ref}$	10
$\dot{m}_s$	$\frac{\left(\dot{Q}_{ext,ref}-\dot{Q}_{loss}\right)M_{O_2}}{\beta \Delta H_{RXN}}$	0.75 g/s	3 g/s	0.1, 0.5, 2
$\dot{m}_{g,recup}$	$\frac{c_{p,s}}{c_{p,g}}\dot{m}_s - \dot{m}_{g,ext}$	0.1 g/s	3 g/s	0.1, 0.5, 2
$T_C - T_D$	0	-	-	0, 1, 5, 20
$\Delta\left(\dot{m}_s\right)$	N/A	-	-	0, 0.1, 0.5
$\Delta\left(\dot{m}_{g,recup}\right)$	N/A	-	-	0, 0.1, 0.5
$\Delta\left(\dot{m}_{g,ext}\right)$	N/A	-	-	0.1

Table 6.2 Tuning parameters for the parametric evaluation of Approach 1.

continuously moving column of particles; this has been experimentally observed to reduce sintering and clogging effects.

The various weights specified in Table 6.2 correspond to 972 unique combinations encompassing the many iterative tuning investigations performed throughout controller development. Documentation for the MATLAB® "mpc" function [110] lays out the following general guidelines for comparing objective weights: 0.05 corresponds to a low priority objective, 0.2 to below-average, 1 to average, 5 to above average, and 20 to high priority. The four most varied weights correspond to T_C, $T_C - T_D$, and $\dot{m}_s$, and $\dot{m}_{g,recup}$, while smaller variations are explored for move suppression (identified as $\Delta()$ in Table 6.2). In accordance with the recommendations of weighting priority, $\dot{m}_{g,ext}$ received a relatively high weight of 10 to track the setpoint established by the rate of energy extraction, and its move suppression cost was set equal to 0.1.

Besides weights and constraints, the controller also relied on several other operational properties to direct performance. Over the two hours simulated by this parametric study, the controller sought to regulate T_C to two setpoints of 1000°C and 1050°C. The rate of energy extraction was specified

Property	Value
$T_{C,ref}$	1000°C, 1050°C
$\dot{Q}_{ext,ref}$	500 W, 300 W
h_p	20
h_c	1
T_s	10 s

Table 6.3 Controller properties for the parametric evaluation of Approach 1.

as 500 W during the first interval, and subsequently 300 W during 1050°C operation, values in line with those previously experimentally observed. The three remaining properties were chosen to facilitate eventual deployment of the controller on the experimental reactor. A period (T_s) of ten seconds was selected to minimize wear on the gas flow controllers of the experimental system. A prediction horizon (h_p) of 20 is the default value for MATLAB®'s "mpc" function, and it was retained here. The control horizon (h_c) was limited to a value of 1 to encourage conservative behavior in the controller. Further explorations of these quantities are considered at the end of this chapter.

The computational model of Chapter 5 was employed to tune the controller weights throughout the parametric study. To assess the controller's handling of nonlinear dynamics and unexpected system conditions, the MPC was deployed with the general initial conditions of most of the experiments of Chapter 4: a bed of fully reduced particles in an oxygen deficient atmosphere at an initial temperature of around 1000°C. Specifically, cells 15 through 30 of the reactor (including the solid, gas, and wall phases) were set to an initial value of 1000°C. A five-hour preheat simulation was performed to bring the reactor to thermal equilibrium with the specified temperatures. All boundary conditions of the simulation remained the same as those employed in Chapter 5.

The MPC was provided with the following initial nominal point $\mathbf{x}_s$:

$$\mathbf{T_s} = \begin{bmatrix} 1000 \\ 1000 \\ 1000 \\ 1000 \\ 1000 \end{bmatrix}, \quad \boldsymbol{\xi}_{\mathbf{ox,s}} = \begin{bmatrix} 0.2315 \\ 0.227 \\ 0.219 \\ 0.174 \\ 0.168 \end{bmatrix}, \quad \boldsymbol{\alpha}_{\mathbf{s,s}} = \begin{bmatrix} 0.7355 \\ 0.7385 \\ 0.6631 \\ 0.3329 \\ 0 \end{bmatrix}, \quad \mathbf{x}_s = \begin{bmatrix} \mathbf{T_s} \\ \boldsymbol{\xi}_{\mathbf{ox,s}} \\ \boldsymbol{\alpha}_{\mathbf{s,s}} \end{bmatrix}$$

where $\mathbf{T_s}$, $\boldsymbol{\xi}_{\mathbf{ox,s}}$, and $\boldsymbol{\alpha}_{\mathbf{s,s}}$ are the constituent components of $\mathbf{x_s}$. The temperature states were based on the initial conditions, while $\boldsymbol{\xi}_{\mathbf{ox,s}}$ and $\boldsymbol{\alpha}_{\mathbf{s,s}}$ were average steady state values observed during various simulations. These two substitutions were made in order to bolster the MPC's state estimation for long runtimes. In addition, the controller began with nominal input values $\mathbf{u_s}$ of:

$$\mathbf{u}_s = \begin{bmatrix} \dot{m}_{s,s} \\ \dot{m}_{g,recup,s} \\ \dot{m}_{g,ext,s} \end{bmatrix}$$

with values of 1.5 g/s, 0.8 g/s, and 0.4 g/s for $\dot{m}_{s,s}$, $\dot{m}_{g,recup,s}$, and $\dot{m}_{g,ext,s}$, respectively. Taken together, $\mathbf{x}_s$ and $\mathbf{u}_s$ provided the initial linearization point for the MPC internal model.

Furthermore, an advective smoothing procedure was applied to the values of $\boldsymbol{\xi}_{\mathbf{ox}}$ and $\boldsymbol{\alpha}_{\mathbf{s}}$ throughout the MPC's operation to ensure faithfulness to the physical constraints of the system. For oxygen mass fraction, the lowest possible value a cell could contain was 0, and the highest was the oxygen mass fraction of the cell below it, from which the oxygen-laden gas stream originated. This can be expressed as:

$$\xi_{ox,i} = \max\left(0, \min\left(\xi_{ox,i}, \xi_{ox,i-1}\right)\right) \tag{6.30}$$

Extent of conversion in a zone was bounded by the fully converted state with a value of 1 and the extent of conversion of the zone before it. As such, the bounds on extent of conversion can be expressed as:

$$\alpha_{s,i} = \max\left(\alpha_{s,i+1}, \min\left(\alpha_{s,i}, 1\right)\right) \tag{6.31}$$

Besides the added stability provided by Equations 6.30 and 6.31, the MPC behaved according to the attributes laid out in Section 6.2 combined with the weights of Table 6.2.

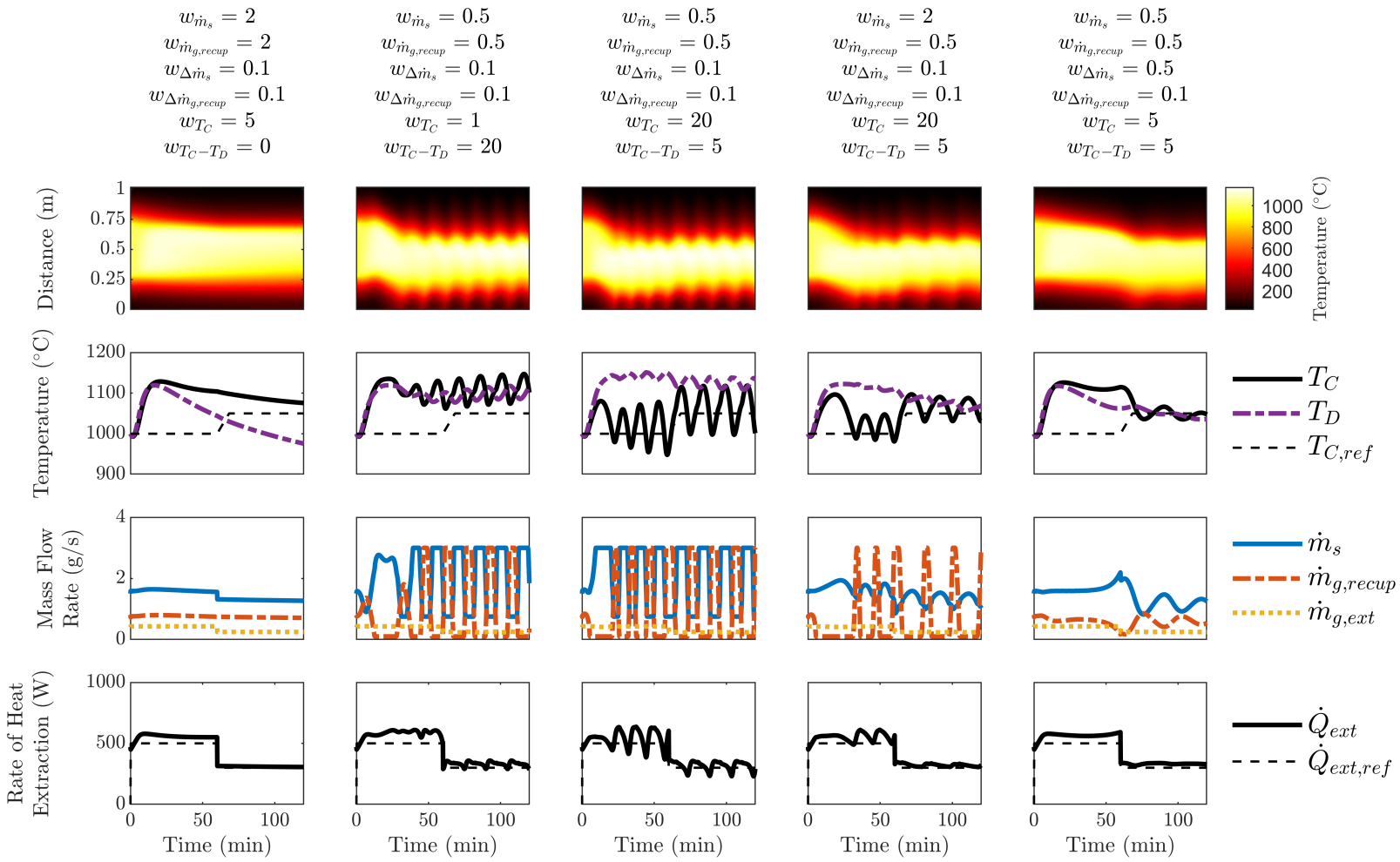

Figure 6.4 Select results from the parametric tuning procedure with a $\Delta T = T_C - T_D$ tracking control scheme. Subplots include a temperature contour for T_w, measurements and tracking for T_C and T_D, system input values, and tracking results for $\dot{Q}_{ext}$, from top to bottom.

Select parametric tuning results are presented in Figure 6.4 to illustrate general controller trends. Five cases are chosen for presentation, and each features four subplots to describe controller performance: a contour plot of the simulated reactor wall temperatures, specific evaluations of T_C and T_D, the manipulated system inputs, and the efficacy of $\dot{Q}_{ext}$ setpoint tracking, from top to bottom. The first case illustrates the impact of giving disproportionate priority to regulating the inputs $\dot{m}_s$ and $\dot{m}_{g,recup}$. While the temperatures of Zones C and D rise together during the initial chemical reaction within the particle bed, over time the relatively constant solid and gas flows produce differing temperatures in the two zones. The controller does not achieve adequate setpoint tracking for T_C during the two hours of simulated operation. $T_{C,ref}$ is poorly tracked in the second case as well, which strongly values the minimization of $T_C - T_D$. This case successfully regulates the placement of the main reaction zone, but the controller fails to achieve its temperature setpoint.

The middle third case exhibits the first instance of setpoint tracking for T_C, albeit with some operational challenges. The MPC is unable to decrease the temperature of Zone D to match that of Zone C, instead producing wild fluctuations of T_C with an amplitude of nearly 50°C. While the input profile of this case closely resembles that of the second example, of note is the high solid flow rate early in the experiment to move sensible energy out of Zone C and into Zone D. Without the regulatory effects of high weights for the system inputs, the third case attains oscillation about $T_{C,ref}$ relatively quickly but struggles to suitably converge on the value. The fourth column of Figure 6.4 showcases a more restrained version of the third approach. $w_{\dot{m}_s}$ is set to a relatively high value of 2, limiting the intensity of solid flow fluctuations. This produces smaller oscillations of T_C and $\dot{Q}_{ext}$ at the cost of slightly longer operation before achieving temperature tracking of Zone C.

The final case considered, shown in the far right column of Figure 6.4, exhibits perhaps the most consistent operational approach. w_{T_C} and $w_{T_C-T_D}$ are assigned equal values of 5, higher than the weights for $\dot{m}_s$ and $\dot{m}_{g,recup}$ but not drastically so. As a result, the controller carefully regulates the magnitude of the system inputs while maintaining decent temperature equivalence between Zones C and D. While it takes the system the first 50 minutes of simulated operation to achieve setpoint tracking of $T_{C,ref}$, upon reaching the value the MPC successfully achieves all

desired system criteria. Parametric cases with differing move suppression weights are not depicted here due to the relatively low impact of the move suppression cost. While the move suppression weights have a marginal impact on the smoothness of reactor operation, they do not impact the overall reactor performance as strongly as the four other weights at the center of this investigation.

The strong oscillatory behavior of T_C and $T_C - T_D$ in Approach 1, especially prevalent in those cases that quickly achieved setpoint tracking for Zone C, points to a shortcoming of the $T_C - T_D$ reaction zone placement scheme. When seeking to minimize $T_C - T_D$, the controller has two properties it can adjust to reach its objective: both T_C and T_D. For cases with large differences between the two measurements, the system may seek to increase and decrease the two simultaneously to rapidly minimize the tracking error, thus disrupting the setpoint tracking of $T_{C,ref}$. An alternative positioning scheme that does not consider T_C in its calculation is proposed as a solution to this phenomenon.

6.4 Control Approach 2: Reference Tracking for T_D

To address the shortcomings of Approach 1, a second approach was considered: using temperature reference tracking in Zone D to regulate the size and position of the reaction zone. Temperature distributions produced by Approach 2 are expected to strongly resemble those depicted in Figure 6.3 for Approach 1, with the hottest part of the reaction zone still positioned beneath the extraction point. The advantage of this approach is the removal of the temperature difference $T_C - T_D$ for positioning: by using an independent reference temperature for T_D, the controller is not incentivized to change T_C in order to satisfy other objectives. No additional tracking expressions were developed beyond $T_{D,ref}$ to implement Approach 2. Whereas $T_{C,ref}$ was provided as a reference value for the temperature of Zone C for the entire controller prediction horizon, $T_{D,ref}$ was applied in a slightly more reserved format. To encourage controller prioritization of T_C, the controller setpoints for T_D were applied in regularly spaced intervals between the currently measured value of T_D and $T_{D,ref}$. A visualization of the difference in controller horizon setpoints for the two values is depicted in Figure 6.5.

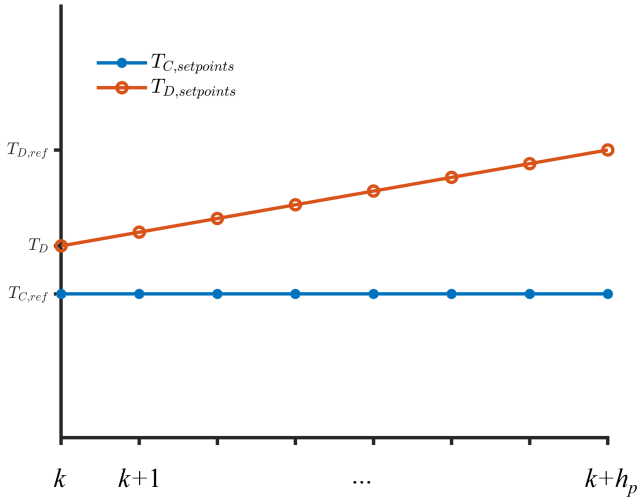

Figure 6.5 Controller setpoints from step k to the prediction horizon. The setpoints for T_D are linearly spaced between the current measured value of T_D and $T_{D,ref}$ to give higher priority to T_C reference tracking.

6.4.1 Parametric Tuning Study for Approach 2

Similar to the procedure for Approach 1, a parametric evaluation was used to summarize the behavior of Approach 2. Once again, the parametric study is representative of the larger trends observed throughout the controller tuning process. Tuning parameters are listed in Table 6.4, and their values exhibit some differences when compared to the procedure of Approach 1. First, an additional constraint was applied to the system for Zone B, the region directly above Zone C: an upper limit of $T_{C,ref}$. While the well-tuned cases of Approach 1 did not exhibit any thermal runaway in the system, this added constraint on T_B provided an extra layer of protection for system operation. Even with a maximum allowable value of $T_{C,ref}$, T_B still received no weighting or setpoint for operation. Weights for T_C and T_D were considered up to values higher than those of Approach 1 to investigate the impact of dramatically favoring these quantities over other criteria. $\dot{m}_s$ and $\dot{m}_{g,recup}$ featured a wider range of weights as well, while all move suppression weights were assigned a standard value of 0.1 $w_{\dot{m}_{g,ext}}$ maintained its previously assigned value of 10 from Approach 1.

As previously mentioned, reference targets for most quantities - T_C and the system inputs - remained true to their formulations from Approach 1. A new reference value was established for T_D, specified as $T_{C,ref}$ + 50°C. This arbitrary assignment sought to ensure that Zone D maintained

Quantity	Target	Lower Limit	Upper Limit	Weights
T_B	-	-	$T_{C,ref}$	-
T_C	$T_{C,ref}$	-	-	5, 10, 20, 40
T_D	$T_{C,ref}$ + 50°C	-	-	1, 5, 10, 20
$\dot{m}_{g,ext}$	$\frac{\dot{Q}_{ext,ref}}{c_{p,g}\left(T_{C,ref}-T_{amb}\right)}$	0	$2 \times \dot{m}_{g,ext,ref}$	10
$\dot{m}_s$	$\frac{\left(\dot{Q}_{ext,ref}-\dot{Q}_{loss}\right)M_{O_2}}{\beta\Delta H_{RXN}}$	0.75 g/s	3 g/s	0.1, 0.5, 2, 5
$\dot{m}_{g,recup}$	$\frac{c_{p,s}}{c_{p,g}}\dot{m}_s - \dot{m}_{g,ext}$	0.1 g/s	3 g/s	0.1, 0.5, 2, 5
$\Delta\left(\dot{m}_s\right)$	N/A	-	-	0.1
$\Delta\left(\dot{m}_{g,recup}\right)$	N/A	-	-	0.1
$\Delta\left(\dot{m}_{g,ext}\right)$	N/A	-	-	0.1

Table 6.4 Tuning parameters for the parametric evaluation of Approach 2.

a higher operating temperature than Zone C above it. Besides slight differences among weights, constraints, and targets, deployment of the tuning procedure for Approach 2 followed the same process as Approach 1. Over the course of two hours of simulated runtime, the MPC was instructed to achieve two one-hour periods of setpoint tracking: 1000°C and 500 W during the first hour and 1050°C and 300 W during the second hour for $T_{C,ref}$ and $\dot{Q}_{ext,ref}$, respectively. The period, control horizon, and prediction horizon remained the same as those specified in Table 6.3. The controller was similarly deployed on the model of Chapter 5 as described in Section 6.3.1.

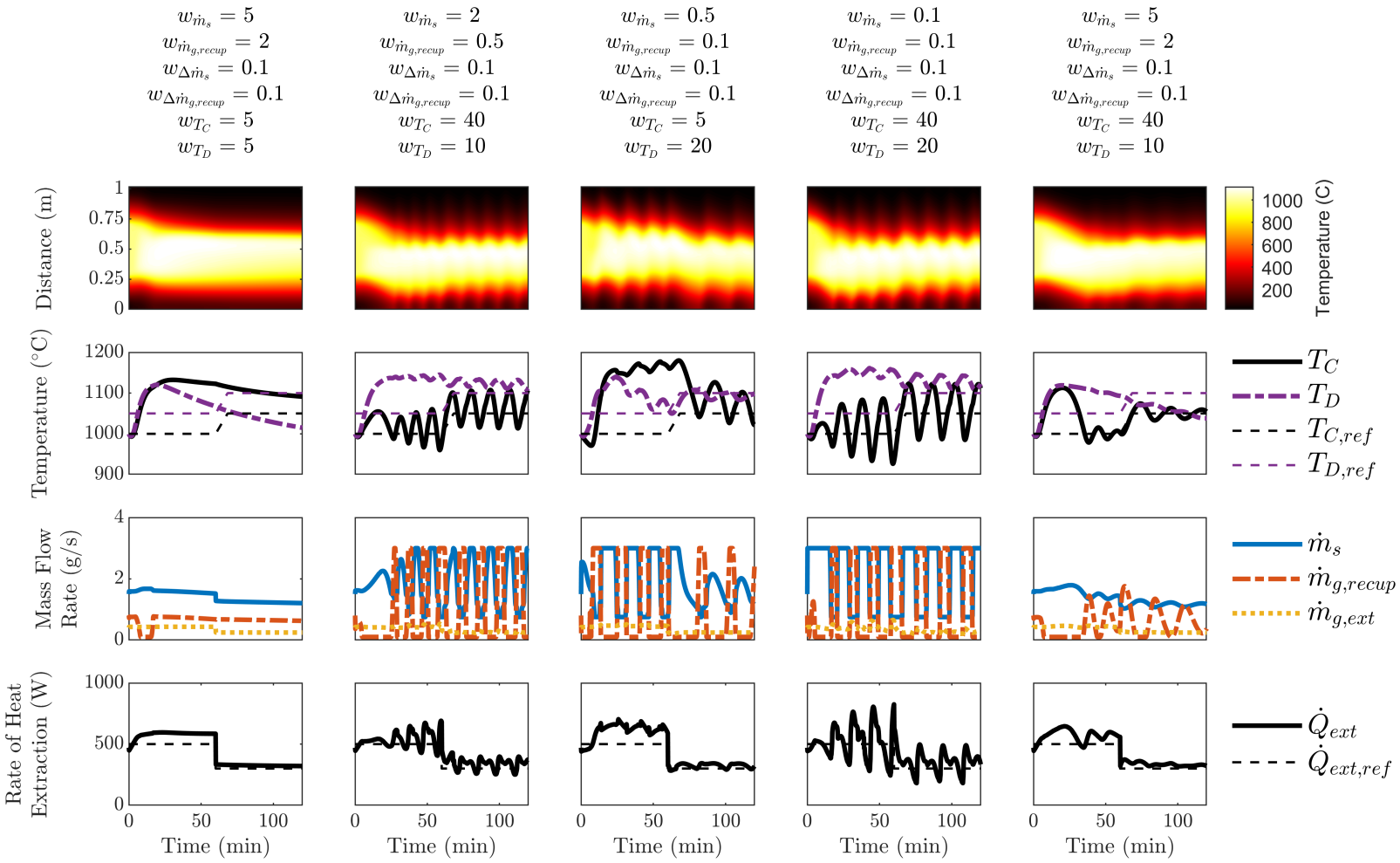

Figure 6.6 Select results from the parametric tuning procedure with a T_D tracking control scheme. Subplots include a temperature contour for T_w, measurements and tracking for T_C and T_D, system input values, and tracking results for $\dot{Q}_{ext}$, from top to bottom.

Figure 6.6 depicts the general tuning trends of the T_C and T_D temperature tracking control scheme. The subplots present similar information to those first depicted in Figure 6.4, though Figure 6.6 now features a tracking setpoint for T_D. The leftmost case corresponds to a controller that prioritizes conservative system inputs, with $w_{\dot{m}_s}$ and $w_{\dot{m}_{g,recup}}$ featuring similar values as w_{T_C} and w_{T_D}. The controller reacts in much the same way that it did under such conditions with Approach 1, holding to relatively steady values for $\dot{m}_s$ and $\dot{m}_{g,recup}$ and neglecting maintenance of any temperature setpoints. Increasing the weights of T_C and T_D to values of 40 and 10, respectively, while slightly decreasing the input weights produces the second set of results. The MPC achieves setpoint tracking for T_C fairly quickly, and successfully tracks both the 1000°C and 1050°C references, although oscillations still occur. While T_D eventually comes close to its setpoint in the second half of the controller's operation, it appears to be buoyed by the oscillating temperature of T_C rather than focusing on setpoint tracking. Overall, the controller does a modest job of tracking both $T_{C,ref}$ and $\dot{Q}_{ext,ref}$, though the overall controller behavior does not differ much from Approach 1.

The third set of results illustrated in Figure 6.6 showcases controller operation for a weighting scheme where T_D dominates controller behavior. As depicted in the second plot, the controller seeks to track the provided reference temperatures for T_D, although the alternative setpoint approach for Zone D leads to less stringent tracking than the previous example. T_C eventually comes close to its setpoint, although large oscillations remain. The fourth example of Approach 2 considers a less modulated version of the second controller formulation: $w_{\dot{m}_s}$ and $w_{\dot{m}_{g,recup}}$ are reduced to values of 0.1, and the weighting for T_D is increased to 20. The lack of any input regulation leads the controller to swing wildly about its setpoint for T_C, as both the solid and gas flow are manipulated in an attempt to drive T_C back toward its setpoint as quickly as possible.

With the best performing set of parameters (case 2) still exhibiting undesirable oscillation, one final formulation was proposed. The fifth and rightmost case of Figure 6.6 implements strong input regulation as well as strong output tracking, especially for T_C. After initial temperature increases due to large-scale chemical reaction within the particle bed, the MPC successfully steers T_C toward

its setpoints of 1000°C and 1050°C without the violent oscillations of previous tuning cases. $\dot{Q}_{ext}$ is observed to track its setpoint relatively closely as well. The temperature of Zone D is the only output that exhibits poor tracking, with a decreasing value over the course of the simulation. Even with this shortcoming, the fifth approach exhibits the best overall performance among the permutations presented in Figure 6.6. While the controller formulations achieve varying degrees of success in achieving the various controller objectives, all strategies successfully implement the framework of Approach 2 to mitigate thermal runaway and maintain consistent reaction zones.

6.4.2 On-Reactor Evaluation of Approaches 1 and 2

Having gained insights into some appropriate weighting schemes for Approaches 1 and 2, the strategies were deployed on the experimental oxidation reactor. Besides the electronics necessary to implement the controller, the only change to the reactor hardware compared to previous on-reactor experiments was the replacement of the 1000 SLPM inlet Alicat gas flow controller with an SMC AR25-N02E-Z-B pressure regulator. Due to the expected variation in the recuperation and extraction flow rates, the pressure regulator required less consistent attention than a flow rate-based input that must be studiously adjusted.

Figure 6.7 depicts input and output signals utilized by the MPC. As previously described in Chapter 3, the five reaction zone type K thermocouples (corresponding to the temperature measurements of $\mathbf{y}$) and the Advanced Micro Instruments oxygen sensors (providing measurements of ξ_C and ξ_A) were connected to a Graphtec GL840 data acquisition system in order to provide input signals to the controller. All other measured signals, including temperatures at either end of the reactor tube, gas flow rates, pressure readings, and the temperature of gas extraction were recorded via the Graphtec system as well. A National Instruments USB-6343 data acquisition system was used to regulate output signals to the solid flow control system, the 500 SLPM Alicat gas flow controller handling the recuperative gas flow, and the 100 SLPM Alicat controller handling the extraction gas flow.

Both the Graphtec and National Instruments devices interfaced with a computer running the "mpc" class from MATLAB®'s Model Predictive Control Toolbox [110]. In order to seamlessly

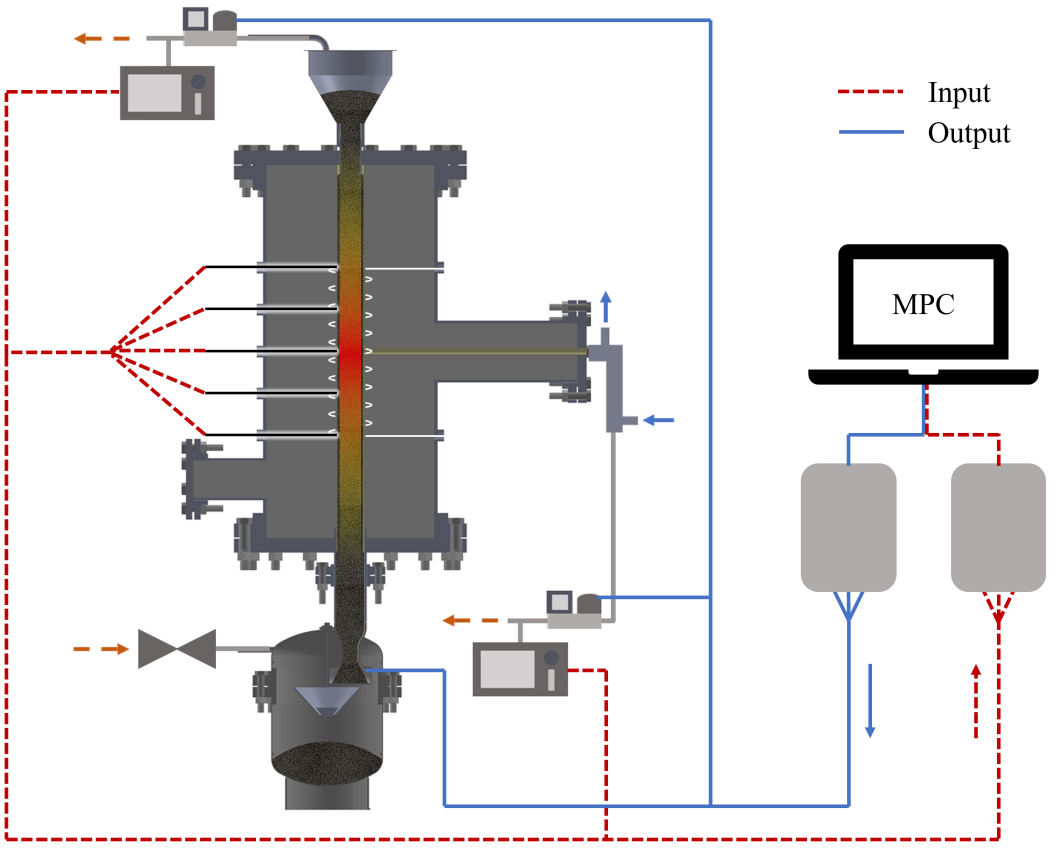

Figure 6.7 Sensors and actuators utilized by the MPC on the experimental setup. Separate DAQs are employed as intermediaries between system inputs (dashed in red) and outputs (in blue) and the controller.

integrate data acquisition signals with MATLAB®'s MPC functionality, the user interface of the control system was built using MATLAB®'s App Designer [112], and system inputs and outputs were handled within a MATLAB® runner script. The user interface deployed in assessing Approaches 1 and 2 is depicted in Figure 6.8. The leftmost panel of the interface contains user-specified parameters for operation, which can be adjusted on the fly as desired. Weights for the reactor inputs, move suppression, and reference tracking of T_C and T_D are shown in the top left corner, while below them lie the operational setpoints of $T_{C,ref}$, $\dot{Q}_{ext,ref}$, and $T_{D,ref}$. Only one constraint, the upper limit for solid flow, can be specified by the interface, although the gas recuperation flow is specified to a limit of one half of this setpoint. The bottom two-thirds of the panel is comprised of an illustration of the 5-zone controller model to provide a visual reference of the various signals.

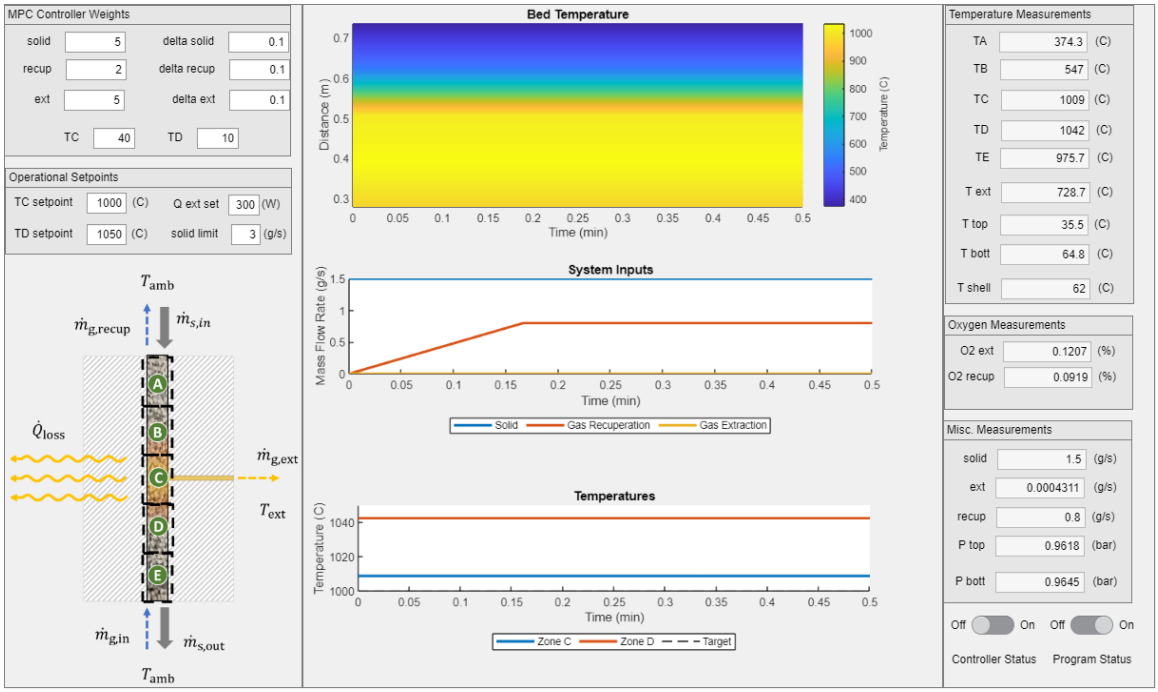

Figure 6.8 The user interface of the MPC for the experimental setup. Running the controller UI through MATLAB® enables easy implementation of functions from the Model Predictive Control Toolbox as well as straightforward networking with various DAQs.

The rightmost sector of Figure 6.8 illustrates the various measurements collected by the Graphtec data logger and passed to the MPC system. These measurements include more than just the outputs that make up $\mathbf{y}$, as additional thermocouples and pressure readings are presented as well. The output values for $\dot{m}_s$, $\dot{m}_{g,recup}$, and $\dot{m}_{g,ext}$ assigned by the MPC are listed under "Misc. Measurements." The central portion of the user interface provides real-time visualizations of system behavior. The familiar five-thermocouple countour plot is located at the top of the section, displaying a linearly-interpolated representation of the current reactor temperature distribution. An illustration of the system input levels is depicted below the contour, and the bottommost plot describes the temperatures of Zones C and D. Plots and measured values throughout the interface were updated every ten seconds, in accordance with the controller period.

The experiment was performed with the same 5.5 mm Mg-Mn-O particles as the latter experiments of Chapter 4. Similar steps were followed to prepare the reactor for operation as those implemented for the Group C on-reactor experiments. The oxidation reactor was filled with room-temperature particles reduced at temperatures of around 1450°C. Once the reactor was full, a small

Quantity	Lower Limit	Upper Limit	Approach 1 Initial Weight	Approach 2 Initial Weight
T_B	-	1000°C	0	0
T_C	-	-	0	40
T_D	-	-	0	10
$\dot{m}_{g,ext}$	0	$2 \times \dot{m}_{g,ext,ref}$	5	5
$\dot{m}_s$	0.75 g/s	3 g/s	5	5
$\dot{m}_{g,recup}$	0.1 g/s	1.5 g/s	2	2
$T_C - T_D$	-	-	10	0
$\Delta(\dot{m}_s)$	-	-	0.1	0.1
$\Delta(\dot{m}_{g,recup})$	-	-	0.1	0.1
$\Delta(\dot{m}_{g,ext})$	-	-	0.1	0.1

Table 6.5 Initial controller weights and constraints for the first on-reactor deployment.

flow of nitrogen gas was initiated and the reactor was preheated to 1000°C. The reactor dwelled at 1000°C for 3.5 hours prior to the onset of the experiment.

Reactor operation can be divided into two control periods. The first encompasses the initial 50 minutes of operation, where Approach 1 was implemented to test the efficacy of the system in matching the temperatures of Zones C and D without regard for other temperature setpoints. The latter half of the experiment leveraged Approach 2, switching to setpoint tracking for T_C and T_D in an attempt to achieve steady operation. Initial weights and constraints for each approach are depicted in Table 6.5. Implemented weights were selected based on the recommendation of previous tuning procedures as summarized by the parametric studies of Sections 6.3.1 and 6.4.1.

Operational results are divided into two distinct figures, each representing one of the implemented control approaches. These figures each contain four different subfigures, with many sharing

similarities with the subfigures common in Chapter 4. Taking Figure 6.9 as an example, the first subplot contains a linearly interpolated contour plot of the five reaction-zone thermocouples over time. Below the contour, in Figure 6.9b, T_C and T_D are shown. Figure 6.9c catalogs the various input values recorded by the system, including the standard volumetric gas flow rates reported as $\dot{V}_{recup}$ and $\dot{V}_{ext}$. An average solid flow rate, $\dot{m}_S$, is calculated for each minute by measuring the first and last mass measurements taken within a 30 second interval on each side. The final subplot recounts the extraction characteristics of the reactor, T_ext (as measured by the extraction thermocouple, not T_C), and $\dot{Q}_{ext}$.

After a slight pause at the onset of operation, Figure 6.9b depicts the controller seeking to match the temperatures of Zones C and D. For an initial bed of reduced particles, the onset of operation is typically characterized by a large, nonlinear release of chemical energy. By maintaining modest solid flow and relatively low recuperative gas flow up to t = 15 min, the controller avoided a single large oxidation event in the bed. Instead, as Figure 6.9a illustrates, the highest recorded reactor wall temperatures occur between t = 20 min and t = 40 min, spreading out the release of the initial chemical energy reservoir. Controller weights were adjusted throughout operation, as can be observed in the dramatic change in the recuperative gas flow at t = 30 min. Over the span of t = 15 min to t = 50 min, the controller showcases excellent minimization of $T_C - T_D$. Even in the face of nonlinear startup dynamics, Approach 1 was successful in relegating the hottest part of the reaction area to Zones C and D, eliminating the possibility of thermal runaway in the upper reaches of the reactor.

Figure 6.10 displays the continuation of the on-reactor experiment utilizing Approach 2. Upon discovering the error in the controller programming that led to the deployment of the modified Approach 1, Approach 2 was applied to the system at approximately t = 50 min, with setpoints of $T_{C,ref}$ = 1000°C, $T_{D,ref}$ = 1050°C, and $\dot{Q}_{ext}$ = 300 W. As illustrated in Figure 6.10b, within fifteen minutes of operation the controller successfully manipulated the system inputs to lower the temperature of Zone C. The remainder of the experiment (between t = 57 min and t = 86 min) showcases excellent tracking of both $T_{C,ref}$ and $T_{D,ref}$. As Figure 6.10 depicts, the temperature

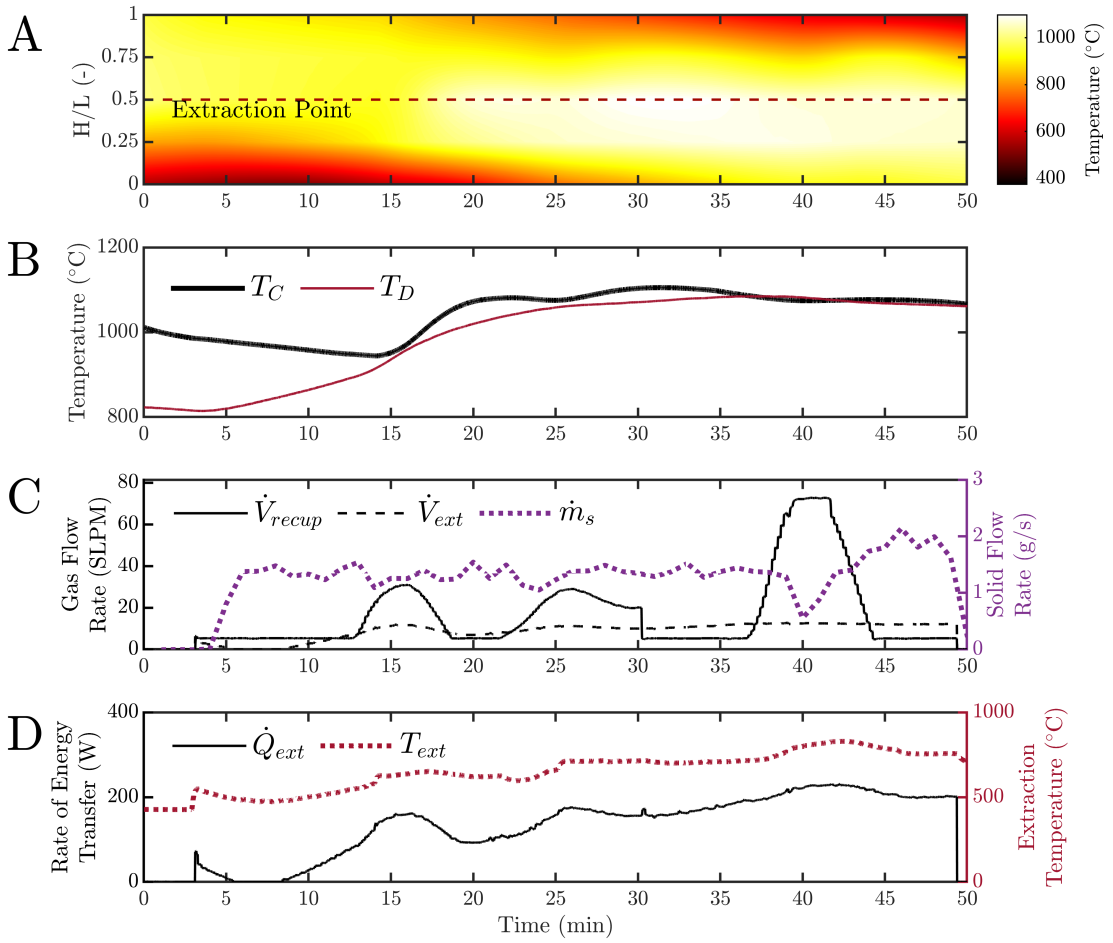

Figure 6.9 Experimental results of the implementation of a modified Approach 1, including (A) Bed temperature contour, (B) Measurements of T_C and T_D, (C) System inputs, and (D) Measured extraction characteristics. The controller successfully achieves its objective of matching T_C and T_D.

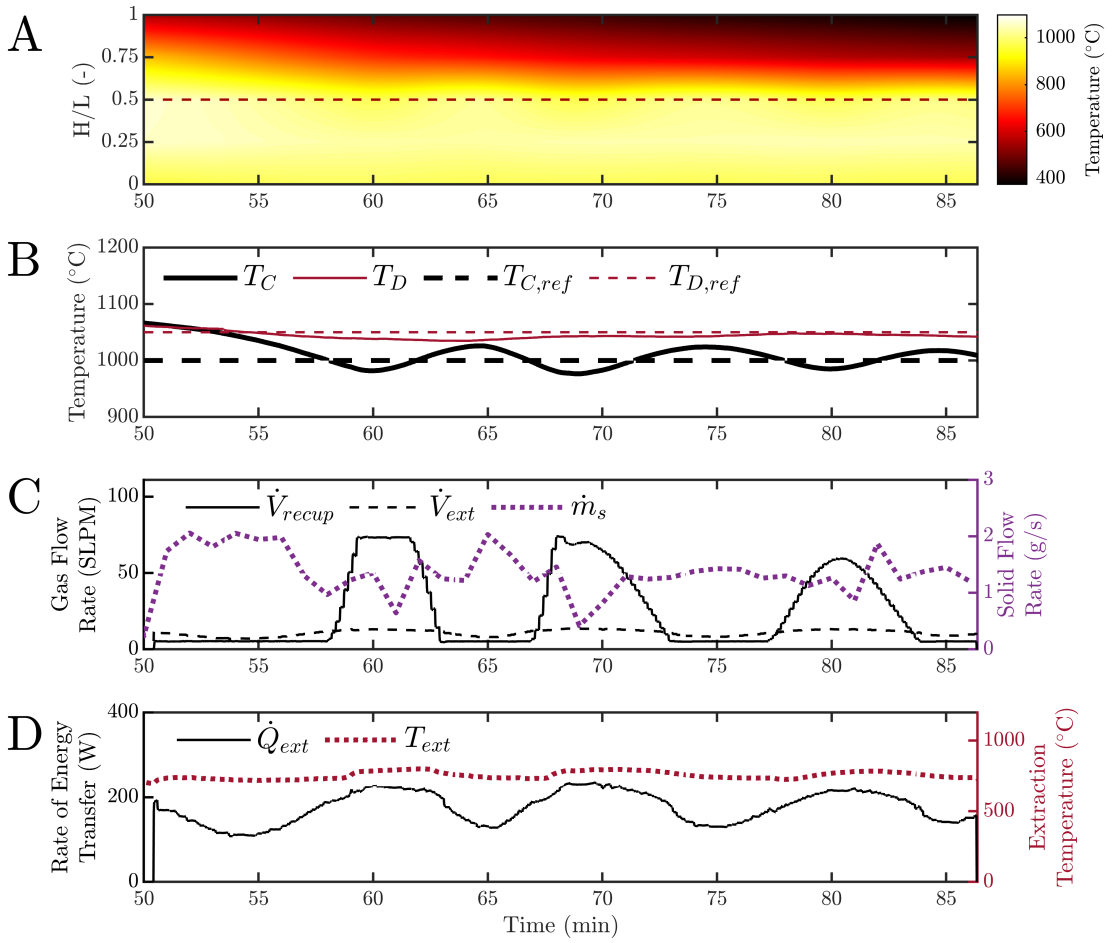

Figure 6.10 Experimental results of the implementation of Approach 2, including (A) Bed temperature contour, (B) Measurements and setpoints for T_C and T_D, (C) System inputs, and (D) Measured extraction characteristics. Approach 2 exhibits excellent setpoint tracking over the course of the experiment.

Interval	T_C (°C)	T_D (°C)	$T_C - T_D$ (°C)	T_{ext} (°C)	$\dot{Q}_{ext}$ (W)
t = 15 to 50 min	N/A	N/A	18.4 ± 16.5°C	711.5 ± 64.5	167.8 ± 44.6
t = 57 to 86 min	1003.1 ± 14.7	1042.1 ± 3.7	N/A	761.1 ± 24.3	185.6 ± 33.2

Table 6.6 Performance metrics from the on-reactor implementation of Approaches 1 and 2.

profile of the reactor follows the desired behavior of Approach 2: the hottest part of the reactor remains positioned below the extraction point for the duration of the experiment. Weights are minimally adjusted throughout the experiment, with values corresponding to the 30-minute period of steady operation of $w_{\dot{m}_s} = 3$, $w_{\dot{m}_{g,recup}} = 2$, $w_{\dot{m}_{g,ext}} = 5$, $w_{T_C} = 40$, and $w_{T_D} = 10$. Although the recuperative gas flow largely follows an on/off profile, Figure 6.10c shows a gradual softening of the input as the experiment progressed, suggesting the approach of a long-duration equilibrium value. The solid flow shows varied behavior as well, albeit adhering better to a moderate value than $\dot{m}_{g,recup}$. $\dot{m}_{g,ext}$ exhibits fluctuations as well, affecting the rate of energy extraction profile of Figure 6.10d.

Performance metrics for Approaches 1 and 2 are shown in Table 6.6. Both approaches showcase excellent performance for their respective goals: Approach 1 achieved equivalence between T_C and T_D within 20°C, while Approach 2 provided average values for T_C and T_D within 10°C of each specified setpoint. The extracted energy, as well as the measured gas extraction temperature T_{ext}, performed well below their specified targets of 300 W and 1000°C, respectively. These discrepancies primarily stem from T_{ext}, as the setpoint for $\dot{m}_{g,ext}$ used to satisfy $\dot{Q}_{ext}$ assumes an extraction temperature of $T_{C,ref}$. Previous experimental results do feature differences between T_C and T_{ext} as well, though not as drastic as the nearly 25% difference observed here. Periodic rises in T_{ext} and $\dot{Q}_{ext}$ correspond to increases in gas flow through the reactor, both from the recuperation and extraction outlets. This observation points to the effect of enhanced convection within the particle bed, which helps to offset the losses experienced along the extraction arm of the setup.

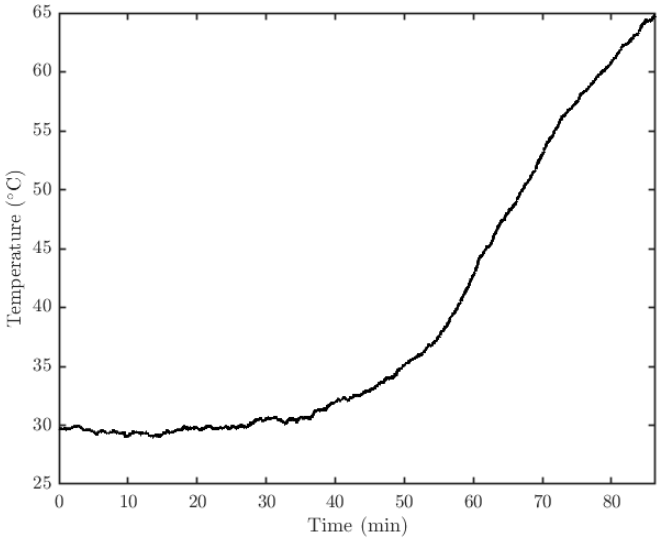

Figure 6.11 Flange temperatures in the bottom of the reactor during the combined testing of Approaches 1 and 2. Elevated temperatures suggest high axial losses, especially as temperatures continue to rise through the end of the experiment.

6.4.3 Evaluation of Approach 2

Setting aside Approach 1 for the moment, Approach 2 showcased excellent experimental control of the oxidation reactor and provided most of the functionality desired of the reactor. Although the measured extraction characteristics fell short of their setpoints, bed temperatures within the reactor remained well-controlled and consistent throughout the experiment. Even without knowing the exact extent of reduction of the incoming solid particles, the system was able to regulate itself and maintained specified temperatures within the reactor.

The shortcomings of this control scheme center on three factors: the size of the reaction zone, the necessity of a solid flow setpoint, and the controller favoring sensible energy sources over chemical ones. The placement of the main reaction zone below the extraction point is an intentional feature of Approaches 1 and 2, meant to improve heat transfer between the solid and gas phases of the system. A separate consequence of this placement is depicted in Figure 6.11. Over the course of the experiment the gas inlet flange temperature, measured where the steel reactor shell is coupled to the collection tank, exhibited a dramatic increase in temperature. This can be directly mapped to the downward shifting of the reaction zone throughout the experiment, in particular as Approach 2

is implemented to provide setpoints for T_C and T_D. The flange temperature shown in Figure 6.11 does not reach a steady value during the operation of the experiment, suggesting that even higher temperatures are possible should Approach 2 be implemented for longer durations. Furthermore, although the lower reaction zone is meant to bolster gas extraction temperatures, the temperature setpoint of $T_{C,ref} + 50°C$ imposed for Zone D does introduce greater losses to the system via radial conduction. Approach 2 does not directly specify to the controller the location of the hottest area of the reactor, which could feasibly lie in Zone E for some operating conditions. A wider, hotter reaction zone introduces higher losses to the system, which by extension does not efficiently utilize the chemical energy of the solid particles passing through. Additional strategies must be explored that seek to maximize the usage of chemical energy from particles.

Another operational downside of Approaches 1 and 2 is the necessity of having heat loss estimates for each zone in order to calculate a reasonable estimate for $\dot{m}_{s,ref}$. $\dot{m}_{g,recup,ref}$ and $\dot{m}_{g,ext,ref}$ both rely on either user-defined setpoints or other system inputs for their determination, whereas $\dot{m}_{s,ref}$ relies on reactor-specific knowledge that may be difficult to estimate for some systems. This shortcoming makes Approaches 1 and 2 less straightforward to apply to different reactor systems, necessitating additional analysis prior to operation in order to determine suitable loss estimations.

Tied to the approximate solid flow setpoint is the final, and perhaps most crucial, disadvantage of the proposed approaches: the MPC favors utilizing sensible energy reservoirs rather than shifting the production of chemical energy. As illustrated in Figure 6.10, during periods where T_C drops below its setpoint the system always responds in the same way: by lowering $\dot{m}_s$ and increasing $\dot{m}_{g,recup}$. Similar behavior is observed throughout Figures 6.4 and 6.6. Although one of the benefits of Approaches 1 and 2 is the establishment of a a thermal reservoir that the system can draw upon as needed, the current control schemes favor the expedient usage of sensible energy to chemical sources in all cases. Such an approach does not favor efficient usage of reduced particles; during oscillations above $T_{C,ref}$, the current control scheme increased the solid flow to convey energy out of Zone C rather than lowering it to conserve particles for future use. An improved controller design

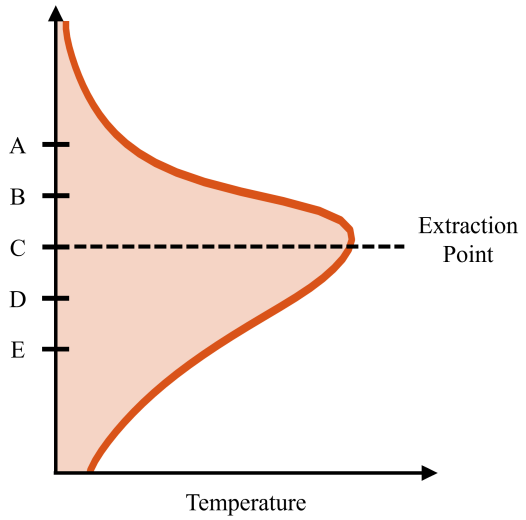

Figure 6.12 Reaction zone positioning for a $\Delta T = T_B - T_D$ tracking control scheme. This approach maximizes the chemical energy of the particles and seeks to minimize system losses.

would favor the adjustment of chemical energy supplies to Zone C instead of utilizing sensible sources.

6.5 Control Approach 3: Minimizing $\Delta T = T_B - T_D$ and Reformulating the System Model

To address the operational shortcomings of the previously considered approaches, a third concept was considered. The emphasis of Approach 3 is on the maximization of chemical conversion of the Mg-Mn-O particles, analogous to minimizing the solid flow rate. For such an approach, the hottest area of the reactor is centered directly over the extraction point, as illustrated in Figure 6.12. To achieve reaction zone centering, Approach 3 implemented a new formulation of the ΔT term of $\mathbf{y}$:

$$\Delta T = T_B - T_D \tag{6.32}$$

Equation 6.32 is analogous to a first-order central finite difference approximation of the axial temperature gradient in Zone C. For $\Delta T = 0$, the controller can verify that the highest recorded temperatures in the reactor occur at the extraction point.

While a revised formulation for ΔT offers greater efficiency in terms of reaction zone placement and loss minimization, the controller will likely still favor shifting sensible energy sources rather than throttling chemical energy production, as observed for Approaches 1 and 2. A novel strategy was

employed for Approach 3 to remove sensible energy considerations from the controller's decision making process. As originally depicted in Equation 6.6, the linearized controller system model employed by the controller considers four effects that impact the temperature of each control zone: sensible energy transfer by the moving particles, sensible energy transfer by the gas phase, radial losses through the reactor tube, and chemical energy release due to oxidation. When minimizing the quantity $T_B - T_D$, as Approach 3 directs the controller to do, the sensible energy transfer across the boundaries of Zone C due to $\dot{m}_s$ and $\dot{m}_{g,recup}$ are approximated as zero, and can thus be omitted from consideration of the linearized dynamics of Zone C. To further refine controller decision making, the impact of changes to $\dot{m}_{g,ext}$ on the temperature of Zone C is removed as well. Removing this functionality ensures that the controller will not seek to adjust the extraction gas flow to achieve a desired temperature setpoint, instead opting solely to adjust the solid flow rate. The remaining energy balance for the extraction zone is:

$$\left(m_s c_{p,s} + m_g c_{p,g}\right) \frac{\partial T_i}{\partial t} = \frac{V_s \left(\rho_{ox} - \rho_{red}\right) \Delta H_{rxn}}{M_{O_2}} \left(\frac{\partial \alpha_s}{\partial t}\right)_{RXN,i} - 2\pi \Delta x k_{ins} \frac{T_i - T_{amb}}{\ln\left(r_{out} - r_o\right)} \quad (6.33)$$

During the linearization procedure, the derivative of the chemical reaction term is not considered with respect to the oxygen mass fraction of the system, eliminating the final mechanism by which the controller could use an input other than the particle flow rate to adjust the temperature of Zone C. All other zones retain the full formulation of Section 6.2, and the complete linearized model employed by the controller can be found in the Appendix.

6.5.1 Parametric Tuning Study for Approach 3

Similar to the previous two approaches, a number of iterative, trial-and-error approaches were employed throughout the tuning of Approach 3. A summative parametric study was performed to quantify the behaviors of these investigations. Tuning parameters for the simulations are listed in Table 6.7. While the constraints on T_B, $\dot{m}_{g,ext}$, and $\dot{m}_{g,recup}$ remained consistent from the previous investigations, the bounds for $\dot{m}_s$ were altered to values of 0.25 g/s and 2 g/s. The lower limit in particular was reduced to provide the controller leeway in slowing the particle bed to decrease

Quantity	Target	Lower Limit	Upper Limit	Weights
T_B	-	-	$T_{C,ref}$	0
T_C	$T_{C,ref}$	-	-	20, 40
$\dot{m}_s$	-	0.25 g/s	2 g/s	0
$\dot{m}_{g,ext}$	$\frac{\dot{Q}_{ext,ref}}{c_{p,g}\left(T_{C,ref}-T_{amb}\right)}$	0	$2 \times \dot{m}_{g,ext,ref}$	10
$\dot{m}_{g,recup}$	$\frac{c_{p,s}}{c_{p,g}}\dot{m}_s - \dot{m}_{g,ext}$	0.1 g/s	2.5 g/s	0, 0.1, 0.5, 2
$T_B - T_D$	0	-	-	0.1, 0.5, 2, 5, 10, 20
$\Delta\left(\dot{m}_s\right)$	N/A	-	-	0, 0.1, 0.5
$\Delta\left(\dot{m}_{g,recup}\right)$	N/A	-	-	0, 0.1, 0.5
$\Delta\left(\dot{m}_{g,ext}\right)$	N/A	-	-	0.1

Table 6.7 Tuning parameters for the parametric evaluation of Approach 3.

reactor temperatures. Move suppression weights and $w_{\dot{m}_{g,ext}}$ featured their previously considered values, with the most prominent weighting studies considering $\dot{m}_{g,recup}$ and $T_B - T_D$. T_C was evaluated at high weights of 20 and 40. Several values of move suppression weights for $\dot{m}_s$ and $\dot{m}_{g,recup}$ were considered as well.

The parametric evaluation employed the same controller properties listed in Table 6.3, including initial setpoints for $T_{C,ref}$ and $\dot{Q}_{ext,ref}$ of 1000°C and 500 W, respectively, followed by 1050°C and 300 W for the second half of each simulation. The initial nominal operating point of the MPC was identical to that established in Section 6.3.1 for Approach 1. The controller was once again deployed on the computational model of Chapter 5 utilizing the previously established boundary conditions and all of the same initial conditions but one: the particles stationed in the main reaction zone began in the fully oxidized state. The parametric investigations for Approaches 1 and 2 considered a bed of unreacted particles, in line with previous bench-scale oxidation experiments. A more accurate use-case for the reactor, however, is to begin operation with a reaction zone full

of oxidized particles. If the system is operated intermittently to produce extraction gases only as needed, there will likely be long periods of time when the reactor sits idle. During this time particles in the high temperature zone will oxidize, necessitating the introduction of fresh particles to begin the extraction process anew. Experiment 5 from Chapter 4 proved that such a startup procedure is possible on the oxidation reactor, and the evaluations of Approach 3 further utilized this initial condition for the extent of conversion.

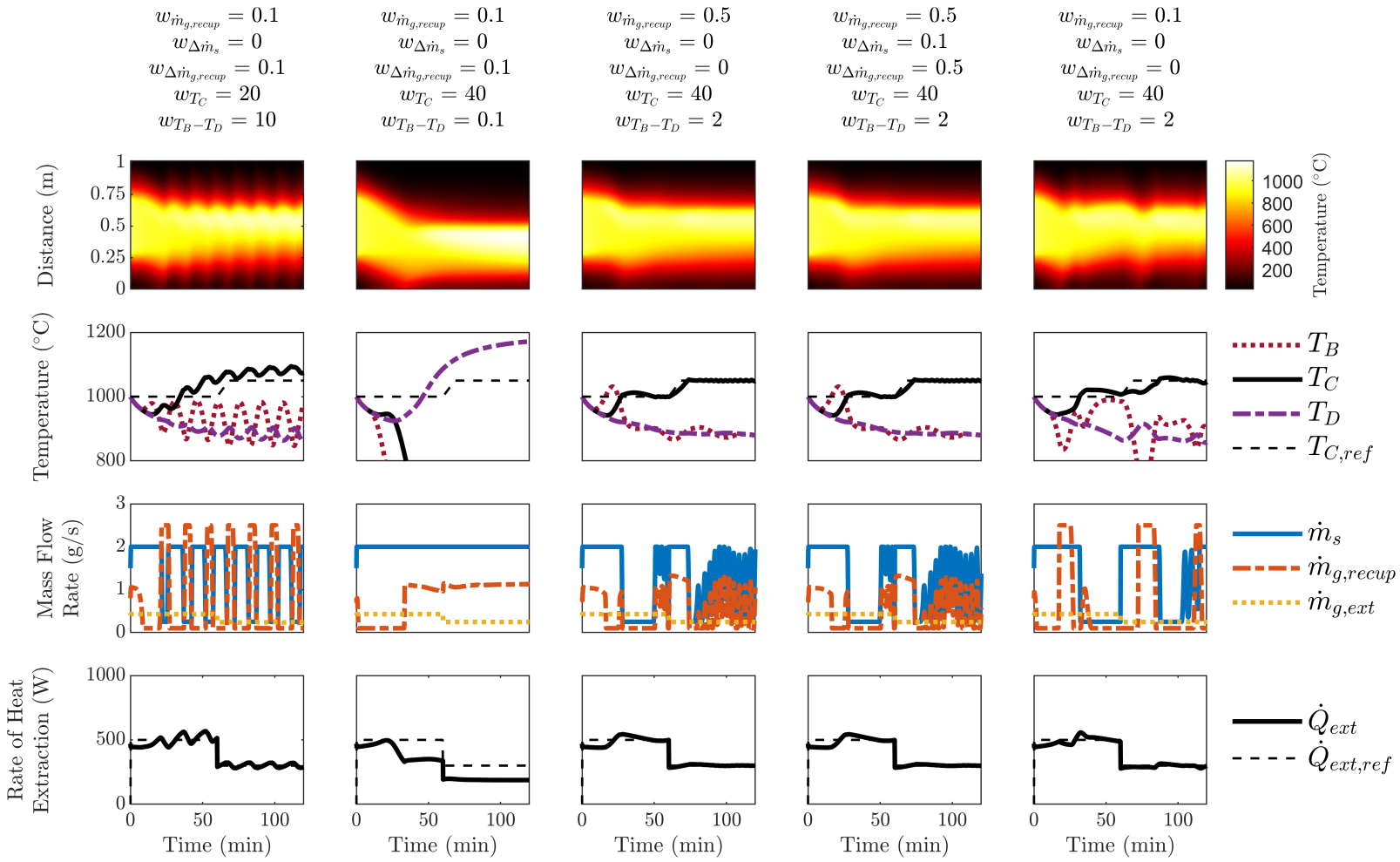

Figure 6.13 Select results from the parametric tuning procedure with a $T_B - T_D$ tracking control scheme. Subplots include a temperature contour for T_w, measurements and tracking for T_B, T_C and T_D, system input values, and tracking results for $\dot{Q}_{ext}$, from top to bottom.

The parametric study confirmed the applicability of Approach 3 for regulating reactor operation. As with the previously explored approaches, several parametric cases are selected to illustrate the effect of different weighting strategies; these five examples are depicted in Figure 6.13. Figure 6.13 is once again formatted in the style of Figure 6.4, this time including both T_B and T_D in the second row of subplots. By utilizing the revised initial condition for extent of conversion, all simulated trials depict an initial decrease in the temperature of the reactor prior to feeding fresh particles into the reaction zone. The first case emphasizes the importance of prioritizing the temperature of Zone C over matching T_B and T_D. When the weight for $T_B - T_D$ is comparable to that of T_C the controller produces strongly oscillatory behavior, as shown in the temperature contour of the first simulation of Figure 6.13. Furthermore, the MPC underperforms in tracking the setpoints for T_C. However, undervaluing the temperature difference term leads to poor performance as well. The sensible energy balance assumption of Section 6.5 means that the controller must ensure sufficient recuperative gas flow in order to maintain operation - a directive that is largely ignored in the second set of results in Figure 6.13. With $w_{T_C} = 40$ and $w_{T_B-T_D} = 0.1$, matching the temperatures of Zones B and D is not a priority for the MPC, which ignores the need for additional recuperation gas. The solid flow remains notably high for the duration of the simulation, as the controller attempts to raise the temperature of the reaction zone in the only way it is able. Tracking of $T_{C,ref}$ and $\dot{Q}_{ext,ref}$ suffer as a result, and the reaction zone falls below the reactor extraction point.

The third case presented in Figure 6.13 emphasizes the modulating effect of $w_{\dot{m}_{g,recup}}$. With a value of 0.5, the weight for the gas flow competes with the minimization of $T_B - T_D$ for priority in the controller's calculations. This leads to fewer periods of long on/off behavior, instead producing a mores responsive controller implementing smaller oscillations more regularly. The tuning strategy produces effective results for both T_C and $\dot{Q}_{ext}$, exhibiting excellent setpoint tracking and flexibility in reaching revised targets for both quantities partway through the simulation. The behavior of the fourth simulation case appears very much like its predecessor; it retains the same values for $w_{\dot{m}_{g,recup}}$, w_{T_C}, and $w_{T_B-T_D}$, with the only difference being higher move suppression weights. These are observed to have only a small effect on overall system behavior, succeeding in producing smaller

oscillations among the input values but little change to overall reactor performance. Both the third and the fourth cases showcase excellent reaction zone stability, with good matching between T_B and T_D and consistent thermal gradients throughout the experiment.

The fifth and final case depicts a slightly more aggressive approach than its predecessors, with larger swings in recuperative gas flow. $w_{\dot{m}_{g,recup}}$ and $w_{T_B-T_D}$ are reduced in comparison to the other high-performing cases, while w_{T_C} is maintained at its elevated value. The MPC underperforms its predecessors, both in terms of $T_{C,ref}$ tracking and $T_B - T_D$ minimization, with larger overshoots and larger fluctuations between T_B and T_D. Nevertheless, over long durations the strategy is still able to successfully regulate the operation of the oxidation reactor.

6.5.2 On-Reactor Evaluation of Approach 3

An on-reactor experiment was conducted to assess the effectiveness of Approach 3. Although the experiment for the most part followed the procedure of Section 6.4.2, several modifications were implemented. First, the MATLAB® user interface was updated with additional functionality. The revised interface is depicted in Figure 6.14. The primary changes to the program can be found in the leftmost panel: minimums and maximums for $\dot{m}_s$ and $\dot{m}_{g,recup}$ can be specified in real-time rather than as hard-coded values in the controller. In addition, the entry field for w_{T_D} was removed, replaced by the "dTdx" field, which represents the spatial derivative of the temperature in Zone C analogous with $T_B - T_D$. The final component added to the controller interface was a real-time measurement of $\dot{Q}_{ext}$ based on the extraction thermocouple temperature. All other functionality was retained from the previous formulation.

In order to better track the controller's behavior and performance, the MATLAB® code was further adjusted to record controller weights and constraints for each sampling period. The initial values selected for the experiment are listed in Table 6.8. The controller was directed to pursue an aggressive approach to tracking $T_{C,ref}$, with a much higher w_{T_C} than $w_{T_B-T_D}$. The weights selected were the result of the numerous tuning simulations and evaluations represented by the parametric study of Section 6.5.1. To begin the experiment, 5.5 mm Mg-Mn-O particles were once again loaded into the oxidation reactor. Oxidized particles (with no stored chemical energy) were added

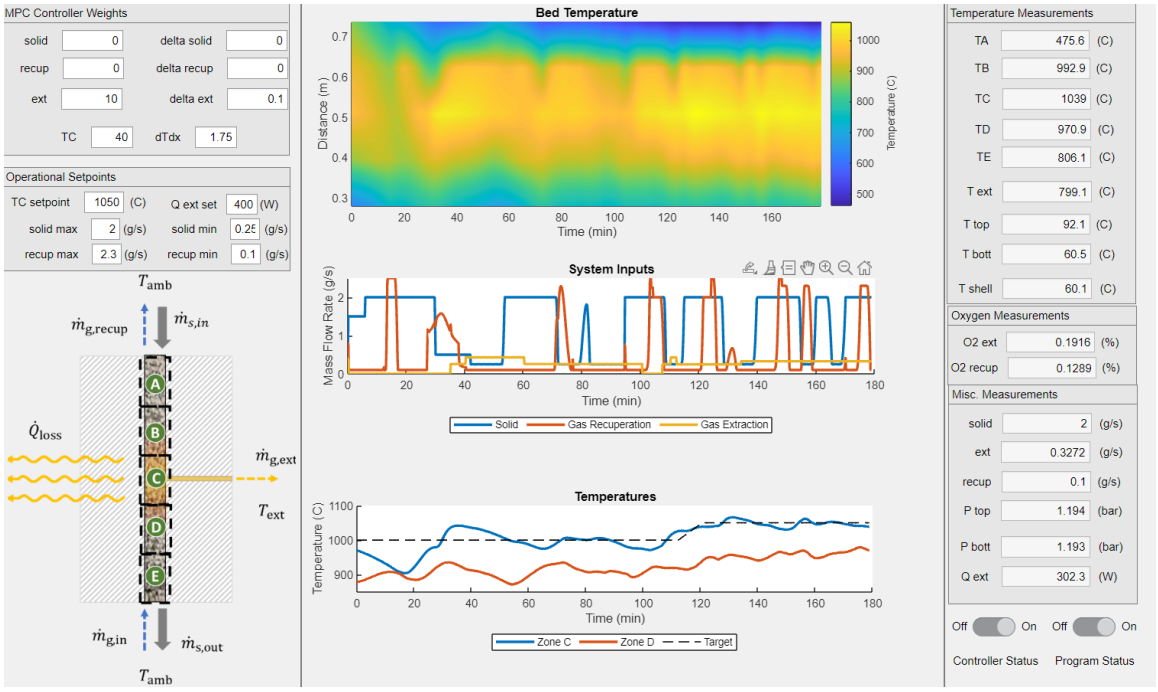

Figure 6.14 The revised user interface of the MPC for the experimental setup. Additional weights and limits are available beyond those offered in the first iteration of Figure 6.8.

until the main reaction zone was full, after which reduced particles comprised the remainder of the particle bed. In contrast to the experiment evaluating Approaches 1 and 2, the particle bed was allowed to ramp up to 1000°C without a nitrogen counterflow, ensuring a fully converted state for all particles in the reaction zone. The system was pressurized to an operating pressure of approximately 1.4 bar for the ensuing experiment.

Figure 6.15 depicts the operational performance of the over three hour long oxidation experiment. Due to the oxidized condition of the bed particles at the onset of the experiment, $\dot{Q}_{ext.ref}$ was set to zero until the reactor was able to reach the desired T_C of 1000°C. As Figures 6.15a and b depict, temperatures in the bed initially declined while reduced particles were slowly introduced to the system. The reactor operates $\dot{m}_s$ it its maximum allowable value to expedite the introduction of chemical energy into the system. Following the overshoot of $T_{C,ref}$ around t = 40 min, the controller feeds fewer solid particles. Due to the restriction of the minimum solid flow rate, the extraction setpoint was increased to help cool down Zone C more quickly. Returning the controller to $\dot{Q}_{ext,ref}$ = 300 W produces over 20 minutes of favorable setpoint tracking for T_C; at the same

Quantity	Lower Limit	Upper Limit	Approach 3 Initial Weight
T_B	-	1000°C	0
T_C	-	-	40
$\dot{m}_{g,ext}$	0	$2 \times \dot{m}_{g,ext,ref}$	10
$\dot{m}_s$	0.75 g/s	1.5 g/s	0
$\dot{m}_{g,recup}$	0.1 g/s	2 g/s	0.1
$T_B - T_D$	-	-	0.75
$\Delta(\dot{m}_s)$	-	-	0
$\Delta(\dot{m}_{g,recup})$	-	-	0
$\Delta(\dot{m}_{g,ext})$	-	-	0.1

Table 6.8 Initial controller weights and constraints for the second on-reactor deployment.

time, as Figure 6.15b illustrates, T_B and T_D are regulated to modestly track one another. Operation of the reactor ceased at t = 92 min so that additional particles could be added to the system. All mass flows were set to zero, and the system was depressurized for approximately 8 min as new reduced particles were added and oxidized particles were drained from the bottom of the reactor.

Following the repressurization of the system to approximately 1.4 bar, the reactor resumed operation. Similar to the initial conditions of the experiment, the reaction zone was expected to experience continued oxidizing during the particle loading process, leading to an oxidized reaction zone. As Figure 6.15b shows, T_C experiences a decrease during the first ten minutes of resumed operation. The rate of energy extraction was decreased to zero to aid the reactor in recovering high-temperature operation. At t = 120 min, a new temperature setpoint of $T_{C,ref}$ = 1050°C was set, prompting the reactor to flow particles at a high rate to supply additional chemical energy for the system. After some time operating at 1050°C, $\dot{Q}_{ext,ref}$ was set to 500 W. The controller

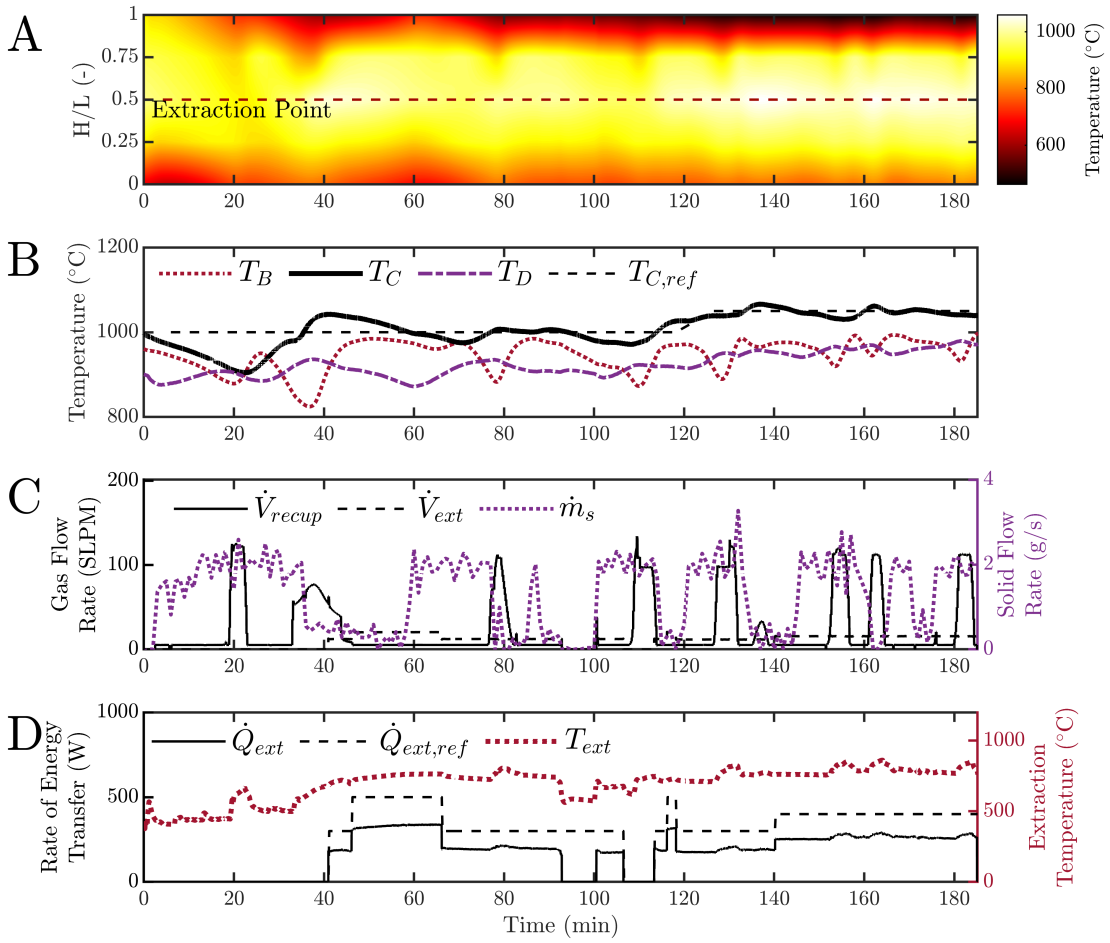

Figure 6.15 Experimental results of the implementation of Approach 3, including (A) Bed temperature contour, (B) Measurement and tracking for T_B, T_C, and T_D, C) System inputs, and D) Measured extraction characteristics. The MPC successfully regulates the reaction zone to remain in the center of the reactor while tracking $T_{C,ref}$.

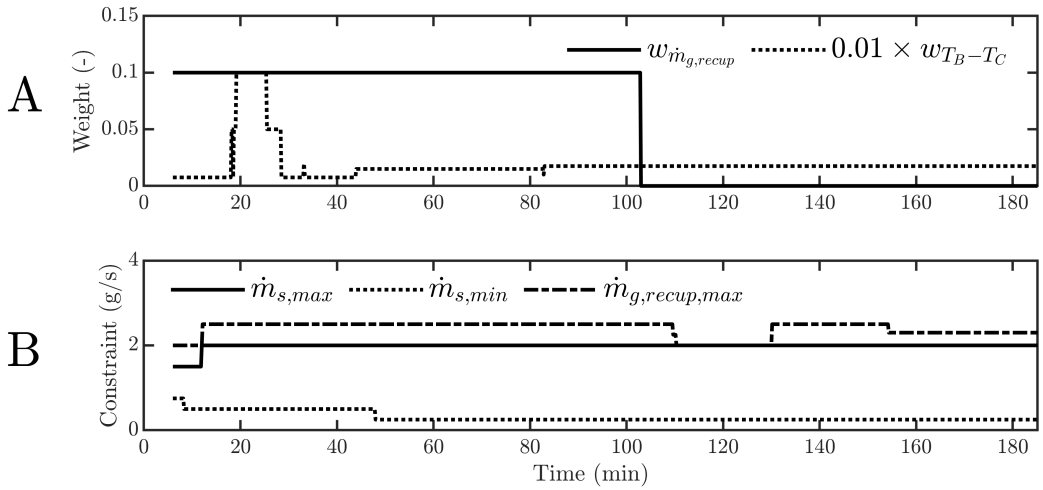

Figure 6.16 Controller characteristics manipulated over the course of the experiment including (A) Weights and (B) Constraints.

responded by flowing additional particles, resulting in excellent setpoint tracking for T_C even with an increased energy demand. The MPC produced improved matching between T_B and T_C while operating at 1050°C as well. After over three hours of operation, the reactor finally ran out of particles and the experiment concluded.

Most controller weights and constraints remained constant throughout the experiment, but those that were changed via the user interface are recorded in Figure 6.16. As Figure 6.16a illustrates, $w_{\dot{m}_{g,recup}}$ was reduced to zero shortly after the reactor was repressurized, and $w_{T_B - T_D}$ underwent some initial fluctuations before a final value of 1.75 was selected. These changes were made to improve the minimization of $T_B - T_D$ and to allow the controller greater flexibility in its usage of $\dot{m}_{g,recup}$ - as a result, however, gas flow in the reactor experienced long periods of on/off status rather than shorter bursts. The constraints of 6.16b showcase the wider functionality provided to the controller as the experiment progressed. By decreasing the solid flow minimum and increasing the solid and gas maximum flows, the MPC could take more drastic action to regulate the system to match the desired operational profile.

Without the benefit of setpoint tracking for $\dot{m}_s$, the results of Figure 6.15 generally showcase more irregularity and less smooth tracking of $T_{C,ref}$ compared to Figure 6.10. Even so, the controller still performs well in regulating the temperature of Zone C. Two distinct operational

Interval	T_C (°C)	$T_B - T_D$ (°C)	T_{ext} (°C)	$\dot{Q}_{ext}$ (W)
t = 35 to 92 min	1007.7 ± 19.4	40.8 ± 56.6	735.7 ± 39.4	222.6 ± 98.5
t = 133 to 185 min	1047.9 ± 9.4	9.1 ± 23.4	787.9 ± 30.2	254.0 ± 27.7

Table 6.9 Performance metrics from the on-reactor implementation of Approach 3.

periods are identified: reaching and operating at 1000°C (spanning t = 35 to 92 min), and reaching and operating at 1050°C (spanning t = 133 to 185 min). Performance metrics for these two intervals are listed in Table 6.9. The controller achieves tight temperature tracking in Zone C comparable to the functionality of Approach 2, and the increase of $w_{T_B-T_D}$ and decrease of $w_{\dot{m}_{g,recup}}$ appear to bolster the minimization of $T_B - T_D$. While the average extraction temperatures lie over 250°C short of T_C over the same intervals, the difference between average values of T_{ext} for the two periods suggests that increasing T_C from 1000°C to 1050°C has an analogous effect on the extraction temperature. Due to the discrepancy between T_{ext} and T_C, the average measurements of $\dot{Q}_{ext}$ differ from those of $\dot{Q}_{ext,ref}$ throughout the experiment.

6.5.3 Evaluation of Approach 3

Considering the second on-reactor control experiment as a whole, Approach 3 performed well in achieving specified temperatures for the extraction zone of the reactor while maximizing chemical energy usage. Figure 6.15a makes clear that T_C is the highest recorded temperature in the reactor system during on-reactor operation, ensuring that particles flowed through the system only as necessary to satisfy minimum energy requirements. Comparisons between Approach 2 and Approach 3 using the performance metrics of Tables 6.6 and 6.9 emphasize the advantages of the different methods. During the sampled operational interval of Approach 2, an average rate of 1.27 g/s of particles was supplied to the reactor to maintain T_C = 1003.1 ± 14.7°C and $\dot{Q}_{ext}$ = 185.6 ± 33.2 W. For Approach 3, the average value of $\dot{m}_s$ utilized to produce T_C = 1007.7 ± 19.4°C and $\dot{Q}_{ext}$ = 22.6 ± 98.5 W over the course of nearly an hour was 0.94 g/s. Furthermore, Approach 3 utilizes a comparable solid flow rate to Approach 2, 1.28 g/s, to supply a temperature

of 1047.9 ± 9.4°C in Zone C and an extraction rate of 254.0 ± 27.7 W. Such results suggest that Approach 3 is the favorable method for maximizing solid particle usage and minimizing system losses. Approach 2 does outperform Approach 3 regarding extraction temperature at a specified T_C, with the schemes producing gas measured at 761.1 ± 24.3°C and 735.7 ± 39.4°C, respectively. The additional high-temperature length below the extraction point appears to bolster heat transfer to the gas extraction flow in Approach 2, although the relatively small amount of extracted energy still means that losses reduce the experimentally measured T_{ext} to a lower value than T_C.

Approach 3 provides not only sufficient setpoint tracking in multiple categories, but the control strategy also exhibits excellent flexibility and adaptibility to adverse operating conditions. The MPC is able to handle the "unexpected" initial condition of having a reaction zone full of oxidized particles by increasing the solid flow rate and eventually maintaining consistent temperatures. At multiple points throughout the second on reactor experiment, the recuperation oxygen sensor was observed to have disconnected as well. Even without exact data, the controller succeeded in steering operation with insufficient output measurement. In addition, all three approaches considered experimentally received an erroneous value for the oxygen mass fraction of Zone E - rather than the assumed mass fraction of air of 0.23197, ξ_E was provided an output value of zero. The advective smoothing approach of the controller ensured that this user-error did not adversely impact the state estimation and behavior of the controller.

Due in part to lacking $\dot{m}_s$ tracking, Approach 3 did not maintain as consistent of a solid flow rate as Approach 2, producing a more jagged temperature distribution in the bed and periods of on/off behavior for the particle flow. Further tuning is anticipated to help address these occurrences.

6.6 Additional Controller Considerations

The three control approaches described in this chapter provide several proven options for regulating the behavior of the direct-contact thermochemical oxidation reactor. Each control scheme provides unique functionality to the system, with Approach 1 emphasizing agreement between T_C and T_D, Approach 2 maintaining elevated temperatures in Zones C and D, and Approach 3 successfully throttling the solid flow rate to dictate reaction zone temperatures. All three of these

approaches make use of a first-principles, linearized system model to dictate controller behavior. This procedure allows for the same framework to be deployed on various reactor shapes, sizes, and thermochemical storage materials, in contrast to most investigations in the literature that develop simplified reactor-specific models through on-reactor parameter identification studies.

Such an advantage, however, loses its potency if the conservation equations utilized by the controller model make inappropriate assumptions or misrepresent thermophysical properties of the system. One simplification in particular has a readily observable effect on the behavior of the oxidation reactor: the assumption of thermal equilibrium between the solid, gas and wall phases utilized in the linearized reactor model employed by the MPC for all three proposed approaches. The model formulation of Section 6.2 assumes a single, average temperature for all phases of the reactor in a given zone. In contrast, the higher-fidelity computational model of Chapter 5 considers each phase individually, linking the various temperatures by means of several heat transfer coefficients. The difference between these two approaches is illustrated in Figure 6.17, which revisits the second controller tuning simulation from Section 6.4.1. This particular case, with $w_{\dot{m}_s} = 2$, $w_{\dot{m}_{g,recup}} = 0.5$, $w_{T_C} = 40$, $w_{T_D} = 10$, and move suppression weights of 0.1, exhibits oscillatory reaction zone behavior useful for comparing solid and gas behavior to that of the reactor tube wall.

Figure 6.17 is comprised of three contour plots, listed from top to bottom as the solid, gas, and wall temperatures of the simulation. The wall temperature contour matches its original characterization from Figure 6.6, but drastic differences can be observed between the wall temperature and its two peers. First, the solid and gas phases exhibit higher temperatures than the tube wall. More notable, though, is the jaggedness of the solid and gas temperature profiles in comparison to that of the wall. Both of these observations can be attributed to the high rate of heat transfer between the solid and gas phases and the comparatively lower transfer between these phases and the reactor wall. The contents of the reactor tube respond quickly to changes to the system inputs, while wall temperatures experience a delay and general feature a smoother profile governed by conduction. While future MPC strategies may seek more accurate temperature measurements throughout the interior of the oxidation reactor, obtaining such measurements may prove challenging. Even though

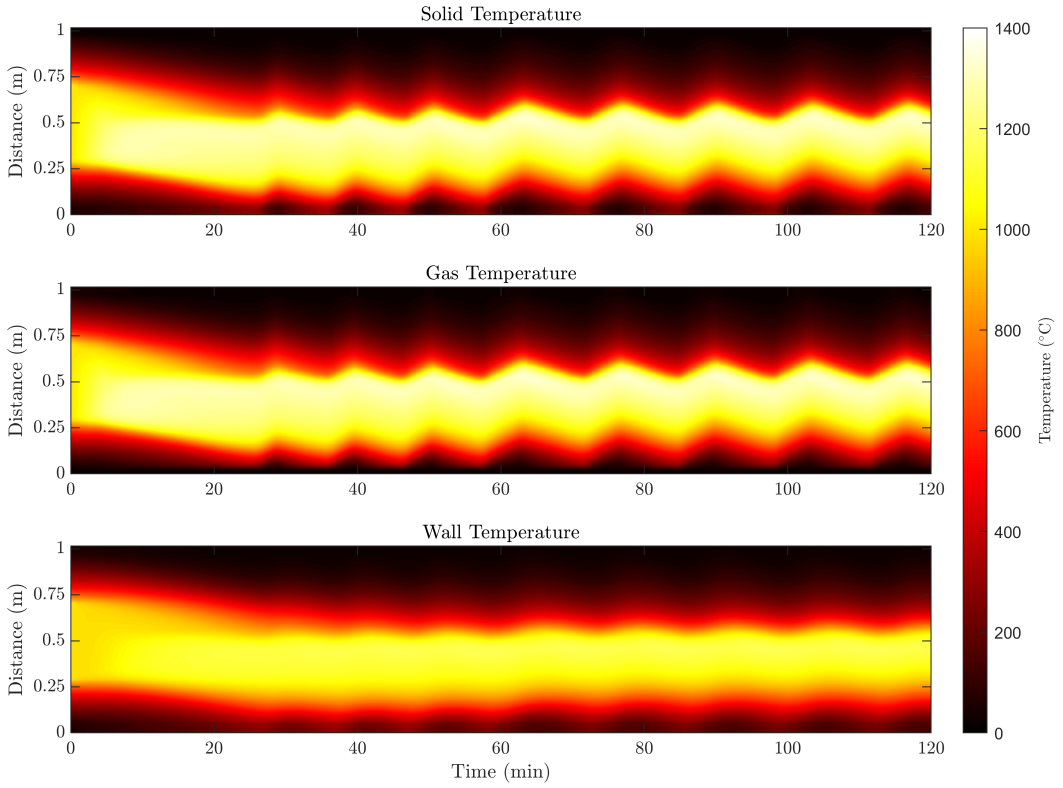

Figure 6.17 A comparison between (A) Solid temperatures, (B) Gas temperatures, and (C) Wall temperatures for simulated reactor operation. Fluctuations in the reactor tube are more muted than those occurring within the particle bed.

the thermal equilibrium assumption within each reactor zone does not truly map system behavior, it still has allowed the MPC to achieve reasonable results.

Other considerations for future thermochemical MPC designs may consider controller properties not rigorously evaluated in this work: the controller sampling period T_s, the control horizon h_c, and the prediction horizon h_p. While these quantities are important to controller formulation, conventional tuning practices advise against adjusting them while determining suitable controller weights. The values of $T_s = 10$, $h_c = 1$, and $h_p = 20$ were initially selected for various reasons, including hardware limitations, to encourage conservative controller behavior, and to maintain the default value provided by MATLAB®, respectively. A short computational investigation was performed to retroactively determine how such system properties could impact future reactor MPC development. The second case of Section 6.4.1 was once again used as a baseline case due to the

Trial	T_s (s)	h_c	h_p
Baseline	10	20	1
1	10	20	5
2	10	20	10
3	5	20	1
4	30	20	1
5	60	20	1
6	10	10	1
7	10	30	1

Table 6.10 Performance metrics from the on-reactor implementation of Approach 3.

presence of strong oscillatory behavior. Parameters for the computational investigations are listed in Table 6.10.

The simulations were run using the same profile as the baseline case, with the only changes being to T_s, h_c, or h_p individually in each case. Results from the controller period simulations (Trials 3, 4, 5, and the baseline) are illustrated in Figure 6.18. Perhaps as expected, increasing the sampling period harms the performance of the reactor. Longer controller timesteps require the MPC to predict behavior for conditions that deviate more and more from the current operating conditions upon which the linearized model is based. The ineptitude of such a long period is on full display for the T_s = 60 s case, where the controller is unable to achieve any setpoint tracking. In contrast, at T_s = 5 s, half of the value previously utilized throughout this work, the controller showcases far weaker oscillatory behavior than its usual formulation. Such a low sampling period was not implemented on the experimental setup in order to avoid wear to the gas flow controllers.

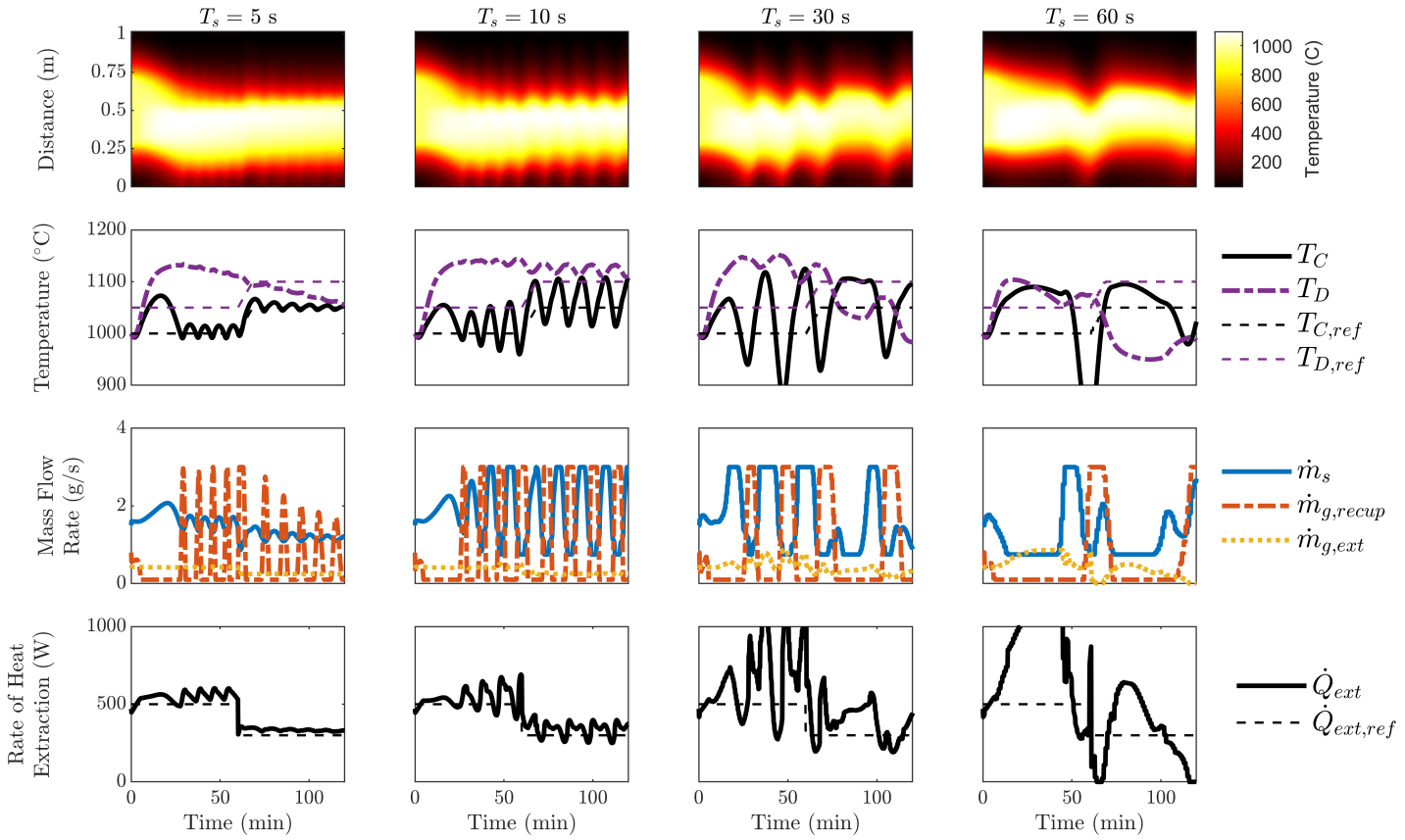

Figure 6.18 Simulated results of the impact of T_s, depicting decreasing controller functionality for higher sampling periods. Subplots include a temperature contour for T_w, measurements and tracking for T_C and T_D, system input values, and tracking results for $\dot{Q}_{ext}$, from top to bottom.

The control horizon study, as shown in Figure 6.19, does not exhibit a strong affect on controller performance, aside from an increase in the temperature of Zone D. The oscillatory behavior of T_C remains largely consistent across all three cases considered. h_p, on the other hand, showcases similar trends to those observed for T_s. With a lower prediction horizon, the controller operates closer to the nominal linearization point and can better regulate system behavior. The $h_p = 10$ case of Figure 6.20 depicts much better tracking for $T_{C,ref}$ than the $h_p = 30$ case, although all cases presented succeed in placing the reaction zone in the desired position. These insights regarding T_s, h_c, and h_p will help to inform future controller strategies for the oxidation reactor.

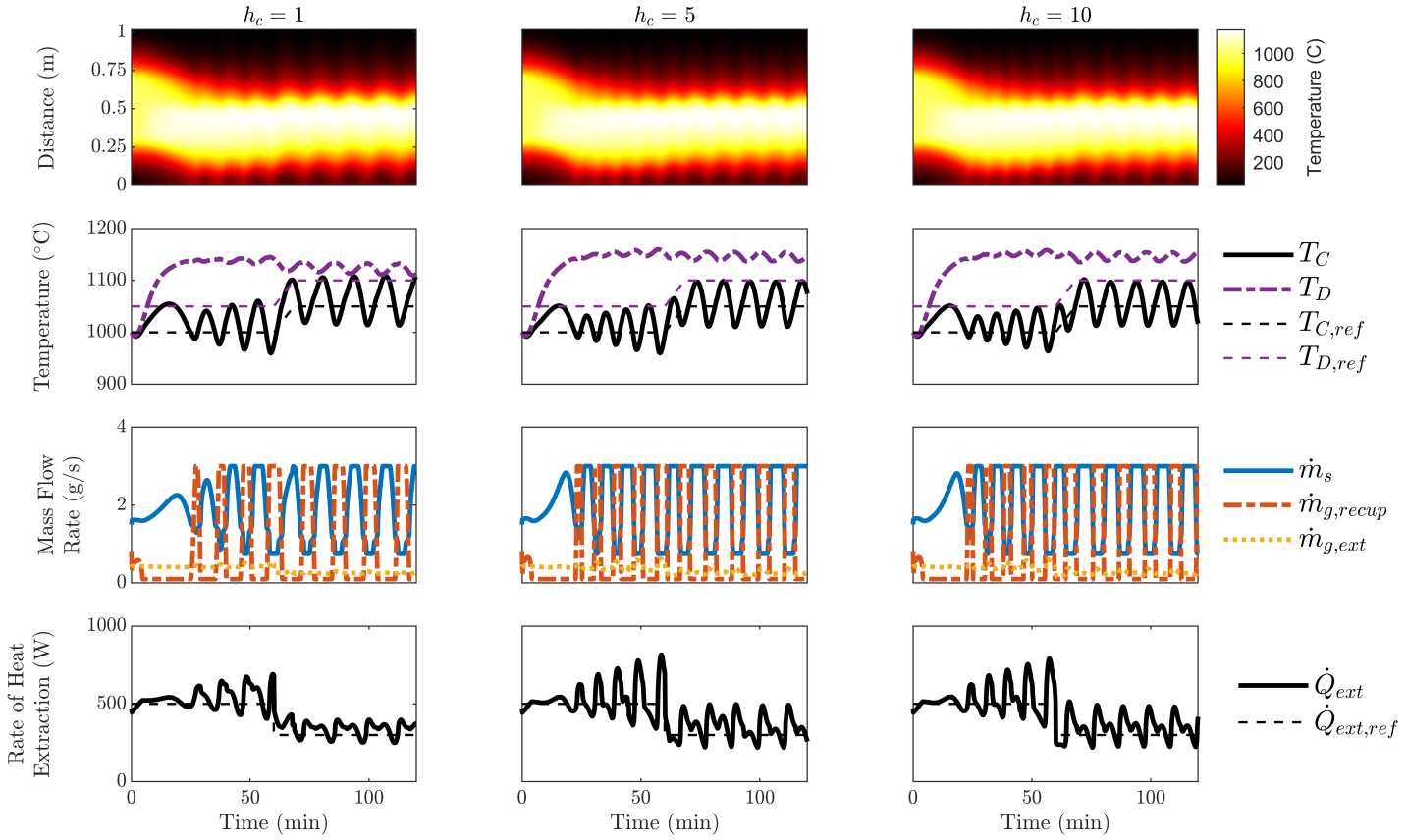

Figure 6.19 Simulated results of the small impact of h_c on controller performance. Subplots include a temperature contour for T_w, measurements and tracking for T_C and T_D, system input values, and tracking results for $\dot{Q}_{ext}$, from top to bottom.

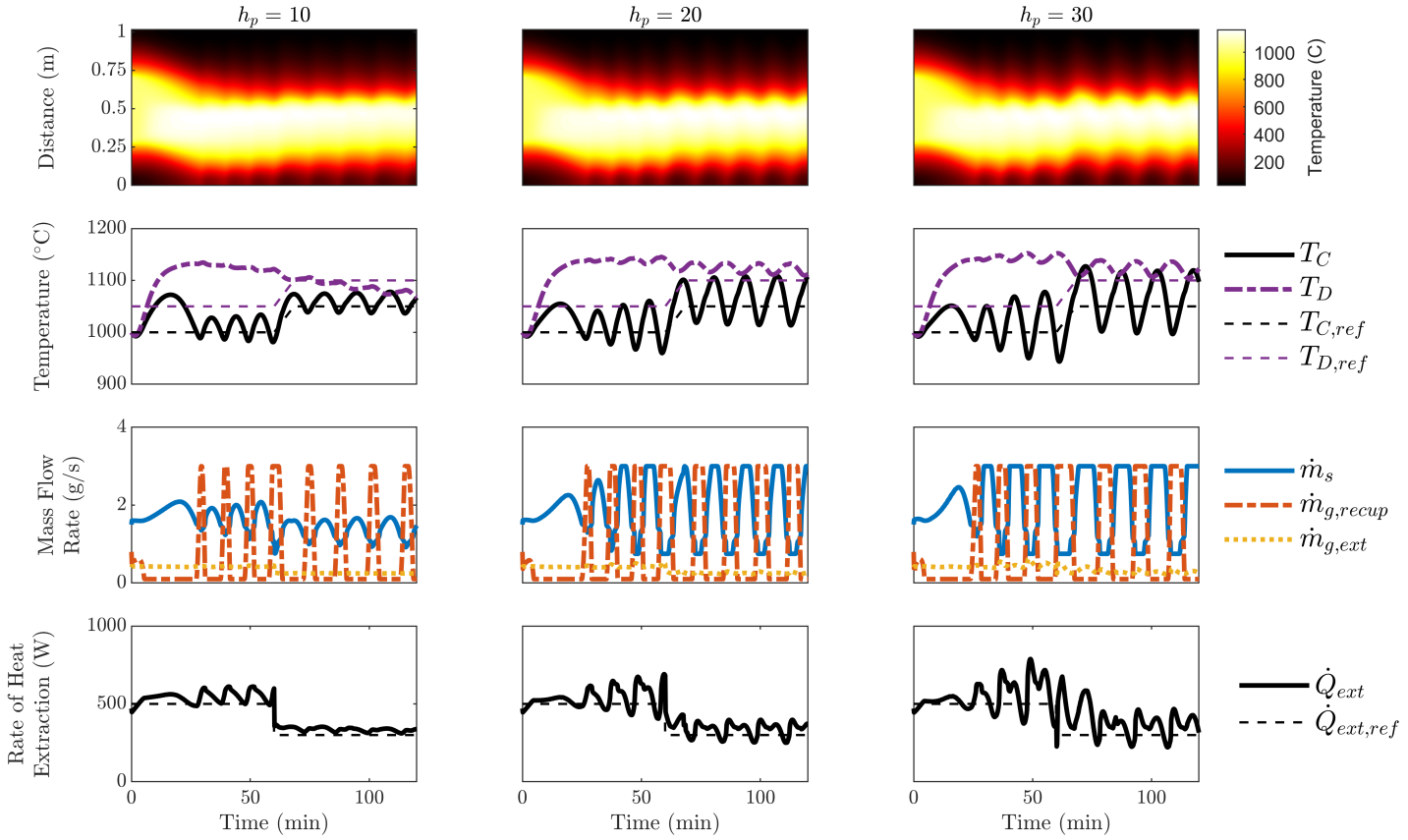

Figure 6.20 Simulated results of the impact of h_p, demonstrating decreasing controller performance for higher prediction horizons. Subplots include a temperature contour for T_w, measurements and tracking for T_C and T_D, system input values, and tracking results for $\dot{Q}_{ext}$, from top to bottom.

CHAPTER 7

SUMMARY AND FUTURE WORK

This dissertation has detailed the comprehensive study of a novel counterflow, direct-heat transfer thermochemical oxidation reactor. The counterflow character of the reactor sets it apart from other comparable designs in the literature. By flowing solid and gas streams opposite each other, Mg-Mn-O particles can enter and exit the reactor at close to ambient temperatures, enabling long-duration room temperature storage and simple material handling. While an extraction gas flow is implemented to remove high-temperature gas from the reactor, it alone is not sufficient to enable stable, long-duration operation for a bench-scale reactor. A recuperative gas flow moving through the upper reaches of the particle bed must be included to ensure sufficient heat recuperation. The fabrication procedure for the reactor was described in detail, including components such as the solid flow control system, extraction heat exchanger, steel reactor shell and ceramic tube, and a variety of other sensors and actuators.

The experimental reactor was evaluated across a variety of different operational cases, exhibiting extraction temperatures in excess of 950°C and efficiencies up to 41.3 ± 6.0%. Through characterization experiments performed at constant solid and gas flow rates, reaction zone temperature and position were identified as important factors of long-duration steady state operation. Both simple on/off control for the recuperative flow and user modification of input setpoints produced stable behavior, but further control methodologies were required to ensure optimal operation. To this end, a 1D computational model was developed and validated, providing both a deeper understanding of system dynamics and a cheap, iterative platform for evaluating reactor control strategies. Through the use of a simple linearized system model, three model predictive control approaches were successfully deployed on the experimental apparatus, demonstrating stable temperature tracking and reaction zone regulation. The insights and accomplishments of this work provide a strong foundation for future thermochemical oxidation investigations utilizing a counterflow approach.

7.1 Reactor Scale-up

Enlarging the current thermochemical oxidation reactor requires an understanding of the operational limits of a given reactor geometry. For a straight, uniform-diameter reactor tube (as implemented in this work), these considerations are primarily based on the intersection of two factors: the gas velocity at which the particle bed will begin to fluidize and the particle flow rate suitable for energy recuperation with the gas. As previously explored for the SoFuel reduction setup by Schimmels et al. [113], fluidization of the reactor bed threatens to halt downward solid flow and choke operation. The minimum gas fluidization velocity can be calculated via the following:

$$u_{mf} = \frac{\mathrm{Re}_{mf}(1-\varepsilon)}{d_p \rho_g} \tag{7.1}$$

where the minimum fluidization Reynolds number is determined as a function of the Archimedes number:

$$\mathrm{Re}_{mf} = \sqrt{33.7^2 + 0.0408\mathrm{Ar}} - 33.7 \tag{7.2}$$

And the Archimedes number of the Mg-Mn-O particles is defined using its typical formulation:

$$\mathrm{Ar} = \frac{\rho_g d_p^3 \left(\rho_s - \rho_g\right) g}{\mu_g^2} \tag{7.3}$$

To capture the operational limits of a given reactor configuration, u_{mf} ought to be calculated where fluidization is most likely to occur: at the maximum reactor temperature. A conservative value of 1200°C is selected for determining gas properties. System pressure is further required to calculate the density of the gas phase; this value will be considered in greater detail later in the scale-up analysis. In conjunction with the gas viscosity and the cross-sectional area of the reactor tube determined via the diameter, D, a maximum operating mass flow rate of the gas can be determined for a given tube size:

$$\dot{m}_{g,max} = \pi \left(\frac{D}{2}\right)^2 \rho_g u_{mf} \tag{7.4}$$

with $\dot{m}_{g,max}$ comprised of both the recuperative and extraction gas flows. An established maximum gas flow provides a maximum solid flow via the recuperative principle of the reactor:

$$\dot{m}_{s,max} = \frac{\dot{m}_{g,max} c_{p,g}}{c_{p,s}} \tag{7.5}$$

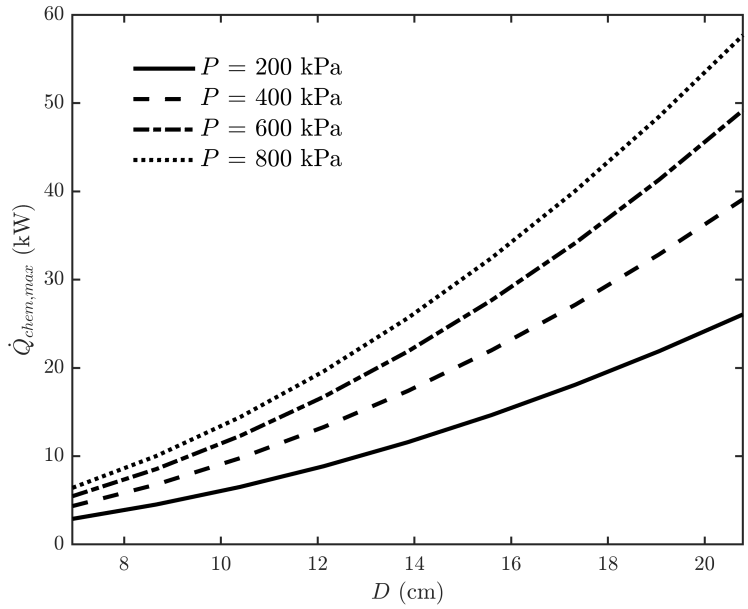

Figure 7.1 Maximum rates of chemical energy production for various reactor diameters and operating pressures. Modest increases beyond the current tube diameter (6.93 cm) yield improved energy production rates.

The previously implemented estimate of chemical energy based on solid flow is once again employed, yielding a maximum anticipated rate of chemical energy release for a given reactor geometry:

$$\dot{Q}_{chem,max} = \frac{\dot{m}_{s,max} \Delta H_{rxn} \beta \Delta\alpha}{M_{O_2}} \tag{7.6}$$

where $\Delta\alpha$ is estimated at a conversion of 0.8 based on previous experimental and simulation results.

Evaluating the previously listed equations at a variety of tube diameters provides estimates for the maximum chemical energy possible for each size. In addition, the operating pressure of the reactor is another parameter that strongly impacts fluidization, and thus operational limits. Results of varying the two reactor properties are depicted in Figure 7.1. The current tube diameter of 7.79 cm lies at the far left side of the figure, with a maximum estimated rate of chemical energy release of 3.66 kW when operating at 200 kPa. This estimate is of a comparable order to the rates of chemical energy release experimentally observed during operation of the current reactor geometry. As anticipated, increasing the diameter of the reactor tube allows for higher values of $\dot{Q}_{chem}$, on the order of tens of kilowatts, to be reached for a straight-tube configuration.

Figure 7.1 further illustrates the impact of pressure on reactor performance. Higher pressures increase gas density within the reactor, allowing the system to operate at increased mass flow rates and produce more chemical energy. While only providing modest gains at the current reactor size, Figure 7.1 showcases the drastic improvements to $\dot{Q}_{chem,max}$ produced for large tube diameters. Not captured in the current scale-up model is the impact of higher oxygen partial pressure on reaction kinetics. While a value of $\Delta\alpha = 0.8$ is assumed for this introductory investigation, higher conversions would be expected for elevated pressure in the reactor. Such a level of detail is beyond the scope of this study.

7.2 Reactor Autoignition

An additional consideration for future reactor development is the determination of suitable startup conditions for reactor autoignition. Most of the experiments and simulations throughout this work considered a main reaction zone encompassing the five measurement thermocouples preheated to temperatures close to 1000°C, but this practice is disadvantageous for several reasons. First, preheating the oxidation system to 1000°C requires a larger initial energy investment than dwelling at a lower temperature. Additionally, preheating a large swath of the reactor tube to 1000°C produces larger losses during both heat-up and reactor operation. The ideal conditions for beginning reactor operation, then, should be a combination of low temperatures and a narrow reaction zone that are still able to facilitate autoignition in the particle bed in a timely manner.

General analysis of thermal autoignition processes has been explored for reacting systems [114], including specific analyses on fixed-bed reactors [115]. Generally speaking, thermal runaway occurs when the rate of chemical energy production in a system exceeds the rate at which energy leaves the system:

$$\dot{Q}_{chem} > \sum \dot{Q}_{out} \tag{7.7}$$

While lumped-sum analyses could be performed on the oxidation reactor to determine estimates of autoignition behavior, temperature gradients within the system and the desire to investigate differing reaction zone sizes make the 1D model of Chapter 5 a better option for evaluating thermal runaway.

A parametric investigation was performed to determine the occurrence of thermal runaway for

various initial reaction zone temperatures and sizes. Temperatures ranged from 600°C to 975°C in intervals of 25°C, while the initial heated zone began at 2.07 cm centered on the extraction point and increased to 43.5 cm in increments of 4.15 cm. The simulation used the established boundary conditions of Chapter 5. To establish initial temperature conditions, a five hour simulation with no solid or gas flows was performed, imposing the specified heated zone temperatures and sizes on the solid, gas, and wall phases. The extent of conversion for particles from the bottom of the reactor to the top of the initial heated zone were specified as fully oxidized, with $\alpha_s = 0.05$ for cells above the heated area. Simulations utilized the MPC strategy of Approach 3 to regulate reactor operation and seek a maximum temperature centered over Zone C. The controller implemented the targets and limits of Table 6.7, as well as weights of $w_{\dot{m}_{g,recup}} = 0.5$, $w_{\dot{m}_{g,ext}} = 10$, $w_{T_C} = 40$, $w_{T_B - T_D} = 2$, and move suppression weights of 0.1. No rate of energy extraction was specified in order to minimize the energy leaving the reactor. Each combination of temperature and heated zone size was allowed two hours of simulated operation to reach $T_{C,ref} = 1000$°C.

Results from the start-up study are depicted in Figure 7.2. The simulations showcase a wide array of feasible initial conditions, although high initial temperatures and a wide heated zone produce the shortest times to reach 1000°C. Of particular note is the wide temperature envelope within which the reactor can achieve steady 1000°C operation. Even initial temperatures as low as 700°C can be leveraged to achieve autoignition, albeit requiring more time to heat the reactor to 1000°C via the exothermic oxidation reaction. The strong impact of initial heated length on the success of autoignition is indicative of the axial and radial heat transfer that strongly affects reactor start-up - without a sufficiently large reaction zone, too much energy is lost to sustain continued chemical reaction.

Due to the simulation model's specificity to the experimental reactor system (in terms of size, shape, insulation, and other factors), the exact results of Figure 7.2 are not directly applicable to other direct contact, countercurrent oxidation reactors. The general observations from this analysis, however, further support the applicability of the SoFuel oxidation reactor for intermittent usage. Even on the laboratory scale and limited to a maximum solid flow rate of 2 g/s, the system was able

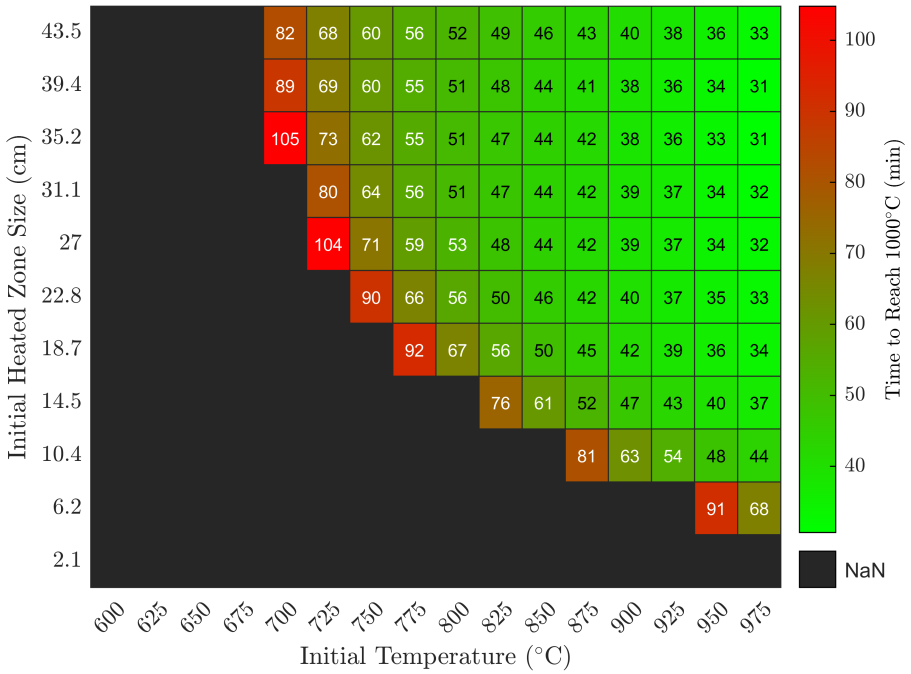

Figure 7.2 The impact of initial heated zone size and temperature on reactor autoignition. Higher starting temperatures and wider reaction zones lead to the most rapid development of steady 1000°C temperatures for T_C.

to reinstate operation from temperatures below the specified operational threshold of 1000°C. For a system seeking to supplement intermittent renewables or supply energy to industrial processes, such flexibility is an important factor in successful scale-up opportunities.

BIBLIOGRAPHY

[1] K. Randhir, M. Hayes, P. Schimmels, J. Petrasch, and J. Klausner, "Zero carbon solid-state rechargeable redox fuel for long duration and seasonal storage," *Joule*, vol. 6, 11 Nov. 2022.

[2] M. Hayes, D. Korba, P. Schimmels, *et al.*, "Experimental demonstration of high-temperature (>1000°C) heat extraction from a moving-bed oxidation reactor for thermochemical energy storage," *Applied Energy*, vol. 349, Nov. 2023.

[3] IPCC, "Global warming of 1.5°C," Jun. 2022.

[4] U.S. Energy Information Administration, "U.S. energy consumption by source and sector, 2021," 2022.

[5] U.S. Energy Information Administration, "Annual Energy Outlook 2022 (AEO2022)," 2022. [Online]. Available: www.eia.gov.

[6] J. L. Aleixandre-Tudó, L. Castelló-Cogollos, J. L. Aleixandre, and R. Aleixandre-Benavent, "Renewable energies: Worldwide trends in research, funding and international collaboration," *Renewable Energy*, vol. 139, pp. 268–278, Aug. 2019.

[7] A. C. Ari, A. Arregui, S. Black, *et al.*, "Surging energy prices in Europe in the aftermath of the war: How to support the vulnerable and speed up the transition away from fossil fuels," International Monetary Fund, Jul. 2022. [Online]. Available: https://ssrn.com/abstract=4184693.

[8] V. Lekavičius, A. Galinis, and V. Miškinis, "Long-term economic impacts of energy development scenarios: The role of domestic electricity generation," *Applied Energy*, vol. 253, Nov. 2019.

[9] I. Stadelmann-Steffen and C. Eder, "Public opinion in policy contexts. A comparative analysis of domestic energy policies and individual policy preferences in Europe," *International Political Science Review*, vol. 42, pp. 78–94, 1 Jan. 2021.

[10] International Renewable Energy Agency, "Renewable power generation costs in 2019," 2020. [Online]. Available: www.irena.org.

[11] V. Balaram, "Rare earth elements: A review of applications, occurrence, exploration, analysis, recycling, and environmental impact," *Geoscience Frontiers*, vol. 10, pp. 1285–1303, 4 Jul. 2019.

[12] M. Beaudin, H. Zareipour, A. Schellenberglabe, and W. Rosehart, "Energy storage for mitigating the variability of renewable electricity sources: An updated review," *Energy for Sustainable Development*, vol. 14, pp. 302–314, 4 2010.

[13] I. Hadjipaschalis, A. Poullikkas, and V. Efthimiou, "Overview of current and future energy storage technologies for electric power applications," *Renewable and Sustainable Energy Reviews*, vol. 13, pp. 1513–1522, 6-7 Aug. 2009.

[14] C. J. Barnhart and S. M. Benson, "On the importance of reducing the energetic and material demands of electrical energy storage," *Energy and Environmental Science*, vol. 6, pp. 1083–1092, 4 2013.

[15] J. Wu and X. F. Long, "Research progress of solar thermochemical energy storage," *International Journal of Energy Research*, vol. 39, pp. 869–888, 7 Jun. 2015.

[16] A. H. Abedin and M. A. Rosen, "A critical review of thermochemical energy storage systems," *The Open Renewable Energy Journal*, vol. 4, pp. 42–46, 2011.

[17] S. Wu, C. Zhou, E. Doroodchi, R. Nellore, and B. Moghtaderi, "A review on high-temperature thermochemical energy storage based on metal oxides redox cycle," *Energy Conversion and Management*, vol. 168, pp. 421–453, Jul. 2018.

[18] I. Ermanoski, N. P. Siegel, and E. B. Stechel, "A new reactor concept for efficient solar-thermochemical fuel production," *Journal of Solar Energy Engineering, Transactions of the ASME*, vol. 135, 3 2013.

[19] S. Chuayboon and S. Abanades, "An overview of solar decarbonization processes, reacting oxide materials, and thermochemical reactors for hydrogen and syngas production," *International Journal of Hydrogen Energy*, vol. 45, pp. 25 783–25 810, 48 Sep. 2020.

[20] Y. Lu, L. Zhu, C. Agrafiotis, J. Vieten, M. Roeb, and C. Sattler, "Solar fuels production: Two-step thermochemical cycles with cerium-based oxides," *Progress in Energy and Combustion Science*, vol. 75, Nov. 2019.

[21] D. Yadav and R. Banerjee, "A review of solar thermochemical processes," *Renewable and Sustainable Energy Reviews*, vol. 54, pp. 497–532, Feb. 2016.

[22] T. Block and M. Schmücker, "Metal oxides for thermochemical energy storage: A comparison of several metal oxide systems," *Solar Energy*, vol. 126, pp. 195–207, Mar. 2016.

[23] B. Wong, "Thermochemical heat storage for concentrated solar power," General Atomics, Oct. 2011.

[24] C. Agrafiotis, M. Roeb, M. Schmücker, and C. Sattler, "Exploitation of thermochemical cycles based on solid oxide redox systems for thermochemical storage of solar heat. Part 1: Testing of cobalt oxide-based powders," *Solar Energy*, vol. 102, pp. 189–211, 2014.

[25] I. A. Al-Shankiti, B. D. Ehrhart, B. J. Ward, *et al.*, "Particle design and oxidation kinetics of iron-manganese oxide redox materials for thermochemical energy storage," *Solar Energy*,

vol. 183, pp. 17–29, May 2019.

[26] S. Tescari, C. Agrafiotis, S. Breuer, *et al.*, "Thermochemical solar energy storage via redox oxides: Materials and reactor/heat exchanger concepts," *Energy Procedia*, vol. 49, pp. 1034–1043, 2014.

[27] S. Tescari, A. Singh, L. D. Oliveira, *et al.*, "Experimental proof of concept of a pilot-scale thermochemical storage unit," vol. 1850, American Institute of Physics Inc., Jun. 2017.

[28] S. Tescari, A. Singh, C. Agrafiotis, *et al.*, "Experimental evaluation of a pilot-scale thermochemical storage system for a concentrated solar power plant," *Applied Energy*, vol. 189, pp. 66–75, 2017.

[29] M. Wokon, A. Kohzer, and M. Linder, "Investigations on thermochemical energy storage based on technical grade manganese-iron oxide in a lab-scale packed bed reactor," *Solar Energy*, vol. 153, pp. 200–214, 2017.

[30] B. Wang, L. Li, F. Schäfer, *et al.*, "Thermal reduction of iron–manganese oxide particles in a high-temperature packed-bed solar thermochemical reactor," *Chemical Engineering Journal*, vol. 412, May 2021.

[31] M. Neises, S. Tescari, L. de Oliveira, M. Roeb, C. Sattler, and B. Wong, "Solar-heated rotary kiln for thermochemical energy storage," *Solar Energy*, vol. 86, pp. 3040–3048, 10 Oct. 2012.

[32] H. E. Bush and P. G. Loutzenhiser, "Solar electricity via an air Brayton cycle with an integrated two-step thermochemical cycle for heat storage based on Fe2O3/Fe3O4 redox reactions: Thermodynamic and kinetic analyses," *Solar Energy*, vol. 174, pp. 617–627, Nov. 2018.

[33] A. J. Schrader, A. P. Muroyama, and P. G. Loutzenhiser, "Solar electricity via an air Brayton cycle with an integrated two-step thermochemical cycle for heat storage based on Co3O4/CoO redox reactions: Thermodynamic analysis," *Solar Energy*, vol. 118, pp. 485–495, Aug. 2015.

[34] J. E. Miller, A. Ambrosini, S. M. Babiniec, *et al.*, "High performance reduction/oxidation metal oxides for thermochemical energy storage (PROMOTES)," ASME Power and Energy Conference, Jun. 2016.

[35] S. M. Babiniec, J. E. Miller, A. Ambrosini, *et al.*, "Considerations for the design of a high-temperature particle reoxidation reactor for extraction of heat in thermochemical energy storage systems," ASME 2016 10th International Conference on Energy Sustainability, Jun. 2016.

[36] N. C. Preisner and M. Linder, "A moving bed reactor for thermochemical energy storage

based on metal oxides," *Energies*, vol. 13, 5 2020.

[37] A. J. Schrader, G. L. Schieber, A. Ambrosini, and P. G. Loutzenhiser, "Experimental demonstration of a 5 kwth granular-flow reactor for solar thermochemical energy storage with aluminum-doped calcium manganite particles," *Applied Thermal Engineering*, vol. 173, Jun. 2020.

[38] S. Tescari, N. C. Neumann, P. Sundarraj, *et al.*, "Storing solar energy in continuously moving redox particles – experimental analysis of charging and discharging reactors," *Applied Energy*, vol. 308, Feb. 2022.

[39] J. Sment, K. Albrecht, M. J. Martinez, and C. K. Ho, "Design considerations for a high-temperature particle storage bin," Sandia National Laboratories, 2019.

[40] J. Sment, K. Albrecht, J. Christian, and C. K. Ho, "Optimization of storage bin geometry for high temperature particle-based CSP systems," ASME 2019 13th International Conference on Energy Sustainability, Jul. 2019.

[41] J. Vandermeer, M. Mueller-Stoffels, and E. Whitney, "An Alaska case study: Energy storage technologies," *Journal of Renewable and Sustainable Energy*, vol. 9, 6 Nov. 2017.

[42] N. Rahmatian, A. Bo, K. Randhir, J. F. Klausner, and J. Petrasch, "Bench-scale demonstration of thermochemical energy storage using the magnesium-manganese-oxide redox system," *Journal of Energy Storage*, vol. 45, Jan. 2022.

[43] K. Randhir, K. King, N. Rhodes, *et al.*, "Magnesium-manganese oxides for high temperature thermochemical energy storage," *Journal of Energy Storage*, vol. 21, pp. 599–610, Feb. 2019.

[44] K. King, K. Randhir, and J. Klausner, "Calorimetric method for determining the thermochemical energy storage capacities of redox metal oxides," *Thermochimica Acta*, vol. 673, pp. 105–118, Mar. 2019.

[45] K. Randhir, K. King, J. Petrasch, and J. Klausner, "Oxidation kinetics of magnesium-manganese oxides for high-temperature thermochemical energy storage," *Energy Technology*, vol. 8, 10 Oct. 2020.

[46] A. Mishra, D. Korba, J. Zhao, and L. Li, "Heat and mass transfer model for a counter-flow moving packed-bed oxidation reactor/heat exchanger," *Journal of Solar Energy Engineering*, pp. 1–30, Mar. 2024.

[47] W. Huang, D. Korba, K. Randhir, *et al.*, "Thermochemical reduction modeling in a high-temperature moving-bed reactor for energy storage: 1D model," *Applied Energy*, vol. 306, Jan. 2022.

[48] D. Korba, M. Hayes, P. Schimmels, *et al.*, "Continuum modeling of high-temperature (>1000°C) heat extraction from a moving-bed oxidation reactor for thermochemical energy storage," *Journal of Energy Storage*, vol. 82, p. 110 579, Mar. 2024.

[49] *Fact-Web Thermochemical Software*. [Online]. Available: https://www.crct.polymtl.ca/factweb.php.

[50] M. Hayes, P. Schimmels, J. Petrasch, J. Klausner, and A. Benard, "Implementation of a pneumatic L-valve pulsation scheme to achieve low particle flow rates," 2023 AIChE Annual Meeting, Nov. 2023.

[51] U. Arena, C. B. Langeli, and A. Cammarota, "L-valve behaviour with solids of different size and density," *Powder Technology*, vol. 98, pp. 231–240, 3 Aug. 1998.

[52] T. M. Knowlton and I. Hirsan, "L-valves characterized for solids flow.," *Hydrocarbon Processing*, vol. 57, 3 1978.

[53] D. Geldart and P. Jones, "The behaviour of L-valves with granular powders," *Powder Technology*, vol. 67, pp. 163–174, 2 Aug. 1991.

[54] M. A. Daous and A. A. Al-Zahrani, "Modeling solids and gas flow through an L-valve," *Powder Technology*, vol. 99, 1 1998.

[55] S. Bhowmick, N. A. Baveja, G. Varshney, *et al.*, "Experimental study on solid discharge rate from a nonmechanical solid feeding system," *Industrial and Engineering Chemistry Research*, vol. 52, 41 2013.

[56] W. C. Yang and T. M. Knowlton, "L-valve equations," *Powder Technology*, vol. 77, 1 1993.

[57] P. He and L. S. Fan, "A general methodology and the correlation for the prediction of the solids flow rates through the L-valves," *Powder Technology*, vol. 360, 2020.

[58] J. H. Lim, D. H. Lee, H. J. Chae, and S. Y. Jeong, "Pressure change and control of the solid circulation rate of Geldart A particles in a small diameter L-valve," *Powder Technology*, vol. 243, 2013.

[59] E. R. Monazam, R. W. Breault, L. J. Shadle, and J. M. Weber, "Analysis of solids flow rate through nonmechanical L-valve in an industrial-scale circulating fluidized bed using Group B particles," *Industrial and Engineering Chemistry Research*, vol. 57, 33 2018.

[60] K. Smolders and J. Baeyens, "The operation of L-valves to control standpipe flow," *Advanced Powder Technology*, vol. 6, 3 1995.

[61] M. M. Yazdanpanah, A. Forret, T. Gauthier, and A. Delebarre, "An experimental investigation of L-valve operation in an interconnected circulating fluidized bed system," *Powder*

Technology, vol. 221, 2012.

[62] E. R. Monazam, R. W. Breault, and L. J. Shadle, "Operational performance characteristics of an aerated L-valve operated within a closed circulating fluidized bed loop," *Powder Technology*, vol. 354, 2019.

[63] N. Chovichien, S. Pipatmanomai, and S. Chungpaibulpatana, "Estimate of solids circulation rate through an L-valve in a CFB operating at elevated temperature," *Powder Technology*, vol. 235, 2013.

[64] D. Wang and L. S. Fan, "L-valve behavior in circulating fluidized beds at high temperatures for group d particles," *Industrial and Engineering Chemistry Research*, vol. 54, 16 2015.

[65] L. M. Sousa and M. C. Ferreira, "Analysis of the performance of an L-valve feeding spent coffee ground powders into a circulating fluidized bed," *Powder Technology*, vol. 362, 2020.

[66] M. Yazdanpanah, A. Hoteit, A. Forret, A. Delebarre, and T. Gauthier, "Experimental investigations on a novel chemical looping combustion configuration," *Oil & Gas Science and Technology – Revue d'IFP Energies nouvelles*, vol. 66, 2 2011.

[67] G. Zsembinszki, A. Sole, C. Barreneche, C. Prieto, A. I. Fernández, and L. F. Cabeza, "Review of reactors with potential use in thermochemical energy storage in concentrated solar power plants," *Energies*, vol. 11, 9 2018.

[68] L. Farcot, N. L. Pierrès, and J. F. Fourmigué, "Experimental investigation of a moving-bed heat storage thermochemical reactor with SrBr2/H2O couple," *Journal of Energy Storage*, vol. 26, 2019.

[69] A. C. Mejia, S. Afflerbach, M. Linder, and M. Schmidt, "Experimental analysis of encapsulated CaO/Ca(OH)2 granules as thermochemical storage in a novel moving bed reactor," *Applied Thermal Engineering*, vol. 169, 2020.

[70] J. Vogel, W. M. Swift, M. J. McDaniel, G. W. Smith, and A. A. Ziegler, "Testing of a pulsed L-valve feeder for use in fluidized-bed combustion and sorbent regeneration units," Argonne National Lab, Sep. 1978.

[71] F. P. Incropera, D. P. Dewitt, T. L. Bergman, and A. S. Lavine, *Fundamentals of Heat and Mass Transfer*, 6th Edition. Hoboken, NJ: John Wiley and Sons Inc., 2007.

[72] C. L. Yaws, *Yaws' Critical Property Data for Chemical Engineers and Chemists*. Knovel, 2012; 2013; 2014.

[73] R. C. Monroe, "Fans and blowers," in *Kirk-Othmer Encyclopedia of Chemical Technology*. John Wiley and Sons, Inc., Dec. 2000.

[74] N. Mertens, F. Alobaid, L. Frigge, and B. Epple, "Dynamic simulation of integrated rock-bed thermocline storage for concentrated solar power," *Solar Energy*, vol. 110, pp. 830–842, Dec. 2014.

[75] J. F. Hoffmann, T. Fasquelle, V. Goetz, and X. Py, "A thermocline thermal energy storage system with filler materials for concentrated solar power plants: Experimental data and numerical model sensitivity to different experimental tank scales," *Applied Thermal Engineering*, vol. 100, pp. 753–761, May 2016.

[76] N. Vahedi, Q. A. Ranjha, and A. Oztekin, "Numerical study of high temperature thermochemical energy storage using Co3O4/CoO," Proceedings of the ASME 2018 International Mechanical Engineering Congress and Exposition, 2018.

[77] X. Zhou, M. Mahmood, J. Chen, T. Yang, G. Xiao, and M. L. Ferrari, "Validated model of thermochemical energy storage based on cobalt oxides," *Applied Thermal Engineering*, vol. 159, Aug. 2019.

[78] H. Shao, T. Nagel, C. Roßkopf, M. Linder, A. Wörner, and O. Kolditz, "Non-equilibrium thermo-chemical heat storage in porous media: Part 2 - A 1D computational model for a calcium hydroxide reaction system," *Energy*, vol. 60, pp. 271–282, Oct. 2013.

[79] E. Saade, C. Bingham, D. E. Clough, and A. W. Weimer, "Dynamics of a solar-thermal transport-tube reactor," *Chemical Engineering Journal*, vol. 213, pp. 272–285, Dec. 2012.

[80] N. C. Preisner, I. Bürger, M. Wokon, and M. Linder, "Numerical investigations of a counter-current moving bed reactor for thermochemical energy storage at high temperatures," *Energies*, vol. 13, 3 2020.

[81] D. Korba, W. Huang, K. Randhir, *et al.*, "A continuum model for heat and mass transfer in moving-bed reactors for thermochemical energy storage," *Applied Energy*, vol. 313, May 2022.

[82] J. Crank and P. Nicolson, "A practical method for numerical evaluation of solutions of partial differential equations of the heat-conduction type," *Mathematical Proceedings of the Cambridge Philosophical Society*, vol. 43, pp. 50–67, 1 1947.

[83] B. P. Leonard, "A stable and accurate convective modelling procedure based on quadratic upstream interpolation," *Computer Methods in Applied Mechanics and Engineering*, vol. 19, pp. 59–98, 1979.

[84] W. J. Yang, Z. Y. Zhou, and A. B. Yu, "Particle scale studies of heat transfer in a moving bed," *Powder Technology*, vol. 281, pp. 99–111, Sep. 2015.

[85] W. N. Sullivan and R. H. Sabersky, "Heat transfer to flowing granular media," *Int. J. Heat Mass Transfer*, vol. 18, pp. 97–107, 1975.

[86] R. H. S. Winterton, "Where did the Dittus and Boelter equation come from?" *Int. J. Heat Mass Transfer*, vol. 41, pp. 809–810, 1998.

[87] M. J. Moran, H. N. Shapiro, D. D. Boettner, and M. B. Bailey, *Fundamentals of Engineering Thermodynamics*, 8th Edition. Wiley, 2014.

[88] M. Hayes, F. Masoomi, P. Schimmels, K. Randhir, J. Klausner, and J. Petrasch, "Ultra-high temperature thermal conductivity measurements of a reactive magnesium manganese oxide porous bed using a transient hot wire method," *Journal of Heat Transfer*, vol. 143, 10 Oct. 2021.

[89] D. Seborg, T. Edgar, D. Mellichamp, and F. Doyle III, *Process Dynamics and Control*, 2nd Edition. John Wiley and Sons, Inc., 2004.

[90] B. Bequette, *Process Control: Modeling, Design, and Simulation*. Upper Saddle River, NJ: Prentice Hall, 1998.

[91] N. L. Flicker, "Model predictive control of a continuous, nonlinear, two-phase reactor," *J. Proc. Cont*, vol. 3, 2 1993.

[92] M. G. Na, S. H. Shin, and W. C. Kim, "A model predictive controller for nuclear reactor power," *Journal of the Korean Nuclear Society*, vol. 35, pp. 399–411, 5 2003.

[93] J. Wang, S. Wei, Q. Wang, and B. Sundén, "Transient numerical modeling and model predictive control of an industrial-scale steam methane reforming reactor," *International Journal of Hydrogen Energy*, vol. 46, pp. 15 241–15 256, 29 Apr. 2021.

[94] J. Petrasch, P. Osch, and A. Steinfeld, "Dynamics and control of solar thermochemical reactors," *Chemical Engineering Journal*, vol. 145, pp. 362–370, 3 Jan. 2009.

[95] E. Saade, D. E. Clough, and A. W. Weimer, "Model predictive control of a solar-thermal reactor," *Solar Energy*, vol. 102, pp. 31–44, Apr. 2014.

[96] M. Habib, "Control system design for a solar receiver-reactor," Ph.D. dissertation, Australian National University, 2019.

[97] S. C. Rowe, I. Hischier, A. W. Palumbo, *et al.*, "Nowcasting, predictive control, and feedback control for temperature regulation in a novel hybrid solar-electric reactor for continuous solar-thermal chemical processing," *Solar Energy*, vol. 174, pp. 474–488, Nov. 2018.

[98] Y. Karout, A. Curcio, J. Eynard, *et al.*, "Model-based predictive control of a solar hybrid thermochemical reactor for high-temperature steam gasification of biomass," *Clean Technologies*, vol. 5, pp. 329–351, 1 Mar. 2023.

[99] A. Alsahlani, K. Randhir, M. Hayes, P. Schimmels, N. Ozalp, and J. Klausner, "Implemen-

tation of a model predictive control strategy to regulate temperature inside plug-flow solar reactor with countercurrent flow," *Journal of Thermal Science and Engineering Applications*, vol. 15, 2 Feb. 2023.

[100] A. A. Sahlani, K. Randhir, N. Ozalp, and J. Klausner, "A forward feedback control scheme for a solar thermochemical moving bed counter-current flow reactor," *Journal of Solar Energy Engineering*, vol. 144, 3 Jun. 2022.

[101] A. Alsahlani, K. Randhir, M. Hayes, P. Schimmels, N. Ozalp, and J. Klausner, "Design of a combined proportional integral derivative controller to regulate the temperature inside a high-temperature tubular solar reactor," *Journal of Solar Energy Engineering*, vol. 145, 1 Feb. 2023.

[102] I. Y. Smets, D. Dochain, and J. F. V. Impe, "Optimal temperature control of a steady-state exothermic plug-flow reactor," *AIChE Journal*, vol. 48, pp. 279–286, 2 Feb. 2002.

[103] J. Vojtesek and P. Dostal, "Adaptive control of the tubular reactor with co- and counter-current cooling in the jacket," Proceedings of the 23rd European Conference on Modelling and Simulation, 2009.

[104] M. Sudhakar, S. Narasimhan, and N. S. Kaisare, "Method of characteristics based model reduction for control of a counter-current reactor using approximate dynamic programming," IEEE Computer Society, 2013, pp. 4496–4501.

[105] H. Fang, L. Haibin, and Z. Zengli, "Advancements in development of chemical-looping combustion: A review," *International Journal of Chemical Engineering*, 2009.

[106] C. Fan, Z. Cui, J. Wang, Z. Liu, and W. Tian, "Exergy analysis and dynamic control of chemical looping combustion for power generation system," *Energy Conversion and Management*, vol. 228, Jan. 2021.

[107] J. B. Rawlings, "Tutorial overview of model predictive control," *IEEE Control Systems Magazine*, vol. 20, pp. 38–52, 3 2000.

[108] J. H. Lee, "Model predictive control: Review of the three decades of development," *International Journal of Control, Automation and Systems*, vol. 9, pp. 415–424, 3 Jun. 2011.

[109] J. M. Martín-Sánchez, J. M. Lemos, and J. Rodellar, "Survey of industrial optimized adaptive control," *International Journal of Adaptive Control and Signal Processing*, vol. 26, pp. 881–918, 10 Oct. 2012.

[110] The MathWorks Inc., *Model predictive control toolbox version: R2023a*, Natick, Massachusetts, United States, 2023. [Online]. Available: https://www.mathworks.com/help/mpc/.

[111] The MathWorks Inc., *Optimization problem*, Natick, Massachusetts, United States, 2024. [Online]. Available: https://www.mathworks.com/help/mpc/ug/optimization-problem.html.

[112] The MathWorks Inc., *App designer: R2023a*, Natick, Massachusetts, United States, 2023. [Online]. Available: https://www.mathworks.com/products/matlab/app-designer.html.

[113] P. Schimmels, M. Hayes, K. Randhir, J. Petrasch, and J. F. Klausner, "Enhancing the chemical energy flux in a high-temperature tubular counterflow solid fuel synthesis reactor using a bypass," *Industrial and Engineering Chemistry Research*, vol. 62, pp. 14 671–14 678, 36 Sep. 2023.

[114] J.-C. Lermant and S. Yip, "A generalized semenov model for thermal ignition in nonuniform temperature systems," *Combustion and Flame*, vol. 57, pp. 41–54, 1984.

[115] C. Ekici, D. Kipp, C. R. Ho, L. T. Biegler, and P. M. Witt, "Prediction of the thermal runaway limit and optimal operation of heat transfer-limited, fixed-bed reactor systems," *Industrial and Engineering Chemistry Research*, vol. 60, pp. 15 087–15 094, 42 Oct. 2021.

APPENDIX

LINEARIZATION OF THE REACTOR MODEL

This appendix features additional details regarding the linearization procedures for the various MPC formulations.

General Oxidation Reactor Model Linearization

As first described in Chapter 6, a linearized model of the oxidation reactor can be generated via a collection of first-order Taylor approximations. The temperature of Zone C is taken as an example to illustrate the linearization process. T_C has an energy equation of the form:

$$\frac{\partial T_C}{\partial t} = \frac{\dot{m}_s c_{p,s}}{m_s c_{p,s} + m_g c_{p,g}} \left(\frac{T_B - T_D}{2} \right) + \frac{\dot{m}_{g,recup} c_{p,g}}{m_s c_{p,s} + m_g c_{p,g}} \left(\frac{T_D - T_B}{2} \right) + \frac{\dot{m}_{g,ext} c_{p,g}}{m_s c_{p,s} + m_g c_{p,g}} \left(\frac{T_D - T_C}{2} \right) - \frac{2\pi \Delta x k_{ins}}{m_s c_{p,s} + m_g c_{p,g}} \frac{T_C - T_{amb}}{\ln\left(r_{out} - r_o\right)} + \frac{V_s \left(\rho_{ox} - \rho_{red}\right) \Delta H_{rxn}}{\left(m_s c_{p,s} + m_g c_{p,g}\right) M_{O_2}} \left(\frac{\partial \alpha_s}{\partial t} \right)_{rxn,C}$$

To facilitate the notation of linearization, let $\frac{\partial T_C}{\partial t} = f_{T_C}(\mathbf{x}, \mathbf{u})$, where $\mathbf{x}$ and $\mathbf{u}$ are the 15×1 and 3×1 state and input vectors, respectively. Linear coefficients can be generated via the following operations:

$$A_{T_C,j} = \left. \frac{\partial f_{T_C}}{\partial x_j} \right|_{x_{\text{nom}}, u_{\text{nom}}}, \quad B_{T_C,j} = \left. \frac{\partial f_{T_C}}{\partial u_j} \right|_{x_{\text{nom}}, u_{\text{nom}}}$$

where the "nom" subscript denotes the current nominal operating point. A values can be determined with respect to each state:

$$A_{T_C,T_E} = 0$$

$$A_{T_C,T_D} = -\frac{\dot{m}_{s,\text{nom}} c_{p,s}}{2\left(m_s c_{p,s} + m_g c_{p,g}\right)} + \frac{\dot{m}_{g,recup,\text{nom}} c_{p,g}}{2\left(m_s c_{p,s} + m_g c_{p,g}\right)} + \frac{\dot{m}_{g,ext,\text{nom}} c_{p,g}}{2\left(m_s c_{p,s} + m_g c_{p,g}\right)}$$

$$A_{T_C,T_C} = \frac{\dot{m}_{g,ext,\text{nom}} c_{p,g}}{2\left(m_s c_{p,s} + m_g c_{p,g}\right)} - \frac{2\pi \Delta x k_{ins}}{\left(m_s c_{p,s} + m_g c_{p,g}\right) \ln\left(r_{out} - r_o\right)} + \frac{V_s \left(\rho_{ox} - \rho_{red}\right) \Delta H_{rxn}}{\left(m_s c_{p,s} + m_g c_{p,g}\right) M_{O_2}} \frac{\partial}{\partial T_C} \left(\frac{\partial \alpha_s}{\partial t} \right)_{rxn,C}$$

$$A_{T_C,T_B} = \frac{\dot{m}_{s,\text{nom}} c_{p,s}}{2\left(m_s c_{p,s} + m_g c_{p,g}\right)} - \frac{\dot{m}_{g,recup,\text{nom}} c_{p,g}}{2\left(m_s c_{p,s} + m_g c_{p,g}\right)}$$

$$A_{T_C,T_A} = 0$$

$$A_{T_C,\alpha_{s,E}} = 0$$

$$A_{T_C,\alpha_{s,D}} = 0$$

$$A_{T_C,\alpha_{s,C}} = \frac{V_s\left(\rho_{ox} - \rho_{red}\right)\Delta H_{rxn}}{\left(m_s c_{p,s} + m_g c_{p,g}\right) M_{O_2}} \frac{\partial}{\partial \alpha_{s,C}} \left(\frac{\partial \alpha_s}{\partial t}\right)_{rxn,C}$$

$$A_{T_C,\alpha_{s,B}} = 0$$

$$A_{T_C,\alpha_{s,A}} = 0$$

$$A_{T_C,\xi_{ox,E}} = 0$$

$$A_{T_C,\xi_{ox,D}} = 0$$

$$A_{T_C,\xi_{ox,C}} = \frac{V_s\left(\rho_{ox} - \rho_{red}\right)\Delta H_{rxn}}{\left(m_s c_{p,s} + m_g c_{p,g}\right) M_{O_2}} \frac{\partial}{\partial \xi_{ox,C}} \left(\frac{\partial \alpha_s}{\partial t}\right)_{rxn,C}$$

$$A_{T_C,\xi_{ox,B}} = 0$$

$$A_{T_C,\xi_{ox,A}} = 0$$

And B values can be generated for each system input:

$$B_{T_C,\dot{m}_s} = \frac{c_{p,s}\left(T_{B,\text{nom}} - T_{D,\text{nom}}\right)}{2\left(m_s c_{p,s} + m_g c_{p,g}\right)}$$

$$B_{T_C,\dot{m}_{g,recup}} = \frac{c_{p,g}\left(T_{D,\text{nom}} - T_{B,\text{nom}}\right)}{2\left(m_s c_{p,s} + m_g c_{p,g}\right)}$$

$$B_{T_C,\dot{m}_{g,ext}} = \frac{c_{p,g}\left(T_{D,\text{nom}} - T_{C,\text{nom}}\right)}{2\left(m_s c_{p,s} + m_g c_{p,g}\right)}$$

Taken together, $\mathbf{A}_{T_C}$ and $\mathbf{B}_{T_C}$ provide a linear model to describe the behavior of $\frac{\partial T_C}{\partial t}$ as a function of deviations from the current operating point:

$$\frac{\partial T_C}{\partial t} = \mathbf{A}_{T_C}\mathbf{x}' + \mathbf{B}_{T_C}\mathbf{u}'$$

where $\mathbf{x}' = \mathbf{x} - \mathbf{x}_{\text{nom}}$ and $\mathbf{u}' = \mathbf{u} - \mathbf{u}_{\text{nom}}$. The same process can be repeated for all states of $\mathbf{x}$, eventually producing the final linear form for the entire system:

$$\dot{\mathbf{x}} = \mathbf{A}\mathbf{x}' + \mathbf{B}\mathbf{u}'$$

Which can subsequently be converted into discrete form.

Linearization of the Chemical Reaction Term

Due to the nonlinear behvaior of the chemical oxidation reaction, a dedicated procedure was created to evaluate derivatives of the $\left(\frac{\partial \alpha_s}{\partial t}\right)_{rxn}$ term. During the standard linearization procedure, the chemical reaction term is subject to differentiation by three properties: T, α_s, and ξ_{ox}. MATLAB®'s `differentiate` function is employed in each case to provide a numerical approximation of the derivative, rather than seeking an analytical expression.

For $\frac{\partial}{\partial T}\left(\frac{\partial \alpha_s}{\partial t}\right)_{rxn}$, $\left(\frac{\partial \alpha_s}{\partial t}\right)_{rxn}$ is evaluated at $\alpha_{s,\text{nom}}$, $\xi_{ox,\text{nom}}$, and temperature intervals of 100 K between 0 K and 1400 K. A linearly interpolated function is generated for $\left(\frac{\partial \alpha_s}{\partial t}\right)_{rxn}$ on the basis of T, after which the `differentiate` function estimates an approximate derivative with respect to temperature at T_{nom}. This derivative is then provided to the linearized model formulation of the previous section.

Parallel procedures are utilized to estimate $\frac{\partial}{\partial \alpha_s}\left(\frac{\partial \alpha_s}{\partial t}\right)_{rxn}$ and $\frac{\partial}{\partial \xi_{ox}}\left(\frac{\partial \alpha_s}{\partial t}\right)_{rxn}$. In the case of the former, T_{nom} and $\xi_{ox,\text{nom}}$ are held constant while $\left(\frac{\partial \alpha_s}{\partial t}\right)_{rxn}$ is calculated for extents of conversion ranging from 0 to 1 in intervals of 0.01; for the latter, T_{nom} and $\alpha_{s,\text{nom}}$ remain unchanged while

the oxygen mass fraction varies from 0.000001 to 0.5 in intervals of 0.01. Both the extent of conversion and oxygen mass fraction approaches subsequently employ the linear interpolation and `differentiate` approach to provide computational estimates for $\frac{\partial}{\partial \alpha_s}\left(\frac{\partial \alpha_s}{\partial t}\right)_{rxn}$ and $\frac{\partial}{\partial \xi_{ox}}\left(\frac{\partial \alpha_s}{\partial t}\right)_{rxn}$.

Oxidation Reactor Model Linearization for Approach 3

While Approaches 1 and 2 use the linear temperature formulation previously illustrated in this Appendix, the third control approach implements a revised model. The assumptions of Approach 3 include neglecting the impact of sensible energy transfers due to perceived flow balancing and ignoring the impact of oxygen concentration on rate of chemical conversion. The energy balance for Zone C, then, is approximated as:

$$\frac{\partial T_C}{\partial t} = -\frac{2\pi \Delta x k_{ins}}{m_s c_{p,s} + m_g c_{p,g}} \frac{T_C - T_{amb}}{\ln\left(r_{out} - r_o\right)} + \frac{V_s\left(\rho_{ox} - \rho_{red}\right)\Delta H_{rxn}}{\left(m_s c_{p,s} + m_g c_{p,g}\right) M_{O_2}} \left(\frac{\partial \alpha_s}{\partial t}\right)_{rxn,C}$$

and considers changes to T_C solely arising from radial losses and chemical energy production. For comparison to the unmodified linear model, $\mathbf{A}_{T_C}$ is comprised of the following components:

$$A_{T_C,T_E} = 0$$

$$A_{T_C,T_D} = 0$$

$$A_{T_C,T_C} = -\frac{2\pi \Delta x k_{ins}}{\left(m_s c_{p,s} + m_g c_{p,g}\right) \ln\left(r_{out} - r_o\right)} + \frac{V_s\left(\rho_{ox} - \rho_{red}\right)\Delta H_{rxn}}{\left(m_s c_{p,s} + m_g c_{p,g}\right) M_{O_2}} \frac{\partial}{\partial T_C}\left(\frac{\partial \alpha_s}{\partial t}\right)_{rxn,C}$$

$$A_{T_C,T_B} = 0$$

$$A_{T_C,T_A} = 0$$

$$A_{T_C,\alpha_{s,E}} = 0$$

$$A_{T_C,\alpha_{s,D}} = 0$$

$$A_{T_C,\alpha_{s,C}} = \frac{V_s\left(\rho_{ox} - \rho_{red}\right)\Delta H_{rxn}}{\left(m_s c_{p,s} + m_g c_{p,g}\right) M_{O_2}} \frac{\partial}{\partial \alpha_{s,C}} \left(\frac{\partial \alpha_s}{\partial t}\right)_{rxn,C}$$

$$A_{T_C,\alpha_{s,B}} = 0$$

$$A_{T_C,\alpha_{s,A}} = 0$$

$$A_{T_C,\xi_{ox,E}} = 0$$

$$A_{T_C,\xi_{ox,D}} = 0$$

$$A_{T_C,\xi_{ox,C}} = 0$$

$$A_{T_C,\xi_{ox,B}} = 0$$

$$A_{T_C,\xi_{ox,A}} = 0$$

And $\mathbf{B}_{T_C}$ contains:

$$B_{T_C,\dot{m}_s} = 0$$

$$B_{T_C,\dot{m}_{g,recup}} = 0$$

$$B_{T_C,\dot{m}_{g,ext}} = 0$$

These formulations illustrate how the calculation of $\frac{\partial T_C}{\partial t}$ is completely isolated from considering the effect of sensible energy from neighboring zones. As a result, Approach 3 relies solely on regulating the chemical energy supplied to the reactor to control T_C. All other zones follow the standard linearization procedure, as sensible energy considerations are necessary to balance the temperatures of the other zones.